A Multiple-Cathode, High-Power, Rectangular Ion Thruster Discharge Chamber for Increasing Thruster Lifetime

by

Joshua Lucas Rovey

A dissertation submitted in partial fulfillment
of the requirements for the degree of
Doctor of Philosophy
(Aerospace Engineering)
in The University of Michigan
2006

Doctoral Committee:

Professor Alec D. Gallimore, Chair
Professor Iain D. Boyd
Professor Ronald M. Gilgenbach
John E. Foster, NASA Glenn Research Center

I can do all things through Him who gives me strength.

Philippians 4:13

ACKNOWLEDGMENTS

This thesis represents years of work that would not be possible without the assistance, support, help, advice, and patience of many key people. First, I would like to thank my advisor, Prof. Alec Gallimore. Alec is director of PEPL, a truly extraordinary place where students come together to work on state-of-the-art equipment and hardware, solve real-world engineering problems, and become an integral part of the space propulsion research community. Thank you for responding to my persistent requests to work at PEPL and for passing around my resume when I was just a junior AERO student looking for a little lab experience, I definitely got it. Your time and knowledge (drawings on your chalk board, scrap pieces of paper, napkins, etc.) have been instrumental in helping me reach this point. I am lucky to have had an advisor who is both a mentor and a friend. Thank you.

I would also like to thank the other members of my committee for their guidance in preparing this thesis: Prof. Iain Boyd, Prof. Ron Gilgenbach, and Dr. John Foster. Any remaining errors are entirely my own. Thanks also to the Aerospace department technical and administrative staff: Terry, Tom, Dave Chris, Eric, Debbie, Suzanne, Sharon, Cindy, Margaret, and Denise.

Financial support for this research was provided by the NASA Glenn Research Center (GRC) under grant NNC04GA67G monitored by Michael Patterson, the University of Michigan Department of Aerospace Engineering through an Edward A. Stalker fellowship, Dobbins fellowship, and various graduate student instructor positions,

and the Michigan Space Grant Consortium. This support is gratefully acknowledged. Other members of NASA GRC who have aided in this research are Hani Kamhawi, George Williams, and Jim Sovey. I also thank other researchers from various institutions who have assisted with areas of this work, specifically Dr. John Williams of Colorado State University, Dr. Darren Alman of Starfire Industries, and Dr. David Ruzic of the University of Illinois.

I also thank the Kapton tape manufacturers around the globe. For those of you unfamiliar with Kapton tape (also known as magical tape), it's typically a yellowish, slightly-translucent tape used for electrical isolation of various components. However, Kapton also has many other lesser-known uses. For example, did you know that Kapton can serve as a distance marker for dart boards? In the event of an emergency, it can also be used as a band-aid. If you don't have the correct part for your computer, improvise and use Kapton. If you don't have a correctly sized coupler for a translation stage, wrap it and bind it with Kapton and never again worry about positional accuracy. This entire thesis could probably be written and bound using only Kapton. Some students hypothesize that Kapton can even patch up to 3-inch-diameter holes in a high-vacuum facility. With enough Kapton, I suppose we could even accomplish world peace. Regardless of the application, Kapton is a magical laboratory accessory that no struggling graduate student should be without.

PEPL is truly an awesome place, not because its centerpiece is the largest vacuum facility owned and operated by a University, but because of the continuous flow of gifted and talented people through its doors. First, I thank Tim Smith. I first met Tim when I was a sophomore in the Aerospace department and he was GSI for AERO 245. Later on,

Tim decided to take-on a clueless AERO student, whose only experience was raising hogs, and turn him loose on a project with a diode laser. Without Tim's willingness to teach, my PEPL experience may have never been. Thanks Tim. The previous PEPL people I've had the opportunity to learn from are Rich Hofer, Peter Peterson (who introduced me to the joys of MagNet™), Brian Beal, Mitchell Walker (whose new thrust stand platform introduced me to the joys of drilling stainless; i.e., how to make a hand-held drill smoke and master the art of bit sharpening), and Dan Herman (who made me a mu-metal hat when I needed it most). I also thank the current PEPL persons, many of whom I've had the opportunity to share lab time and space, Allen Victor, Jesse Linnell, Dave Kirtley, Kristina Lemmer, Rob Lobbia, Dan Brown, Bryan Reid, Tom Liu, Bailo Ngom, Sonca Nguyen, and Rohit Shastry. I also thank Torsten Stindl of the Universität Stuttgart and UROP student Ryan Kurkul.

I thank my family: Mom, Dad, and Erika. Your support has made this dream a reality. Lastly, and most importantly, I thank my wife, Erin. My gratitude extends far beyond the words expressed here. I will never forget our time spent studying for prelims, your difficult prelim practice question sessions, coming home late from the lab to find the door "accidentally" chained, and your hands-on engineering experience one boring Saturday afternoon. This has truly been a journey for both of us and I couldn't have asked for a better partner. May your retirement be everything you've dreamed. Finally, to our unborn child I say thank you. You have already brought so much joy and love into our lives. I cannot wait to finally meet you.

TABLE OF CONTENTS

LIST OF FIGURES

LIST OF TABLES

LIST OF APPENDICES

LIST OF ACRONYMS

5PLP	5 planar Langmuir probe
5PLPF	5 planar Langmuir probe with propellant flow
7PLP	7 planar Langmuir probe
ACLP	Axial cylindrical Langmuir probe
APLP	Axial planar Langmuir probe
CEX	Charge-exchange
CLP	Cylindrical Langmuir probe
DC	Diagnostic cylinder
DCA	Discharge cathode assembly
DCU	Dormant cathode unit
ELT	Extended life test
FEEP	Field emission electric propulsion
FMT	Functional model thruster
GRC	Glenn Research Center
HARP	High-speed axial reciprocating probe
HET	Hall-effect thruster
HiPEP	High power electric propulsion
JIMO	Jupiter icy moons orbiter
JPL	Jet Propulsion Laboratory
L/D	Length-to-diameter

LaB_6	Lanthanum hexaboride
LEO	Low Earth orbit
LVTF	Large vacuum test facility
MCDC	Multiple-cathode discharge chamber
MFP	Mean free path
Mo	Molybdenum
MPD	Magnetoplasmadynamic
NASA	National Aeronautics and Space Administration
NEAT	New England affiliated technologies
NEP	Nuclear electric propulsion
NEXIS	Nuclear electric xenon ion system
NEXT	NASA evolutionary xenon thruster
NSTAR	NASA solar electric propulsion technology and applications readiness
OD	Outer diameter
OML	Orbital motion limited
PEPL	Plasmadynamics and Electric Propulsion Laboratory
PIT	Pulse-inductive thruster
PLP	Planar Langmuir probe
PPT	Pulsed-plasma thruster
RPA	Retarding potential analyzer
SPT	Stationary plasma thruster
TA	Test article

LIST OF SYMBOLS

Constants

e	Elementary charge (1.60×10^{-19} C)
g_e	Gravitational acceleration at Earth's surface (9.81 m/s^2)
k_B	Boltzmann's constant (1.38×10^{-23} J/K)
m_e	Electron mass (9.11×10^{-31} kg)
M_i	Xenon ion mass (2.18×10^{-25} kg)
R	Specific gas constant for xenon (63.3 J/kg-K)

Variables

A	Orifice area (m^2)
A_c	Collector area (m^2)
A_p	Langmuir probe area (m^2)
$\vec{B}$	Magnetic field (T)
B	Magnetic field magnitude (T)
$B_{1,2,3,4}$	Numerical coefficients
B_x, B_y, B_z	Magnetic field components (T)
$\vec{E}$	Electric field (V/m)
E	Energy (eV)
E_a	Axial electric field component (V/m)
E_{Bohm}	Bohm energy criteria (eV)
E_i	Impacting ion energy (eV)

E_r	Radial electric field component (V/m)
E_s	Sublimation energy (eV)
E_{th}	Threshold energy (eV)
$\vec{F}$	Force (N)
F_T	Thrust (N)
f(V)	Ion voltage distribution function
I	Probe current (A)
I_{emag}	Electromagnet current (A)
I_i	Ion current (A)
I_{si}	Ion saturation current (A)
I_{sp}	Specific impulse (s)
J_b	Beam current (A)
J_d	Discharge current (A)
J_g	Grid-plane current ($J_b + J_s$) (A)
J_s	Collection grid current (A)
$\vec{j}$	Current density (A/m^2)
j	Initial ion current density (A/m^2)
j_{dbl}	Doubly-charged ion current density (A/m^2)
j_{sngl}	Singly-charged ion current density (A/m^2)
j_{total}	Total ion current density (A/m^2)
j_z	Attenuated ion current density (A/m^2)
K	Constant
K_0,K_1,K_2	Exponential fit coefficients

K_n	Knudsen number
m_f	Final rocket mass (kg)
m_i	Initial rocket mass (kg)
m_p	Propellant mass (kg)
m_1	Incident atom mass (kg)
m_2	Target atom mass (kg)
$\dot{m}$	Mass flow rate (kg/s)
$\dot{m}_{sccm}$	Mass flow rate (sccm)
$\hat{\dot{m}}$	Reduced mass flow rate (equivalent Amps)
n_{dbl}	Doubly-charged ion number density (m^{-3})
n_e	Electron number density (m^{-3})
n_i	Ion number density (m^{-3})
n_n	Neutral number density (m^{-3})
n_{sngl}	Singly-charged ion number density (m^{-3})
n_{total}	Total ion number density (m^{-3})
P_b	Base pressure (Torr)
P_c	Corrected pressure (Torr)
P_i	Indicated pressure (Torr)
p	Neutral pressure (Pa)
q	Ion charge (Coulombs)
r	Langmuir probe radius (m)
r_e	Maxwellian-electron cyclotron radius (m)
r_h	Hybrid radius (m)

r_i	Ion cyclotron radius (m)
r_p	Primary-electron cyclotron radius (m)
S	Erosion rate (μm/khr)
T	Neutral temperature (K)
T_e	Electron temperature (eV)
T_i	Ion temperature (eV)
t	Time (s)
$\vec{u}$	Propellant gas velocity (m/s)
u	Neutral velocity (m/s)
$\overline{u}_e$	Exhaust velocity (m/s)
$\vec{v}$	Ion velocity (m/s)
V	Probe voltage (V)
V_d	Discharge voltage (V)
V_f	Floating potential (V)
V_k	Keeper potential (V)
V_p	Plasma potential (V)
v_a	Axial velocity component (m/s)
v_{therm}	Thermal velocity (m/s)
v_i	Average ion velocity (m/s)
v_r	Radial velocity component (m/s)
$v_\circ$	Perpendicular velocity component (m/s)
$\vec{x}$	Spatial location (m)
x_a	Axial location (m)

x_r	Radial location (m)
Y	Sputtering yield (atoms/ion)
Z_i	Ion charge-state
z	Attenuation pathlength (m)
Γ_i	Ion flux (ions/m^2-s)
Δv	Mission energy requirement (m/s)
ε_b	Ion production cost (W/A)
ζ_p	Primary-electron energy (V)
η_{ud}	Propellant utilization efficiency (%)
θ	Impacting ion angle of incidence w.r.t. keeper normal (degrees)
θ_{thru}	Through-sheath ion angle of incidence (degrees)
θ_{pre}	Pre-sheath ion angle of incidence (degrees)
λ	Mean free path of charged particles (m)
λ_{CEX}	Charge-exchange mean free path (m)
λ_D	Debye length (m)
ξ	Non-dimensional current correction
ρ_2	Target material density (kg/m^3)
σ	Gas scalar conductivity ((Ω-m)$^{-1}$)
σ_{ce}	Charge-exchange collision cross section (m^2)
ϕ_i	High-voltage optics ion transparency (~70%)
$\hat{\phi}_i$	Ion collection grid ion transparency

ABSTRACT

Ion thrusters are high-efficiency, high-specific impulse space propulsion systems proposed for deep space missions requiring thruster operational lifetimes of 7-14 years. One of the primary ion thruster components is the discharge cathode assembly (DCA). The DCA initiates and sustains ion thruster operation. Contemporary ion thrusters utilize one molybdenum keeper DCA that lasts only ~30,000 hours (~3 years), so single-DCA ion thrusters are incapable of satisfying the mission requirements. The aim of this work is to develop an ion thruster that sequentially operates multiple DCAs to increase thruster lifetime. If a single-DCA ion thruster can operate 3 years, then perhaps a triple-DCA thruster can operate 9 years.

Initially, a multiple-cathode discharge chamber (MCDC) is designed and fabricated. Performance curves and grid-plane current uniformity indicate operation similar to other thrusters. Specifically, the configuration that balances both performance and uniformity provides a production cost of 194 W/A at 89% propellant efficiency with a flatness parameter of 0.55.

One of the primary MCDC concerns is the effect an operating DCA has on the two dormant cathodes. Multiple experiments are conducted to determine plasma properties throughout the MCDC and near the dormant cathodes, including using "dummy" cathodes outfitted with plasma diagnostics and internal plasma property mapping. Results are utilized in an erosion analysis that suggests dormant cathodes suffer a maximum pre-operation erosion rate of ~5-15 μm/khr (active DCA maximum erosion is

70 μm/khr). Lifetime predictions indicate that triple-DCA MCDC lifetime is approximately 2.5 times longer than a single-DCA thruster. Also, utilization of new keeper materials, such as carbon graphite, may significantly decrease both active and dormant cathode erosion, leading to a further increase in thruster lifetime.

Finally, a theory based on the near-DCA plasma potential structure and propellant flow rate effects is developed to explain active DCA erosion. The near-DCA electric field pulls ions into the DCA such that they bombard and erode the keeper. Charge-exchange collisions between bombarding ions and DCA-expelled neutral atoms reduce erosion. The theory explains ion thruster long-duration wear-test results and suggests increasing propellant flow rate may eliminate or reduce DCA erosion.

CHAPTER 1:

INTRODUCTION

Ion thrusters are high-efficiency, high-specific impulse advanced space propulsion systems that are being proposed for ambitious deep space missions that require thruster operational lifetimes of 7-14 years.[1-6] One of the primary components of an ion thruster is the discharge cathode assembly (DCA). The DCA is responsible for initiating and sustaining ion thruster operation. Contemporary ion thrusters are designed for and utilize only one DCA. Unfortunately, a molybdenum (Mo) keeper DCA can only last 3-5 years,[7-10] therefore contemporary single-DCA ion thrusters are incapable of satisfying the 7-14 year mission requirement. The aim of this work is to develop an ion thruster that sequentially operates multiple DCAs to increase thruster lifetime. If a single-DCA ion thruster can operate 3-5 years, then perhaps a triple-DCA thruster can operate 9-15 years.

The following chapters describe the design and characterization of a multiple-cathode ion thruster discharge chamber and the ability of multiple DCAs to increase thruster lifetime. However, before diving headfirst into the in-depth experimental descriptions and analyses, a basic overview of rocketry fundamentals, the physics of ion thrusters, and the contribution of this thesis is presented.

1.1 Rocket Propulsion Fundamentals

Hero of Alexandria is credited with inventing the rocket principle around 67 AD, however, the early Tang dynasty, which lasted from 618 to 907 AD, is typically credited with the invention of the rocket.[11,12] Regardless of the semantics associated with rocket principles and rocket invention, it is well known that the Chinese were using rockets during the thirteenth century.[11,12] In spite of this early start, much of modern rocketry has been developed in only the last century and the fathers of modern rocketry are arguably Konstantin Eduardovitch Ziolkovsky, Robert Hutchings Goddard, and Hermann Oberth.[11-13]

In a very general sense, propulsion is the act of driving, propelling, pushing, or changing the motion of a body. More specifically, jet propulsion is a method of propelling a body by expelling matter at high velocity, called the exhaust velocity, $\bar{u}_e$. In these systems propulsion is generated by the reaction force imparted by the momentum of the expelled high-velocity matter. Rocket propulsion is a form of jet propulsion in which the expelled matter is stored on or in the body and called propellant. Modern day rocket propulsion is divided into different categories, such as chemical, electric, and nuclear rocket propulsion.

One of the main performance parameters of a rocket is its specific impulse, I_{sp}, which is related to the rocket thrust, F_T, propellant flow rate, $\dot{m}$, exhaust velocity, $\bar{u}_e$, and gravitational acceleration at the Earth's surface, g_e, through Eqn. 1-1.[14-16]

$$I_{sp} \equiv \frac{F_T}{\dot{m} g_e} = \frac{\bar{u}_e}{g_e} \qquad \textbf{Eqn. 1-1}$$

Specific impulse is a measure of the amount of thrust a rocket makes per unit mass flow rate of propellant. Physically, this is typically described as the "miles-per-gallon" rating of a rocket because it describes how efficiently the rocket uses propellant.

Ziolkovsky is credited with the famous rocket equation, Eqn. 1-2, which relates the final and initial rocket mass, m_f and m_i, respectively, to the mission energy requirement, Δv, and the product of the gravitational acceleration at the Earth's surface and the rocket specific impulse.[14-16] Furthermore, Eqn. 1-3 relates the propellant mass, m_p, to the initial and final mass of the rocket.[14-16]

$$\frac{m_f}{m_i} = \exp\left(\frac{-\Delta v}{g_e I_{sp}}\right) \qquad \textbf{Eqn. 1-2}$$

$$m_i = m_f + m_p \qquad \textbf{Eqn. 1-3}$$

Eqn. 1-2 is plotted in Figure 1-1 for various space missions, such as low-earth orbit (LEO) to Mars and the Jupiter Icy Moons Orbiter (JIMO), which is a nuclear powered mission designed to explore three moons of Jupiter.[2] Velocity values given in the legend of this figure are the energy requirement for the mission.[16] Also shown are the state-of-the-art specific impulse values for chemical and nuclear electric propulsion (NEP) systems.

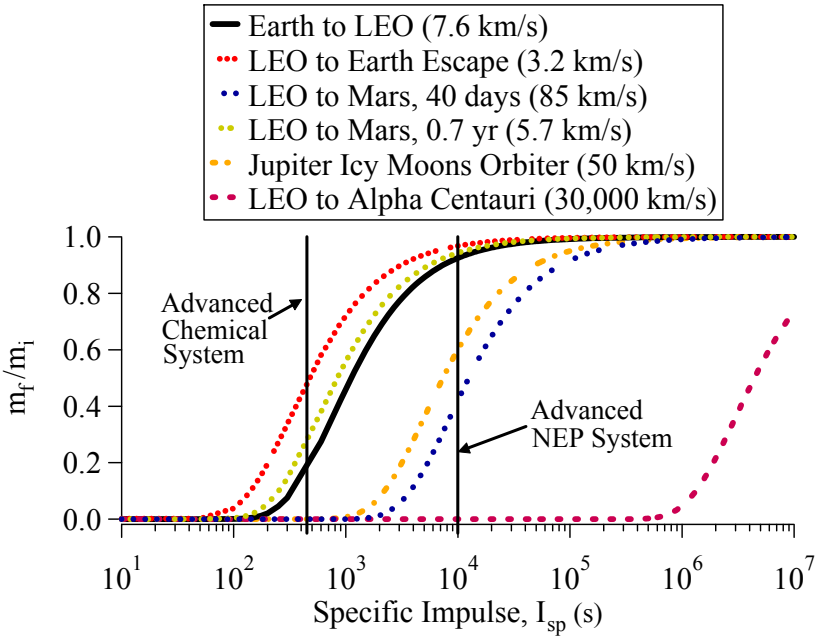

Figure 1-1: Variation of mass ratio with specific impulse for a variety of missions. Also shown is the state-of-the-art in advanced nuclear electric propulsion (NEP) and chemical propulsion systems.

From Figure 1-1 it becomes obvious that more energetic missions (i.e., larger Δv) require a larger specific impulse. Besides our Sun, Alpha Centauri is the closest star to Earth at a distance of 4.3 light years, which means it takes light, traveling at 670,000,000 miles-per-hour, 4.3 years to reach Earth. This distance along with the figure above show how difficult inter-planetary missions are and how truly far we are from leaving our own solar system and exploring other star systems.

1.2 Electric Propulsion

Chemical propulsion systems rely on a chemical reaction to energize the propellant and produce the required high exhaust velocities. Therefore chemical systems are inherently limited by the amount of energy stored within the chemical bonds of the propellant molecules. A familiar chemical system is the Space Shuttle, which uses

chemical solid and liquid rockets. Evidence of a chemical reaction is obvious during Space Shuttle liftoff because of the visible fire and smoke.

In electric propulsion (EP) systems (for example ion thrusters), electrical energy accelerates the propellant to high velocities. Therefore EP offers a significant advantage over chemical rockets because the exhaust velocity is not limited by the amount of energy released from the propellant chemical bonds. This translates into higher exhaust velocities and a higher specific impulse. However, EP systems do not have the large thrust levels associated with chemical rockets due to the limited spacecraft power supply. Therefore, EP is ideal for purely space-based missions, such as orbit-transfer, station-keeping of satellites, and deep-space missions.

As shown in Figure 1-1, EP, with its higher specific impulse, increases the mass ratio of the rocket and also makes more energetic missions possible. For this reason EP is sometimes referred to as a mission-enabling technology. A large mass ratio is important to mission planners because it decreases the amount of propellant required for the mission and increases the amount of deliverable payload. Decreasing the required mission propellant is important in terms of reducing mission costs, while increasing deliverable payload allows more scientific equipment to be used on the spacecraft. Furthermore, the high specific impulse of EP systems increases the lifetime of orbiting satellites by providing more station-keeping maneuvers for a given amount of propellant.

Electric propulsion is typically divided into three main categories: electrothermal, electromagnetic, and electrostatic propulsion.[14,17] Each of these divisions is discussed in more detail in the following sections.

1.2.1 Electrothermal Propulsion

In an electrothermal propulsion system, power provided by the spacecraft is used to electrically heat the propellant gas. A nozzle is then used to expand the gas and convert its thermal energy to directed kinetic energy. This type of EP is most related to chemical propulsion in that a hot gas is expanded through a nozzle to generate thrust. Electrothermal systems are typically classified by the way in which the propellant is heated, either resistively or through an arc discharge.[17]

An electrothermal system that resistively heats the propellant by passing it over an electrically heated surface is called a resistojet. Resistojets have been operated with various propellants, specifically ammonia and hydrogen, with a specific impulse ranging from 250 – 850 s at power levels ranging from 10 W up to 30 kW with thrust efficiencies greater than 85%.[17] More recently, resistojets used on commercial satellites have a specific impulse greater than 300 s at power levels of 400-800 W.[18]

The second form of electrothermal propulsion heats the propellant by passing it through an arc discharge and is called an arcjet. With this type of propulsion, an arc is established between an anode and cathode electrode in the throat of the nozzle. As propellant passes through the throat it is heated and subsequently accelerated to high velocity through the expanding portion of the nozzle.[17] Arcjets can operate on a variety of propellants[19] and have been proposed for a variety of space applications, including station-keeping and a manned mission to Mars.[20] These types of systems typically have a specific impulse between 500 – 2000 s.[17,21,22]

1.2.2 Electromagnetic Propulsion

Electromagnetic propulsion accelerates ionized gas by the interaction of currents driven through the gas with either self or applied magnetic fields. In its simplest form, an electromagnetic accelerator contains an ionized gas with uniform velocity and applied electric and magnetic fields. The gas velocity, electric field, and magnetic field are mutually perpendicular. If the gas has a scalar conductivity, σ, then the current density, $\vec{j}$, is given by Eqn. 1-4. The interaction of the current and the magnetic field is governed by the well known Lorentz force equation, Eqn. 1-5. The Lorentz force accelerates the gas along the same direction as its velocity.

$$\vec{j} = \sigma\left(\vec{E} + \vec{u} \times \vec{B}\right) \qquad \textbf{Eqn. 1-4}$$

$$\vec{F} = \vec{j} \times \vec{B} \qquad \textbf{Eqn. 1-5}$$

Different types of electromagnetic propulsion systems are magnetoplasmadynamic (MPD) thrusters, pulse-inductive thruster (PITs), and pulsed-plasma thruster (PPTs). Because electromagnetic thrusters do not accelerate an ionized gas with an electric field, these types of devices can produce high current densities and are not space-charge limited.

MPD thrusters have an annular anode with a concentric cathode. An arc between the anode and cathode ionizes propellant and drives the current. An azimuthal magnetic field is supplied either by the current returning to the cathode (self-field MPD thruster) or by external means (applied field thruster). Interaction of the magnetic field with the radial discharge current produces an axial electromagnetic body force, the Lorentz force, on the ionized propellant. This force causes the gas to be accelerated and expelled, generating thrust.

1.2.3 Electrostatic Propulsion

Electrostatic propulsion uses electric fields to accelerate and expel ionized propellant to generate thrust. Some of the devices in this area of electric propulsion are Hall effect thrusters (HETs), gridded ion thrusters, colloid thrusters, and field effect electric propulsion (FEEP). The force on a charged particle in an electric field is given by Eqn. 1-6.

$$\vec{F} = q\vec{E} \qquad \textbf{Eqn. 1-6}$$

Gridded ion thrusters are the focus of this work and an entire section is devoted to the physics and operation of an ion thruster. The following section describes another type of electrostatic propulsion device, the HET, shown in Figure 1-2.

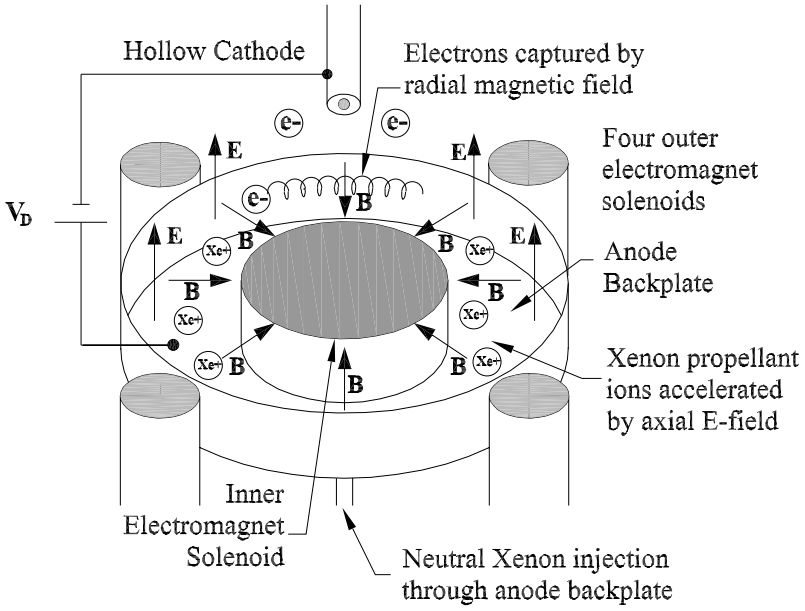

Figure 1-2: Schematic of a Hall effect thruster (HET).

A HET is a coaxial device that utilizes a radial magnetic field crossed with an axial electric field. Electrons emitted by the cathode drift in the $\vec{E} \times \vec{B}$ direction, forming an azimuthal Hall current. Neutral xenon atoms injected through the anode collide with

these electrons producing xenon ions that are subsequently accelerated by the electric field to produce thrust. A mixture of electrons and ions in the acceleration zone creates a quasi-neutral plasma and thus the operation of the HET is not space-charge limited in ion current density as is the case with gridded ion thrusters.

1.3 Ion Thruster Physics

Ion thrusters are the subject of this thesis and are discussed in detail in the following sections. Ion thruster operation can be divided into three main processes or stages. The first stage is the generation of electrons. Next, electrons collide with neutral propellant atoms (in this case xenon) to generate an ionized gas called plasma. This type of plasma generation is called electron-bombardment. Finally, the third stage extracts the positively-charged xenon atoms with an electric field. A substantial overview of the technology of electron-bombardment ion thrusters is given by Kaufman.[23] Schematics of an ion thruster and ion thruster operation are shown in Figure 1-3 and Figure 1-4, respectively. Typical ion thruster potentials and temperatures are shown in Figure 1-5 and Figure 1-6, respectively.[24]

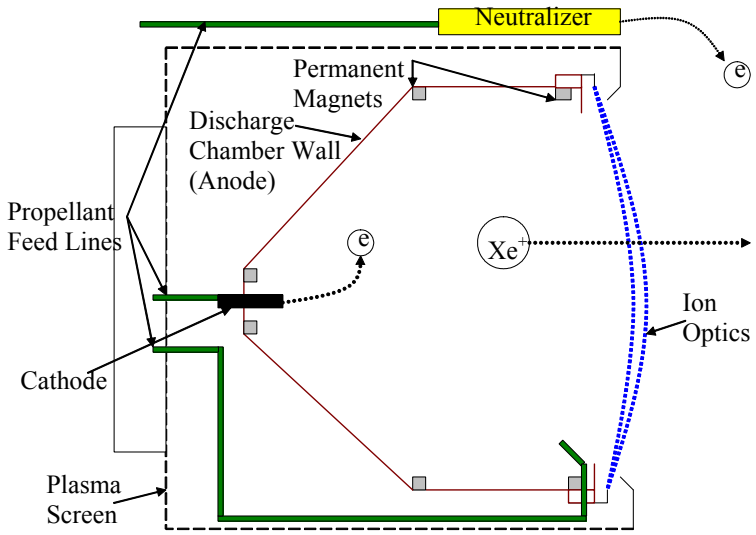

Figure 1-3: Schematic of an ion thruster.

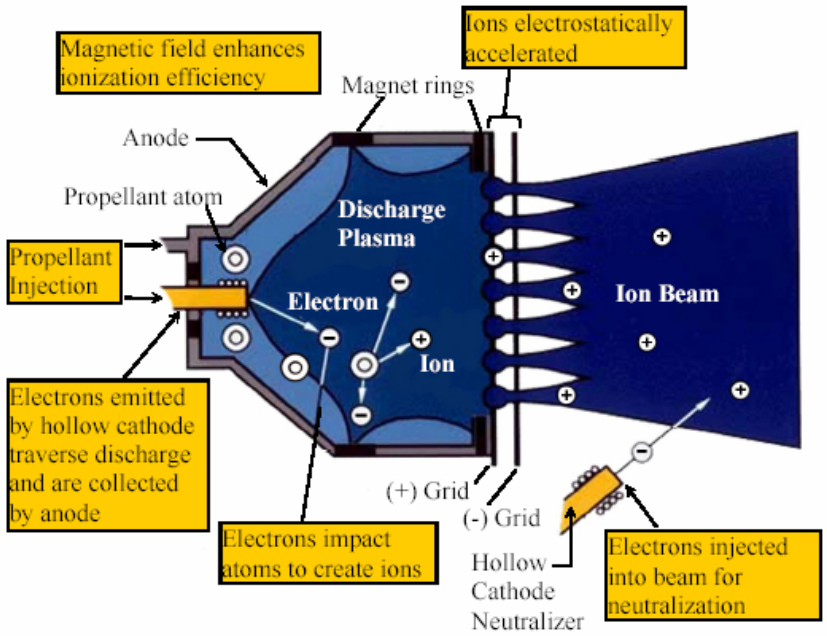

Figure 1-4: Schematic of ion thruster operation (used with NASA GRC permission).

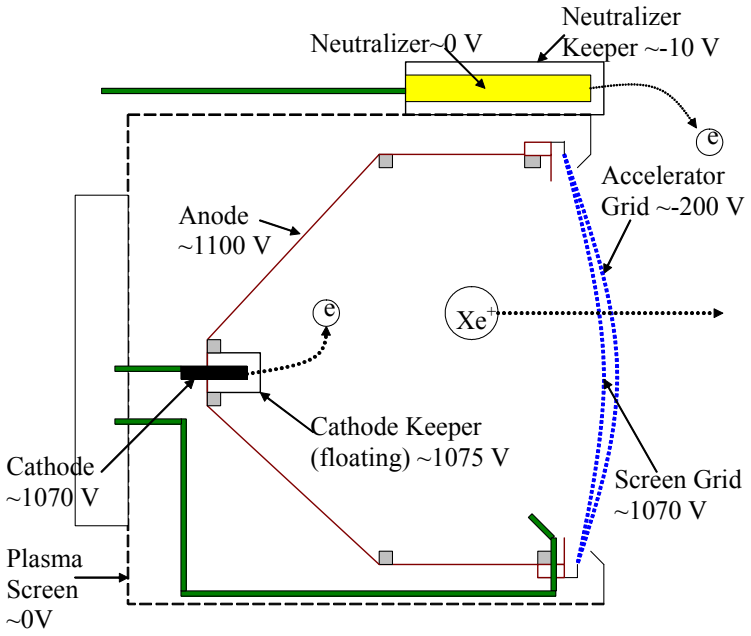

Figure 1-5: Typical potentials of an ion thruster. Potentials referenced with respect to the neutralizer cathode.

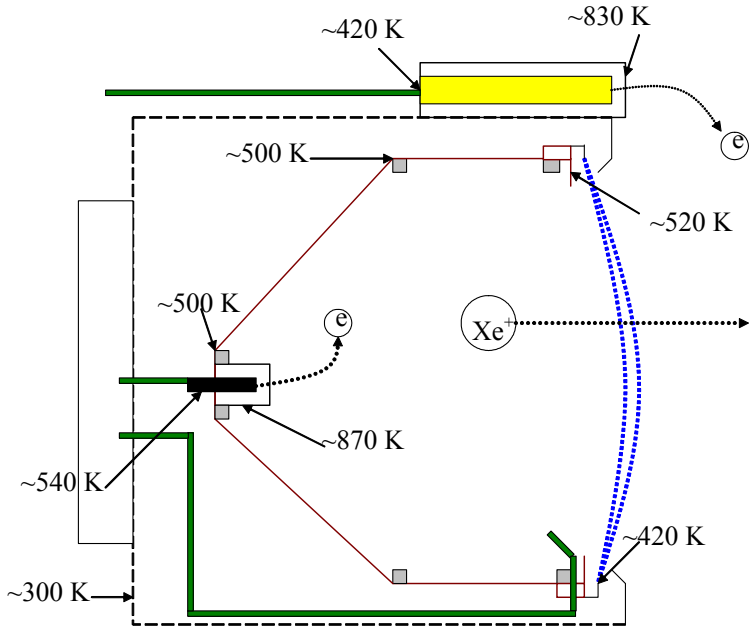

Figure 1-6: Typical temperatures of an ion thruster.[24]

The first stage of an ion thruster requires the generation of electrons and is typically accomplished with a device called a cathode. Previous ion thrusters utilized a

wire filament cathode, which emits electrons when sufficiently heated with current. Contemporary thrusters use hollow cathodes with a barium-oxide impregnated insert and future thrusters may use lanthanum hexaboride (LaB_6) hollow cathodes[25] or even microwave cathodes.[26] Ion thrusters that operate without a hollow cathode and utilize microwaves to generate a plasma discharge are also being investigated.[27-31] The basic layout of a hollow cathode is shown in Figure 1-7.

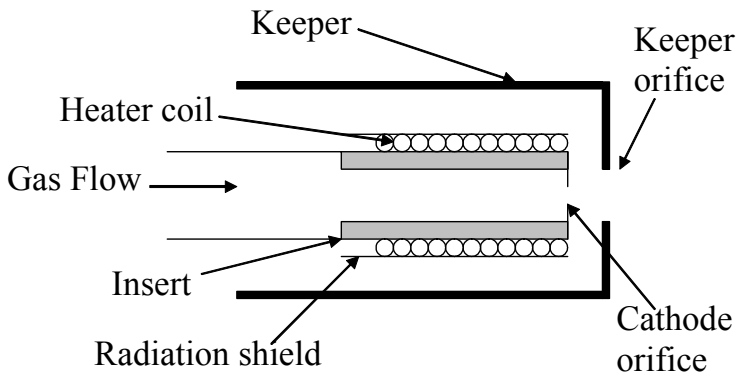

Figure 1-7: Schematic of a hollow cathode with keeper (DCA).

Hollow cathodes are ignited by first supplying a current to the heater coil, which heats the insert to approximately 1000 °C. Next, gas flow is supplied while a potential is applied between the cathode and an external anode. This causes electrons to be thermionically emitted from the insert and then interact with the gas flow, creating plasma inside the cathode tube. At this point the cathode becomes self-sustaining and the heater current is eliminated because plasma ions recombine at the insert, depositing their energy and sustaining the cathode insert temperature required for electron emission. Electrons are pulled through the cathode orifice by the potential between the cathode and anode. Emitted electrons enter the discharge chamber to have ionization collisions with neutral atoms and create the discharge plasma. A keeper electrode can also be placed

around the cathode to assist cathode ignition and to protect the cathode from external ion bombardment. The cathode and surrounding keeper utilized inside the discharge chamber of an ion thruster is called the discharge cathode assembly (DCA).

During the second stage of ion thruster operation, the emitted electrons from the cathode collide with neutral propellant atoms to create an ionized gas called plasma. This process occurs within the discharge chamber of the ion thruster, which typically has a cylindrical "coffee can" or cylindrical-conical shape. However, some new ion thrusters are being constructed with a rectangular discharge chamber.[32] Emitted electrons leave the cathode and accelerate toward the anode potential surface, which is typically the discharge chamber wall. As electrons move toward the anode they suffer collisions with neutral propellant atoms and some of these collisions result in ionization of the neutral atoms. An ionizing collision causes the neutral atom to lose an electron and become an ion. Because of these collisions, two types of electrons are present within the discharge chamber, primary- and Maxwellian-electrons.

Primary-electrons are cathode emitted electrons that have not undergone a collision and have been accelerated by the full anode-to-cathode potential difference. The second group, Maxwellian-electrons, is present due to the inelastic collisions between primary-electrons and neutral atoms. These collisions tend to reduce the energy of the primary-electrons and an electron is no longer considered a primary-electron if it has undergone an inelastic collision. The inelastic collision process of most interest in ion thrusters is ionization, which results in the release of low-energy secondary-electrons. Primary-electrons that have undergone inelastic collisions and secondary-electrons released during ionization thermalize to form an electron population with a nearly

Maxwellian energy distribution. The temperature of this distribution is typically a few eV (~2-5 eV) and these two populations can simultaneously exist due to the low interaction rate between primary- and Maxwellian-electrons.[33,34]

Neutral density within the discharge chamber is low enough (~10^{18} m^{-3}) that the ionization mean free path for primary-electrons in neutral atoms is significantly larger than the dimensions of the thruster. In order to increase the probability of electron-neutral ionization collisions, a magnetic field is created and sustained within the interior volume of the discharge chamber to restrict the access of primary-electrons to anode potential surfaces. Permanent magnets are typically used to create the magnetic field, but electromagnets have also been utilized.[35-37] Previous ion thrusters used a divergent magnetic field, while contemporary thrusters employ a ring-cusp magnetic field configuration. These configurations are shown in Figure 1-8.

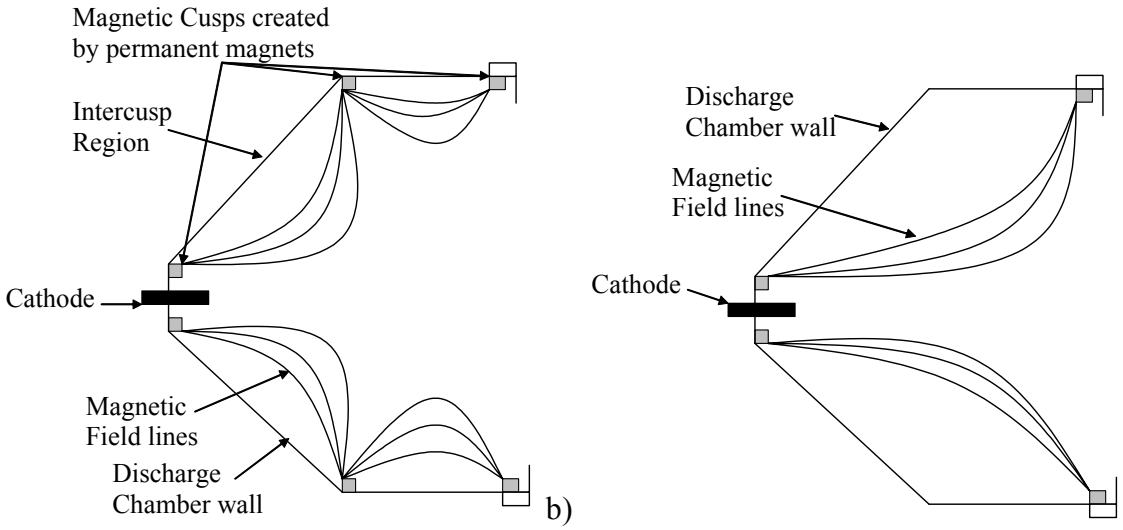

Figure 1-8: Comparison of a) ring-cusp and b) divergent ion thruster magnetic field configurations.

Ring-cusp configurations have been shown to increase the performance of an ion thruster due to stronger magnetic fields near the anode potential surfaces, which aid ion and

primary-electron containment.[38-40] Furthermore, ring-cusp thrusters have a more uniform beam profile, which reduces centerline ion optics grid erosion and increases grid lifetime.[41]

Energetic primary-electrons leaving the cathode are confined to spiral along the magnetic field lines with a cyclotron radius defined by Eqn. 1-7. [38,42,43]

$$r_p = \frac{m_e v_\perp}{|q|B} \qquad \textbf{Eqn. 1-7}$$

In this equation, r_p is the primary-electron cyclotron radius, m_e is the mass of an electron, q is the charge, B is the magnetic flux, and $v_\perp$ is the velocity of the electron perpendicular to the magnetic field line. Lower-energy Maxwellian-electrons diffuse across the field lines into the intercusp region more readily[38] and are known to obey classical diffusion, not Bohm diffusion.[44] The effective area for electron collection in the magnetic cusps is larger for low-energy electrons than it is for higher-energy primaries.[45-50] The ratio of these areas is found to agree well with the ratio of the hybrid cyclotron radius, Eqn. 1-8, to the primary cyclotron radius, Eqn. 1-7.[38]

$$r_h = \sqrt{(r_e r_i)} \qquad \textbf{Eqn. 1-8}$$

In this equation, r_h is the hybrid radius, r_e is the Maxwellian-electron cyclotron radius, and r_i is the ion cyclotron radius. The result in a ring-cusp thruster is that higher-energy primary-electrons bound to anode intersecting field lines are reflected by the cusps due to mirroring effects and a limited conduction area. This effectively confines the higher-energy primary-electrons, leading to more ionization collisions and more efficient production of plasma ions.

The last stage of ion thruster operation is the acceleration and expulsion of ions from the discharge chamber to generate thrust. Ions created within the discharge chamber preferentially drift to the acceleration grids (the ion optics) at the ion-acoustic or Bohm velocity,[38,51,52] where the Bohm energy criterion for a purely Maxwellian plasma is given in Eqn. 1-9.[53]

$$E_{Bohm} \geq \frac{T_e}{2} \qquad \textbf{Eqn. 1-9}$$

Contemporary ion thrusters utilize a two-grid system for the ion optics, a screen grid and accelerator grid. The grids of the ion optics are spaced a few millimeters apart and have a potential difference of ~1200 V, however, this value changes depending on thruster operating condition, size, and power-rating. The screen grid is on the discharge chamber side of the optics and is maintained at cathode potential. As ions reach the screen grid they are accelerated out of the accelerating grid to very high velocity (~30 km/s or 67,000 miles-per-hour). In order to obtain such high ion exhaust velocities, the entire discharge chamber and cathode surfaces must be biased over 1000 V above space ground as shown in Figure 1-5.

To prevent space-charge build-up of the thruster and spacecraft, the high-velocity ion exhaust beam is neutralized using a hollow cathode called the neutralizer (shown in Figure 1-3 and Figure 1-4). The neutralizer is a hollow cathode placed external to the thruster that emits electrons into the ion beam. Without this device a spacecraft obtains a net negative charge due to the loss of positive charge through the ion beam. Ion thruster operation without a neutralizer can cause beam ions to reverse direction and impinge upon the spacecraft. To keep neutralizer emitted electrons from backstreaming and

entering the thruster discharge chamber, the accelerator grid is biased a few hundred volts below space ground.

1.4 Motivation

NASA's Project Prometheus is advancing the future of space exploration by developing NEP technology for deep space missions. Ion thrusters are high-efficiency high-specific impulse propulsion systems that are being proposed as the primary propulsion source for such missions. An ion thruster that can satisfy the mission requirements must have long life, high-power, and high-specific impulse. NASA Glenn Research Center (GRC) and Jet Propulsion Laboratory (JPL) have both developed such an ion thruster through the High Power Electric Propulsion (HiPEP) and Nuclear Electric Xenon Ion System (NEXIS) projects, respectively.[32,54-61] Because an ion thruster must operate continuously for perhaps as long as 7-14 years for Prometheus-class missions,[1-6] assessing and increasing thruster lifetime is of foremost importance.

The potential failure mechanisms for ion thrusters are generally classified into four categories: 1.) discharge cathode failure; 2.) neutralizer failure; 3.) ion optics failure; and 4.) electron backstreaming. Erosion of the screen and accelerator grids due to ion impingement is the primary cause of failure mode 3. As the accelerator grid apertures widen due to erosion, mode 4 becomes important because the number of backstreaming electrons increases and eventually destroys the cathode. Methods for increasing accelerator grid lifetime and reducing electron backstreaming have been developed.[62-65] Failure of the hollow cathode is the primary cause of modes 1 and 2. Hollow cathode failure is known to be caused by either depletion of the barium insert, the formation of

tungstates in the barium, or physical erosion. Physical erosion of both the discharge hollow cathode and ion optics are the primary lifetime limiting ion thruster phenomena.

Erosion of the discharge cathode has been noted in three wear tests performed on a 30-cm engine and an extended life test (ELT) on the flight spare Deep Space One NASA Solar Electric Propulsion Technology and Applications Readiness (NSTAR) ion engine.[7,8,66-72] During the first wear test, erosion of the discharge cathode was noted,[66] and the engineering solution was to utilize a sacrificial keeper maintained at an intermediate potential between the discharge cathode and anode. The subsequent 1,000-h and 8,200-h wear tests showed erosion of the DCA keeper occurring primarily from the downstream keeper face. However, during the ELT, the primary erosion location changed from the keeper downstream face to the keeper orifice. Consequently, the lifetime of the NSTAR ion thruster is limited to ~30,000 hours[7,8] and recent results suggest the NASA Evolutionary Xenon Thruster (NEXT) may have a comparable lifetime.[9,10] It is important to note that contemporary ion thruster technology utilizing Mo DCA keepers is incapable of providing Prometheus-class mission lifetimes due to discharge cathode erosion, which limits the operational life to approximately 3-5 years.[7-9]

Post-ELT analysis of the DCA further illustrates the importance of eliminating or mitigating DCA erosion.[73] The tantalum heater radiation shield is shown to have released relatively large flakes and the cathode faceplate weld has been completely eroded. Large flakes removed from the tantalum heater shield have the potential to short the ion optics, prematurely ending thruster operation. These flakes may also be responsible for the keeper-to-cathode short during the ELT. Erosion of the cathode faceplate weld can potentially allow the faceplate to detach from the cathode tube, eliminating DCA and

thruster operation. During the ELT the faceplate remained attached because thermal loads fused the faceplate to the cathode tube.[73] Post-test analysis of the cathode heater also reveals significant erosion because it was exposed to discharge plasma ion bombardment following removal of the keeper faceplate. Significant heater erosion may eliminate the ability of the thruster to initiate a plasma discharge during startup. Unrelated to ion bombardment erosion, but still cause for concern, arc tracking is noticed on the low-voltage propellant isolator screen, suggesting that joint failure due to arcing is a potential DCA failure mechanism.[73] Based on the ELT and wear-test results, the forefront of ion thruster research is concerned with determining DCA erosion mechanisms, developing methods of eliminating or mitigating them, and developing new technologies that increase thruster lifetime.

1.5 Contribution of Research

The state-of-the-art in multiple cathode electric propulsion devices consists of two previous research endeavors: a double cathode ion thruster developed by Hughes Research Laboratories[74] and the Stationary Plasma Thruster, SPT-100.[75] In order to reduce the bombardment of high-energy ions on a single cathode operated at large discharge currents, the Hughes Research Laboratories developed a discharge chamber containing two hollow cathodes. Operation of the discharge chamber was accomplished with both cathodes operating together at multiple discharge conditions, including low-discharge-current idling and operation with and without beam extraction. However, the cathodes were placed inside a plenum to facilitate uniform electron distribution, which caused significant increases in ion production cost. In fact, the plenum walls collected more ion current than was extracted in the ion beam.[74]

Results from a 5,700-h life test of the SPT-100 at JPL showed that an operating cathode can cause significant erosion of the non-operating cathode, thus reducing overall lifetime.[76-78] Propellant leaking through the inactive cathode created a "glow" discharge that produced enough ions to cause significant erosion of the dormant cathode. The unused cathode actually eroded at the higher rate. Eliminating the "glow" discharge may reduce the dormant cathode erosion, but results still indicate the inactive cathode collects an order of magnitude higher current density than the active cathode.[78]

The aim of this thesis is to investigate the ability of multiple discharge cathodes to increase ion thruster lifetime. With this approach, a new discharge cathode is ignited when the previous one fails. The hypothesis is that a triple-cathode ion thruster will increase discharge lifetime threefold, making longer mission times a possibility. The initial step of this work is to design an ion thruster discharge chamber that utilizes three sequentially operated cathodes, and this is accomplished by reviewing the design criteria for previous ion thrusters. After the discharge chamber is constructed, the thesis investigation is divided into four main parts: 1) performance, stability, and uniformity determination; 2) dormant cathode plasma property investigation; 3) internal plasma property structure mapping; and 4) ion trajectory and erosion analysis.

First, the fabricated multiple-cathode discharge chamber (MCDC) is operated to determine the performance, stability, and uniformity of the device. This work was the first operation of a high-power rectangular MCDC with centerline and off-centerline DCA operation. Changes in performance, stability, and uniformity are monitored while the MCDC is operated in a variety of configurations. The two dormant cathodes are operated electrically connected or disconnected from the MCDC electrical circuit, as well

as with or without propellant flow. Results are compared with other ion thruster discharge chambers to validate that the MCDC has similar performance and uniformity.

The second portion of this work is the investigation of the dormant cathode plasma properties. Because of the results obtained during the SPT-100 life test, the potential erosion of a dormant cathode inside a MCDC is investigated. If the dormant cathodes inside an MCDC have reduced lifetimes due to pre-operation erosion, ion thruster lifetime may not increase as much as expected. The plasma properties near the dormant cathodes in the MCDC are studied utilizing diagnostic cylinders (DCs) designed to appear similar to the active DCA, but outfitted with plasma diagnostics, such as Langmuir probes and a retarding potential analyzer. This work represents the first use of "dummy" cathode devices to study plasma properties at other possible DCA locations within a discharge chamber.

The third portion uses two-dimensional internal plasma property mapping to analyze the plasma structure in the MCDC. A high-speed probe positioning system with a single-Langmuir probe is used to map the interior plasma structure of the MCDC for both centerline and off-centerline DCA operation, as well as for various magnetic field configurations. This work is the first to complete plasma property mapping for different magnetic field configurations and show the effect of the magnetic field on the internal discharge plasma. Analysis of the results shows the variation of plasma parameters throughout the discharge chamber. Specifically, the cusp and intercusp regions are compared to show how the discharge plasma is magnetically contained. Furthermore, results in the near-DCA region show different plasma structures than the dormant cathode

locations. The variation of electron temperature throughout the discharge chamber can be used to explain all other plasma-related properties.

The final investigation uses the DC results, the plasma property mapping results presented in this work, and the plasma property data obtained by Herman[79] to analyze the erosion of the active and dormant cathodes. This work represents the first use of ion trajectory-erosion profile modeling to analyze the near-DCA plasma potential structure contribution to DCA keeper erosion and keeper erosion of dormant cathodes. Based on the ion trajectory-erosion profile results a DCA erosion theory is developed. Lastly, sputter erosion theory is used to determine if the dormant cathodes suffer pre-operation erosion and the effects of this phenomenon on the ability of a MCDC to increase ion thruster discharge life.

CHAPTER 2:
MULTIPLE-CATHODE DISCHARGE CHAMBER DESIGN

In an effort to extend the lifetime of an ion thruster, a multiple-cathode discharge chamber (MCDC) that operates three discharge cathode assemblies (DCAs) sequentially is designed and fabricated. One important component of an ion thruster is a properly designed discharge chamber magnetic field. As previously described, the ion thruster magnetic field is responsible for confining electrons and increasing their path length so that ionization collisions become more probable.[38,74] Investigation of various MCDC magnetic field designs is initiated utilizing the NASA Evolutionary Xenon Thruster (NEXT) ring-cusp magnetic field topology. Several MCDC ring-cusp magnetic field designs are investigated and "graded" based on a set list of criteria. Each design is solved numerically using the 3D magnetostatic code MagNet™ 6.0, which provides a magnetic field topology from which each design is evaluated. The following sections describe the criteria used to determine the selected discharge chamber magnetic field, the designs that are numerically investigated, the results of the numerical solutions, and the selected MCDC.

2.1 Design Criteria

In order to facilitate the operation of three DCAs, a discharge chamber must have a magnetic field that fulfills certain criteria. More specifically, the magnetic field must exhibit similar characteristics at each of the three DCA locations inside the chamber. The

design goal is to place each DCA in a magnetic field environment similar to the NEXT DCA. Accomplishing this objective assures that each DCA functions in a manner similar to the proven electron source of the NEXT.

The NEXT magnetic field exhibits the following characteristics, each of which the selected MCDC design is also required to meet. First, the magnetic field lines at the exit of the cathode are uniform and parallel to the cathode axis. This allows exiting electrons to essentially spiral away along the field lines.[43,80] Second, the exit of the cathode is located downstream of the peak magnetic field strength. This feature assists electrons in falling away from the cathode and out into the discharge chamber. Placing the cathode upstream of the peak field strength may lead to mirroring effects and instabilities.[43,80] Third, the magnitude of the flux at the cathode exit plane is set equivalent to the NEXT in order to facilitate the collision processes necessary for propellant ionization. Finally, the permanent magnet ring spacing is designed such that the intercusp field strength is similar to the NEXT. It is important to note that some ion thruster magnetic field designs enclose the 50 G line within the discharge chamber,[57] however, the NEXT does not satisfy this criteria and yet it operates efficiently.

2.2 Discharge Chamber Modeling: Round 1

In order to evaluate each MCDC design, the 3D magnetostatic code MagNet™ 6.0 is used to numerically solve for the magnetic field topology produced by each of the designs. Each design is modeled and solved in order to evaluate its ability to produce a NEXT-like magnetic field environment at each of the three DCA locations and throughout the discharge chamber. Many MCDC designs are modeled and are classified into three main categories based on geometry: “coffee can”, conical, and rectangular.

Examples of the “coffee can”, conical, and rectangular models are shown in Figure 2-1, Figure 2-2, and Figure 2-3, respectively.

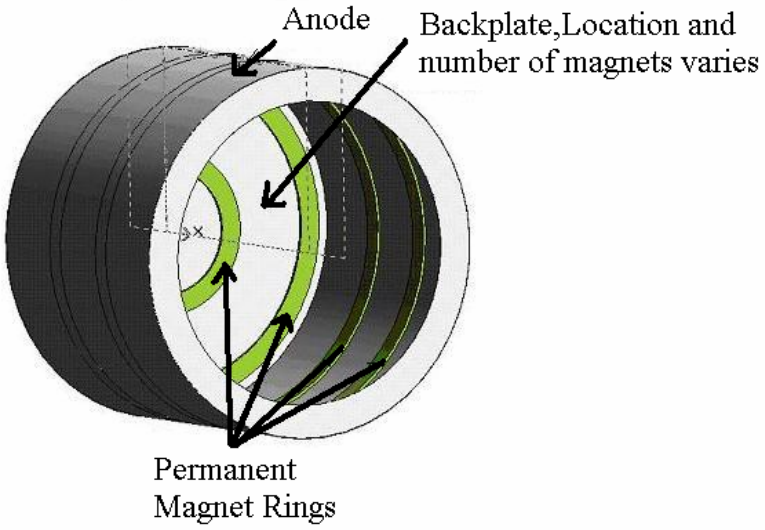

Figure 2-1: Example model for the “coffee can” geometry.

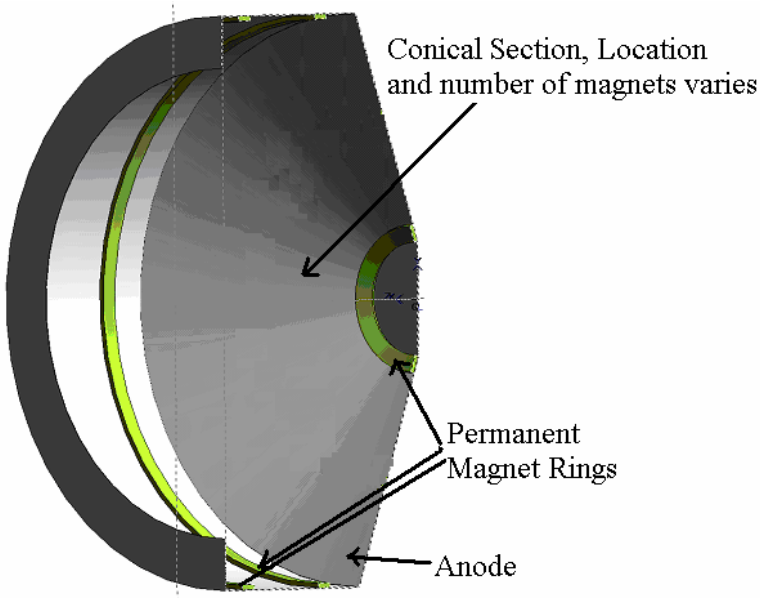

Figure 2-2: Example model for the conical geometry.

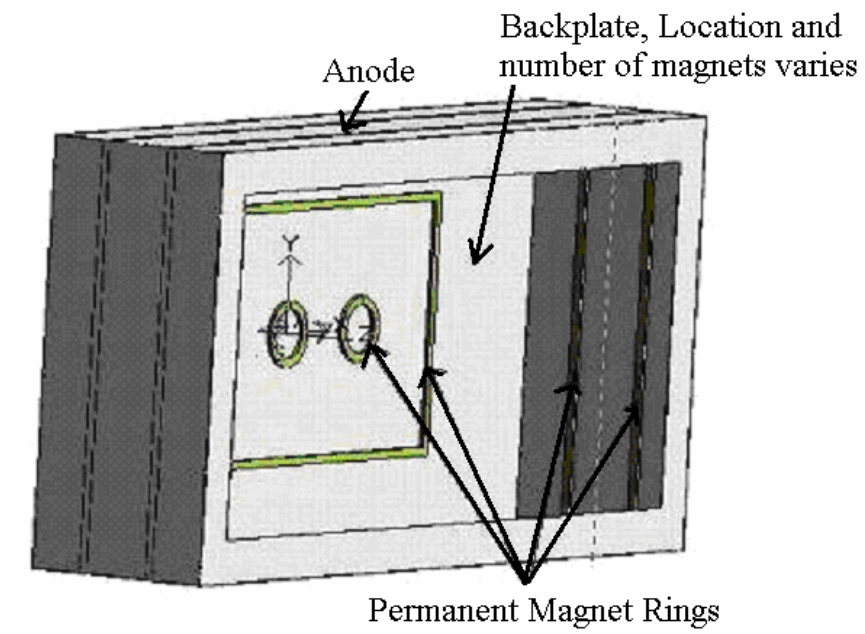

Figure 2-3: Example model for the rectangular geometry.

Each design contains a non-magnetic stainless steel anode shell with samarium cobalt permanent magnet rings located on the shell wall. The number and location of magnets on the backplate or in the conical section of the discharge chamber varies with each design and is adjusted in an attempt to obtain the desired magnetic field.

2.2.1 "Coffee Can" Geometry

Modeling of the "coffee can" MCDC is initiated by scaling up the 30-cm-diameter ring-cusp thrusters analyzed by Sovey[39] to a 50 cm ion extraction diameter. Variations of backplate permanent magnet configurations, including using either two or four backplate ring magnets, are investigated in an attempt to develop the desired magnetic field topology. The two magnet case consists of an outer ring magnet and a smaller concentric inner ring magnet with the cathodes spaced symmetrically either inside the smaller ring or between the two rings. This model is shown in Figure 2-4.

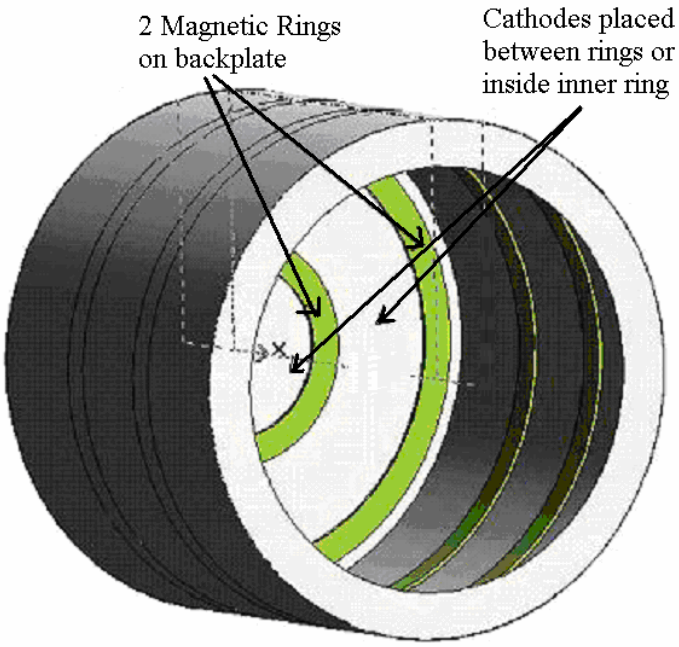

Figure 2-4: Example "coffee can" model with 2 backplate ring magnets. DCAs placed symmetrically inside the inner ring or between the 2 rings.

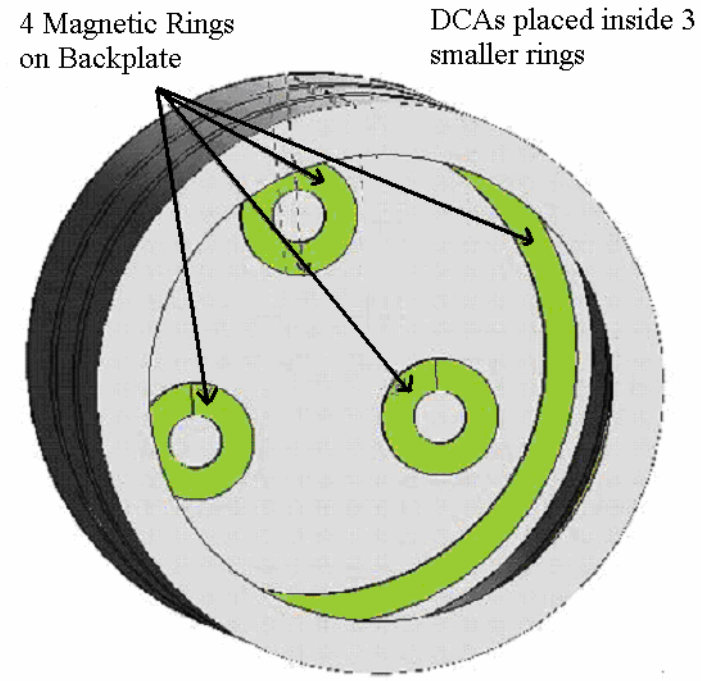

Figure 2-5: Example "coffee can" model with 4 backplate ring magnets. DCAs placed inside the 3 smaller inner rings.

The four magnet case consists of an outer ring magnet and three smaller ring magnets—one around each cathode—that are spaced symmetrically inside the large ring magnet. This model is shown in Figure 2-5.

2.2.2 Conical Geometry

A conical MCDC is investigated by scaling up the 40 cm NEXT to a 50 cm ion extraction diameter. Two and four backplate permanent ring magnet configurations are investigated in the same manner as the "coffee can" geometry. Placing the DCAs inside the inner ring or between the rings is modeled for the two magnet case. This model is shown in Figure 2-6. In the four magnet case, each of the cathodes is modeled on a separate backplate with its own ring magnet. In both cases, canting of the cathodes toward the thruster centerline is also considered. The four backplate magnet model is shown in Figure 2-7.

2.2.3 Rectangular Geometry

Modeling of the rectangular geometry is based on specifications obtained from the NASA Glenn Research Center (GRC) that require the MCDC to be identical in size and shape to the High Power Electric Propulsion (HiPEP) thruster.[32,55] Two and four ring permanent magnet configurations are again considered with the cathodes placed linearly across the backplate. Design variations of the rectangular theme are shown in Figure 2-8 and Figure 2-9. Notice that due to symmetry, only one-fourth of the two ring configuration is shown and numerically solved.

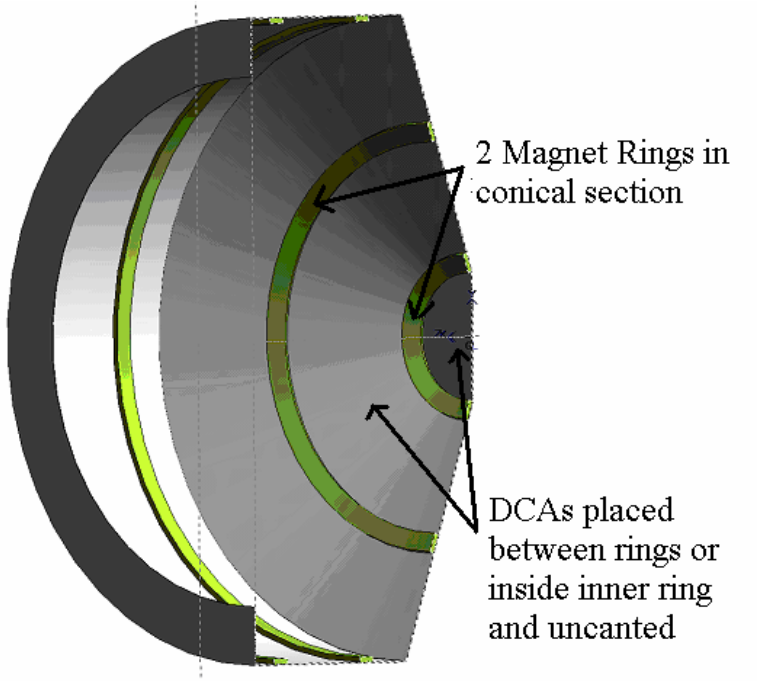

Figure 2-6: Example conical model with 2 backplate ring magnets. DCAs placed symmetrically inside the inner ring or between the 2 rings.

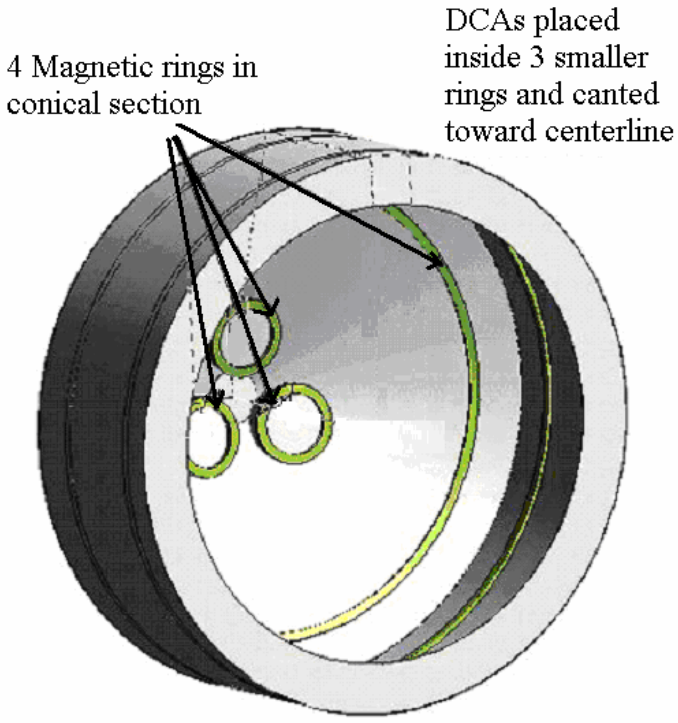

Figure 2-7: Example conical model with 4 backplate ring magnets. DCAs placed inside the 3 smaller inner rings.

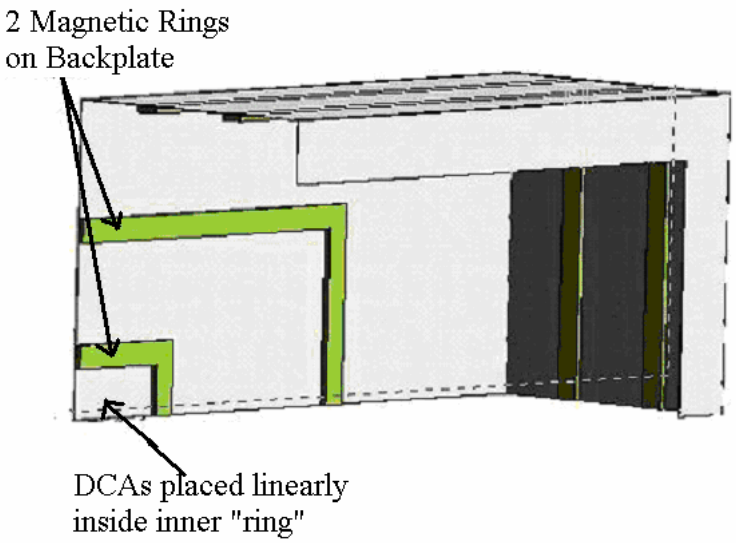

Figure 2-8: Example rectangular model with 2 backplate ring magnets. DCAs placed linearly inside the inner ring. Only one quadrant of the model is solved due to symmetry.

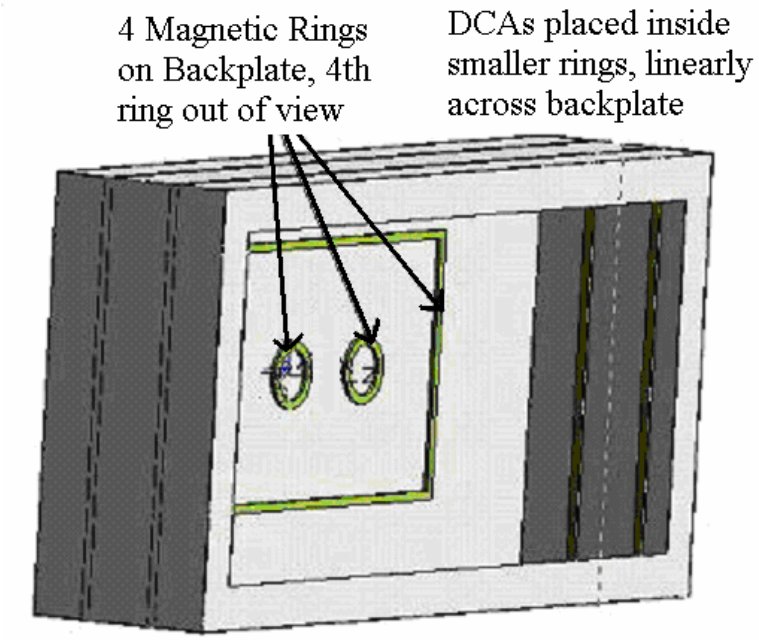

Figure 2-9: Example rectangular model with 4 backplate ring magnets. DCAs placed inside the 3 smaller inner rings and spaced linearly across the backplate.

2.3 Modeling Results: Round 1

Using the solved magnetic field topology provided by MagNet™ 6.0, each design is analyzed and evaluated on its ability to create a NEXT-like magnetic field environment at each of the three DCA locations and throughout the discharge chamber. Many of the designs are quickly eliminated due to violation of the criteria obtained from the NEXT magnetic field map. Specifically, those designs that do not place the DCAs inside a smaller ring of permanent magnets are rejected because the direction of the magnetic field lines at the cathode exit plane inhibit electrons from escaping the DCA and entering the discharge chamber. The rejected designs include all two backplate ring magnet designs; i.e., those with the DCAs spaced between the two ring magnets and those with the DCAs inside the inner ring magnet.

Based on these results and recommendations from the NASA GRC, a rectangular HiPEP-derivative discharge chamber is chosen. Advantages of a rectangular geometry are scalability to higher powers by simply increasing the lateral dimension of the chamber, without significant modeling and subsequent redesign of the magnetic circuit,[55] and the ability to easily cluster thrusters for spacecraft missions requiring an array of propulsion sources. Furthermore, a rectangular design can accommodate increasingly large rectangular ion optics without the potential manufacturing/vibrational limitations imposed on circular ion optics.[32,56]

The dimensions of the chosen rectangular design also provide other benefits for increasing thruster lifetime and performance. In analyzing ring-cusp ion thrusters with length-to-diameter (L/D) ratios of 0.53, 0.30, and 0.23, Beattie found that a decrease in L/D ratio increased beam flatness and decreased discharge power loss.[41] Although a

rectangular thruster inherently lacks a diameter, an equivalent thruster diameter can be defined from a circle with an area equal to the rectangular ion extraction area or through pipe flow theory; i.e., hydraulic diameter. Using these two approaches, the rectangular MCDC has an L/D ratio of ~1/3 and 0.4, respectively. A small L/D ratio allows an ion thruster to extract a relatively flat ion beam, further increasing thruster lifetime by reducing centerline grid erosion, a known failure mechanism.[62,81-87]

2.4 Discharge Chamber Modeling: Round 2

Discharge chamber magnetic field design is continued using MagNet™ 6.0 and the selected rectangular design geometry. Design variations are investigated by adjusting the number, spacing, and shape of the permanent magnet rings shown in the models above. Along with the all-permanent-magnet design variations, electromagnets are also considered as a possible magnetic field generating option. The following sections describe the all-permanent-magnet, all-electromagnet, and combination electro-permanent-magnet investigated designs.

2.4.1 All-Permanent-Magnet Designs

Each of the all-permanent-magnet designs consists of a rectangular non-magnetic stainless steel anode shell with samarium cobalt permanent magnet rings located on both the anode walls and backplate. Some of the variables manipulated between models are:

- Number, Shape, Location of Backplate Magnet Rings
  - Shapes: All Rectangular, Combination Circular and Rectangular, Hexagonal
  - Number: 2, 3, 4, 5, or 6 total rings
- Number, Location of Anode Wall Magnet Rings

- Number: 2, 3, or 4 total rings

- Permanent magnet size (width 1.27 cm or 0.64 cm) (thickness 0.51 cm or 1.02 cm)
- DCA locations on backplate

An example model is shown in Figure 2-10.

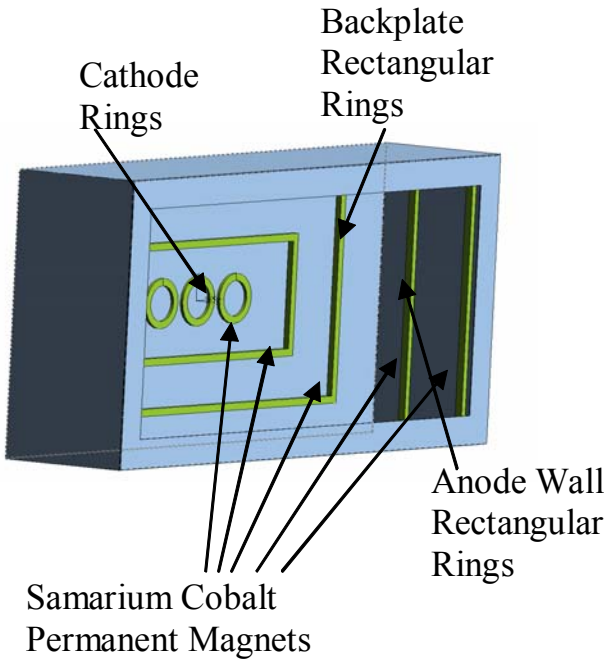

Figure 2-10: Example all-permanent-magnet MCDC model.

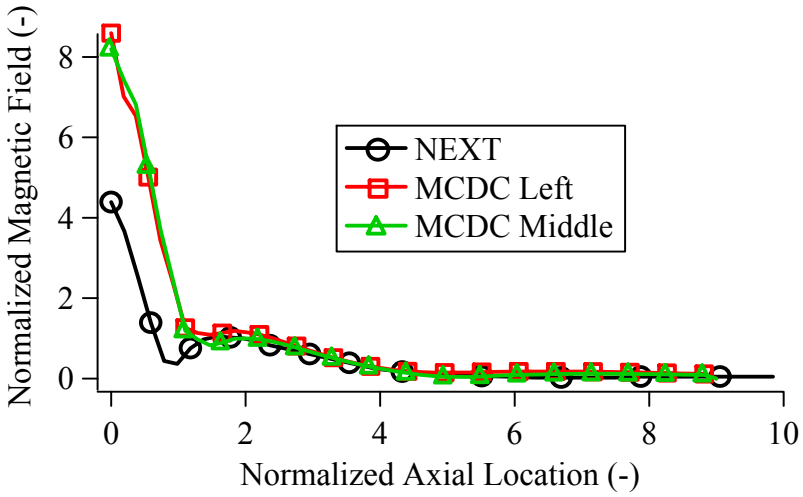

Figure 2-11: Axial profile of magnetic field strength for the internally mounted circular backplate magnetic rings configuration.

Axial magnetic field profiles for the all-permanent-magnet MCDC model in Figure 2-10 are shown in Figure 2-11. In this figure the axial distance and magnetic field are normalized by the NEXT DCA keeper diameter and exit-plane magnetic field strength, respectively. The model magnetic field exhibits characteristics similar to the NEXT and the DCA exit plane (~axial location 2) is located downstream of the peak magnetic field location. Discrepancies near the backplate (axial location 0) are attributed to the experimental NEXT magnetic field measurements being compared with the numerically simulated MCDC magnetic field.

Axial magnetic field profiles for an all-permanent-magnet MCDC model similar to Figure 2-10 except with the magnets mounted external to the MCDC is shown in Figure 2-12. The profiles are very similar to the internal configuration and differ only slightly near the backplate.

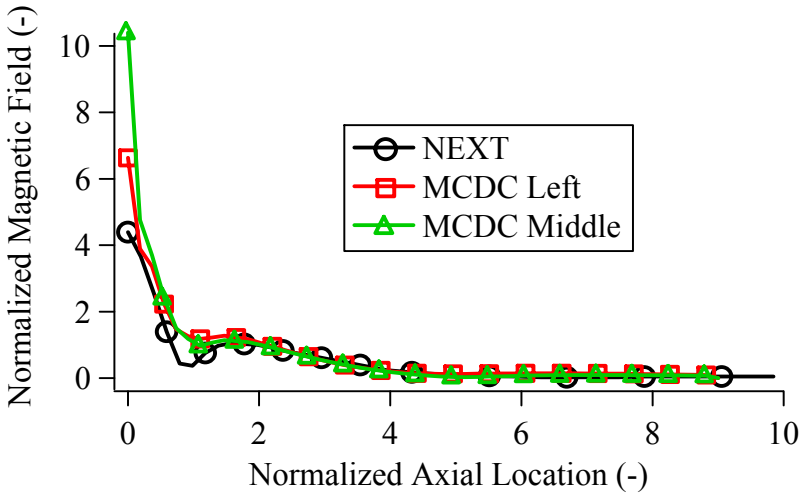

Figure 2-12: Axial profile of magnetic field strength for an externally mounted circular backplate magnetic rings configuration.

2.4.2 All-Electromagnet Designs

All-electromagnet design models only utilize electromagnets to generate a ring-cusp magnetic field inside the rectangular geometry. For the all-electromagnet designs, electromagnets are mounted external to the rectangular discharge chamber. Each electromagnet is rectangular and consists of a copper wire coil surrounded by a magnetic iron c-channel. The two sides of the c-channel function as the magnetic cusp locations, similar to alternating the polarity of permanent magnets. A schematic of the electromagnet is shown in Figure 2-13. An example of the axial magnetic field profile for an all-electromagnet design is shown in Figure 2-14. The model corresponding with the figure utilizes four anode wall and two concentric backplate electromagnets that cause the left and middle profiles to differ slightly. This profile shows that the NEXT (all permanent magnets) has a significantly larger backplate magnetic field strength than an all-electromagnet configuration.

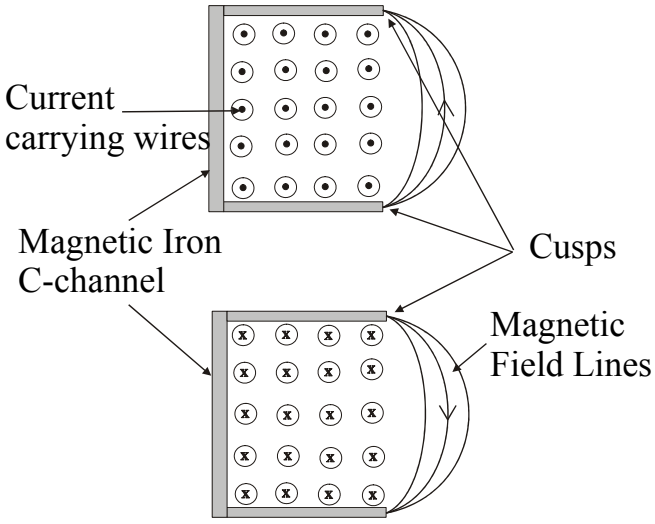

Figure 2-13: Schematic of the electromagnet with magnetic iron c-channel and magnet wire windings.

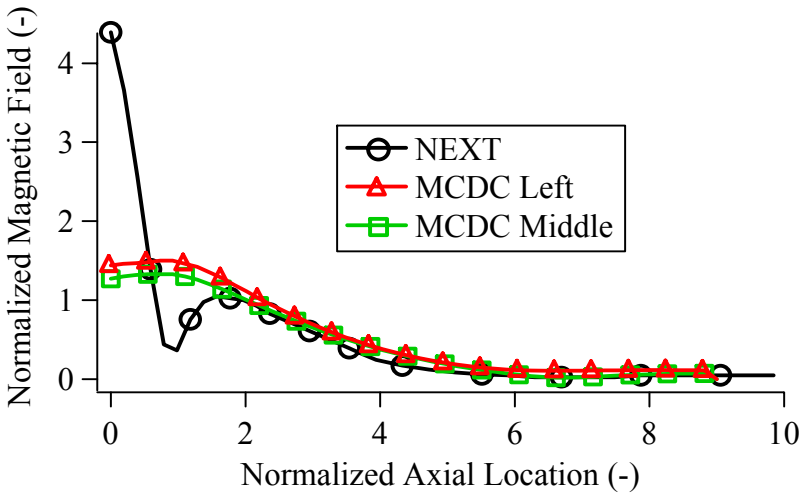

Figure 2-14: Axial profile of magnetic field strength for an all-electromagnet design. Backplate magnet field (axial location 0) can be adjusted using the backplate electromagnets.

2.4.3 Combination Electro-Permanent-Magnet Designs

Combination electro-permanent-magnet design models utilize electromagnets and permanent magnets to generate a ring-cusp magnetic field inside the rectangular geometry. The combination designs place permanent magnets internal to the discharge chamber (similar to Figure 2-10) and electromagnets are mounted externally to augment (increase or decrease) the magnetic field. Model variations include using a single or multiple electromagnets, as well as adjusting electromagnet location (backplate only, anode walls only, or both backplate and anode walls). Each electromagnet consists of a copper wire coil surrounded by a magnetic iron c-channel, identical to the electromagnet previously described in Figure 2-13. The c-channel is designed such that the two sides of the channel are located at the magnetic cusp locations. Adjusting the current through the electromagnet coil changes the magnetic field. An example of the axial magnetic field profile for a combination electro-permanent-magnet design is shown in Figure 2-15. The model corresponding with the figure has only permanent magnets on the anode walls and

one electromagnet on the backplate. This profile shows that the NEXT (all permanent magnets) has a significantly larger backplate magnetic field strength. This result is due to the absence of permanent magnets on the backplate of the MCDC design model.

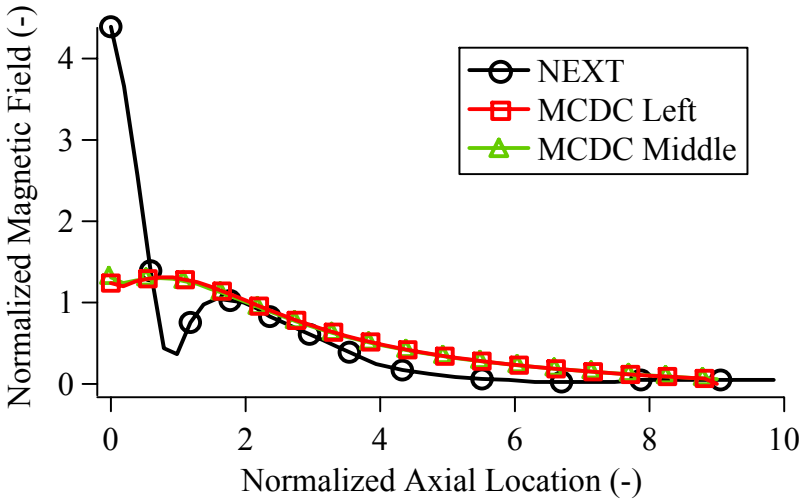

Figure 2-15: Axial profile of magnetic field strength for a combination electro-permanent-magnet design. Backplate magnet field (axial location 0) can be adjusted using the backplate electromagnets.

2.5 Modeling Results: Round 2

Using the simulated magnetic field results, each rectangular discharge chamber magnetic field model is judged based on its ability to create a NEXT-like magnetic field. Models placing only an electromagnet on the backplate are immediately eliminated due to their inability to generate the increased magnetic field strengths evidenced by the all-permanent-magnet NEXT magnetic field. It is unclear if an electromagnet alone is capable of generating the cusp field strengths required to decrease the primary-electron collection area.[36] This leaves only the combination electro-permanent-magnet and all-permanent-magnet design models as viable options.

Utilizing electromagnets to provide *in situ* magnetic field adjustment is desirable because a rectangular MCDC has never been investigated and augmentation of the magnetic field may be necessary for stable discharge operation. Therefore the all-permanent-magnet designs are eliminated. Those designs placing 4 electromagnets on the anode walls (one on each of the 4 walls) are eliminated due to weight, cost constraints, and complexity. Plus, varying the anode wall magnetic field is of less interest than the near-DCA backplate magnetic field. However, empty magnetic iron c-channels (no electromagnet only a magnetic iron shell) are retained as a magnetic field augmentation option and are further discussed below in section 2.6.4. A baseline all-permanent-magnet magnetic field is selected with a single backplate electromagnet utilized to augment the near-DCA magnetic field.

The permanent magnet geometry in the MCDC is selected to contain 2 anode wall rectangular rings, 2 concentric backplate rectangular rings, and 3 smaller circular rings spaced linearly inside the inner backplate rectangular ring. This design utilizes the larger magnet dimensions. The smaller magnet dimensions can also be used to produce the desired magnetic field. However, more total magnet rings and subsequently more magnetic cusps are required. Because the majority of plasma electrons are collected at the cusps,[39,45-49] decreasing the total rings can lead to increased electron collection at intercusp surfaces.[44] NEXT-like intercusp field strengths can still be obtained using fewer rings and the larger magnets. Plus, utilizing fewer rings reduces the overall mass of the engine.

2.6 Selected MCDC

The following sections describe the various components of the MCDC and the multiple magnetic field configurations. Furthermore, the coordinate system for the MCDC that is utilized throughout this thesis is described.

2.6.1 Anode

The selected rectangular MCDC design has dimensions identical to the NASA GRC HiPEP ion thruster[32,56] and an identical ion extraction area. Non-magnetic stainless steel sheet metal with 1.5 mm thickness is used to construct the backplate and the rectangular shell. Four corner brackets are welded to the sheet metal to form the rectangular shell and the backplate is bolted to the shell to form the five sided rectangular anode. Three holes centered in the backplate are spaced linearly apart for placement of the DCAs.

2.6.2 Permanent Magnets

Samarium Cobalt permanent magnets are utilized to form the baseline magnetic circuit. Three circular magnet rings are formed, each using 16 smaller rectangular magnets as shown in Figure 2-16, and mounted to the backplate at each DCA location. Two concentric rectangular rings surround the three DCAs and two more rectangular rings are located on the anode walls. Each of the rectangular rings is constructed of smaller rectangular magnets. Simulations show that this configuration places each DCA in a NEXT-like magnetic field environment and provides similar intercusp field strengths.

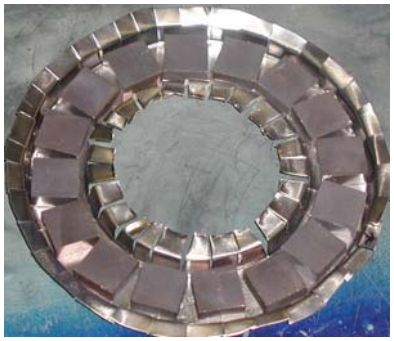

Figure 2-16: Permanent magnets arranged in a circular ring. A circular ring is placed at each of the three DCA locations.

2.6.3 Electromagnet

In addition to the baseline all-permanent-magnet magnetic circuit, an electromagnet is utilized to augment and change the magnetic field configuration. A coil with 280 turns of 15 gauge magnet wire is wrapped in a double-conductor configuration around a rectangular aluminum bobbin and placed inside a magnetic iron channel. The use of two conductors reduces the length of a single wire and subsequently its resistance so that a lower voltage can be used to drive the electromagnet current. The magnetic channel increases the efficiency of the electromagnet by directing the flux, thus the electromagnet requires fewer turns and less current than if operated without the magnetic iron. The near-DCA magnetic field is adjusted by mounting the electromagnet to the external side of the backplate and supplying a current within the range of ±10 A. Negative current decreases the near-DCA magnetic field and positive current increases it. With the electromagnet attached, the DCA exit-plane magnetic field strength can be adjusted from 15 G to over 100 G. In order to recover the baseline all-permanent-magnet configuration, the electromagnet must be operated at -5 A because the presence of the magnetic iron increases the magnetic field even without a supplied current.

2.6.4 Magnetic Field Configurations

Although an infinite number of magnetic field configurations are possible because the electromagnet can be set at any desired current level, only seven are investigated in this work. Five magnetic field configurations are studied by setting the electromagnet current at ±10 A, ±5 A, and 0 A. A sixth configuration encloses the 50 G line within the MCDC by attaching the electromagnet (operated at 0 A) and 4 magnetic iron c-channels to each of the anode walls. The c-channels are empty magnetic iron shells without an electromagnet coil. Placing the magnetic iron c-channels at the cusp locations increases the strength of the intercusp field and effectively encloses the 50 G line. By definition the 50 G line is considered enclosed if it does not intersect with the anode walls or backplate. As mentioned previously, some ion thruster discharge chamber designs utilize this criterion,[57] while others do not. The seventh configuration is asymmetric with an increase in magnetic field strength near the off-centerline DCA.

2.6.5 MCDC Coordinate System

A coordinate system is constructed such that the center DCA opening in the backplate of the MCDC is considered the origin. Looking downstream from behind the MCDC, the positive Z-axis extends in the downstream direction, the positive X-axis extends to the left, and the positive Y-axis extends in the upward direction. A graphical representation of the coordinate system is shown in Figure 2-17 and Figure 2-18.

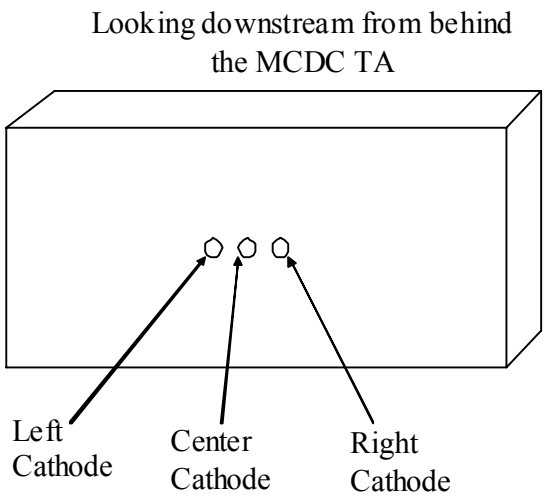

Figure 2-17: MCDC coordinate system looking downstream.

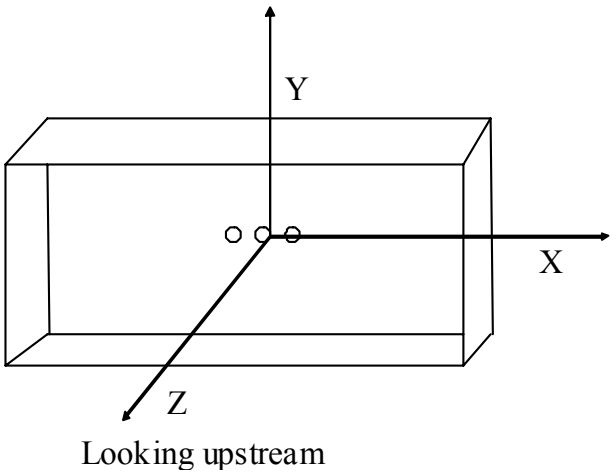

Figure 2-18: MCDC coordinate system looking upstream.

2.7 Magnetic Field Mapping

In order to validate that the designed and simulated magnetic field topology is identical to the actual MCDC magnetic field, 2-D experimental magnetic field maps are compared with the simulation data over 6 planes for 7 magnetic field configurations. The following sections describe the magnetic field mapping setup and results.

2.7.1 Experimental Setup

Two horizontal and four vertical 2-D magnetic field maps are obtained for 7 MCDC magnetic field configurations. Alteration of the magnetic field is done with the MCDC backplate electromagnet operated at different current settings and by adding the magnetic iron c-channels to the anode walls of the MCDC. Horizontal (X-Z) maps are taken at Y = 0 cm and Y = -12.7 cm, whereas the vertical (Y-Z) maps are completed at X = 0 cm, X = 10.2 cm, X = 25.4 cm, and X = 40.6 cm. Symmetry of the MCDC magnetic field about the X-Z and Y-Z planes is assumed.

Experimental mapping of the MCDC is accomplished utilizing the setup shown in Figure 2-19.

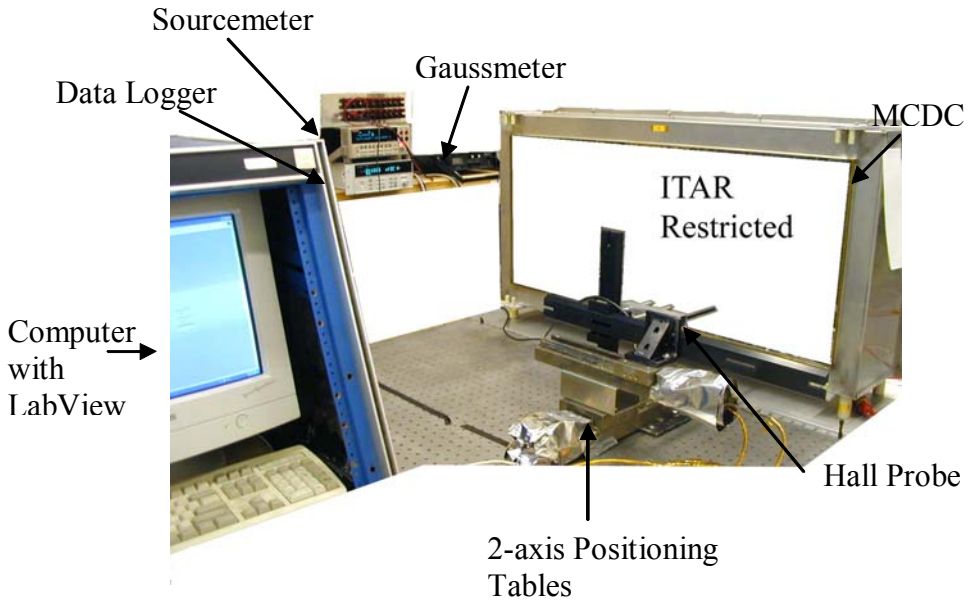

Figure 2-19: MCDC magnetic field mapping experimental setup.

The MCDC is mounted to a laser positioning table and the magnetic field is mapped by positioning a Hall probe at discrete points within a 2-D grid. Either an axial or transverse Hall probe is connected to a Walker Scientific, Inc. MG-5D gaussmeter to measure the

magnetic field. The axial field (Bz) is measured using an HP-245-S axial probe. Horizontal (Bx) and vertical (By) magnetic field values are measured with a HP-145-R transverse probe. A 34970A 22-bit Agilent data logger with a 34901A 20-channel multiplexer is used to measure the analog voltage output from the gaussmeter. The conversion factor for the voltage output is 10^{-3} V/Gauss.

Two stepper motor controlled New England Affiliated Technologies (NEAT) translation stages move the probe between grid points. A NEAT TMS-1100-SM table controls the axial (Z-axis) dimension and a NEAT RMS-800-SM table controls the horizontal (X-axis) or vertical (Y-axis) dimension depending on the map being recorded. Each table stepper motor is controlled with a NEAT-310/M stepper motor controller with a MDM7 drive module. Further automation of the mapping process is accomplished by utilizing a voltage-controlled current supply to adjust the MCDC electromagnet current. A Keithley 2410 sourcemeter is used to supply a 0-5 V signal to a Sorenson DLM 40-15 power supply (not pictured). The entire mapping process is controlled through a LabView interface. LabView sets the electromagnet current through the Keithley, moves the NEAT tables, and records the proportional voltage output through the data logger. Data are acquired at a grid spacing of 0.5 cm and a two-dimensional plane requires approximately 100 minutes to complete.

2.7.2 Results and Analysis – Magnetic Field Comparison

Experimentally measured magnetic field maps and MagNet^{TM} 6.0 simulated fields are compared to validate the actual MCDC magnetic field. A total of 42 different experimental magnetic field maps are compared with their numerically simulated counterparts and the following figures show typical results. Each figure shows a 2-D

plane, either an X-Z horizontal or Y-Z vertical plane. Spatial dimensions are normalized by the NEXT DCA keeper diameter and magnetic field values are normalized by the center DCA keeper exit-plane magnetic field strength for the 0 A electromagnet configuration. This allows different magnetic field configurations to be compared with the normalized dimensions. One or two notional DCAs are also shown in the appropriate figures. In each figure, the left (or top) plot is the experimentally measured field and the right (or bottom) plot shows the simulation results.

Figure 2-20 shows the experimental and simulated magnetic field for the X = 0 cm vertical plane for the 0 A electromagnet configuration. Figure 2-21 shows the experimental and simulated magnetic field for the Y = 0 cm horizontal plane for the 0 A electromagnet configuration. More of the compared magnetic field maps can be found in APPENDIX A; however, all of the recorded maps are not shown.

Comparison of the experimentally measured magnetic field at the investigated 2-D planes for all magnetic field configurations shows good agreement with the simulated MagNet^{TM} results. For all experimental maps, as the magnetic field decreases with axial distance far from the permanent magnets the deviation from the simulation increases because the signal-to-noise ratio of the gaussmeter output increases. Noise is particularly evident in profiles where the contours are significantly peaked and larger in magnitude than the simulation results. Regions within the MCDC where the magnetic field is large (greater than approximately 20 G) show excellent agreement with the profiles predicted by MagNet^{TM}; i.e., near the backplate of the MCDC at smaller Z-values.

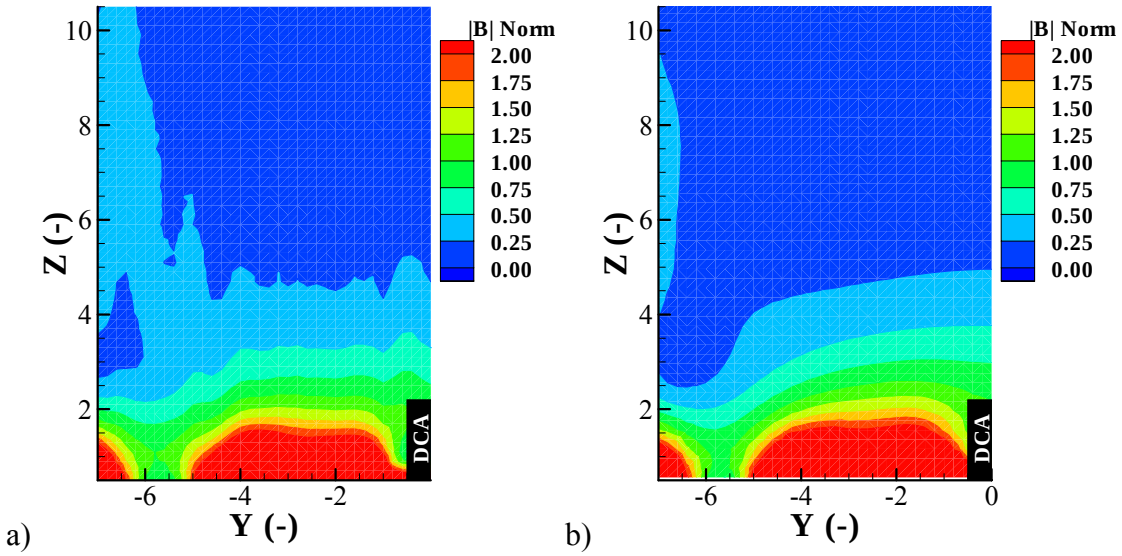

Figure 2-20: Comparison of a) experimentally measured and b) simulated magnetic field for the X = 0 cm plane with I_{emag} = 0 A.

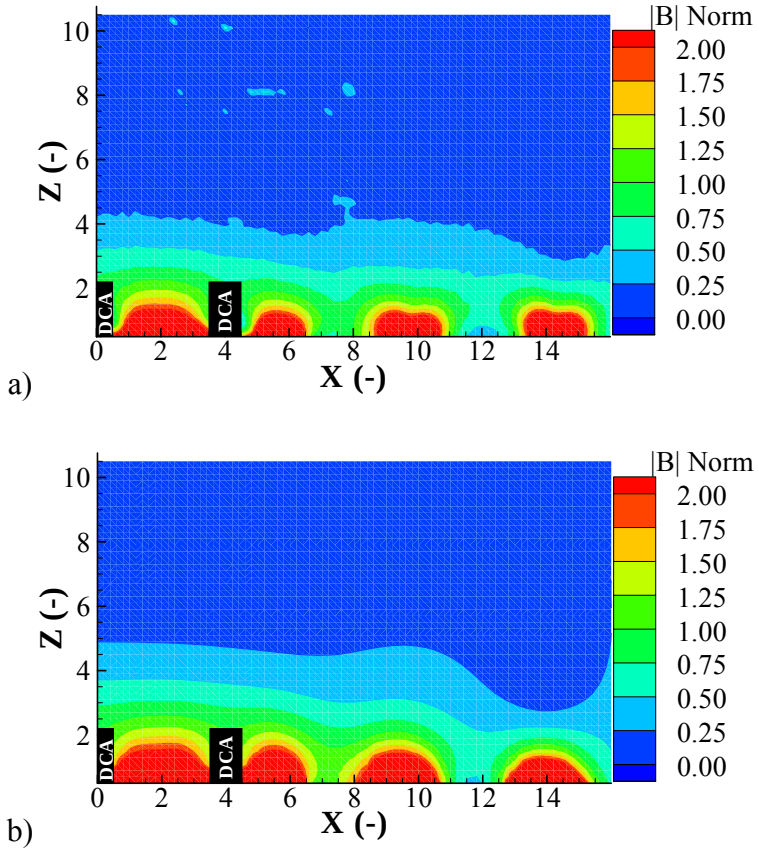

Figure 2-21: Comparison of a) experimentally measured and b) simulated magnetic field for the Y = 0 cm plane with I_{emag} = 0 A.

Percent differences are also calculated at each spatial location throughout the MCDC. Percent difference is defined as the difference between the simulation and experimental value divided by the simulation value. At spatial locations near the permanent magnets an average percent difference of approximately ±15% is obtained. However, in the lower field regions away from the magnets, the percent difference can grow to as large as 200%. These results are also attributed to the signal-to-noise ratio of the gaussmeter.

Maps of the X = 0 cm and X = 10.2 cm planes are shown in Figure 2-22 and are nearly identical. These are the planes that intersect the DCA locations and the experimental results validate the placement of each DCA in a similar magnetic field environment. Furthermore, analysis of these planes for the 5 electromagnet configurations verifies that the DCA exit-plane magnetic field strength can be varied from approximately 15 G to greater than 100 G by adjusting the electromagnet current from -10 A to +10 A. It is also important to note that the electromagnet does not change the location of the peak magnetic field strength. The DCA exit-plane is always located downstream of the peak field strength, an important design criteria.

Comparison of the all-permanent-magnet (no electromagnet) configuration with the 5 electromagnet configurations shows that a -5 A electromagnet current is required to generate the all-permanent-magnet case. This result is shown in Figure 2-23 and validates that an all-permanent-magnet configuration can be generated from the electromagnet configuration. A similar argument can be made for the other electromagnet configurations. By increasing or decreasing the strength of the permanent magnets, the other electromagnet configurations could be generated using only permanent magnets.

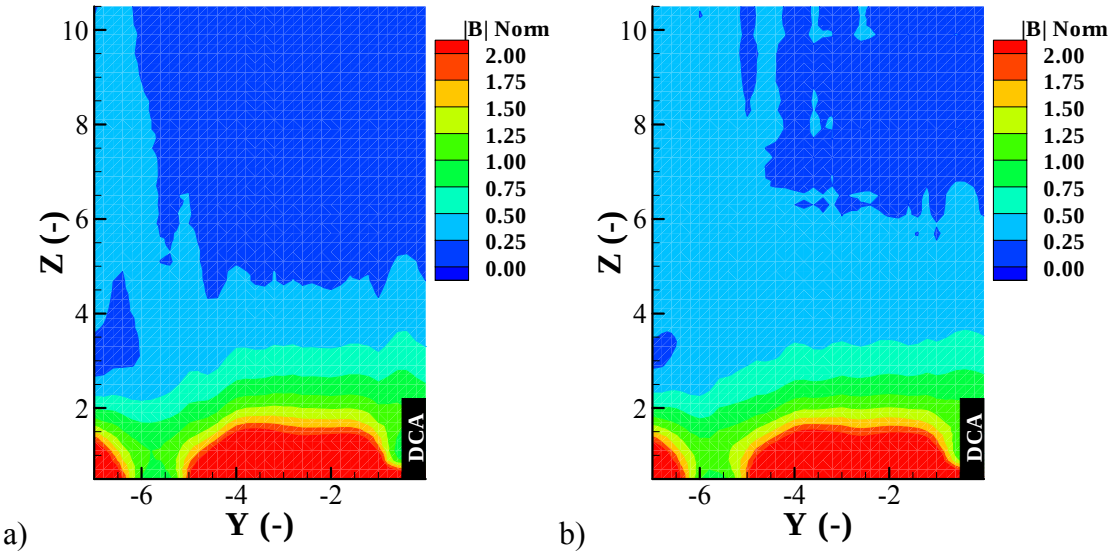

Figure 2-22: Comparison of experimentally measured magnetic field profiles for the a) X = 0 cm and b) X = 10.2 cm vertical planes with I_{emag}= 0 A.

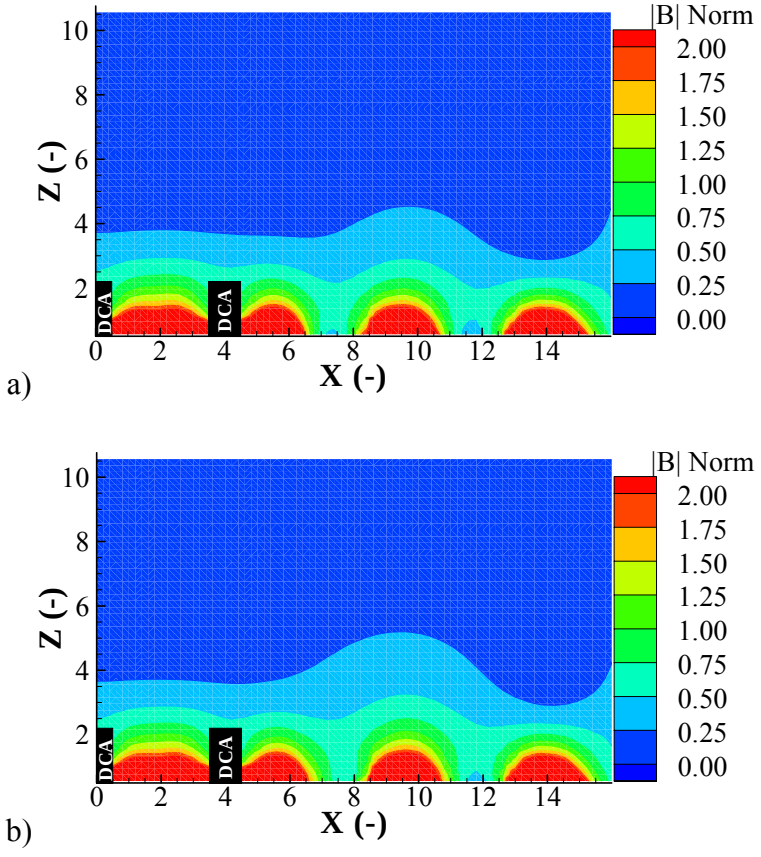

Figure 2-23: Comparison of simulated magnetic field profiles for the a) all-permanent-magnet (no backplate electromagnet) and b) I_{emag}= -5 A configurations.

Unfortunately data for the 50 G line enclosed configuration is unattainable in the near-anode wall region due to the masked extraction dimensions. Experimental validation that the 50 G line is enclosed must be inferred by comparison with the simulation results in the near-DCA region. Because the experimental maps agree with the simulations in the near-DCA regions, it is assumed that agreement is also obtained in areas not experimentally measured; i.e., near the anode walls. Therefore enclosure of the 50 G line inside the MCDC is validated for the 50 G enclosed configuration.

2.7.3 Magnetic Field Mapping Conclusions

In general, excellent agreement is obtained between the experimentally measured profiles and the MagNet^{TM} simulations. At spatial locations near the permanent magnets an average percent difference of approximately ±15% is obtained. Furthermore, the experimental maps verify that each DCA is located in a similar magnetic field environment. Comparisons of the all-permanent-magnet and 5 electromagnet configurations show that a -5 A electromagnet current is required to generate the all-permanent-magnet case. This result also suggests that it may be possible to recover any all-permanent-magnet magnetic field from the electromagnet augmented configuration. Finally, verification of the enclosure of the 50 G line is obtained. This configuration requires the electromagnet (operated at 0 A) and the magnetic iron c-channels to effectively keep the 50 G contour line from intersecting the anode.

CHAPTER 3:

EXPERIMENTAL APPARATUS

To analyze the ability of a multiple-cathode discharge chamber (MCDC) to increase ion thruster lifetime, a variety of experimental apparatus is required. For the experimental investigations presented in this work, a MCDC test article (TA) is operated in a vacuum facility to simulate space conditions. Furthermore, a variety of diagnostics is utilized to determine the TA performance, stability, uniformity, and plasma properties. The following sections describe these different types of experimental hardware and diagnostic devices.

3.1 Vacuum Facility

The University of Michigan Large Vacuum Test Facility (LVTF) is used for all experiments presented here. The LVTF is a stainless-steel vacuum chamber with a diameter of 6 m and a length of 9 m. A schematic of the vacuum chamber is shown in Figure 3-1. Four 400 CFM mechanical pumps and two 2,000 CFM blowers evacuate the chamber to a moderate vacuum (30 – 100 Torr). In order to reach high vacuum, the facility employs seven CVI TM-1200 re-entrant cryopumps, each of which is surrounded by an LN_2 baffle. The cryopump system can be operated with any number of pumps in use. With all seven pumps operating, the facility pumping speed is 240,000 l/s on xenon with a base pressure of 2.5×10^{-7} Torr. For the experiments described here, only two cryopumps are operated, yielding a base pressure of 5.2×10^{-7} Torr.

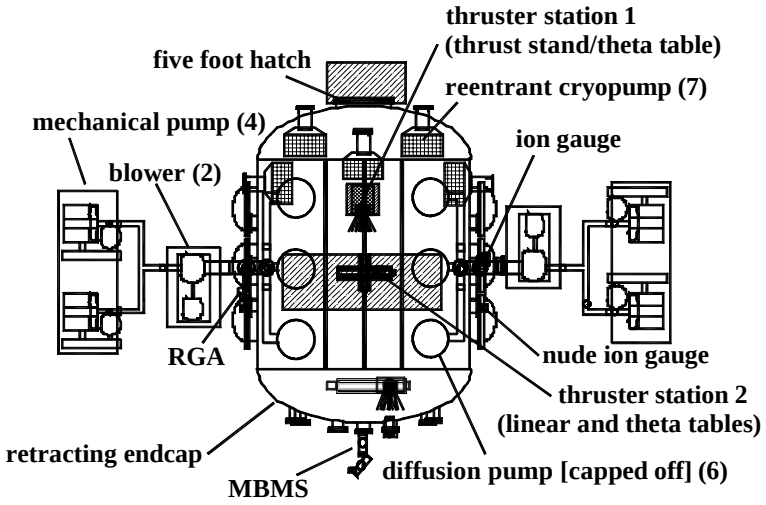

Figure 3-1: Schematic of the Large Vacuum Test Facility (LVTF). Not to scale.

The chamber pressure is monitored using two hot-cathode ionization gauges, as shown in Figure 3-1. The first gauge, a Varian model 571 gauge with an HPS model 919 Hot Cathode Controller, is connected to the chamber by a 25-cm-long by 3.48-cm-inner-diameter tube. The second is a Varian model UHV-24 nude gauge with a Varian UHV senTorr Vacuum Gauge Controller. Pressure measurements from the gauges are corrected for xenon using the known base pressure on air and a correction factor of 2.87 for xenon according to Eqn. 3-1,[88]

$$P_c = \frac{P_i - P_b}{2.87} + P_b \qquad \textbf{Eqn. 3-1}$$

where P_c is the corrected pressure on xenon, P_b is the base pressure, and P_i is the indicated pressure when xenon is flowing into the vacuum chamber. Corrected pressure for the nude ion gauge is reported as the background pressure in the chamber. A recent investigation of the pressure inside the LVTF during Hall thruster cold-flow operation has shown that the nude gauge provides better agreement with the true pressure of the

facility.[89-91] Corrected operating pressures for all experiments reported here are below 4.0×10^{-6} Torr on xenon.

3.2 MCDC Test Article (TA)

The MCDC described in Chapter 2 is placed inside the LVTF and the electromagnet is mounted to the backplate for all experiments. Those experiments requiring enclosure of the 50 G line also utilize the magnetic iron c-channels mounted to the anode walls. Two dormant cathode units (DCUs) or diagnostic cylinders (DCs) are mounted at two of the discharge cathode assembly (DCA) locations and a NASA Evolutionary Xenon Thruster (NEXT) DCA is attached at the 3rd location. An ion collection grid is mounted at the ion extraction plane because the MCDC is operated as a simulated ion thruster without beam extraction.[92] A reverse-feed plenum is designed and mounted inside the MCDC. Attachment of the ion collection grid, the NEXT DCA, the DCUs or DCs, and the plenum to the MCDC is referred to as the MCDC TA or simply, TA.

3.2.1 Ion Collection Grid

Because only discharge chamber performance and plasma properties are being investigated, the TA is operated as a simulated ion thruster without beam extraction.[92] Simulated operation is accomplished by mounting an ion collection grid at the ion extraction plane, high-voltage ion optics are not required. The ion collection grid is constructed of 0.32-cm-thick non-magnetic stainless steel with outer dimensions of 45.7 cm x 96.5 cm. A total of 1300 - 0.38-cm-diameter holes are arranged in a 0.72 cm staggered pattern over the 40.6 cm x 91.4 cm active area of the grid. The open area

fraction of the ion collection grid is measured to be 24%, similar to the HiPEP ion optics open area fraction.[93]

Herman has recently reported that the DCA plume and near-DCA plasma properties in a discharge chamber change when the thruster is taken from high-voltage to discharge-only operation.[79,94-98] However, discharge-only operation is not identical to simulated operation. During simulated operation the ion optics or ion collection grid is biased to collect ions, while discharge-only operation allows the optics to float by disconnecting the high-voltage power supply. Therefore simulated operation has a method of removing ions from the discharge chamber (the biased collection grid), while discharge-only operation does not. Also, the basis of this work focuses on the ability of multiple DCAs to increase thruster lifetime, so plasma properties near the dormant DCAs are of primary importance. The dormant DCAs are located within the bulk discharge of the chamber, away from the near-DCA plasma structures determined by Herman. Finally, as will be shown later in this thesis, plasma property data obtained at the dormant DCA locations is similar to internal bulk plasma measurements obtained by Herman and other researchers.

3.2.2 Discharge Cathode Assembly (DCA)

A NEXT 1.27-cm-diameter hollow cathode with a surrounding keeper is utilized in the TA. Only one DCA is used for all experiments presented here. The DCA is simply moved from the center to the left or right position for off-centerline DCA operation.

3.2.3 Reverse-feed Plenum

A reverse-feed plenum is designed based on the NEXT propellant feed system. This type of configuration has been shown to increase ion engine performance.[99] Two - 152.4-cm-long by 0.32-cm-diameter specification 401 electropolish tubes are modified by placing 16 – 0.34-mm-diameter holes along the entire length. Each tube is bent into a half-rectangle shape and a tube is placed on the right and left side of the MCDC ion extraction plane upstream surface. This ensures that injected xenon propellant is directed toward the DCA and expelled along the entire perimeter of the ion extraction plane.

3.2.4 Electrical Circuit

Electrically the TA is setup for simulated ion thruster operation described by Brophy.[92] An engine bias supply is used to raise the TA cathode potential above facility ground. This prevents electrons from leaving the TA and also allows the extracted current to be measured. The collection grid is biased negative of cathode potential to measure the ion current to the grid. Each DCA, DCU, and DC is electrically connected or isolated by two switches: one for the cathode and one for the keeper. During TA operation the DCA is always connected to the circuit. Each of the three keepers is connected to the anode through a 10 kΩ resistor. A schematic of the engine electrical circuit is shown in Figure 3-2. The electromagnet is not shown in the schematic because it is electrically isolated from the TA electrical circuit. Four Kepco 30-30 power supplies are used for the heater, grid bias, engine bias, and electromagnet supplies. An EMS 60-40 power supply is used as the main discharge or anode supply.

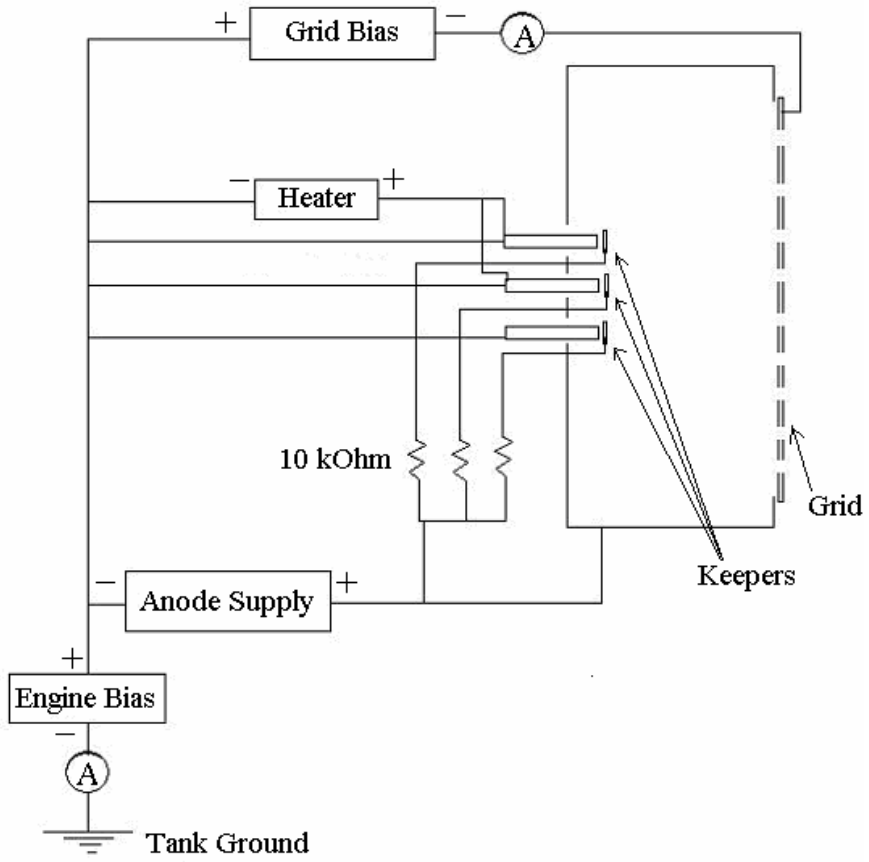

Figure 3-2: Electrical schematic for simulated ion thruster MCDC TA operation.

3.2.5 R-C Filter

In order to prevent discharge oscillations from affecting the discharge power supply, an R-C filter is designed and utilized. Initially all possible plasma related frequencies are calculated based on assumed number densities and temperatures. This analysis includes the plasma frequency, electron and ion cyclotron frequencies, collision rates, and charge collection rates. Based on these calculations an R-C filter is designed to eliminate all frequencies above the lowest calculated frequency. The cutoff frequency for an R-C filter is defined by Eqn. 3-2.[100] A 1500 mF capacitor and a 0.1 Ω resistor are utilized to ensure that frequencies above approximately 1000 Hz are cutoff. This setup is similar to that used for Hall thruster discharge supplies.[101]

$$\omega_{cutoff} = \frac{1}{RC} \qquad \textbf{Eqn. 3-2}$$

3.2.6 TA Operational Configurations

Different TA configurations are investigated by changing the active DCA location, TA magnetic field (electromagnet current and/or magnetic iron c-channels), DCU or DC electrical connectivity, and DCU or DC flow rate. Because so many variables are adjusted, a total of 108 configurations can be investigated. Table B-1 in APPENDIX B shows the possible TA configurations and the configuration nomenclature used throughout this thesis.

3.3 Dormant Cathode Units (DCUs)

Two DCUs are designed and constructed to appear as similar to the active DCA as possible. Each DCU has a copper cathode tube with a chamfered orifice and a surrounding copper keeper tube with an orifice. Copper is utilized due to its relatively large sputtering yield[102,103] in order to visualize any erosion phenomena that may be present during TA operation. High-temperature ceramic is used to hold the cathode and keeper tubes at the required orifice spacing. An aluminum mounting flange attaches to the ceramic. Along with the active DCA, each DCU is also connected to a propellant feed system through a propellant isolator. This allows the effect of propellant flow through the DCUs on TA performance, grid-plane uniformity, DCU erosion, and internal plasma properties to be studied. Photographs of the DCUs are shown in Figure 3-3.

Figure 3-3: Photographs of the dormant cathode units (DCUs).

3.4 Langmuir Probes

Langmuir probes are among the oldest and most widely used types of electrostatic probes for plasma characterization.[104,105] A single-Langmuir probe consists of a single electrode connected to an external circuit that allows the probe voltage, V, to be varied with respect to the local plasma. The operational regimes of a Langmuir probe are further discussed in section 4.1.

3.4.1 Grid-Plane Langmuir Probe

During the performance, stability, and uniformity study described in Chapter 5, a cylindrical single-Langmuir probe is placed on the ion collection grid to determine plasma properties at the grid plane. The electrode of the probe is sized such that the probe operates in the thin-sheath regime, as described in section 4.1.1. A single-Langmuir probe with a 5.1-mm-diameter, 5.4-mm-long tungsten electrode housed inside two concentric alumina tubes with outer diameters of 6.60 cm and 1.63 cm is used. A large length-to-diameter ratio is utilized to minimize end effects and the total probe area is calculated to be 8.82 mm^2. The probe is mounted to the grid at the location shown in Figure 3-7 and the electrode is located approximately 3 cm into the discharge chamber.

A Hiden Analytical system utilizing ESPsoft software obtains the I-V characteristics. However, the results calculated by the Hiden system assume the probe is operated in the Orbital Motion Limited (OML) regime, so a thin-sheath analysis is manually applied to determine the plasma properties. The thin-sheath analysis described in the data analysis section, section 4.1.1, is used to obtain the results.

3.4.2 Plasma Mapping Langmuir Probe

A cylindrical single-Langmuir probe is used for the internal plasma property mapping described in Chapter 7. A 0.25-mm-diameter tungsten wire is enclosed in two concentric alumina tubes and a concentric non-magnetic stainless steel tube with outer diameters (OD) of 1.2 mm, 6.7 mm, and 8.0 mm, respectively. The probe area is calculated to be 2.01 mm^2. A schematic of the probe is shown in Figure 3-4.

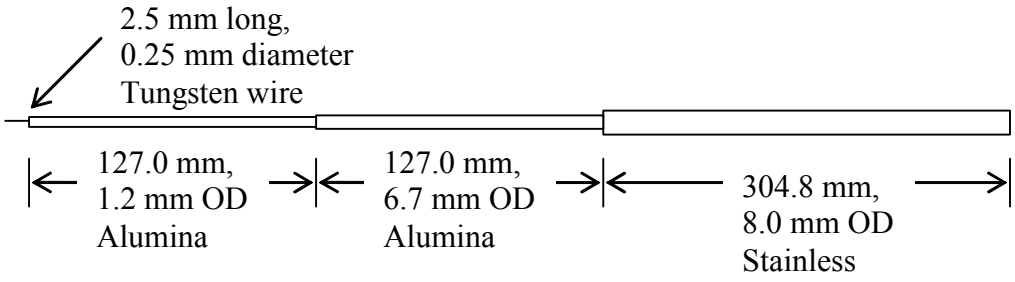

Figure 3-4: Langmuir probe schematic.

The probe is connected to a Kepco BOP 100-2M programmable bipolar power supply that is driven by a signal generator. The bipolar power supply and generator are used to rapidly sweep the bias voltage, permitting continuous I-V curves to be recorded. The Langmuir probe is biased with respect to ground and the subsequent I-V curves are corrected to cathode common by subtracting the TA cathode bias potential (+25 V). A function generator provides a ramping voltage signal at 280 Hz with the resulting bipolar

sweep from approximately -25 V to +35 volts with respect to discharge cathode common, covering both electron and ion saturation regions.

The isolated voltage and current measurement circuit is a modified version of the Langmuir probe circuit used for ion thruster[97,98] and Hall thruster[106,107] testing. The circuit is built around two Analog Devices AD210 wide bandwidth isolation amplifiers, each capable of handling up to 2,500 volts of common mode voltage with an input impedance of 10^{12} Ω and a full-power bandwidth of 20 kHz. The low-impedance output (1 Ω maximum) is connected to the data acquisition system that acquires the I-V data and saves it to a computer. Figure 3-5 illustrates the electronics and circuitry used to operate the Langmuir probe.

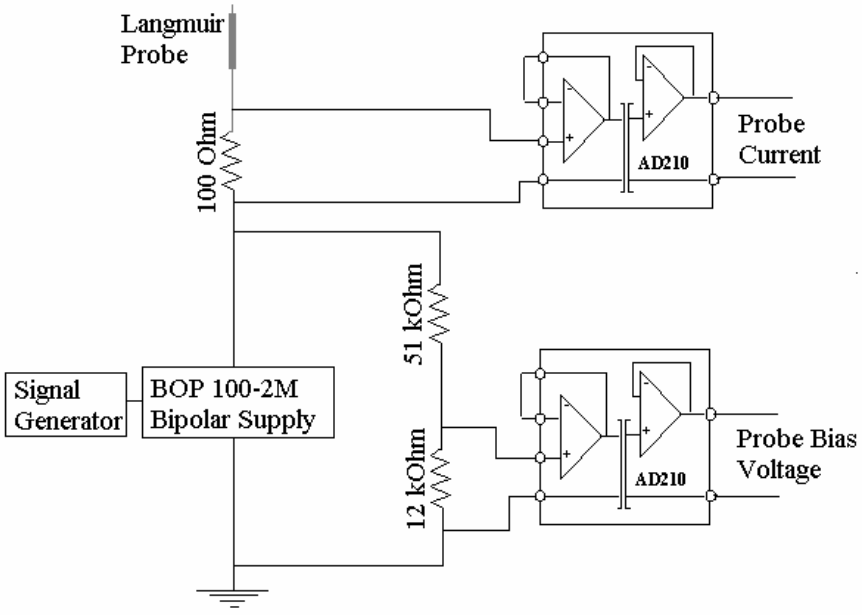

Figure 3-5: Langmuir probe electrical circuit.

3.5 Button Probes

In order to obtain an approximation of the grid-plane current density distribution, 13 button probes are placed at multiple locations on the ion collection grid. Intercusp

electron collection on the anode backplate is monitored with 2 button probes, one at the corner and one at the mid-plane of the backplate intercusp region. Each button probe consists of a 0.32-cm-diameter stainless steel rod flush mounted inside an alumina tube. The button probes are essentially planar Langmuir probes except the bias voltage is no longer adjusted but held constant in either the ion saturation (ion current) or electron saturation (electron current) regime, similar to a Faraday probe. Collected current is calculated by measuring the voltage drop across a current shunt and dividing by the known resistance (10 kΩ). A schematic of the probes and their electrical setup is shown in Figure 3-6. The location of the 13 button probes on the ion collection grid is shown in Figure 3-7 and Figure 3-8.

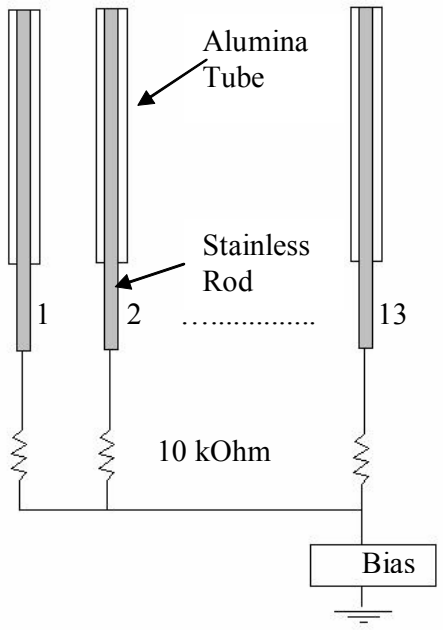

Figure 3-6: Schematic of the button probes and the electrical setup.

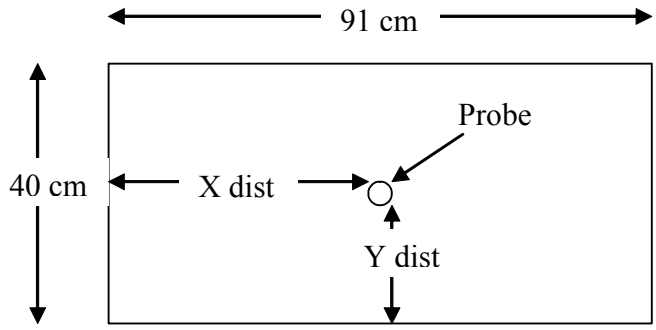

Looking upstream at the ion extraction area

Grid Plane Probe Number	X dist (cm)	Y dist (cm)
1	17.0	20.8
2	46.2	20.8
3	75.4	20.8
4	6.8	13.0
5	32.5	13.0
6	61.8	13.0
7	85.6	13.0
8	17.0	5.08
9	46.2	5.08
10	75.4	5.08
11	17.0	36.8
12	46.2	36.8
13	75.4	36.8
14 – Langmuir probe	51.6	20.8

Figure 3-7: Grid-plane button probe locations.

Figure 3-8: Photograph of the MCDC ion collection grid showing the button probe locations.

Because the magnetic circuit of the MCDC utilizes rectangular magnet rings, the electron deposition to the intercusp region corners is characterized. Button probes number 15 and 16 are mounted to the backplate of the anode on the left side of the left DCA and biased to collect electron current. Both probes are located midway between the magnetic cusps; i.e., in the middle of the intercusp region. Probe number 16 is placed between the corners of the rectangular cusps, while number 15 is placed at the vertical midpoint. A schematic of the probe locations is shown in Figure 3-9. This setup allows the intercusp corner electron deposition to be compared with that obtained at the mid-plane. The results presented utilize the ratio of the currents (corner probe current, probe 16, divided by mid-plane probe current, probe 15).

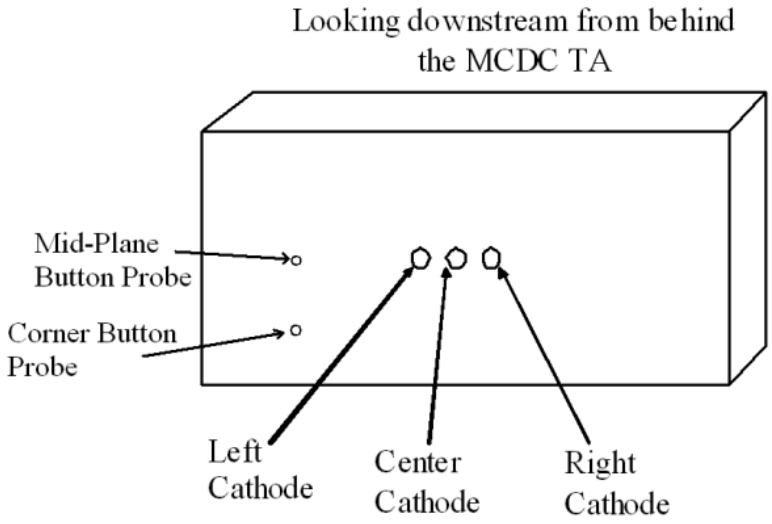

Figure 3-9: Locations of mid-plane and corner electron collecting button probes.

3.6 Current Probe

An F.W. Bell model IHA-100 current probe is utilized to monitor discharge current oscillations. A full scale DC current rating of ±100 A over a ±5 V range provides

a sensitivity of 50 mV/A. The probe is located on the plasma discharge side of the RC-filter in order to monitor discharge current oscillations.

3.7 Diagnostic Cylinders (DCs)

Dormant cathode plasma properties are analyzed by designing and implementing DCs that appear similar in size and shape to the active DCA. This ensures that the TA plasma interacts with the DCs similar to a dormant DCA. Six different DCs are presented in this study and they are a 5 planar Langmuir probe DC (5PLP-DC), 7 planar Langmuir probe DC (7PLP-DC), axial planar Langmuir probe DC (APLP-DC), axial cylindrical Langmuir probe DC (ACLP-DC), retarding potential analyzer DC (RPA-DC), and a 5 planar Langmuir probe DC with propellant flow (5PLPF-DC). The following sections describe the design, fabrication, and operation of each of the DCs.

3.7.1 5 Planar Langmuir Probe-DC (5PLP-DC)

Two 5PLP-DCs are fabricated to make plasma property measurements at the two dormant cathode locations internal to the TA. Each DC appears similar to the active DCA; however, each DC "keeper" is outfitted with 5 planar Langmuir probes (PLPs). A schematic of the 5PLP-DC is shown in Figure 3-10 and the 5 PLPs are placed at the spatial locations shown in Figure 3-11.

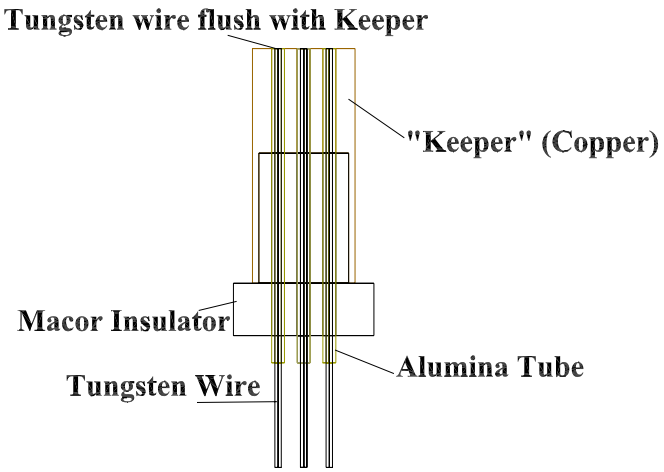

Figure 3-10: Schematic of the 5PLP-DC.

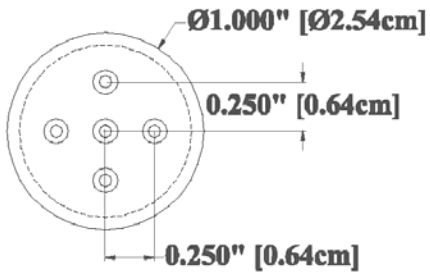

Figure 3-11: Probe locations on the 5PLP-DC "keeper" faceplate.

A cylindrical copper "keeper" is attached to a ceramic insulator to form the base of the DC. The 5PLP-DCs do not contain a "cathode" electrode. Ten PLPs are constructed of 0.16-cm-diameter tungsten wire surrounded by a 0.32-cm-outer-diameter alumina tube yielding a probe area of 2.01 mm^2. Each PLP is inserted axially into the DC such that the probe collecting surface is flush with the "keeper" faceplate. 5 PLPs are placed into each of the two DCs in a symmetrical pattern with each probe spaced 0.64 cm from the centerline axis. Ceramic epoxy is utilized to construct the probes, as well as to mate the probes, "keeper", and ceramic insulator. Finally, an aluminum mounting flange is utilized to attach the DC to the TA at one of the dormant cathode locations.

Electrically each of the probes is connected to the biasing power supply through a 100 Ω shunt resistor as shown in Figure 3-12.

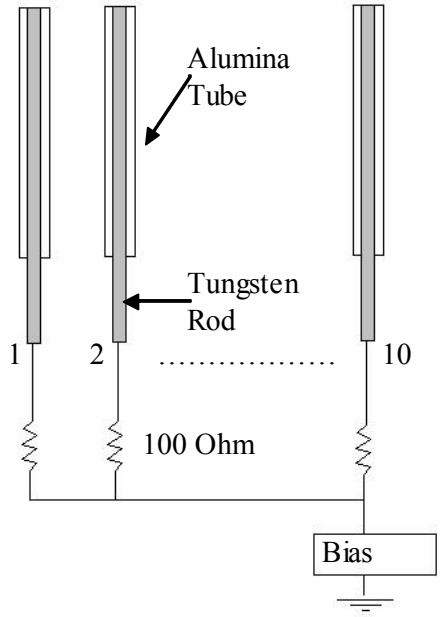

Figure 3-12: Electrical schematic of the planar Langmuir probes.

Each probe bias voltage is set with the bias supply and the corresponding voltage drop across the shunt resistor is measured. Collected current is then calculated by dividing the measured voltage drop by the shunt resistance. In this way the I-V characteristic for each probe is determined. Only one of the 5PLP-DCs is utilized during left DCA and middle DCA TA operation because the RPA-DC is placed at the other dormant cathode location. Both 5PLP-DCs are utilized during right DCA TA operation. Data are acquired for electromagnet currents of 0 A, +5 A, and +10 A, as well as with the DC electrically connected and electrically isolated from the TA. During electrically connected operation the "keeper" is connected to the anode through a 10 kΩ resistor. As mentioned above, the 5PLP-DC does not have a "cathode" electrode.

3.7.2 7 Planar Langmuir Probe-DC (7PLP-DC)

Two 7PLP-DCs are also fabricated to make plasma property measurements at the two dormant cathode locations. Each DC appears similar to the active DCA; however, each DC "keeper" is outfitted with 7 PLPs at different spatial locations as shown in Figure 3-13.

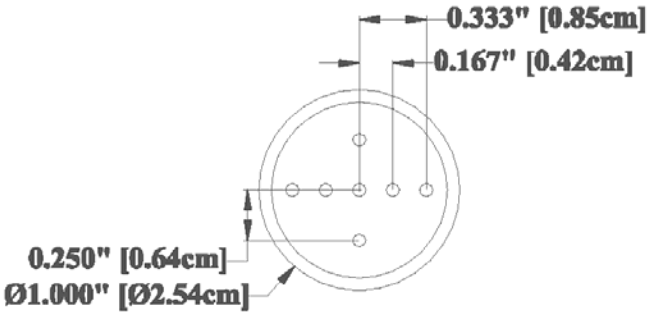

Figure 3-13: Probe locations on the 7PLP-DC "keeper" faceplate.

Fourteen PLPs are constructed of 0.08-cm-diameter tungsten wire surrounded by a 0.16-cm-outer-diameter alumina tube yielding a probe area of 0.50 mm^2. This device is constructed similar to the 5PLP-DC. A photograph of the 7PLP-DC mounted inside the TA is shown in Figure 3-14.

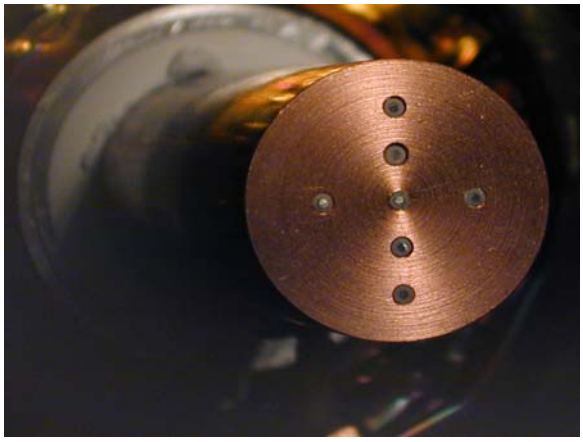

Figure 3-14: Photograph of a 7PLP-DC mounted inside the MCDC.

Electrically each of the probes is connected identical to the probes in the 5PLP-DCs shown in Figure 3-12, except a total of 14 probes and shunt resistors are utilized. 7PLP-DC I-V characteristics are obtained by the same procedure described for the 5PLP-DCs. Both of the 7PLP-DCs are utilized during left, middle, and right DCA operation. Data are acquired with electromagnet currents of 0 A, +5 A, and +10 A, as well as with the DC electrically connected and electrically isolated from the TA. During electrically connected operation the "keeper" is connected to the anode through a 10 kΩ resistor. Because the probes are not symmetric about the DC centerline axis, during experimental testing one of the 7PLP-DCs is oriented with the TA Y-axis and the other is oriented with the TA X-axis.

3.7.3 Axial Planar Langmuir Probe-DC (APLP-DC)

The axial planar Langmuir probe (APLP) DC appears similar in size and shape to the active DCA. Concentric "cathode" and "keeper" tubes are constructed out of copper and held in place by a ceramic insulator. "Keeper" and "cathode" orifice diameters are chosen to be identical to the active DCA. A ceramic insulator is utilized to hold the "keeper" and "cathode" at the required spacing. Two PLPs are constructed of 0.25-mm-diameter tungsten wire housed in a 1.24-mm-outer-diameter alumina tube yielding a probe area of 0.049 mm^2. Each PLP is 17.8-cm-long and is inserted through the DC "cathode" tube to extend in the positive Z-axis of the TA. The probe is concentric with the "cathode" and "keeper" tubes and is moved axially with respect to the "cathode" orifice. A 5.1 cm alumina guide tube is inserted in the "cathode" tube to assist the PLP in passing through the "cathode" and "keeper" orifices. This setup allows the planar probe to be positioned over a 12.7 cm range (10.2 cm external and 2.5 cm internal to the

"cathode"). A schematic of the APLP-DC is shown in Figure 3-15 and a photograph is shown in Figure 3-16.

Langmuir probe I-V characteristics are obtained at various axial locations to determine axial plasma properties at the dormant cathode positions. Axial probe location is adjusted using a stepper motor controlled translation stage mounted with a custom-made probe alignment stand. Utilizing the stand greatly reduces the time required to align each probe with the DC "cathode" guide tube and "cathode" orifice. Data are obtained for both left and middle DCA operation with the electromagnet at 0 A, +5 A, and +10 A. APLP-DC data are not obtained for right DCA operation due to time constraints. The APLP-DC is operated both electrically connected and electrically isolated from the TA. During electrically connected operation the APLP-DC "cathode" is connected to cathode common and the "keeper" is connected to the anode through a 10 kΩ resistor.

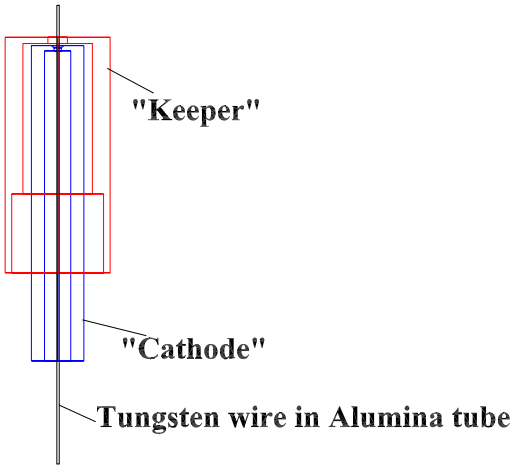

Figure 3-15: Schematic of the APLP-DC.

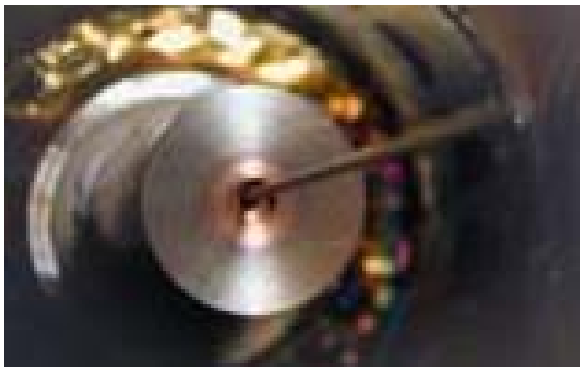

Figure 3-16: Photograph of a APLP-DC inside the MCDC. Note the PLP protruding from the "cathode" orifice.

3.7.4 Axial Cylindrical Langmuir Probe-DC (ACLP-DC)

Axial cylindrical Langmuir probe (ACLP) DC construction and appearance is nearly identical to the APLP-DC. In this case a cylindrical Langmuir probe (CLP) is utilized. Two CLPs are constructed of 0.25-mm-diameter tungsten wire housed in a 1.24-mm-outer-diameter alumina tube with the tungsten extending 3.2 mm beyond the tube. This yields a probe area of 2.56 mm^2. Each of the CLPs is 15.2-cm-long and is inserted through the DC "cathode" tube to extend in the positive Z-axis of the TA. This setup allows the probe to be positioned over a 10.2 cm range (7.6 cm external and 2.5 cm internal to the "cathode"). This setup is referred to as the ACLP-DC.

ACLP-DC operational setup is identical to the APLP-DC and data are obtained for both left and middle DCA operation with the electromagnet at 0 A, +5 A, and +10 A. ACLP-DC data are not obtained for right DCA operation due to time constraints. The ACLP-DC is operated both electrically connected and electrically isolated from the TA. During electrically connected operation the ACLP-DC "cathode" is connected to cathode common and the "keeper" is connected to the anode through a 10 kΩ resistor.

3.7.5 Retarding Potential Analyzer-DC (RPA-DC)

The retarding potential analyzer (RPA) DC appears similar in size and shape to the active DCA. However, the "cathode" tube has an internal miniature RPA. The miniature RPA is designed based on the multi-gridded energy analyzer described in Ref. 108, and the RPA described by Hofer,[109] Azziz,[110], and Beal.[111] Outer dimensions of the miniature RPA are approximately the same as the RPA described by Azziz,[110] which is approximately 50% smaller than that described by Hofer.[109]

The miniature RPA outer body is constructed of stainless steel with a diameter of 1.3 cm (0.50") and has an entrance aperture identical to the active DCA orifice. Internal to the RPA are three grids, four ceramic spacers, and a collector. Each grid is stainless steel with a 0.13-mm-thickness and 0.28-mm-diameter holes arranged in a staggered pattern with a center-to-center spacing of 0.43 mm, yielding an open area fraction of 38%. The first grid is allowed to float to reduce the number density internal to the RPA. The second grid is biased 25 V below cathode common to repel electrons from reaching the collector. The potential of the third grid is swept from -25 V to +45 V with respect to cathode common to repel ions. Finally the collector is connected to ground through an ammeter to measure the collected current. Ceramic boron nitride spacers are used to electrically isolate the grids and collector. The electrical connectivity for each grid and the thickness of the spacers is described in Table 3-1, which corresponds with Figure 3-17.

Spacer	Thickness (mm)
1	3.4
2	3.4
3	1.0
4	1.0
Grid	Potential w.r.t. Cathode Common (V)
1	Float
2	-25
3	-25 to 45
4	Collector -25 V

Table 3-1: RPA spacer dimensions and grid electrical bias setup.

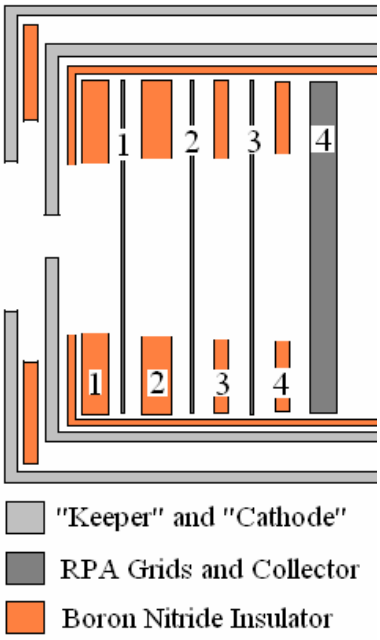

Figure 3-17: Schematic of the RPA-DC.

The miniature RPA is placed inside a stainless steel “keeper” tube and electrically isolated by another ceramic spacer. The body of the miniature RPA functions as the dormant “cathode” with the grids located internal to the “cathode”. A photograph and schematic of the RPA-DC are shown in Figure 3-17 and Figure 3-18, respectively.

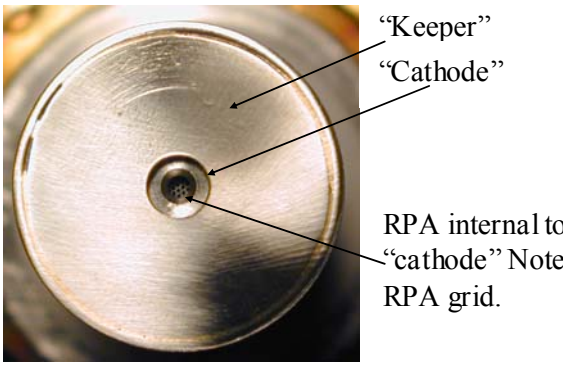

Figure 3-18: Photograph of the RPA-DC. Note the RPA grid internal to the "keeper" and "cathode".

Not shown in the photograph or the schematic are the two grids placed external to the RPA-DC covering the "keeper" orifice. These grids are required to reduce the plasma number density internal to the RPA. In order to function properly the gap distance between grids 2 and 3 must be less than approximately 4 times the Debye length (λ_D) to avoid space-charge-limitation of the grids.[108] Initial operation of the RPA is unsuccessful due to a large internal number density and hence a small Debye length. Adding grids external to the "keeper" is required to lower the RPA internal number density such that the Debye length meets the required criteria. The external grids act only to reduce the open area fraction of the "keeper" orifice and reduce the quantity of plasma present. Therefore the energy distribution of ions entering the RPA through the grid-covered "keeper" orifice is assumed to be unaffected by the external grids.

The RPA-DC is utilized for left and middle DCA operation with electromagnet currents of 0 A, +5 A, and +10 A. RPA-DC data are not obtained for the right DCA operational configuration. Electrical connectivity of the DC is also investigated by either isolating the RPA-DC or connecting it to the TA. During electrically connected operation

the RPA body acts as the "cathode" and is connected to cathode common, while the "keeper" is connected to the anode through a 10 kΩ resistor.

3.7.6 5 Planar Langmuir Probe with propellant Flow-DC (5PLPF-DC)

Two 5PLPF-DCs are fabricated to make plasma property measurements at the two dormant cathode locations internal to the TA. Each DC appears similar to the active DCA; however, each DC "keeper" is outfitted with 5 PLPs at different spatial locations as shown in Figure 3-19.

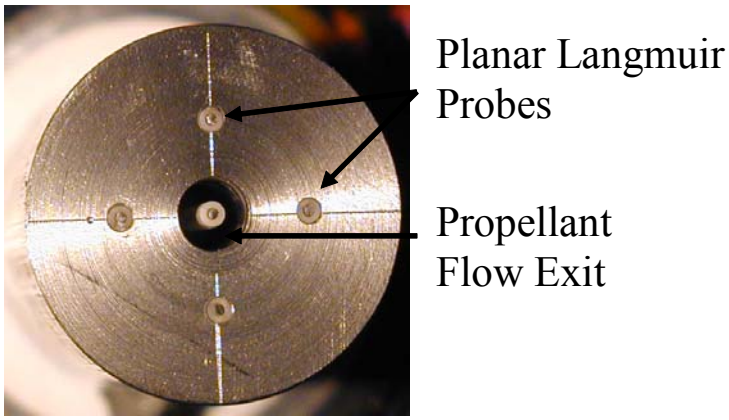

Figure 3-19: Photograph of a 5PLPF-DC inside the TA. Note the 5 planar Langmuir probes and propellant flow exhaust "keeper" orifice.

A stainless steel "keeper" is attached to a ceramic insulator to form the base of the DC. The 5PLPF-DCs do not contain a "cathode" electrode. Ten PLPs are constructed of 0.08-cm-diameter tungsten wire surrounded by a 0.16-cm-outer-diameter alumina tube yielding a probe area of 0.50 mm^2. 5 PLPs are placed into each of the two DCs in a symmetrical pattern with each probe spaced 0.64 cm from the centerline axis.

A 3.18-mm-outer-diameter tube is inserted off-centerline into the DC to feed propellant through the "keeper" orifice. A small internal channel is used to transfer the off-axis propellant tube exhaust to the "keeper" orifice. A schematic of this setup is

shown in Figure 3-20. Electrically each of the 5PLPF-DCs is operated identically to the 5PLP and 7PLP-DCs described above.

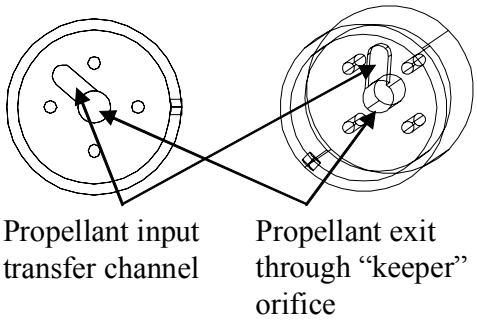

Figure 3-20: Schematic of the 5PLPF-DC internal gas feed system. Propellant enters off-axis and is then transferred to the "keeper" orifice by a small channel.

3.8 High-Speed Axial Reciprocating Probe Positioning System

The high-speed axial reciprocating probe (HARP) positioning system consists of a three-phase Trilogy 210 brushless dc servo motor with a linear "U"-shaped magnet track and a "T"-shaped coil moving on a set of linear tracks. The linear encoder for the system provides a positioning resolution of 5 μm.[112] The DC motor is controlled by a Pacific Scientific SC950 digital brushless servo drive controller and the controller also outputs the HARP position as a voltage signal. The HARP has a maximum sweep length of 559 mm and is capable of moving probes at speeds above 250 cm/s with acceleration rates on the order of 7 g's. The entire HARP assembly is enclosed within a stainless steel shroud with a small slot through which the probe can pass. The HARP system has had extensive use at PEPL and has been used to interrogate the internal plasma of both Hall thrusters[106,107,113-115] and ion thrusters.[79,94-98,116-118]

3.9 Radial and Axial Translation Stages

Radial and axial TA position is adjusted with a custom-built two-axis positioning system. This crossed-stage positioning system is composed of a 1.8-m-long linear stage in the radial direction mounted on a 0.9-m-long linear stage in the axial direction. Each stage is driven by a stepper motor and both stages have an absolute linear position accuracy of 0.15 mm. For those experiments utilizing the ACLP-DC and APLP-DC, a New England Affiliated Technologies (NEAT) RMS-800 single-axis ball-screw table with a stepper motor is utilized to adjust probe position. This table has a lead screw accuracy of 80 mm and a range of motion of 20 cm. A National Instruments NuDrive 4SX-411 powers the stepper motors and control of the tables is provided by a National Instruments PCI-7344 stepper controller through a LabView interface.

3.10 Data Acquisition Systems

3.10.1 Data Logger

A 34970A 22-bit Agilent data logger with 2 - 34901A 20-channel multiplexers (a total of 40 channels are available) is used to monitor TA operating parameters and record Langmuir probe characteristics. For the experimental investigations presented in this work, the data logger always records discharge current and voltage, three cathode and keeper currents, three cathode and keeper floating voltages, collection grid bias voltage and current, cathode common bias voltage and extracted current, cathode heater voltage and current, and electromagnet voltage and current. For those experiments utilizing various Langmuir probe diagnostics, the data logger also records the 15 button probe currents, 10 5PLP-DC currents, 14 7PLP-DC currents, and 10 5PLPF-DC currents. In the

case where a current is recorded, the voltage across a current shunt is measured and then divided by the known resistance. With this setup real-time performance data are obtained and data collection is extremely time efficient. One sweep through all utilized channels requires approximately 1.5 seconds.

3.10.2 Oscilloscope

A Tektronix TDS 3034B oscilloscope is utilized to measure discharge voltage and current oscillations. Reported peak-to-peak voltage oscillations are the difference between maximum and minimum values recorded during a 4 msec oscilloscope trace sweep. Voltage output from the discharge current Hall probe described above is recorded and converted to current using a known calibration curve.

3.10.3 Power DAQ

For some experiments a United Electronics Industries, Inc. Power DAQ PD2-MFS-8-500/14 PCI simultaneous sampling multifunction board with 8 channels is used to acquire and save data through a LabView interface. A dedicated computer operates the Power DAQ, which has 14 bit resolution and a maximum sampling frequency of 500 kS/s. Because of the need for fast sampling rates and storage of large amounts of data, the high-speed Power DAQ is utilized for the plasma property mapping portion of this work (Chapter 7).

CHAPTER 4:
DATA ANALYSIS TECHNIQUES

For the experimental investigation presented in this work, plasma property data inside the multiple-cathode discharge chamber (MCDC) test article (TA) are recorded using Langmuir probes and a retarding potential analyzer (RPA). Both planar and cylindrical single-Langmuir probes are utilized. The following sections describe the data analysis techniques used to analyze the probe data.

4.1 Langmuir Probe Analysis

A single-Langmuir probe consists of a single electrode connected to an external circuit that allows the probe voltage, V, to be varied with respect to the local plasma. Measuring the collected probe current, I, as a function of the probe voltage provides the I-V characteristic. A typical characteristic is shown in Figure 4-1.

The characteristic is divided into three main regions. At low voltages with respect to the plasma potential (V_p), the probe collects ions and repels electrons. This region is called ion saturation (Region I) and the current in this region represents the ion-saturation current. The point at which the probe collects zero net current (collected electron current equals collected ion current) is termed the floating potential, V_f. As the probe bias voltage increases, more electrons become capable of surmounting the potential-hill and the probe electron current increases. This is the electron retarding region of the probe trace (Region II). The final region is termed electron saturation (Region III) and collects the electron-

saturation current. V_p is called the plasma potential (or space potential) and represents the point at which the probe only collects electron current.[108]

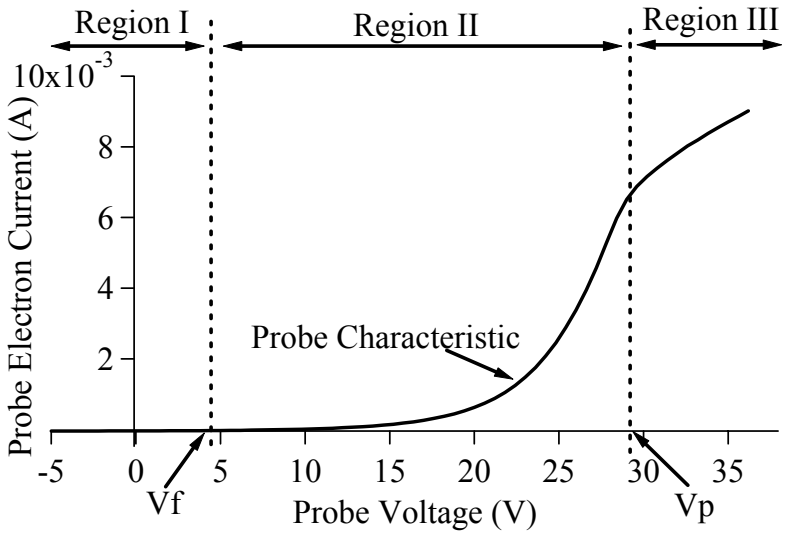

Figure 4-1: Example Langmuir probe I-V characteristic.

Langmuir probe I-V characteristics are typically analyzed based on two parameters: the Knudsen number (K_n) and Debye length (λ_D). The equation for the Knudsen number is given in Eqn. 4-1 and represents the transition between collisionless and continuum plasmas.

$$K_n = \frac{\lambda}{r} \qquad \textbf{Eqn. 4-1}$$

In this equation, λ is the mean free path (MFP) of charged particles and r is the probe radius. The MFP of ions and electrons in the discharge chamber of an ion thruster is on the order of meters, whereas the discharge chamber and probe radius are on the order of centimeters and millimeters, respectively. Therefore a collisionless analysis is appropriate. The relationship of the Debye length to electron number density, n_e, and electron temperature, T_e, is illustrated in the following equation.[43,80,119]

$$\lambda_D = 743\sqrt{\frac{T_e[eV]}{n_e[cm^{-3}]}} \qquad \textbf{Eqn. 4-2}$$

The ratio of the Debye length to the probe radius determines if a thin-sheath or orbital motion limited (OML) assumption is used.

The following sections describe the thin-sheath and OML analyses. A thin-sheath assumption is applied to the majority of I-V characteristics presented in this thesis and an OML analysis is applied to the axial cylindrical Langmuir probe (ACLP) diagnostic cylinder (DC) when the probe is internal to the DC. Finally, an attempt at analyzing data based on a dual primary-Maxwellian electron population is also described.

4.1.1 Thin-Sheath

Langmuir probes are typically sized such that the probe operates in the thin-sheath regime. Number density and electron temperature inside the TA are expected to have values within the range of 10^{10}-10^{13} cm^{-3} and 2-15 eV,[38,41,57,79,94-98,118,120-123] respectively. In the thin-sheath regime, the flux of particles entering the sheath can be calculated without considering the details of the orbits of these particles in the sheath.[105,108,119,124] For a large ratio of probe radius, r, to Debye length, λ_D, the collection area of the probe can be approximated as the area of the probe.[105,108,119,124] A large probe radius helps to minimize edge effects for planar probes (5PLP-DC, 7PLP-DC, 5PLPF-DC, and APLP-DC) and a large ratio of length to radius minimizes end effects for cylindrical probes (ACLP-DC, grid-plane probe, plasma mapping probe).

Because there are over 6 million I-V characteristics to analyze, the software IGOR Pro 4.0 by WaveMetrics, Inc. is utilized to analyze the data. IGOR loads the data files containing I-V pairs of data for each of the probe sweeps and then applies a thin-

sheath data analysis. Initially the floating potential is determined by locating the voltage value corresponding to zero current. Ion-saturation current is calculated as the average current obtained within Region I of the probe trace (i.e., the average current collected at voltages less than the floating potential). Plasma potential is then calculated by finding the maximum in the derivative of the I-V curve.

Based on the floating potential and plasma potential, IGOR determines the electron retarding region of the probe trace (Region II) and attempts to fit a line to the natural log of the electron current versus voltage data. The fit is made progressively better by removing I-V data pairs from the beginning and end of the electron retarding region. This procedure is repeated until a specified chi-squared parameter for the fit is achieved. The procedure loop is also plotted so that the user can visually validate the fit being obtained. Electron temperature is then calculated as the inverse of the slope of the log-linear I-V curve. The measured ion-saturation current, electron temperature, and the Bohm approximation for ion velocity[43,53,105,119,125] readily give the ion number density by the following equation.

$$I_{si} = 0.61 e n_i \sqrt{\frac{eT_e}{M_i}} A_p \qquad \textbf{Eqn. 4-3}$$

In this equation, T_e is electron temperature, e is the elementary charge, A_p is the probe area, I_{si} is the ion-saturation current, n_i is ion number density, and M_i is the ion mass.

4.1.2 Orbital Motion Limited

In the OML or "thick-sheath" regime the sheath dimensions and orbits of particles entering the sheath must be considered. This regime is analyzed by the techniques developed by Laframboise[126,127] that assume a cylindrical probe immersed in a cold,

collisionless, stationary plasma. In this case the sheath dimensions are assumed to increase with probe bias such that the collected ion current is affected. Ion current collected by a probe biased below the floating potential is defined by Eqn. 4-4.[127]

$$I_i = \xi e n_i \sqrt{\frac{eT_e}{2\pi M_i}} A_p \qquad \textbf{Eqn. 4-4}$$

In this equation ξ is a dimensionless current correction developed by Laframboise that depends on probe size, plasma number density, and temperature. For the temperatures and number densities obtained in most ion thruster plasma, Steinbrüchel suggests that ξ is given to within 3% error by Eqn. 4-5.[128]

$$\xi = \sqrt{\frac{1.27V}{T_e}} \qquad \textbf{Eqn. 4-5}$$

Combining Eqn. 4-4 and Eqn. 4-5 allows I^2 to be plotted as a linear function of V and the ion number density can then be calculated as a function of the slope of I^2 versus V as illustrated in Eqn. 4-6.

$$n_i = \frac{1}{A_p} \sqrt{\left(dI_i^2 \Big/ dV \right) \frac{2\pi M_i}{1.27e^3}} \qquad \textbf{Eqn. 4-6}$$

In this equation, n_i is ion number density, A_p is probe area, I_i is ion current, V is probe voltage, M_i is ion mass, and e is the elementary charge.

Chen suggests that the OML regime is entered when the ratio of probe radius to Debye length is less than approximately three.[119] Since only the number density calculation changes in this OML analysis, the IGOR thin-sheath analysis described above is augmented to contain an OML option. The thin-sheath analysis is initially blindly applied, however, if the Debye length is calculated to be less than a third of the probe

radius the OML number density calculation is utilized. An OML calculation is unnecessary for a planar probe,[119,126] and the grid-plane and plasma mapping probes always operate in the thin-sheath regime, so only the ACLP-DC results are subjected to the OML subroutine option. More discussion about the ACLP-DC axial locations over which OML is necessary can be found in section 6.2.4.

4.1.3 Dual Primary-Maxwellian

In addition to the thin-sheath and OML analyses, a dual primary-Maxwellian electron population analysis is also attempted. In plasma consisting of primary- and Maxwellian-electrons, the current to a biased Langmuir probe can be represented by Eqn. 4-7.[129]

$$I = B_1 + B_2 V + B_3 \exp(B_4 V) \qquad \textbf{Eqn. 4-7}$$

In this equation primary- and Maxwellian-electron current are represented by the linear and exponential terms, respectively. The B_i coefficients can be numerically determined from a least-squares differential-correction technique[130] utilizing the electron retarding region of the experimental data and the plasma properties subsequently calculated based on these coefficients.[129] For instance, the primary-electron energy is given by the following equation.

$$\zeta_p = V_p + {}^{B_1}\!/_{B_2} \qquad \textbf{Eqn. 4-8}$$

In this equation ζ_p is primary electron energy and V_p is plasma potential.

Unfortunately the dual population analysis is unable to be successfully applied. The numerically determined coefficients are found to be extremely sensitive to the initial conditions. Specifically, the experimental data voltage range can significantly affect the

sign and magnitude of the B_1 and B_2 values. For instance, removing one I-V data pair from the electron retarding region can cause the calculated primary-electron energy to fluctuate from 30 V to 10 V and the primary-electron current contribution to become negative. This result is inconsistent with that presented by Beattie,[129] who found that calculated plasma properties were insensitive to the range of the electron retarding region utilized to determine the coefficients. Beattie also suggests that a 20-25 V data range with a maximum 1 V increment be used to minimize the sensitivity of the calculated coefficients to noise within the data, a requirement satisfied by data presented here.

The sensitivity described may be caused by a variety of reasons, for example: 1) there are no primaries present at the DC locations; 2) the primary-current is orders of magnitude smaller than the Maxwellian-current, which may explain why the coefficients associated with the linear primary electron current (B_1 and B_2) are so sensitive; 3) there may be too much noise in the data; 4) the voltage range is too small, 20 V is near the edge of the range suggested by Beattie; 5) Beattie utilized a mercury ion thruster plasma, primary-electrons may not be as easily detected with this method in the TA xenon plasma. It is important to note that Herman has also had difficulty applying this analysis to the NEXT discharge plasma.[118]

4.1.4 Magnetic Field Effects

The presence of a magnetic field can alter the I-V characteristic obtained by a single-Langmuir probe. The electron retarding region used to determine the electron temperature is generally not affected, but the electron saturation current is.[131-133] Because electrons spiral around magnetic field lines, if the cyclotron radius of electrons is of the same magnitude as the probe radius, then probe sheath structures can become non-

symmetric or oblong causing the electron saturation current of the probe trace to be reduced. As magnetic field strength increases the electron saturation current decreases because spiraling electrons are unable to cross the magnetic field lines and become collected by the probe.[131-133] However, the analysis presented here obtains the number density from the ion-saturation current and the magnetic field in the bulk discharge region of the MCDC is not large enough to have an appreciable effect on ion collection. Even in the cusp regions of the MCDC where the magnetic field can be on the order of 1,000 G, the ion cyclotron radius is an order of magnitude larger than the radius of the probe. Therefore the presence of the magnetic field is not expected to affect the number density measurement.

Because the electron saturation current is reduced due to the presence of a magnetic field, the resulting plasma potential, which is typically determined from the knee of the electron retarding region (or the maximum of the first derivative), is affected. Specifically, the magnetic field causes the calculated plasma potential to be less than its true value. This shift can be accounted for and is dependent on the orientation of the probe with respect to the magnetic field, the electron temperature, and the mean free path of electrons.[133] However, for the results presented here, the shift of the plasma potential due to the magnetic field is less than the error associated with the calculation of plasma potential from the single-Langmuir probe data. Therefore the effect of the magnetic field is not considered in the analysis algorithm.

4.1.5 Error Analysis

Traditional error estimates for electrostatic single-Langmuir probes are typically 50% and 20% for number density and electron temperature, respectively.[108,134] However,

the relative error between measurements using the same experimental setup is expected to be considerably smaller. Using methods similar to those presented here, Foster estimated the overall uncertainties in Langmuir probe measurements and found 15% and 25% for electron temperature and number density, respectively.[44] The uncertainty in the number density is determined by the sum of the fractional uncertainty in the ion current (15%) and the fractional uncertainty in the square root of the electron temperature (7.5%).

Comparison of data taken during different facility pump downs show excellent agreement and comparable results for both the near-DCA and bulk plasma discharge regions. This result illustrates the small relative error expected between data acquired with an identical experimental setup. Data acquired in the near-DCA plume region during plasma property mapping (Chapter 7) are considerably more difficult to analyze due to rounding of the electron retarding-to-electron saturation region (knee) of the probe I-V trace. This phenomenon may be caused by a variety of factors, such as high-frequency large-amplitude plasma potential fluctuations, the presence of flowing plasma, magnetic field effects, or a dual primary-Maxwellian electron population. This result is further discussed in Chapter 7.

4.2 Retarding Potential Analyzer (RPA)

An RPA is utilized in the RPA-DC in order to analyze ion voltage distributions at the dormant cathode locations. In an RPA a series of grids are utilized to selectively filter ions depending on their energy-to-charge ratios. Specifically, the derivative of the resulting I-V characteristic is proportional to the ion voltage distribution function as illustrated in Eqn. 4-9.[75,109]

$$\frac{dI}{dV} = -\frac{Z_i^2 e^2 n_i A_c}{M_i} f(V) \qquad \textbf{Eqn. 4-9}$$

In this equation, Z_i is the charge-state of the ion, e is the elementary charge, n_i is the ion density, A_c is the collection area, f(V) is the ion voltage distribution function, and M_i is the ion mass. Of primary importance for the research presented here is the voltage value for the peak in the distribution function, otherwise known as the most-probable-voltage. Because the acquired raw data have enough noise to make the derivative meaningless, a certain amount of averaging, data interpolation, and smoothing are required.

Input data sweeps are initially averaged in order to reduce noise associated with these data. Then the data analysis routine is applied utilizing an IGOR 4.0 function that 1) interpolates; 2) smoothes; 3) takes the derivative; and 4) determines the most-probable-voltage. Each interpolated I-V data pair is determined by linearly interpolating the preceding and following experimental data pair. Next, the interpolated data are smoothed utilizing a smoothing spline, which is a built-in IGOR function based on the algorithm described by Reinsche,[135] that requires a user-defined filter factor to determine the amount of smoothing. Next, the derivative of the smoothed data is taken to determine the ion voltage distribution function (the E/q distribution function). The last step in the RPA data analysis routine determines the most-probable-voltage by locating the voltage at which the peak in the distribution function occurs.

For the data presented, various levels of smoothing are required ranging from a filter factor of 0.05 (less smoothing) to 0.5 (more smoothing) depending on the noise in the data. Filter factors are determined on a trial and error basis by visually watching the

output profiles as shown in Figure 4-2. The filter factor is increased until a discernable derivative is obtained.

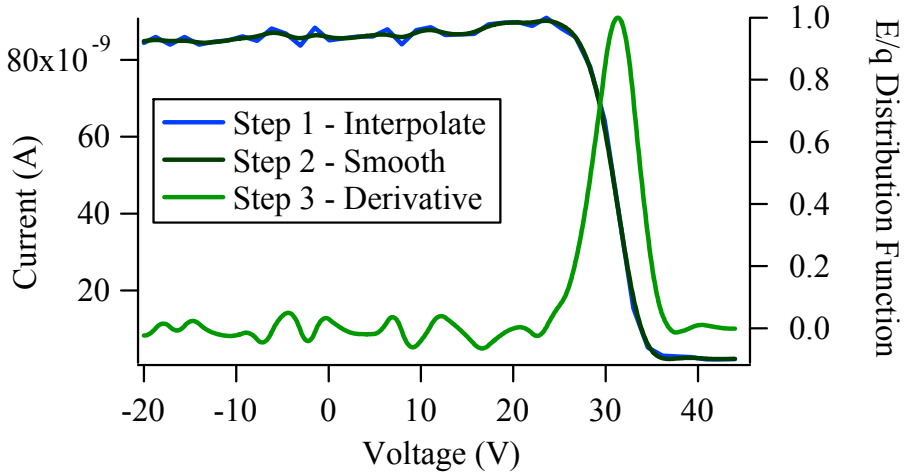

Figure 4-2: Example retarding potential analyzer (RPA) analysis routine results.

CHAPTER 5:
PERFORMANCE, STABILITY, AND UNIFORMITY

Validation that the multiple-cathode discharge chamber (MCDC) test article (TA) functions similar to other ion thruster discharge chambers is completed by investigating TA performance, stability, and uniformity. For the experimental investigation presented in the following sections, TA operational parameters are monitored using the data logger. The button probes are mounted to the backplate of the TA and ion collection grid, and the grid-plane cylindrical single-Langmuir probe is also utilized. Lastly, the DCUs are mounted at the TA dormant cathode locations.

5.1 Flow Rate Determination

Because the TA is operated as a simulated ion thruster without beam extraction, the flow rate into the discharge chamber must be reduced to keep the neutral density equal to that during beam extraction. A relationship for the reduced flow rate as a function of the beam extraction flow rate is shown in the equation below.[92]

$$\hat{\dot{m}} = \dot{m}\left[1 - \eta_{ud}\left(1 - \frac{\hat{\phi}_i}{\phi_i}\right)\right] \qquad \textbf{Eqn. 5-1}$$

$\hat{\dot{m}}$ is the reduced propellant flow rate, $\dot{m}$ is the propellant flow rate during beam extraction (eq. A), $\hat{\phi}_i$ is the ion collection grid transparency to ions, ϕ_i is the high-voltage ion optics transparency to ions, and η_{ud} is the propellant utilization efficiency.

The beam extraction flow rate for the TA is not known and cannot be assumed equal to the NASA Glenn Research Center (GRC) High Power Electric Propulsion (HiPEP) thruster extraction flow rate because the TA has a different magnetic field topology. Consequently, the reduced flow rate for the TA must be experimentally determined by measuring the grid-plane ion current as a function of mass flow rate.

The grid-plane ion current is monitored while both the discharge cathode assembly (DCA) and main plenum flow is reduced. The flow rate corresponding with the maximum grid-plane ion current is assumed to be the reduced flow rate. These experiments are conducted for both centerline and off-centerline DCA positions and for multiple magnetic field configurations. A wait time of approximately 2 minutes is used to allow the flow rate adjustment to equilibrate inside the TA.

Initially, the DCA and main plenum flow rates are set at the GRC HiPEP beam extraction level.[32,56] First, the main plenum flow is held constant while the DCA flow is reduced. As the DCA flow decreases, the grid-plane current increases and peak-to-peak discharge voltage oscillations increase for all DCA and magnetic field configurations investigated. The DCA flow rate that provides the largest grid-plane current and relatively low peak-to-peak discharge voltage oscillations is considered the optimized reduced DCA flow rate. In some cases the DCA flow is optimized at 5.73 sccm, however, for other cases the flow is set to 6.12 sccm because lower flow rates cause peak-to-peak discharge voltage oscillations greater than +5 V. Large voltage oscillations are known to be the difference between cathode spot and plume mode, and these oscillations can be detrimental to the cathode.[136] Previous researchers have suggested that peak-to-peak

voltage oscillations should be less than +5 V during the preferred "spot mode" operation.[7,8]

After determining the DCA flow rate, the main plenum flow is obtained by setting the DCA flow to its reduced value and then decreasing the main plenum flow. As the plenum flow decreases an increase in grid-plane current and peak-to-peak discharge voltage oscillations is observed for all DCA and magnetic field configurations investigated. A peak in the grid-plane current is typically obtained at a main plenum flow rate of 30.9 sccm. However, for the 50 G enclosed magnetic field configuration the peak occurs at 24.8 sccm. Examples of the trends obtained during this study are shown in Figure 5-1 and Figure 5-2 for the DCA and main plenum, respectively.

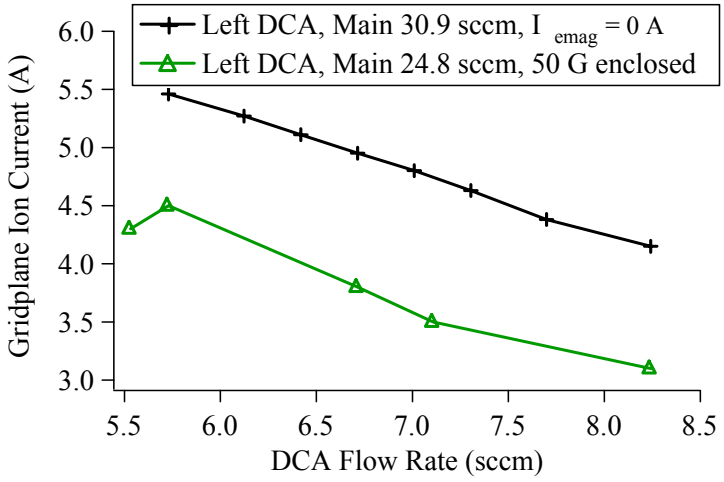

Figure 5-1: Flow rate study results for the DCA.

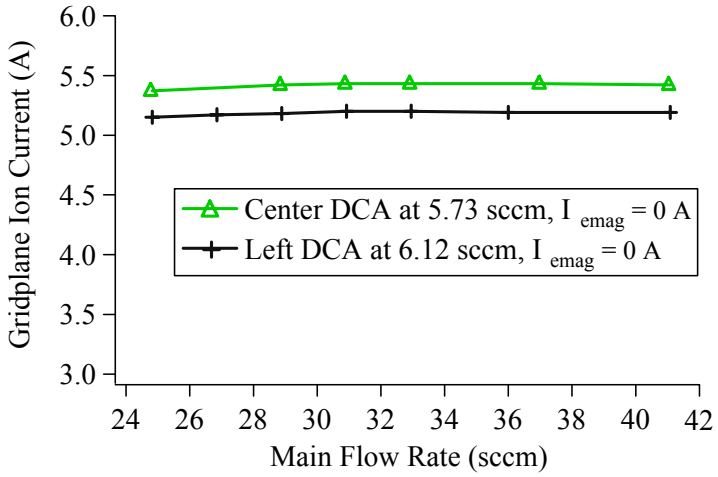

Figure 5-2: Flow rate study results for the main plenum.

Configuration		DCA (sccm)	Main (sccm)
Left Active	50 G Enclosed	5.73	24.8
	Asymmetric	6.12	30.9
	Electromagnet -10 A	6.12	30.9
	Electromagnet -5 A	N/A	N/A
	Electromagnet 0 A	6.12	30.9
	Electromagnet +5 A	6.12	30.9
	Electromagnet +10 A	6.12	30.9
Center Active	50 G Enclosed	5.73	24.8
	Electromagnet -10 A	5.73	30.9
	Electromagnet -5 A	N/A	N/A
	Electromagnet 0 A	5.73	30.9
	Electromagnet +5 A	5.73	30.9
	Electromagnet +10 A	5.73	30.9

Table 5-1: TA mass flow rates.

Based on these results the DCA and main plenum flow rates for all investigated DCA and magnetic field configurations are determined and are summarized in Table 5-1. For the configuration with the electromagnet at -5 A the peak-to-peak discharge voltage oscillations increase significantly above +5 V and therefore the TA is unable to be operated at this condition. More information regarding this configuration is provided in the following sections.

5.2 Bias Voltage Studies

In conjunction with the flow rate study, multiple bias voltage studies are conducted to ensure that the ion collection grid, cathode common bias, and button probes are in the saturation regime. The cathode common bias study is completed by adjusting the bias voltage and monitoring the extracted current. Results indicate that cathode common should be biased at 25 V above facility ground. The ion collection grid is biased negative with respect to cathode common in order to measure ion current. As the bias voltage becomes more negative, ion saturation is achieved. Results show that an ion collection grid bias voltage of -20 V with respect to cathode common is required. These results are consistent with those found by other researchers.[57,92]

Lastly, a bias voltage study on the button probes is completed. Results show that the grid probes require the same bias voltage as the collection grid, -20 V with respect to cathode common. The backplate electron probes are biased +35 V with respect to cathode common (+60 V with respect to ground) based on a bias voltage study and internal ion thruster plasma data obtained by Herman.[117,118] Typical profiles for the bias voltage studies are shown in Figure 5-3. For all results reported here, cathode common is biased 25 V above facility ground, the ion collection grid and grid-plane ion button probes are biased -20 V with respect to cathode common, and the backplate electron button probes are biased +35 V with respect to cathode common.

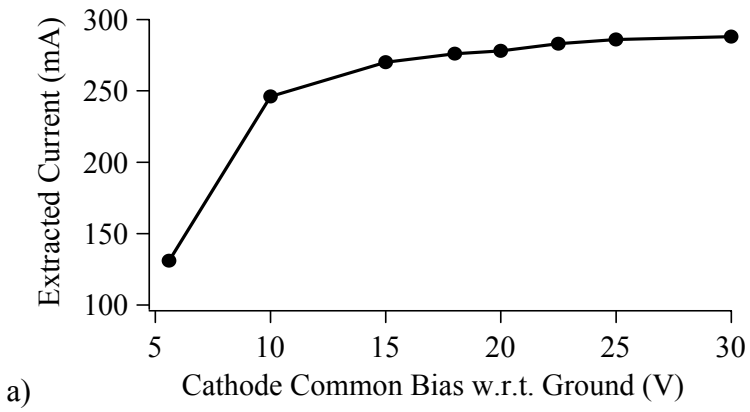

a)

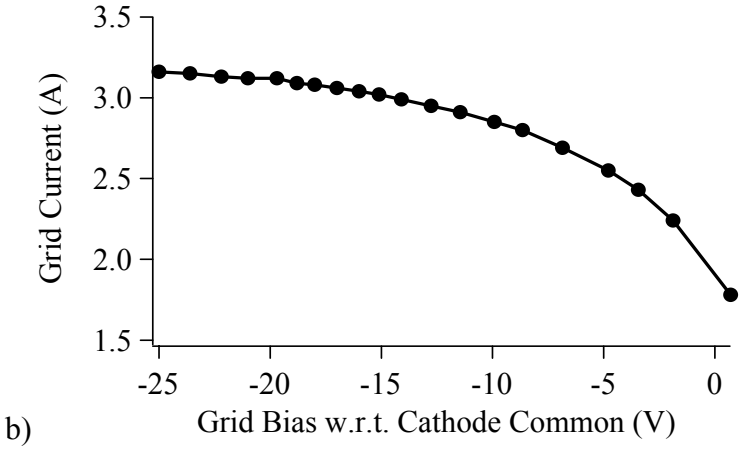

b)

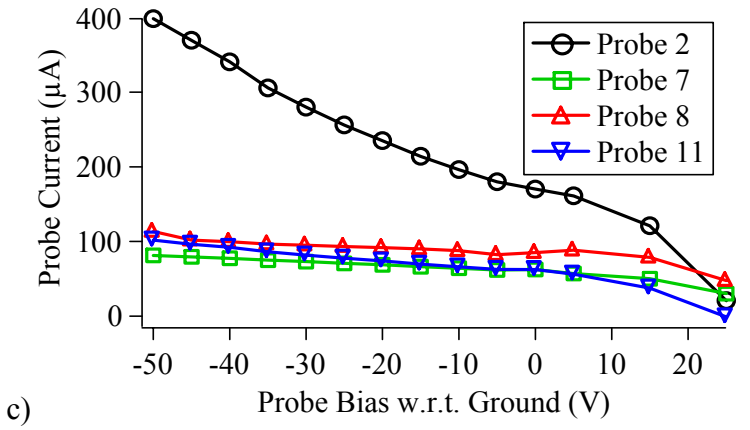

c)

Figure 5-3: Bias voltage study results for a) cathode common, b) ion collection grid, and c) grid-plane probes.

5.3 Performance and Flatness Calculations

Analysis of the performance and beam flatness of the TA is critical for determining its ability to function as an efficient ion thruster discharge chamber. Performance curves are generated by plotting ion production costs as a function of propellant utilization efficiency.[32,57,92] The following equations are utilized to determine the performance of the TA.

$$\hat{\phi}_i = \frac{0.35J_s + J_b}{J_g} \qquad \textbf{Eqn. 5-2}$$

$$\eta_{ud} = \frac{\phi_i J_g}{\hat{m} + \phi_i J_g \left(1 - \frac{\hat{\phi}_i}{\phi_i}\right)} \qquad \textbf{Eqn. 5-3}$$

$$\varepsilon_b = \frac{\left(J_d - \phi_i J_g\right) V_d}{\phi_i J_g} \qquad \textbf{Eqn. 5-4}$$

J_g is the grid-plane ion current (summation of J_s, current collected by the grid, and J_b, the extracted or beam current), ϕ_i is the high-voltage ion optics transparency to ions (estimated at 70% based on the HiPEP optics),[93] η_{ud} is the propellant utilization efficiency, $\hat{\dot{m}}$ is the reduced propellant flow rate in equivalent amperes, $\hat{\phi}_i$ is the ion collection grid transparency to ions, J_d is the discharge current, V_d is the discharge voltage, and ε_b is the ion production cost in W/A. ε_b and η_{ud} are calculated by setting J_d and $\hat{\dot{m}}$, and then measuring J_s, J_b, and V_d. With these parameters known the calculation is straightforward. Performance curves are generated by incrementally

decreasing J_d from the nominal 30 A value and recording the new values. Unfortunately, increasing J_d is not an option because the DCA has a maximum current rating of 30 A. $\hat{\dot{m}}$ does not include the ingested flow due to background gas because this contribution is determined to be less than 1% of the total flow rate.

Physically, the propellant utilization efficiency, η_{ud}, is the fraction of input propellant that becomes ionized and utilized as the ion beam, and ion production cost, ε_b, is the amount of energy required to create an ion (eV/ion) or an amp of current (W/A, assuming purely singly-charged plasma W/A = eV/ion). In general, ion thrusters are quite good at producing plasma and have propellant utilization efficiencies and ion production costs of ~90% and ~200 W/A, respectively.

The value of 0.35 in Eqn. 5-2 represents the fraction of ions that strike the ion collection grid and subsequently exit the discharge chamber. Previous researchers have found this value to be closer to 0.50 or 0.55.[57,92] However, those results were obtained when utilizing the high-voltage ion optics as the ion collection grid. For the experiments presented here high-voltage ion optics are not utilized as the ion collection grid. Instead, a grid with the same open area fraction and larger diameter holes is utilized. In this case, if an exiting ion fraction of 0.50 is utilized, the propellant utilization efficiency is calculated to be greater than 1, an obviously anomalous result. An exiting ion fraction of 0.35 is chosen because this value ensures that all calculated propellant utilization efficiencies are less than 1.

Beam flatness is calculated as the average beam current density divided by the peak beam current density.[137] In this case the current density is measured at discrete points at the grid plane by the 13 grid-plane button probes. Flatness is calculated by

averaging the current density of the 13 probes and then dividing by the maximum. Unfortunately, for the experiments presented here a grid-plane button probe is not located directly downstream of the left DCA. Therefore when the left DCA is active the current density directly downstream of this DCA is not measured. Presumably this location would be the peak (or close to the peak) current density during left DCA operation. The flatness calculated during left DCA operation assumes a peak current density value equal to that measured during center DCA operation. This correction is believed to provide a better approximation of the true flatness.

Utilizing the 13 grid-plane button probes to calculate flatness assumes that the probes are both uniformly distributed on the grid and that a sufficient number of probes are utilized. Figure 3-7 and Figure 3-8 give the locations of the 13 grid-plane button probes. The bottom-half of the grid contains 10 uniformly distributed probes, while the other 3 probes are located on the top-half of the grid. The 3 probes on the top-half of the grid validate the grid-plane current density symmetry about the MCDC mid-plane. A sufficient number of probes are utilized because the average current density obtained by the probes shows good agreement with the grid-plane current density, calculated by dividing the collected grid current by the grid collection area.

Another method for determining the average grid-plane current density is to curve-fit the button probe data in both the lateral and transverse (X and Y) dimensions. The average grid-plane current density is then obtained by integrating in two dimensions and dividing by the grid collection area. Although this method may prove to be more accurate, due to time constraints it is not utilized for this study.

5.4 Results

The following sections and sub-sections are divided based on the TA magnetic field configuration and DCA activity. The effect of DCU electrical connectivity and DCU propellant flow rate on performance, flatness, DCU currents and voltages, backplate electron deposition, and grid-plane plasma properties is described. TA operation is validated for all of the 7 magnetic field configurations and for both left and center active DCAs. The DCUs are operated both electrically connected and isolated from the electric circuit. DCU flow rates are set at no flow, half the active DCA flow, and the full DCA flow rate while the discharge current is maintained at the nominal 30 A and the total flow rate is kept constant. Performance curves are generated by incrementally decreasing the discharge current from 30 A to 25 A.

5.4.1 50 G Enclosed Configurations

For the 50 G enclosed configuration the electromagnet is set at 0 A and the 4 magnetic iron c-channels are attached to the sides of the anode. The c-channels are designed to correspond with the locations of the rectangular permanent magnet rings; i.e. the magnetic cusps. A topological profile of the magnetic field configuration is shown in Figure 5-4.

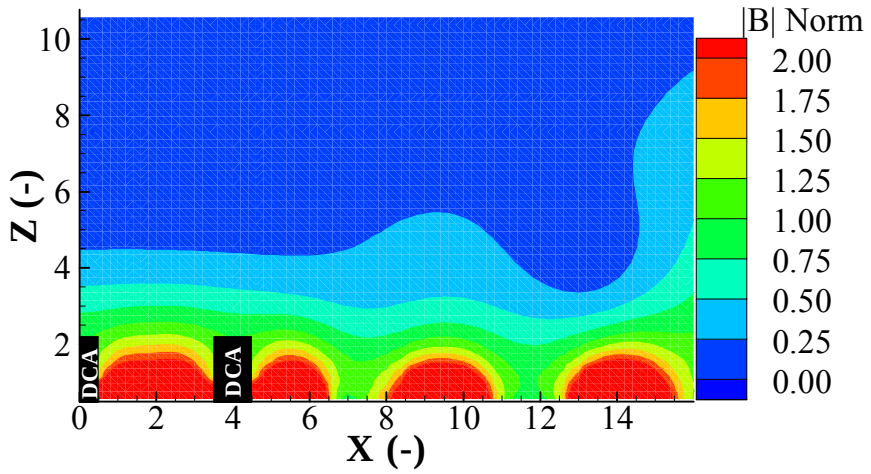

Figure 5-4: TA 50 G enclosed magnetic field topology.

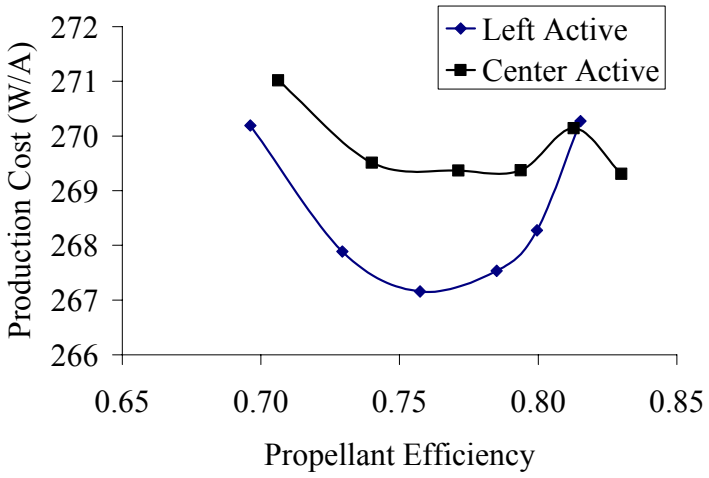

Figure 5-5: TA performance curves for 50 G enclosed, left and center active DCA configurations. DCU propellant flow and electrical connectivity do not affect these results.

5.4.1.1 Left DCA Active

Steady operation of the TA is validated for the 50 G enclosed configuration with the left DCA active. The discharge voltage is on the order of 27 V and the grid-plane ion current is on the order of 4 A for all investigated settings. The performance curve for the 50 G enclosed configuration with the DCUs electrically isolated and no flow is shown in

Figure 5-5. Performance curves with the DCUs electrically connected and with a propellant flow rate show no appreciable difference in magnitude or trend.

During performance mapping, as the discharge current is decreased from 30 A to 25 A (i.e., as the propellant utilization decreases) several trends become apparent. The discharge voltage decreases by only approximately 1 V and grid-plane ion current decreases by 0.7 A. The calculated flatness parameter decreases from 0.35 to 0.33 and the backplate current ratio (corner probe current divided by mid-plane probe current) decreases from 8.0 to 6.2. The center and right DCU display the same floating potential trends and magnitudes during performance mapping, cathode floating voltage increases from -10.6 V to -9.6 V and keeper floating voltage increases from 7.0 V to 7.3 V.

Discharge current is fixed at 30 A and the total flow rate is kept constant as the DCU flow rates are increased and set at zero, half the DCA flow, and then the full DCA flow rate. As the flow rate increases a purple spot becomes visible downstream of each DCU. During this procedure several trends become apparent. For both the electrically connected and electrically isolated cases, as the DCU flow rate increases the discharge voltage decreases only 0.5 V and the grid-plane current only decreases approximately 0.05 A. Propellant efficiency and ion production costs remain approximately constant at 0.81 and 270 W/A, respectively. Flatness remains relatively constant at 0.35. The backplate electron current ratio decreases as DCU flow increases for both electrical cases. DCU floating voltages typically increase with DCU flow rate. DCU cathode current shows no clear trend and the DCU keeper current decreases with increasing flow rate. These results are illustrated in Figure 5-6 and Figure 5-7.

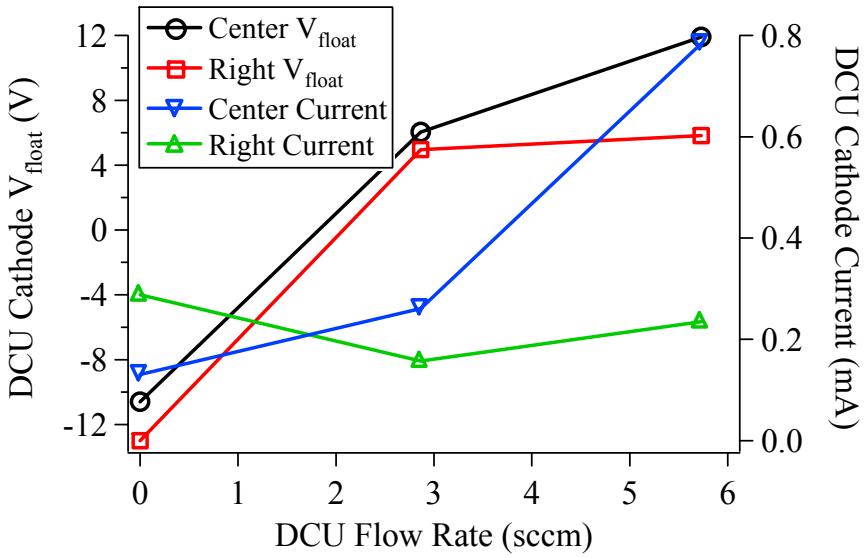

Figure 5-6: DCU cathode floating voltage and collected current as a function of DCU flow rate for the 50 G enclosed, left active DCA configurations.

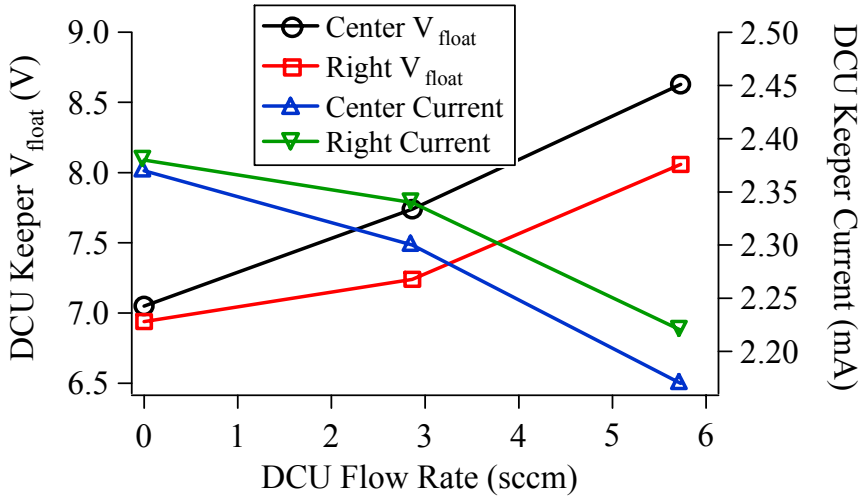

Figure 5-7: DCU keeper floating voltage and collected current as a function of DCU flow rate for the 50 G enclosed, left active DCA configurations.

Results from the Langmuir probe show grid-plane floating potential, plasma potential, electron temperature, and ion number density are on the order of 4.7 V, 27 V, 4.2 eV, and 8.5×10^{10} cm^{-3}, respectively. Note that voltages are referenced with respect to cathode common. Peak-to-peak discharge voltage oscillations are on the order of 3.4 V

for all investigated settings. DCU electrical connectivity and flow rate do not significantly affect these results.

5.4.1.2 Center DCA Active

Steady operation of the TA is validated for the 50 G enclosed configuration with the center DCA active. The discharge voltage increases to 28 V, but the grid-plane ion current and flatness remain the same at 4 A and 0.35, respectively. Although the flatness does not change, the peak in the profile moves to the center of the TA. The same trends and magnitudes in discharge voltage, grid-plane ion current, and flatness are obtained during performance mapping. The backplate current ratio displays the same trend, however, the magnitude increases to almost 12 (corner probe measures 12 times the current of the midpoint probe). The performance curve for the center DCA active has slightly larger losses than when the left DCA is active and this is shown in Figure 5-5. Again, performance curves with the DCUs electrically connected and with a propellant flow rate show no appreciable difference in magnitude or trend.

As the DCU flow rate is increased, the discharge current and total propellant flow rate are kept constant. As the flow rate increases a purple spot becomes visible downstream of each DCU. Discharge voltage decreases 0.5 V and grid-plane ion current decreases 0.05 A over the full range of DCU flow rates. Propellant efficiency and ion production costs remain approximately constant at 0.83 and 270 W/A. These results are similar to the left active DCA configuration. Flatness decreases slightly from 0.35 to 0.33 as DCU flow rate is increased to its full DCA value. Backplate electron current ratio does not display a significant trend and remains approximately constant at 12. Finally, DCU floating potentials tend to increase with DCU flow rate, while DCU cathode currents

increase and keeper currents decrease with increasing DCU flow rate. These trends are illustrated in Figure 5-8 and Figure 5-9.

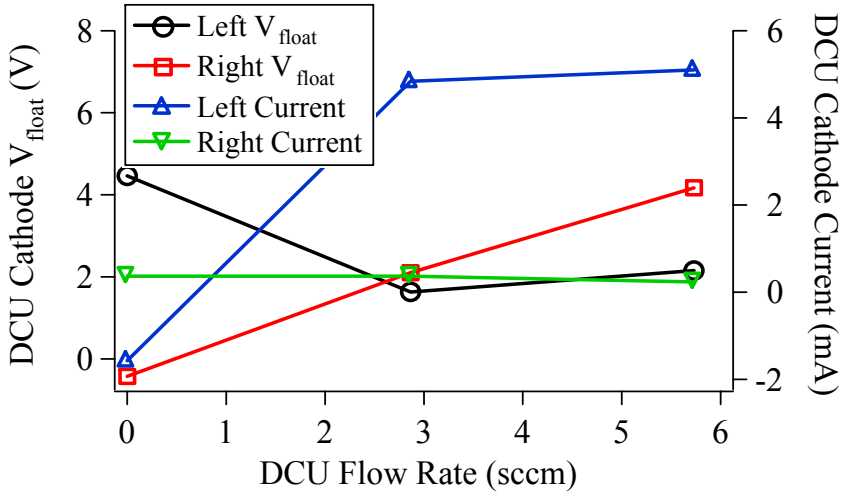

Figure 5-8: DCU cathode floating voltage and collected current as a function of DCU flow rate for the 50 G enclosed, center active DCA configurations.

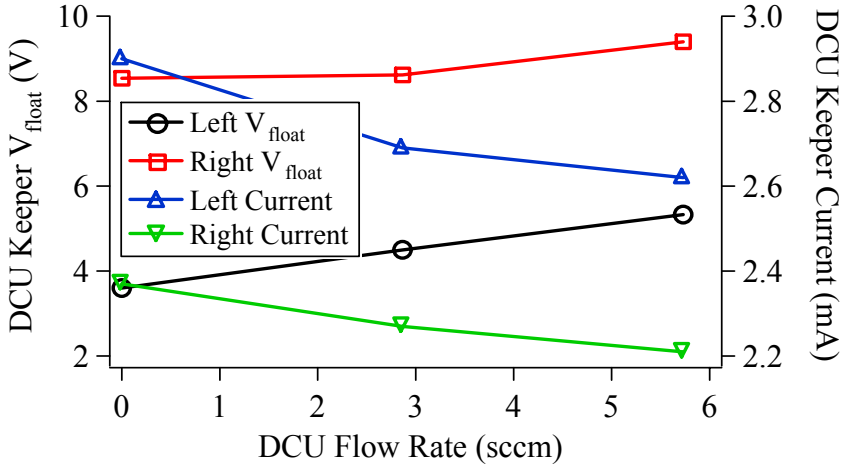

Figure 5-9: DCU keeper floating voltage and collected current as a function of DCU flow rate for the 50 G enclosed, center active DCA configurations.

Results from the Langmuir probe show grid-plane floating potential, plasma potential, electron temperature, and ion number density are on the order of 4.2 V, 27 V, 4.4 eV, and 7.8×10^{10} cm^{-3}, respectively. Note that voltages are referenced with respect to

cathode common. Peak-to-peak discharge voltage oscillations are on the order of 4.0 V for all investigated settings. DCU electrical connectivity and flow rate do not significantly affect these results.

5.4.2 Electromagnet -10 A Configurations

For the -10 A electromagnet configuration the backplate electromagnet is operated at -10 A. A topological profile of this configuration is shown in Figure 5-10.

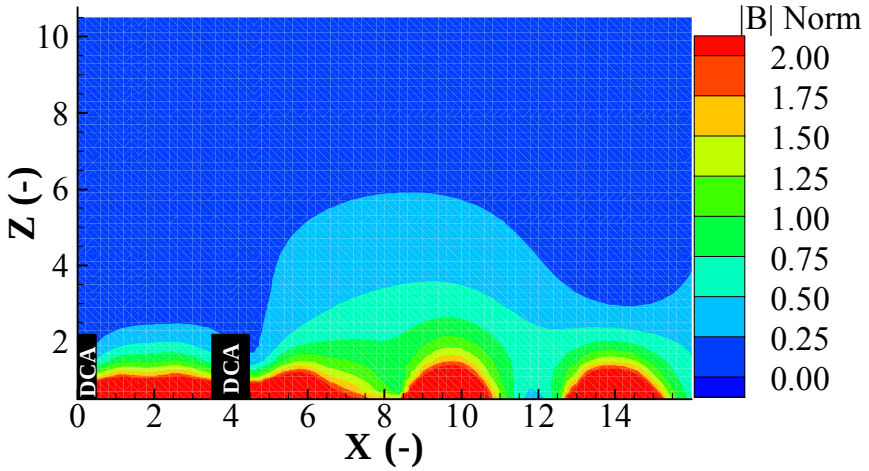

Figure 5-10: TA -10 A electromagnet configuration magnetic field topology.

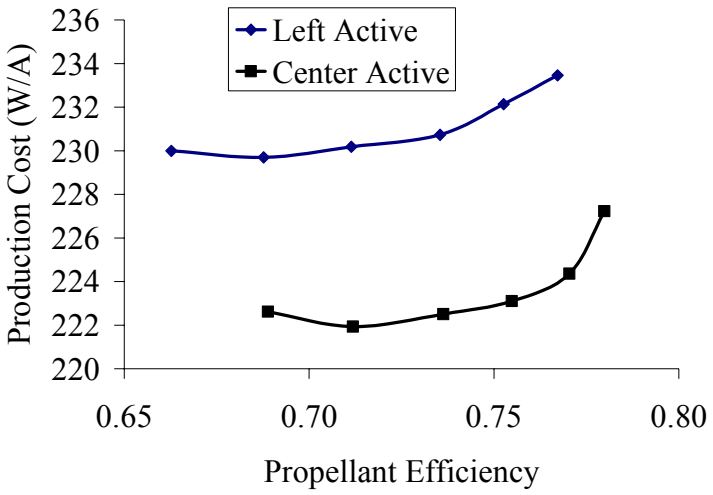

Figure 5-11: TA performance curves for the -10 A electromagnet, left and center active DCA configurations. DCU propellant flow and electrical connectivity do not affect these results.

5.4.2.1 Left DCA Active

Steady operation of the TA is validated for the -10 A electromagnet configuration with the left DCA active. The discharge voltage is on the order of 26 V and the grid-plane ion current is on the order of 4 A for all investigated settings. The performance curve for the -10 A electromagnet configuration with the DCUs electrically isolated and no flow is shown in Figure 5-11. Performance curves with the DCUs electrically connected and with a propellant flow rate show no appreciable difference in magnitude or trend.

During performance mapping, as the discharge current is reduced from 30 A to 25 A, discharge voltage decreases by approximately 1 V, grid-plane current decreases from 4.3 A to 3.5 A, flatness decreases from 0.27 to 0.25, and the backplate current ratio remains relatively constant at 5.5. Center and right DCU floating potentials during performance mapping are not as similar as in the 50 G enclosed configurations. Center DCU cathode potentials are on the order of -5.7 V while right DCU cathode potentials are

on the order of -9.7 V. Center DCU keeper potentials are 7.7 V while right DCU keeper potentials are 7.2 V. Each of these values varies approximately ±0.2 V during performance mapping.

Discharge current is fixed at 30 A and the total propellant flow rate is kept constant as the DCU flow rate is increased and set at three different values; zero, half the DCA flow rate, and the full DCA flow rate. As the flow rate increases a purple spot becomes visible downstream of each DCU. During this procedure discharge voltage decreases only 0.5 V and grid-plane ion current decreases 0.1 A as the DCU flow rate increases to the full DCA flow rate. Propellant efficiency and ion production costs remain approximately constant at 0.77 and 234 W/A, respectively. Flatness and backplate current ratio also remain approximately constant at 0.27 and 5.5, respectively. DCU electrical connectivity does not affect these results. DCU floating voltages increase, cathode current does not display a significant trend, and keeper current decreases with increasing flow rate. These trends are shown in Figure 5-12 and Figure 5-13.

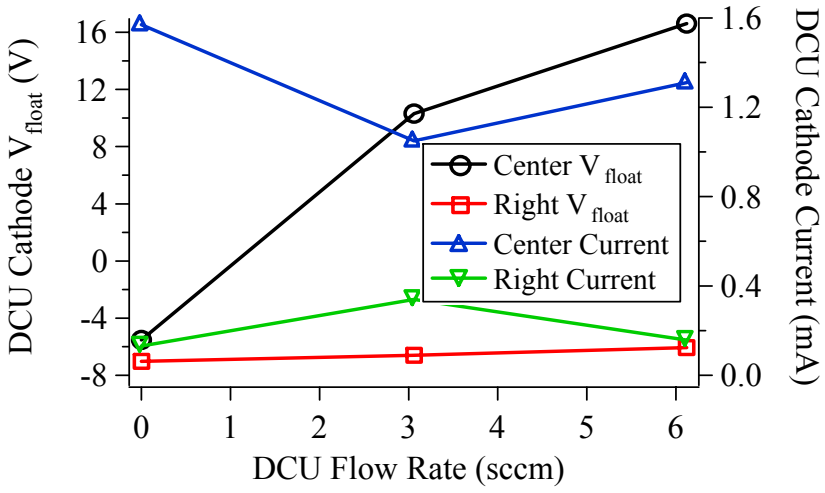

Figure 5-12: DCU cathode floating voltage and collected current as a function of DCU flow rate for the -10 A electromagnet, left active DCA configurations.

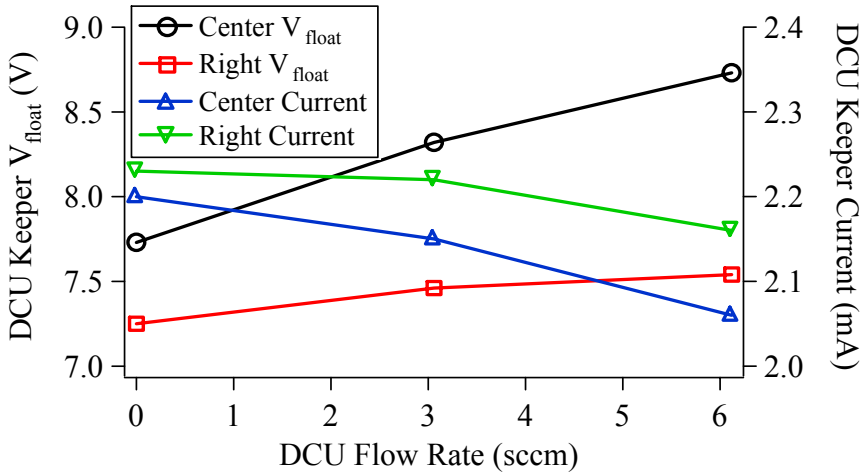

Figure 5-13: DCU keeper floating voltage and collected current as a function of DCU flow rate for the -10 A electromagnet, left active DCA configurations.

Results from the Langmuir probe show grid-plane floating potential, plasma potential, electron temperature, and ion number density are on the order of 5.0 V, 27 V, 4.1 eV, and 9.7×10^{10} cm^{-3}, respectively. Note that voltages are referenced with respect to cathode common. Peak-to-peak discharge voltage oscillations are on the order of 3.0 V for all investigated settings. DCU electrical connectivity and flow rate do not significantly affect these results.

5.4.2.2 Center DCA Active

Steady operation of the TA is validated for the -10 A electromagnet configuration with the center DCA active. Performance for the -10 A electromagnet configuration with the center DCA active is shown in Figure 5-11. Production costs are less for the center active DCA than for the left active DCA. Trends and magnitudes in discharge voltage and grid-plane ion current remain the same as the left active DCA configuration. Trends in flatness and backplate current ratio remain the same, however, the magnitude of the flatness decreases to 0.22 and the backplate current ratio increases to approximately 8.5.

Performance curves with the DCUs electrically connected and with a propellant flow rate show no appreciable difference in magnitude or trend.

As the DCU flow rate is increased, discharge current and total propellant flow rate are kept constant. As the flow rate increases a purple spot becomes visible downstream of each DCU. Discharge voltage decreases 0.5 V and grid-plane ion current decreases 0.05 A, while propellant utilization efficiency and ion production costs remain constant at 0.78 and 228 W/A as the DCU flow increases. Flatness remains constant at 0.22 and backplate current ratio decreases slightly from the nominal 8.5. DCU floating voltages increase, cathode currents do not display a consistent trend, and keeper currents decrease with increasing DCU flow rate. These trends are shown in Figure 5-14 and Figure 5-15.

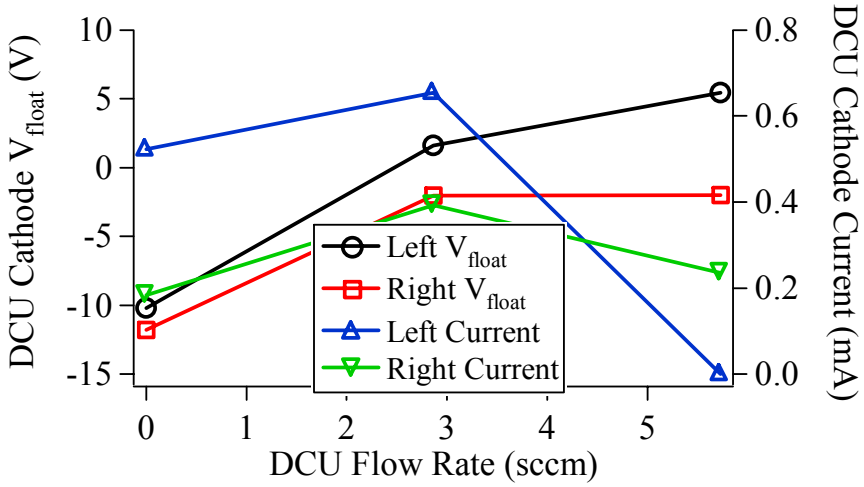

Figure 5-14: DCU cathode floating voltage and collected current as a function of DCU flow rate for the -10 A electromagnet, center active DCA configurations.

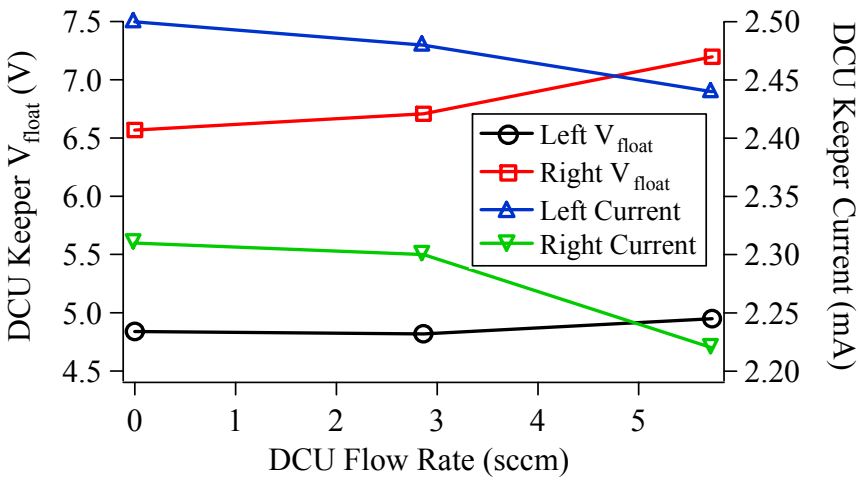

Figure 5-15: DCU keeper floating voltage and collected current as a function of DCU flow rate for the -10 A electromagnet, center active DCA configurations.

Results from the Langmuir probe show grid-plane floating potential is on the order of 3.3 V. Anomalous results for plasma potential, electron temperature, and ion number densities are obtained for this condition because the analysis provides plasma potential values significantly larger than the discharge voltage. Peak-to-peak discharge voltage oscillations are on the order of 3.4 V for all investigated settings. DCU electrical connectivity and flow rate do not significantly affect these results.

5.4.3 Electromagnet -5 A Configurations

For the -5 A electromagnet configuration the backplate electromagnet is operated at -5 A and this configuration is identical to the all-permanent-magnet case. A topological profile of this configuration is shown in Figure 5-16.

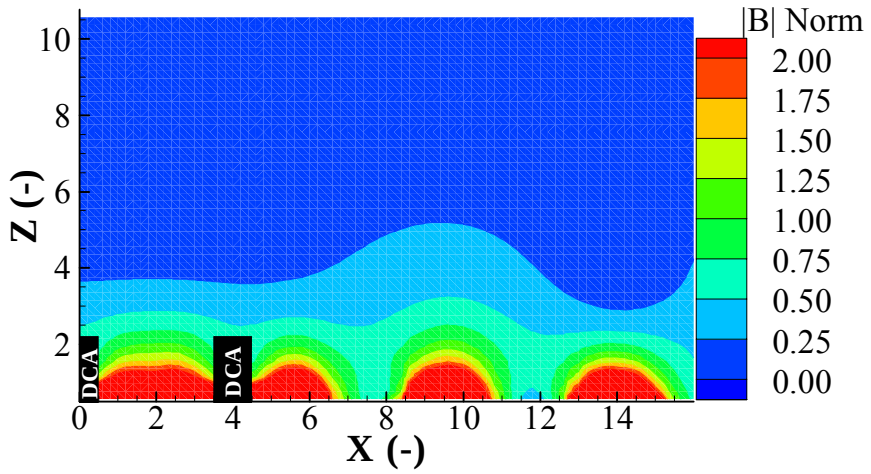

Figure 5-16: TA -5 A electromagnet configuration magnetic field topology.

Steady operation of this configuration is only possible at increased DCA flow rates on the order of 6.60 sccm with a main plenum flow rate of 30.9 sccm. Values lower than 6.60 sccm cause the peak-to-peak discharge voltage oscillations to increase well above +5 V. At flow rates similar to those used for the other magnetic field configurations the peak-to-peak discharge voltage oscillations increase to as much as the full discharge potential. Furthermore, the ion production cost and propellant utilization efficiency never decrease below 450 W/A and 0.55, respectively. Because of these results the -5 A electromagnet configuration is not investigated further. Performance curves are not obtained and DCU flow rate affects are not studied. An explanation for these results is not attempted here.

5.4.4 Electromagnet 0 A Configurations

For the 0 A electromagnet configuration the backplate electromagnet is operated at 0 A. A topological profile of this configuration is shown in Figure 5-17.

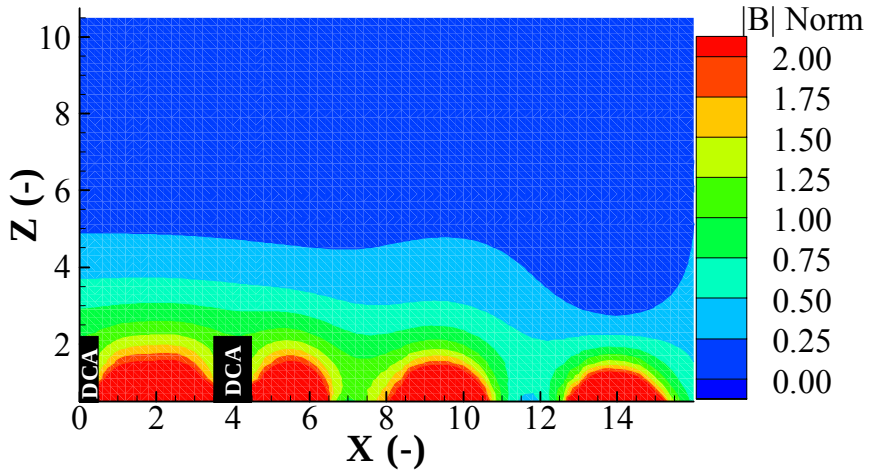

Figure 5-17: TA 0 A electromagnet configuration magnetic field topology.

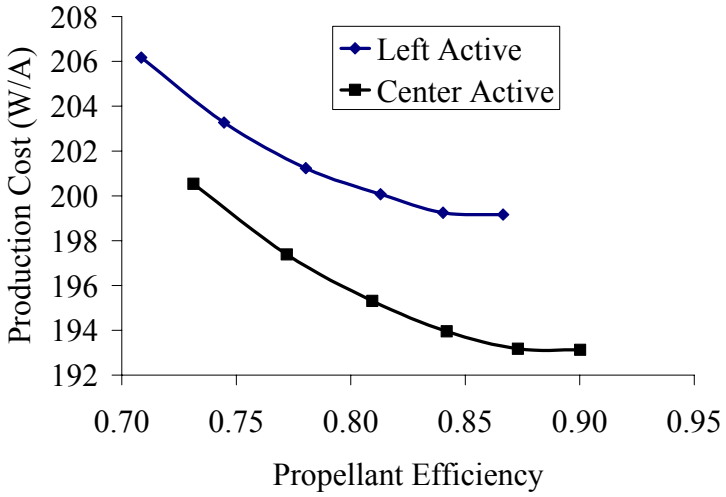

Figure 5-18: TA performance curves for the 0 A electromagnet, left and center active DCA configurations. DCU propellant flow and electrical connectivity do not affect these results.

5.4.4.1 Left DCA Active

Steady operation of the TA is validated for the 0 A electromagnet configuration. A bluish oval region is visible in the center of the TA. Visually, this configuration generates the largest and most uniform plasma distribution The discharge voltage is on the order of 27 V and the grid-plane ion current is on the order of 5 A for all investigated

settings. The performance curve for the 0 A electromagnet configuration with the DCUs electrically isolated and no flow is shown in Figure 5-18. Performance curves with the DCUs electrically connected and with a propellant flow rate show no appreciable difference in magnitude or trend.

During performance mapping, as the discharge current is reduced from 30 A to 25 A, discharge voltage decreases by approximately 1 V, grid-plane current decreases from 5.2 A to 3. 9 A, flatness decreases from 0.53 to 0.50, and the backplate current ratio decreases from 17 to 11. Center DCU cathode potentials are on the order of -5.2 V while right DCU cathode potentials are on the order of -1.2 V. Center DCU keeper potentials are 7.8 V while right DCU keeper potentials are 8.0 V. Each of these values varies approximately ±0.2 V during performance mapping.

Discharge current is fixed at 30 A and the total propellant flow rate is kept constant as the DCU flow rate is increased and set at three different values; zero, half the DCA flow rate, and the full DCA flow rate. As the flow rate increases a purple spot becomes visible downstream of each DCU. During this procedure discharge voltage decreases only 1 V and grid-plane ion current decreases 0.15 A as the DCU flow rate increases to the full DCA flow rate. Propellant efficiency and ion production costs remain approximately constant at 0.86 and 199 W/A, respectively. Flatness increases and backplate current ratio decreases significantly with increasing DCU flow rate. Flatness changes from 0.53 to 0.63 and backplate current ratio changes from 17 to 4. DCU electrical connectivity does not affect these results. DCU floating voltages increase, cathode current does not display a significant trend, and keeper current decreases with increasing flow rate. These results are shown in Figure 5-19 and Figure 5-20.

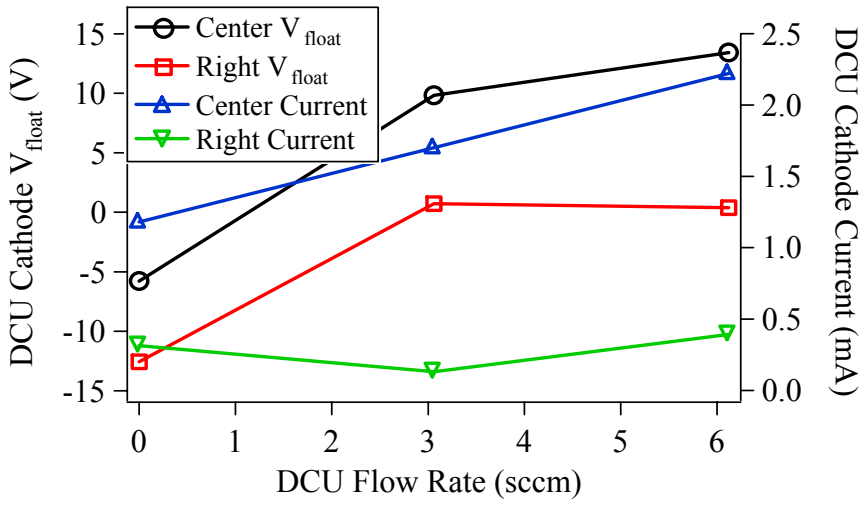

Figure 5-19: DCU cathode floating voltage and collected current as a function of DCU flow rate for the 0 A electromagnet, left active DCA configurations.

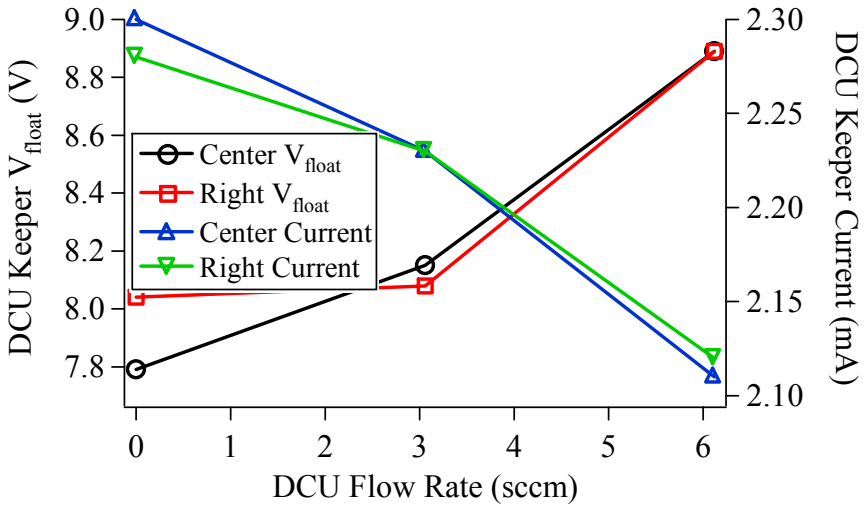

Figure 5-20: DCU keeper floating voltage and collected current as a function of DCU flow rate for the 0 A electromagnet, left active DCA configurations.

Results from the Langmuir probe show grid-plane floating potential, plasma potential, electron temperature, and ion number density are on the order of 7.5 V, 27 V, 3.5 eV, and 6.7×10^{10} cm^{-3}, respectively. Note that voltages are referenced with respect to cathode common. Peak-to-peak discharge voltage oscillations are on the order of 3.5 V

for all investigated settings. DCU electrical connectivity and flow rate do not significantly affect these results.

5.4.4.2 Center DCA Active

Steady operation of the TA is validated for the 0 A electromagnet configuration with the center DCA active. Performance for the 0 A electromagnet configuration with the center DCA active is shown in Figure 5-18. Production costs are less for the center active DCA than for the left active DCA. Discharge voltage increases to 28 V and grid-plane ion current increases to 5.4 A, but trends associated with performance mapping remain the same as the left active DCA configuration. Flatness decreases from 0.55 to 0.52 and backplate current ratio decreases from 18 to 12 during performance mapping. Performance curves with the DCUs electrically connected and with a propellant flow rate show no appreciable difference in magnitude or trend.

As the DCU flow rate is increased, discharge current and total propellant flow rate are kept constant. As the flow rate increases a purple spot becomes visible downstream of each DCU. Discharge voltage decreases 1 V and grid-plane ion current decreases 0.15 A, while propellant utilization efficiency and ion production costs remain constant at 0.89 and 194 W/A as the DCU flow increases. Flatness remains constant at 0.55 and backplate current ratio decreases considerably from 18 to 10. DCU floating voltages increase, cathode currents do not display a common trend, and keeper currents decrease with increasing DCU flow rate. These trends are shown in Figure 5-21 and Figure 5-22.

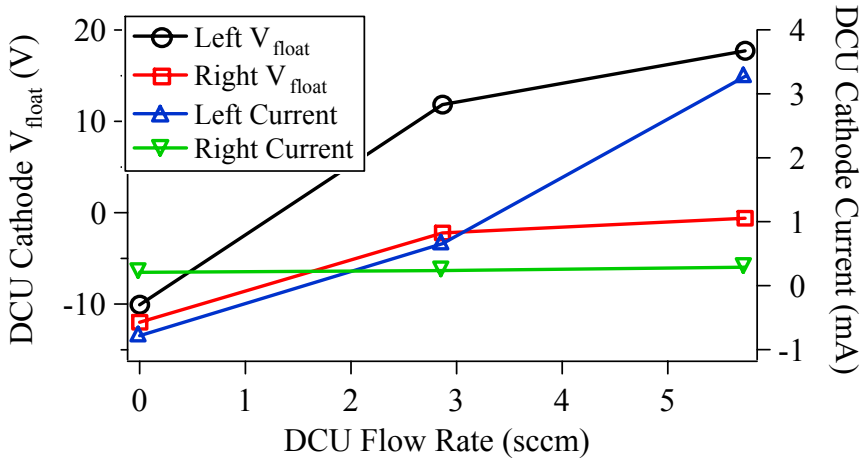

Figure 5-21: DCU cathode floating voltage and collected current as a function of DCU flow rate for the 0 A electromagnet, center active DCA configurations.

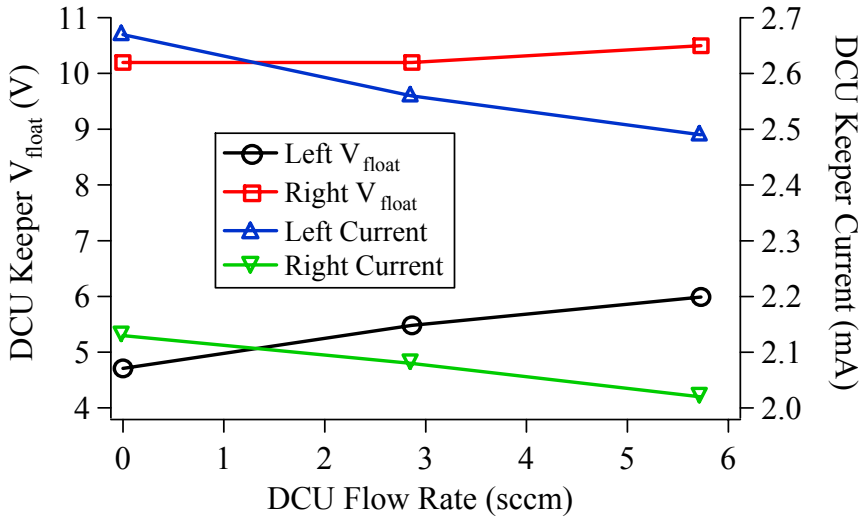

Figure 5-22: DCU keeper floating voltage and collected current as a function of DCU flow rate for the 0 A electromagnet, center active DCA configurations.

Results from the Langmuir probe show grid-plane floating potential, plasma potential, electron temperature, and ion number density are on the order of 7.4 V, 27 V, 3.7 eV, and 6.5×10^{10} cm^{-3}, respectively. Note that voltages are referenced with respect to cathode common. Peak-to-peak discharge voltage oscillations are on the order of 3.6 V

for all investigated settings. DCU electrical connectivity and flow rate do not significantly affect these results.

5.4.5 Electromagnet +5 A Configurations

For the +5 A electromagnet configuration the backplate electromagnet is operated at +5 A. A topological profile of this configuration is shown in Figure 5-23.

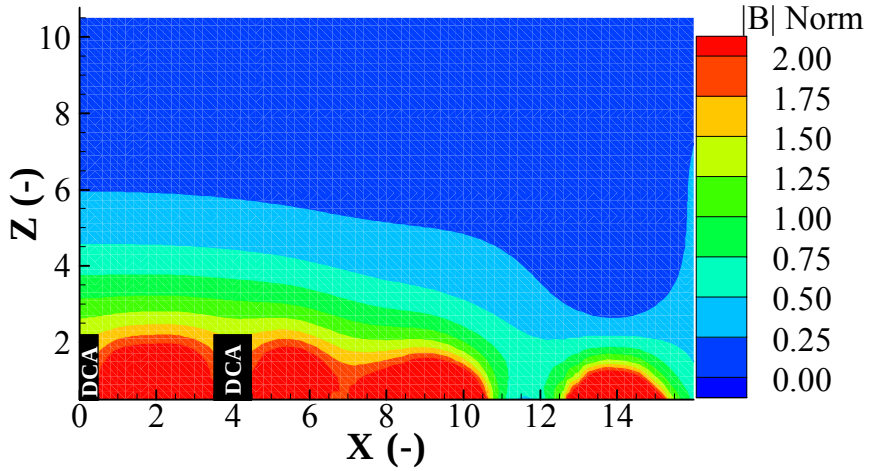

Figure 5-23: TA +5 A electromagnet configuration magnetic field topology.

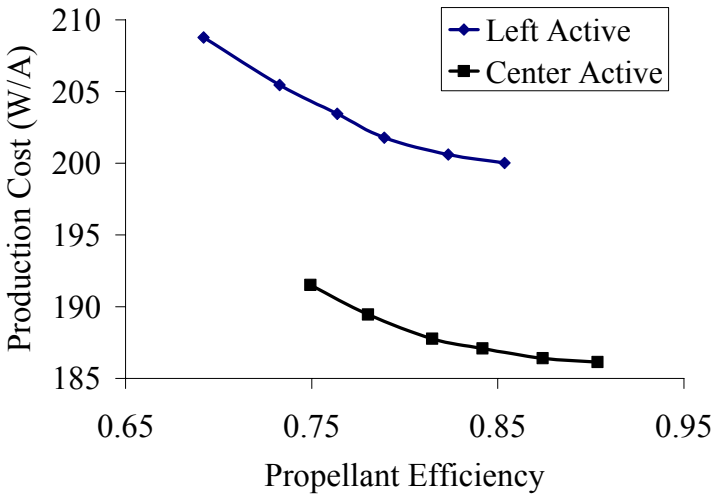

Figure 5-24: TA performance curves for the +5 A electromagnet, left and center active DCA configurations. DCU propellant flow and electrical connectivity do not affect these results.

5.4.5.1 Left DCA Active

Steady operation of the TA is validated for the +5 A electromagnet configuration. The discharge voltage is on the order of 27 V and the grid-plane ion current is on the order of 5 A for all investigated settings. The performance curve for the +5 A electromagnet configuration with the DCUs electrically isolated and no flow is shown in Figure 5-24. Performance curves with the DCUs electrically connected and with a propellant flow rate show no appreciable difference in magnitude or trend.

During performance mapping, as the discharge current is reduced from 30 A to 25 A, discharge voltage decreases by approximately 2.5 V, grid-plane current decreases from 5.1 A to 3.7 A, flatness decreases from 0.47 to 0.42, and the backplate current ratio decreases from 21 to 15. Center DCU cathode potentials are on the order of -3.8 V while right DCU cathode potentials are on the order of -8.0 V. Center DCU keeper potentials are 12.0 V while right DCU keeper potentials are 13.0 V. Each of these values varies approximately ±1 V during performance mapping.

Discharge current is fixed at 30 A and the total propellant flow rate is kept constant as the DCU flow rate is increased and set at three different values; zero, half the DCA flow rate, and the full DCA flow rate. As the flow rate increases a purple spot becomes visible downstream of each DCU. During this procedure discharge voltage decreases only 1 V and grid-plane ion current decreases 0.01 A as the DCU flow rate increases to the full DCA flow rate. Propellant efficiency and ion production costs remain approximately constant at 0.85 and 199 W/A, respectively. Flatness increases and backplate current ratio decreases significantly with increasing DCU flow rate. Flatness changes from 0.47 to 0.55 and backplate current ratio changes from 21 to 4.5. DCU

floating voltages increase, cathode current does not display a significant trend, and keeper current decreases with increasing flow rate. These trends are illustrated in Figure 5-25 and Figure 5-26.

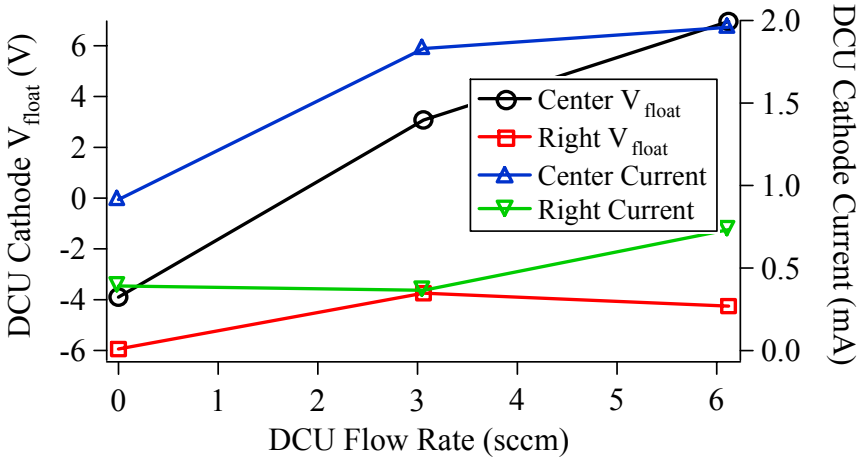

Figure 5-25: DCU cathode floating voltage and collected current as a function of DCU flow rate for the +5 A electromagnet, left active DCA configurations.

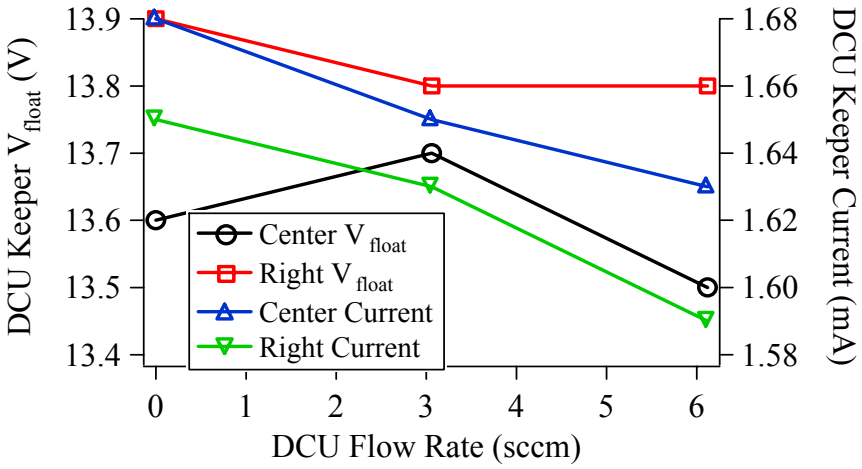

Figure 5-26: DCU keeper floating voltage and collected current as a function of DCU flow rate for the +5 A electromagnet, left active DCA configurations.

Results from the Langmuir probe show grid-plane floating potential, plasma potential, electron temperature, and ion number density are on the order of 8.0 V, 27 V, 3.4 eV, and 6.6×10^{10} cm^{-3}, respectively. Note that voltages are referenced with respect to

cathode common. Peak-to-peak discharge voltage oscillations are on the order of 2.5 V for all investigated settings. DCU electrical connectivity and flow rate do not significantly affect these results.

5.4.5.2 Center DCA Active

Steady operation of the TA is validated for the +5 A electromagnet configuration with the center DCA active. Performance for the +5 A electromagnet configuration with the center DCA active is shown in Figure 5-24. Production costs are less for the center active DCA than for the left active DCA. Discharge voltage remains at 27 V and grid-plane ion current increases to 5.5 A, but trends associated with performance mapping remain the same as the left active DCA configuration. Flatness decreases from 0.47 to 0.42 and backplate current ratio decreases from 24 to 18 during performance mapping. Performance curves with the DCUs electrically connected and with a propellant flow rate show no appreciable difference in magnitude or trend.

As the DCU flow rate is increased, discharge current and total propellant flow rate are kept constant. As the flow rate increases a purple spot becomes visible downstream of each DCU. Discharge voltage decreases 0.7 V and grid-plane ion current decreases 0.08 A, while propellant utilization efficiency and ion production costs remain constant at 0.90 and 185 W/A as the DCU flow increases. Flatness increases and backplate current ratio decreases significantly with increasing DCU flow rate. Flatness changes from 0.47 to 0.50 and backplate current ratio changes from 24 to 13. DCU floating voltages and cathode current do not display a significant trend, and keeper current decreases with increasing flow rate. These trends are illustrated in Figure 5-27 and Figure 5-28.

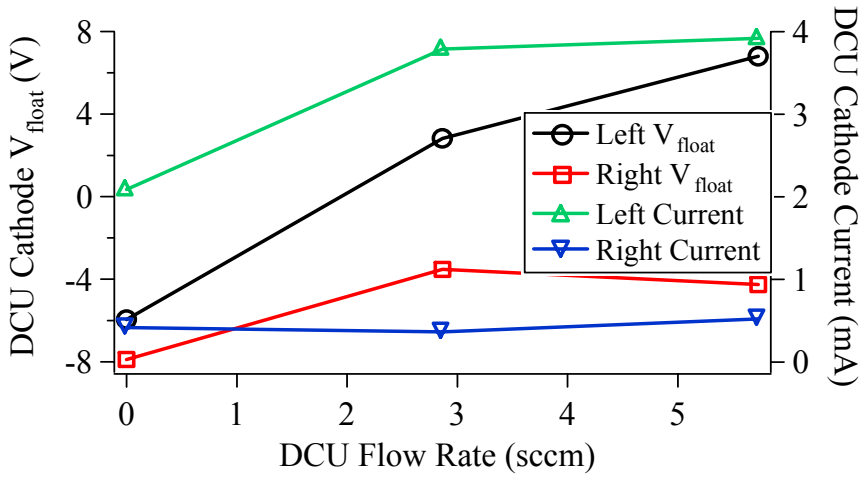

Figure 5-27: DCU cathode floating voltage and collected current as a function of DCU flow rate for the +5 A electromagnet, center active DCA configurations.

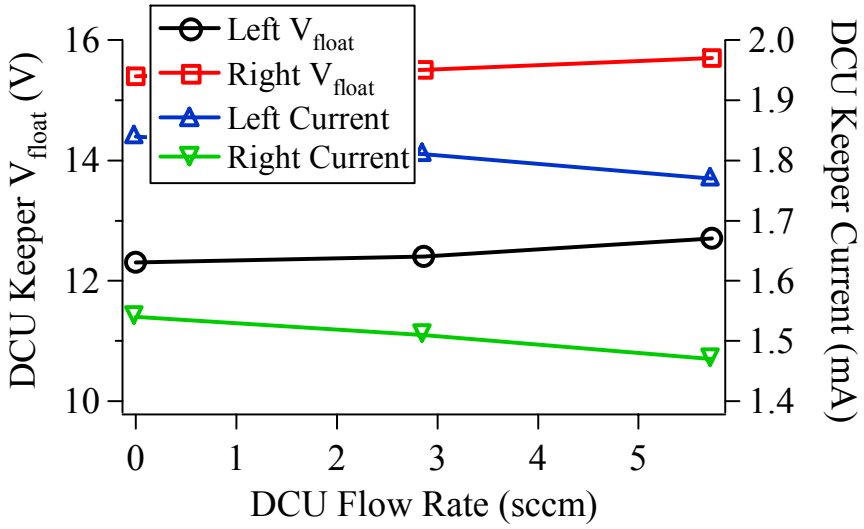

Figure 5-28: DCU keeper floating voltage and collected current as a function of DCU flow rate for the +5 A electromagnet, center active DCA configurations.

Results from the Langmuir probe show grid-plane floating potential, plasma potential, electron temperature, and ion number density are on the order of 8.0 V, 27 V, 3.5 eV, and 8.3×10^{10} cm^{-3}, respectively. Note that voltages are referenced with respect to cathode common. Peak-to-peak discharge voltage oscillations are on the order of 2.4 V

for all investigated settings. DCU electrical connectivity and flow rate do not significantly affect these results.

5.4.6 Electromagnet +10 A Configurations

A topological profile of the +10 A electromagnet configuration is shown in Figure 5-29.

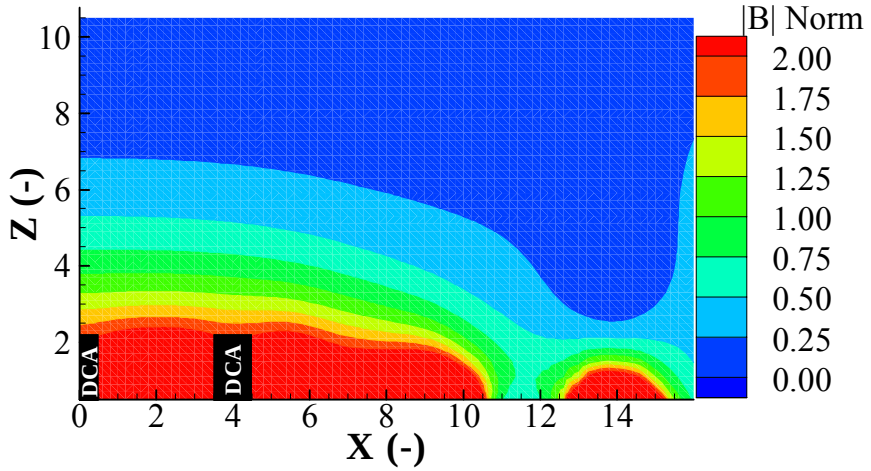

Figure 5-29: TA +10 A electromagnet configuration magnetic field topology.

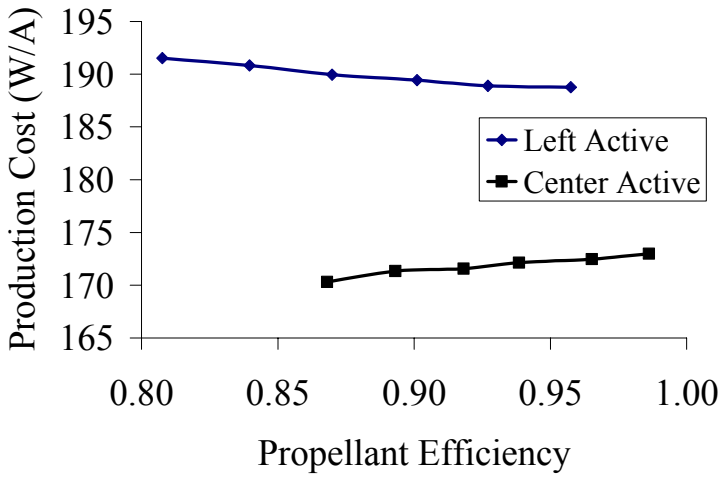

Figure 5-30: TA performance curves for the +10 A electromagnet, left and center active DCA configurations. DCU propellant flow and electrical connectivity do not affect these results.

5.4.6.1 Left DCA Active

Steady operation of the TA is validated for the +10 A electromagnet configuration. The discharge voltage is on the order of 30 V and the grid-plane ion current is on the order of 6 A for all investigated settings. The performance curve for the +10 A electromagnet configuration with the DCUs electrically isolated and no flow is shown in Figure 5-30. Performance curves with the DCUs electrically connected and with a propellant flow rate show no appreciable difference in magnitude or trend.

During performance mapping, as the discharge current is reduced from 30 A to 25 A, discharge voltage decreases by approximately 2.0 V, grid-plane current decreases from 6.0 A to 4.6 A, flatness decreases from 0.28 to 0.25, and the backplate current ratio increases from 8 to 12. Center DCU cathode potentials are on the order of -3.8 V while right DCU cathode potentials are on the order of -8.3 V. Center DCU keeper potentials are 15.0 V while right DCU keeper potentials are 19.0 V. Each of these values varies approximately ±1 V during performance mapping.

Discharge current is fixed at 30 A and the total propellant flow rate is kept constant as the DCU flow rate is increased and set at three different values; zero, half the DCA flow rate, and the full DCA flow rate. As the flow rate increases a purple spot becomes visible downstream of each DCU. During this procedure discharge voltage decreases only 0.5 V and grid-plane ion current decreases 0.06 A as the DCU flow rate increases to the full DCA flow rate. Propellant efficiency and ion production costs remain approximately constant at 0.96 and 188 W/A, respectively. Flatness increases and backplate current ratio does not display a consistent trend with increasing DCU flow rate. Flatness changes from 0.28 to 0.30. DCU floating voltages increase, cathode current does

not display a significant trend, and keeper current decreases with increasing flow rate. These trends are illustrated in Figure 5-31 and Figure 5-32.

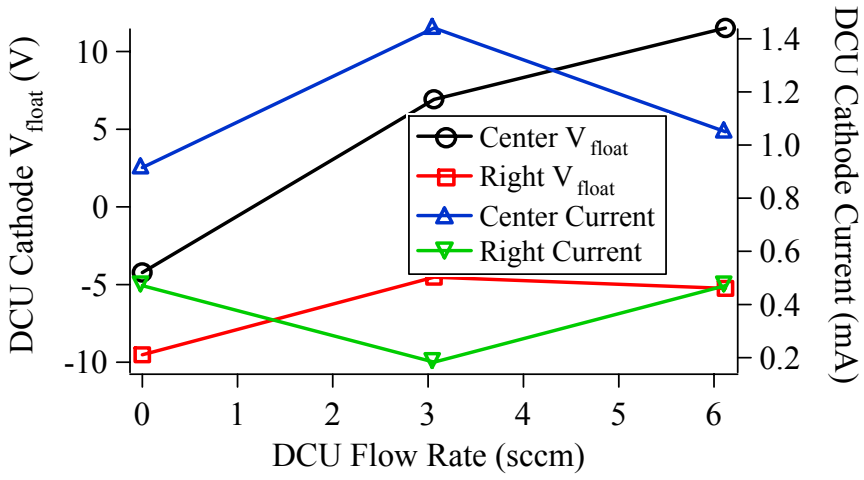

Figure 5-31: DCU cathode floating voltage and collected current as a function of DCU flow rate for the +10 A electromagnet, left active DCA configurations.

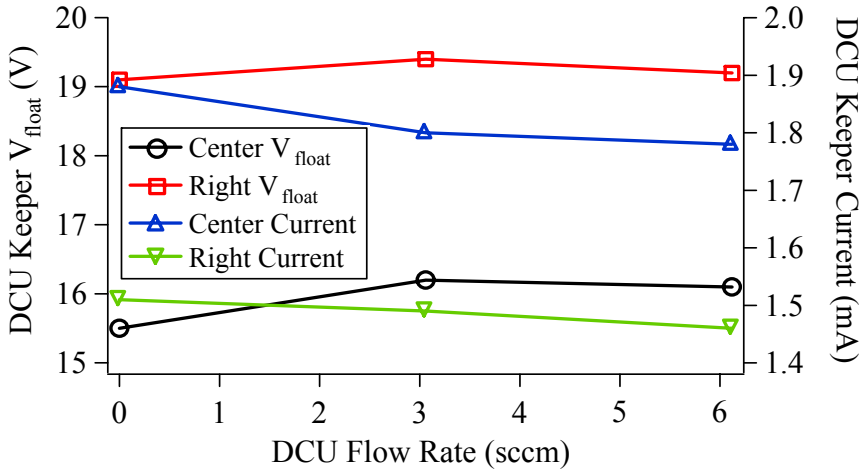

Figure 5-32: DCU keeper floating voltage and collected current as a function of DCU flow rate for the +5 A electromagnet, left active DCA configurations.

Results from the Langmuir probe show grid-plane floating potential, plasma potential, electron temperature, and ion number density are on the order of 9.0 V, 30 V, 4.1 eV, and 7.0×10^{10} cm^{-3}, respectively. Note that voltages are referenced with respect to cathode common. Peak-to-peak discharge voltage oscillations are on the order of 2.0 V

for all investigated settings. DCU electrical connectivity and flow rate do not significantly affect these results.

5.4.6.2 Center DCA Active

Steady operation of the TA is validated for the +10 A electromagnet configuration with the center DCA active. Performance for the +10 A electromagnet configuration with the center DCA active is shown in Figure 5-30. Production costs are less for the center active DCA than for the left active DCA. Discharge voltage remains at 30 V and grid-plane ion current increases to 6.24 A, but trends associated with performance mapping remain the same as the left active DCA configuration. Flatness decreases from 0.25 to 0.24 and backplate current ratio increases from 14 to 19 during performance mapping. Performance curves with the DCUs electrically connected and with a propellant flow rate show no appreciable difference in magnitude or trend.

As the DCU flow rate is increased, discharge current and total propellant flow rate are kept constant. As the flow rate increases a purple spot becomes visible downstream of each DCU. Discharge voltage and grid-plane ion current remain approximately constant. Propellant utilization efficiency and ion production costs remain constant at 0.99 and 171 W/A as the DCU flow increases. Flatness increases and backplate current ratio decreases with increasing DCU flow rate, however, the changes are not as significant for the 0 A and +5 A configurations. Flatness changes from 0.25 to 0.26 and backplate current ratio changes from 14 to 12. DCU floating voltages increase, cathode current does not display a significant trend, and keeper current decreases with increasing flow rate. These trends are illustrated in Figure 5-33 and Figure 5-34.

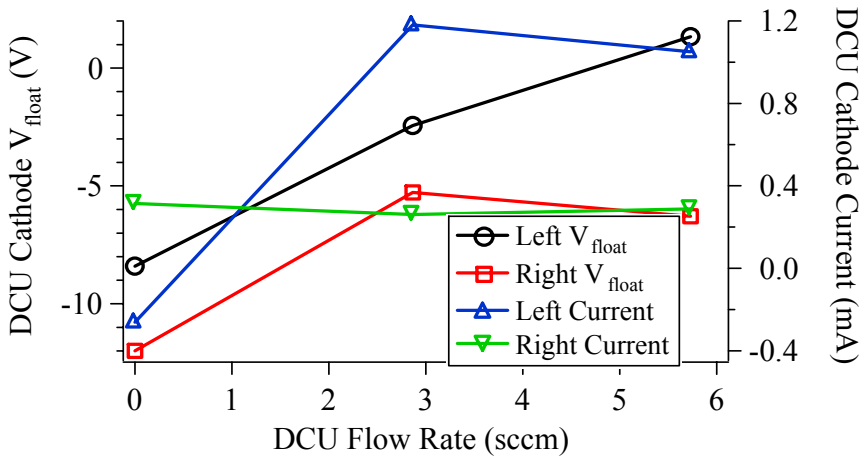

Figure 5-33: DCU cathode floating voltage and collected current as a function of DCU flow rate for the +5 A electromagnet, center active DCA configurations.

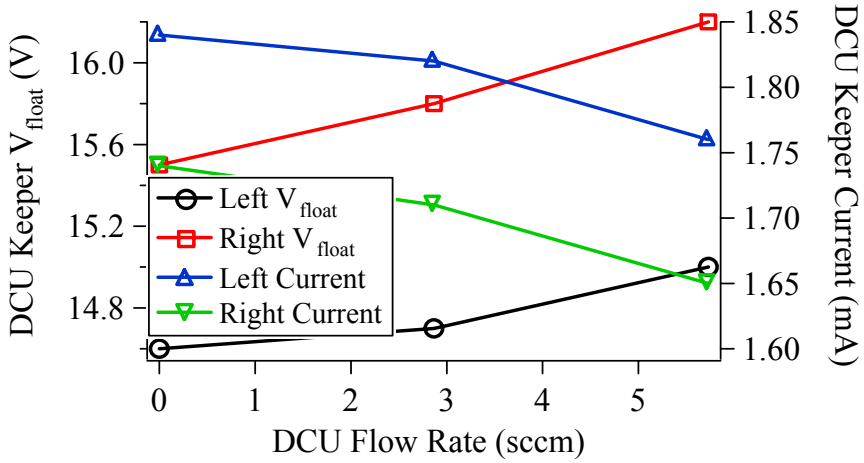

Figure 5-34: DCU keeper floating voltage and collected current as a function of DCU flow rate for the +5 A electromagnet, center active DCA configurations.

Results from the Langmuir probe show grid-plane floating potential, plasma potential, electron temperature, and ion number density are on the order of 4.3 V, 27 V, 4.3 eV, and 1.2×10^{11} cm^{-3}, respectively. Note that voltages are referenced with respect to cathode common. Peak-to-peak discharge voltage oscillations are on the order of 3.5 V for all investigated settings. DCU electrical connectivity and flow rate do not significantly affect these results

5.4.7 Asymmetric Configuration

For the asymmetric configuration the backplate electromagnet is operated at 0 A and a magnetic iron c-channel is attached on the near-DCA anode wall. In this case, the left DCA is active so a magnetic iron c-channel is placed on the left anode wall. The other magnetic iron c-channels are not utilized. This configuration increases the magnetic field on the near-DCA side of the TA.

Steady operation of the TA is validated for the asymmetric configuration. The discharge voltage is on the order of 27 V and the grid-plane ion current is on the order of 5 A for all investigated settings. The performance curve for the asymmetric configuration with the DCUs electrically isolated and no flow is shown in Figure 5-35. Performance curves with the DCUs electrically connected and with a propellant flow rate show no appreciable difference in magnitude or trend.

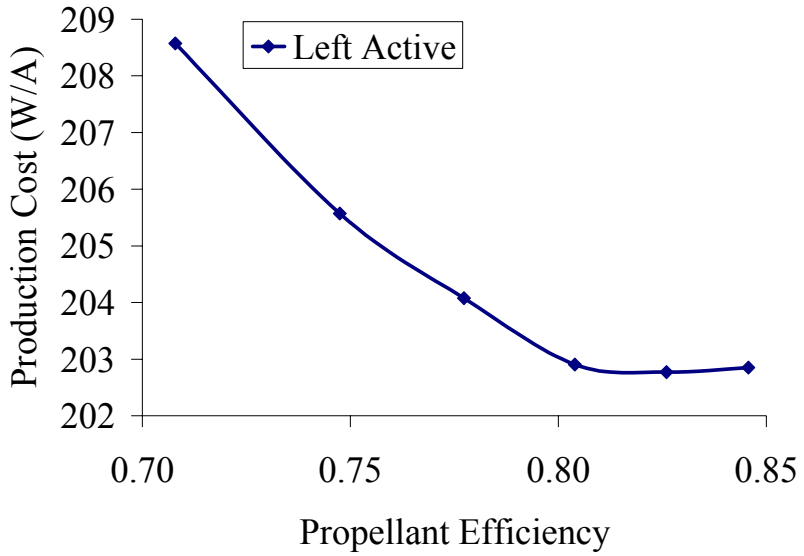

Figure 5-35: TA performance curves for the asymmetric configuration. DCU propellant flow and electrical connectivity do not affect these results.

During performance mapping, as the discharge current is reduced from 30 A to 25 A, discharge voltage decreases by approximately 1.5 V, grid plane current decreases from 5.0 A to 3.9 A, flatness remains constant at 0.46, and the backplate current ratio decreases from 21 to 16. Center DCU cathode potentials are on the order of -3.0 V while right DCU cathode potentials are on the order of -10.0 V. Center DCU keeper potentials are 8.6 V while right DCU keeper potentials are 8.9 V. Each of these values varies approximately ±0.3 V during performance mapping.

Discharge current is fixed at 30 A and the total propellant flow rate is kept constant as the DCU flow rate is increased and set at three different values; zero, half the DCA flow rate, and the full DCA flow rate. As the flow rate increases a purple spot becomes visible downstream of each DCU. During this procedure discharge voltage decreases only 0.4 V and grid-plane ion current remains constant as the DCU flow rate increases to the full DCA flow rate. Propellant efficiency and ion production costs remain approximately constant at 0.85 and 202 W/A, respectively. Flatness increases and backplate current ratio decreases with increasing DCU flow rate. Flatness changes from 0.46 to 0.47. DCU floating voltages increase, cathode current increases slightly, and keeper current decreases with increasing flow rate. These trends are illustrated in Figure 5-36 and Figure 5-37.

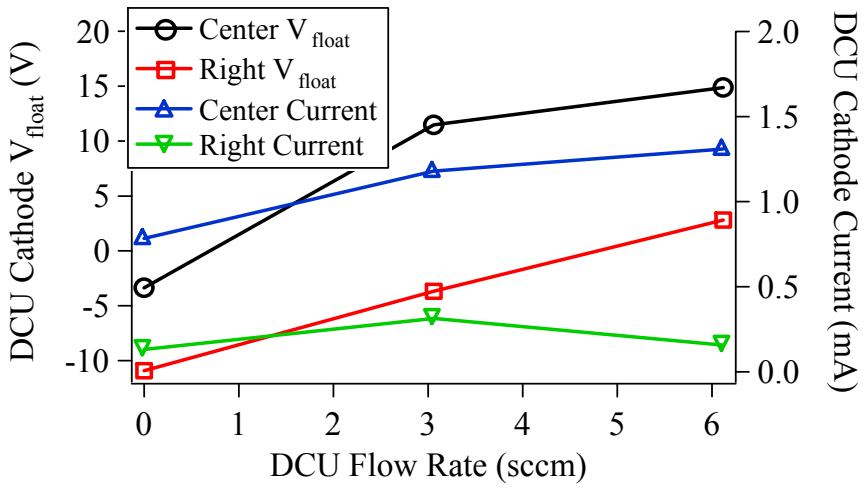

Figure 5-36: DCU cathode floating voltage and collected current as a function of DCU flow rate for the asymmetric configuration.

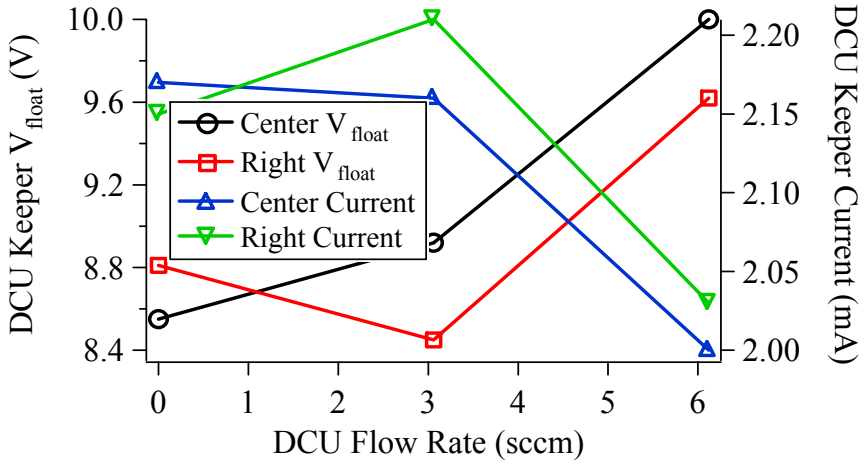

Figure 5-37: DCU keeper floating voltage and collected current as a function of DCU flow rate for asymmetric configuration.

Results from the Langmuir probe show grid-plane floating potential, plasma potential, electron temperature, and ion number density are on the order of 8.6 V, 27 V, 3.4 eV, and 6.5×10^{10} cm^{-3}, respectively. Note that voltages are referenced with respect to cathode common. Peak-to-peak discharge voltage oscillations are on the order of 3.0 V for all investigated settings. DCU electrical connectivity and flow rate do not significantly affect these results.

The asymmetric configuration is investigated primarily to determine if increasing the magnetic field on the near-DCA side of the TA affects the grid-plane current peak location and flatness. By comparing the current recorded by the centerline button probe during left DCA operation for the asymmetric and 0 A electromagnet configuration the effect can be determined. If the peak location has shifted toward the center of the TA for the asymmetric case, an increase in centerline current should be noticed. However, no significant change in centerline button probe current is found, therefore the peak is assumed to remain directly downstream of the active left DCA in spite of the increased magnetic field.

5.5 Analysis

A stable discharge is successfully obtained for all magnetic field configurations investigated. Magnetic field configuration has a profound impact on TA operation. General results for all configurations as well as comparison of the TA with previous and current ion thruster discharge chambers is discussed in the following sections. Finally, the optimized TA magnetic field is determined based on the results and analysis presented.

5.5.1 Performance

Performance curves obtained for the TA do not appear similar to those obtained on other ion thruster discharge chambers. Most performance curves do not display the increase in ion production cost as propellant utilization decreases.[39,57,92] This difference may be explained by the fact that the TA is a rectangular discharge chamber utilizing an entirely rectangular ring-cusp magnetic field, while most previous ion thrusters are cylindrical using a circular ring-cusp magnetic field. Performance curves generated for

the GRC HiPEP ion thruster (rectangular discharge chamber) do display an increase in ion production cost as propellant utilization decreases, however, they also show ion production cost increasing as propellant utilization increases, a trend not seen for the TA. One explanation for this result is that discharge currents larger than 30 A are not investigated because the DCA is limited to 30 A. Decreasing the discharge current below 25 A may also show a change in the performance curve trends.

Magnetic field configuration has a significant effect on discharge chamber performance. As the backplate magnetic field is increased with the electromagnet, the grid-plane ion current increases. This trend has also been documented by Sovey for a 30 cm ring-cusp discharge chamber.[39] By increasing the upstream permanent magnet strength from 0.24 T to 0.32 T, Sovey found that the grid-plane ion current increased 16%. An increase in grid-plane ion current leads to a decrease in ion production costs because more ions are available to be extracted from the discharge chamber into the ion beam. The +10 A electromagnet configuration provided the lowest production costs with the highest propellant utilizations, followed by the +5 A and 0 A configurations, respectively. Although the 50 G enclosed configuration increases the magnetic field along the anode walls of the TA, this does not decrease production costs. Based on this result, the enclosure of the 50 G line may not be an important design criterion for rectangular ring-cusp discharge chambers.

Figure 5-38 shows ion production cost and propellant utilization efficiency as a function of magnetic field configuration for a 30 A discharge with the center DCA active and no flow through the DCUs. Propellant efficiency increases with backplate magnetic field strength, while ion production costs decrease. Compared with contemporary

discharge chambers, ion production costs for magnetic field configurations number 1 and 2 (50 G enclosed and electromagnet at -10 A, respectively) are slightly large, but the other magnetic field configurations obtain values that are reasonable. Performance numbers for other ion thruster discharge chambers can be found in Table 5-2.

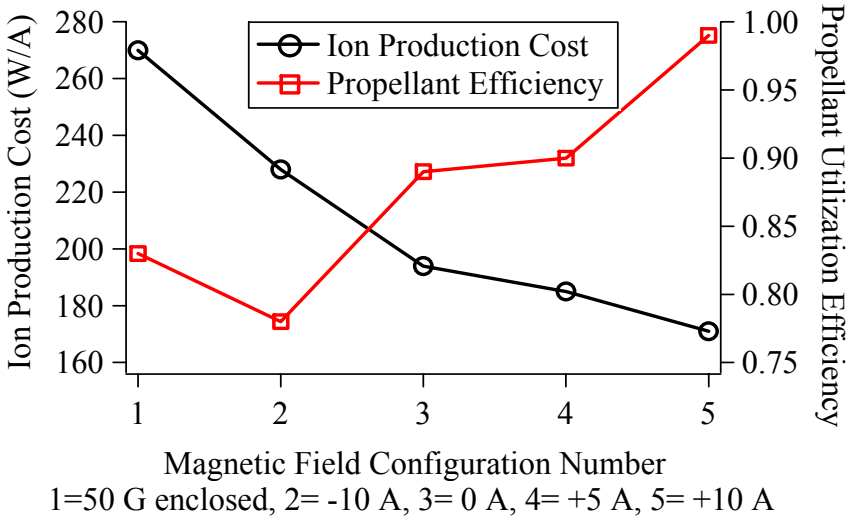

Figure 5-38: Ion production cost and propellant utilization efficiency as a function of magnetic field configuration.

5.5.2 Uniformity and Flatness

Grid-plane uniformity (or beam flatness) is an important criterion because a relatively flat ion beam (flatness = 1) reduces centerline ion optics grid erosion, increasing the operational lifetime of both the optics and the thruster.[62,81-87] Magnetic field configuration has a significant impact on the uniformity of the grid-plane ion current. As the backplate TA magnetic field increases, the measured flatness increases and then subsequently decreases, reaching a value of 0.55 for the 0 A electromagnet configuration with the center DCA active. This trend is illustrated in Figure 5-39. Sovey's investigation found that increasing the upstream permanent magnet strength reduced the flatness.[39] This trend is explained by the TA results, which show that

increasing the upstream magnetic field too much can cause the flatness to decrease. Overall, these results suggest that when designing the magnetic field of a rectangular discharge chamber there is a trade-off between ion production cost, propellant utilization efficiency, and flatness.

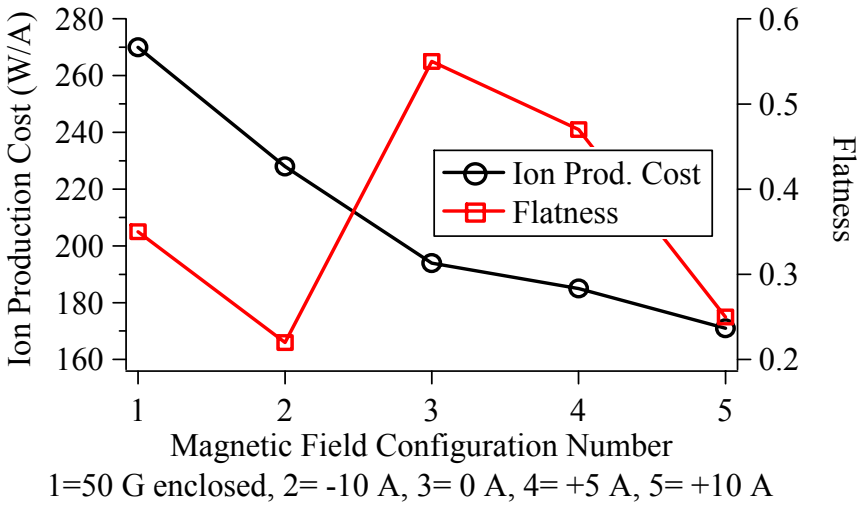

Figure 5-39: Ion production cost and flatness as a function of magnetic field configuration. Both are for a 30 A discharge with the center DCA active and no DCU flow.

Thruster	Geometry	Propellant Efficiency	Ion Production Cost (W/A) or (eV/ion)	Flatness	Real or Simulated Beam Current (A)
NSTAR[69,87]	Cylindrical	0.89	173	0.47	1.76
NEXT[137,138]	Cylindrical	0.89	135	0.66	3.52
NEXT[137,138]	Cylindrical	0.90	205	0.57	1.20
NEXIS[57]	Cylindrical	0.90	160	0.85	3.90
HiPEP[32,55]	Rectangular	0.90	188		3.52
MCDC TA	Rectangular	0.89	194	0.55	3.78

Table 5-2: Comparison of contemporary ion thruster discharge chambers with the MCDC TA operated with the 0 A electromagnet configuration.

Compared with contemporary discharge chambers, flatness for all magnetic field configurations except number 3 and 4 (electromagnet at 0 A and electromagnet at +5 A

respectively) are low since the NSTAR thruster flatness parameter is 0.47. A comparison of the operational characteristics of the TA at the 0 A electromagnet configuration with other contemporary ion thruster discharge chambers is shown in Table 5-2.

5.5.3 DCU Connectivity and Flow Rate

The DCUs are operated either electrically connected or isolated from the electrical circuit while their flow rate is adjusted from zero to half the DCA flow and then to the full DCA flow. Total flow rate is kept constant during this procedure and discharge voltage is found to vary a maximum of 1 V as DCU flow increases. Very little performance change is seen with DCU flow rate and electrical connectivity adjustment. Flatness improves as DCU flow rate increases for all configurations except the 50 G enclosed configuration. Most improvements are only on the order of 2-3%, with a maximum 10% increase for the 0 A configuration with the left DCA operational.

When the DCUs are isolated from the TA electrical circuit, an increase in DCU flow rate causes the floating voltages of both the cathode and keeper to increase. When electrically connected to the TA, the DCU cathode and keepers collect current. DCU keeper currents are similar to the active DCA keeper current, while DCU cathode currents are orders of magnitude less than the DCA cathode current. This trend is to be expected since the active DCA cathode is emitting the bulk of the discharge current through electron and ion production while the DCUs are simply collecting a current. As DCU flow rate increases, DCU keeper current decreases and cathode current does not display a common trend. A decrease in keeper current with increasing DCU flow rate signifies a decrease in plasma bombardment of the keeper. This result suggests the DCUs

are shielded from erosion-causing bombarding ions. The trends observed with the DCUs are summarized in Table 5-3.

As DCU propellant flow rate increases:		
	Collected Current	Floating Voltage
DCU Cathode	No Clear Trend	Increases
DCU Keeper	Decreases	Increases

Table 5-3: Effect of propellant flow rate on DCU cathode and keeper electrodes.

5.5.4 Backplate Electron Current Deposition

The magnetic circuit of the MCDC utilizes rectangular magnet rings, so the electron deposition to the intercusp region corners is characterized. Two button probes are mounted to the backplate of the anode on the left side of the left DCA and biased to collect electron current. Both probes are located midway between the magnetic cusps; i.e. in the middle of the intercusp region. One probe is placed between the corners of the rectangular cusps, while the other is placed at the vertical midpoint between the corners. This allows the intercusp corner electron deposition to be compared with that obtained at the mid-plane. The results presented here utilize the ratio of the currents (corner probe current divided by mid-plane probe current).

Figure 5-40 shows typical trends associated with the backplate current ratio. Corner probe current is always larger than mid-plane probe current. This result suggests that more of the discharge current is deposited into the corners of the TA than in the middle. On average the backplate current ratio is approximately 10, however, it obtains a maximum of 24 and reaches a minimum of 4. DCU connectivity does not affect backplate current ratio; however, DCU flow rate does. For the +5 A electromagnet configuration backplate current ratio decreases from approximately 21 to 4.5 as the DCU flow rate is increased to its maximum value. This same trend is noticeable for the 0 A

configuration as well. Figure 5-40 shows backplate current ratio decreases with increasing DCU flow rate when the left DCA is operational. These results suggest that the internal TA plasma may become more uniform as the DCU flow rate increases.

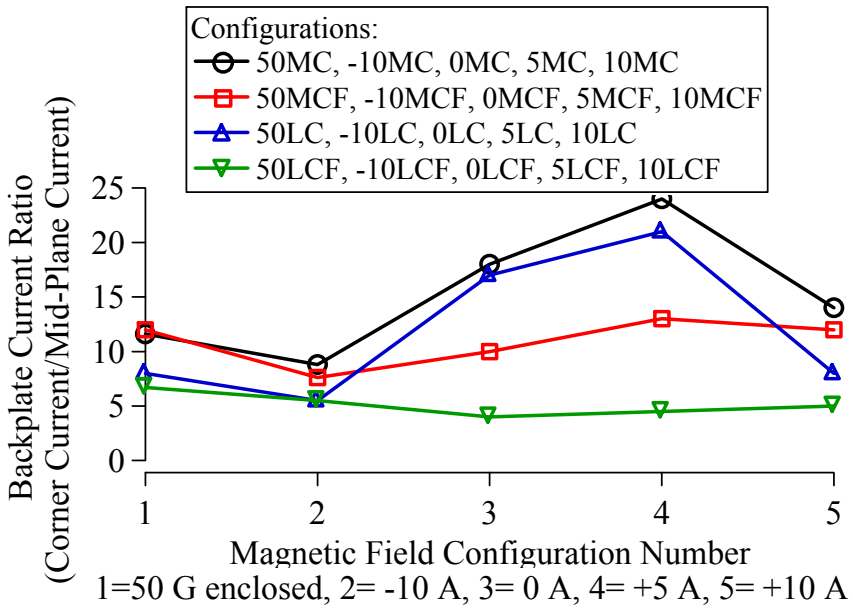

Figure 5-40: Backplate current ratio as a function of magnetic field configuration for both center and left DCA operation with no DCU flow and full DCU flow

5.5.5 Grid-plane Plasma Properties

Figure 5-41 shows the average grid-plane plasma properties as a function of magnetic field configuration. Electron temperature is largest for the 50 G enclosed and +10 A electromagnet configurations. The minimum electron temperature is obtained by the +5 A configuration, which yields a value of 3.5 eV.

Ion number density is lowest for the 0 A configuration and increases with increasing electromagnet current. This is expected because, as described above, an increase in the backplate magnetic field causes the grid-plane current to increase. The number density for the -10 A configuration is not presented because anomalous values for floating potential and plasma potential are obtained, making the calculations

unreliable. Typical values for plasma potential and floating potential at the grid-plane are 27 V and 5 V, respectively.

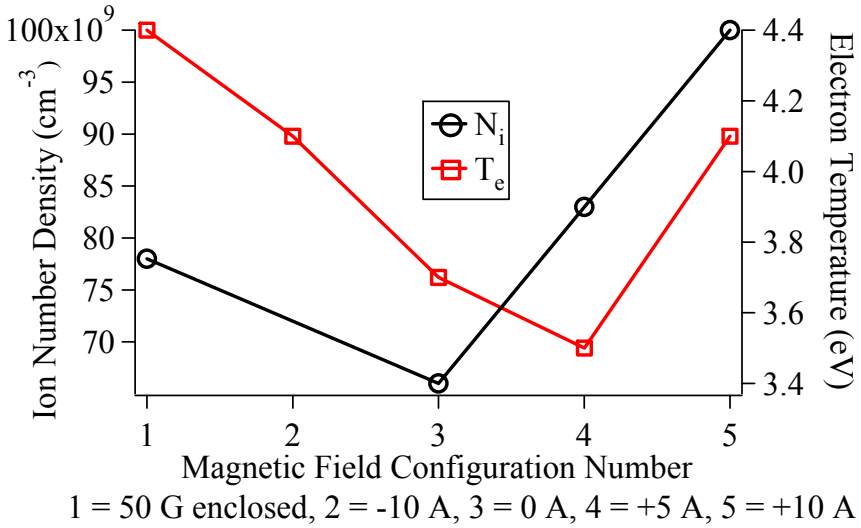

Figure 5-41: Grid-plane ion number density and electron temperature as a function of magnetic field configuration.

5.5.6 Erosion Issues

Each of the two DCUs is constructed of a copper cathode tube with a chamfered orifice and a copper keeper tube with an orifice. Pre- and post-test photographs of the DCUs are shown in Figure 5-42. MCDC TA operation totaled approximately 50 hours. A post-test visual inspection of the DCUs shows changes in the cathode orifice. DCU keeper orifices do not show any changes or wear. The cathode orifice is no longer smooth and circular, but appears to have jagged edges around the inner diameter of the orifice. Changes associated with the left and center DCU (this DCU is on the left during center DCA operation and in the center during left DCA operation) are more pronounced than those for the right DCU.

a.)

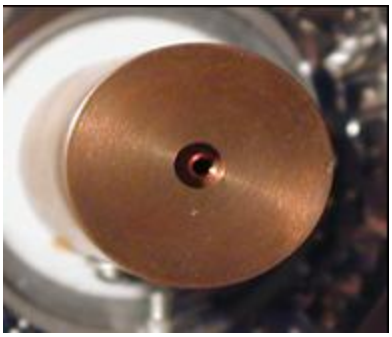

b.)

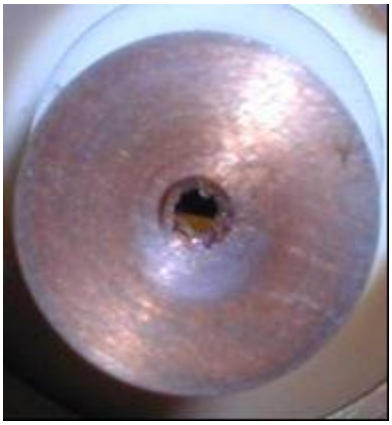

c.)

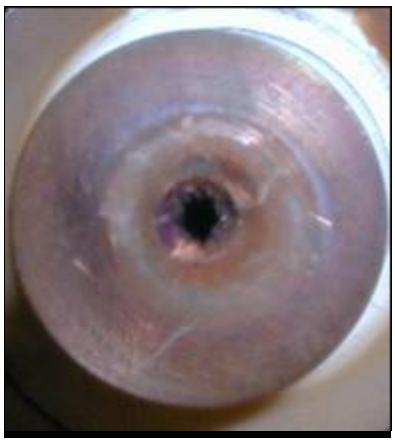

Figure 5-42: a.) Pre-test photograph of copper DCU. b.) Post-test photograph of right DCU cathode orifice. c.) Post-test photograph of left and center DCU cathode orifice.

Visually the DCUs appear to have material deposition in the cathode orifice, a result that is similar to the neutralizer cathode deposition that occurred during the extended life test at JPL.[7,8] Pre- and post-test measurements of the DCU cathode orifice

diameter reveal a decrease of approximately 10%. The deposition to the DCU cathodes may be caused by back-sputtered ion collection grid material. Specifically, back-sputtering of grid material may have occurred during initial TA operation because the DCA flow rate was mistakenly set at an increased level. The increased flow rate effectively created a collimated plasma jet that bombarded the collection grid and may have caused back-sputtering of grid material. However, no noticeable change is noticed on the upstream surface of the collection grid. It is also important to note that subsequent TA experiments with the correct flow rate have not shown back-sputtering material deposition on the DCUs or other TA components. It is unclear if these results can be attributed to DCU propellant flow or DCU electrical connectivity.

The TA operation results suggest it may be possible to reduce dormant cathode keeper erosion. Propellant flow reduces the collected keeper current, which suggests fewer ions are bombarding the keeper. Furthermore, propellant flow causes the keeper floating potential to increase and Kolasinski has shown that higher keeper potentials reduce keeper erosion.[139] Ions bombarding the keeper are typically falling from the plasma potential to the keeper potential. For plasma potentials of 27 V this yields energies within the range of 17 - 23 V.

The decrease in keeper current during propellant flow may be explained by charge-exchange (CEX) collisions. In a CEX collision a “fast” ion interacts with a “slow” neutral, the product of which is a “fast” neutral and a “slow” ion. External propellant flow is known to cause CEX collisions and affect energy distributions near hollow cathodes.[140] Flow through the DCUs may cause bombarding ions to suffer CEX collisions, the result of which could be two possible scenarios. In the first scenario, a

"fast" neutral moving toward the DCU and a "slow" ion moving away from the DCU could be created. In the second scenario, a "slow" CEX ion is created at a potential lower than the plasma potential such that its bombarding energy is significantly less than an ion falling through the full plasma-to-keeper potential. A more detailed analysis of the effects of propellant flow on dormant cathode plasma properties and the ability of CEX collisions to affect such change can be found in Chapter 6.

5.5.7 Optimized TA Magnetic Field Configuration

Overall, the 0 A configuration performed the best. Flatness and performance are both considered to determine the optimum configuration. The 0 A configuration has a relatively high flatness, 0.55 and 0.53, and relatively low discharge losses, 194 W/A at 89% propellant utilization and 199 W/A at 87% propellant efficiency, for both center and left DCA operation, respectively. Other configurations have lower losses, but also have a decrease in flatness. For the 0 A configuration the electromagnet is operated at 0 A. The 50 G line is not enclosed within the TA. Enclosure of the 50 G line is not a requirement for rectangular ring-cusp discharge chambers.

5.6 Performance, Stability, and Uniformity Conclusions

Experimental testing of the TA is conducted in the LVTF at operating background pressures on the order of 4×10^{-6} Torr and the TA is operated as a simulated ion thruster.[92] A DCA is used and two DCUs are also mounted in the TA. Magnetic field configuration, DCU electrical connectivity, and DCU flow rate are adjusted while monitoring performance, uniformity, DCU floating voltages, DCU currents, and backplate electron current ratio.

Both centerline (center) and off-centerline (left) DCA operation within the TA is obtained. Simulated performance curves and calculated flatness parameters show the optimal TA configuration performs within the same operational regimes as contemporary ion thruster discharge chambers. DCU connectivity does not affect TA performance. As DCU flow rate increases, the main plenum flow is reduced such that the total flow rate remains constant. An increase in DCU flow rate does not affect TA performance or flatness. As DCU flow rate increases, DCU floating voltages increase and DCU keeper currents decrease. This result suggests that propellant flow may shield the keeper and reduce keeper erosion.

The TA is a rectangular discharge chamber and the ratio of corner to mid-plane anode electron deposition is monitored. Calculated backplate current ratios are on average 10, suggesting that considerably more discharge current is deposited in the corners of the rectangular TA than at the mid-plane. This ratio decreases with DCU flow rate. Post-test inspections of the DCUs show material deposition in the cathode orifice. This result is most likely due to back-sputtered ion collection grid material caused by a DCA flow rate error. The optimum magnetic field configuration is determined to be the 0 A electromagnet configuration. This configuration does not enclose the 50 G line. Other configurations have lower losses; however, the 0 A configuration balances both performance and flatness.

Any dormant cathode erosion phenomenon in an MCDC may be mitigated by operating those units with propellant flow. Propellant flow reduces the collected keeper current, which suggests fewer bombarding ions are present. Furthermore, propellant flow also increases the keeper floating potential. Kolasinski has shown that increased keeper

potentials reduce erosion.[139] Further investigation into the effect an operating cathode has on the two dormant units is described in Chapter 6.

CHAPTER 6:
DORMANT CATHODE PLASMA PROPERTIES

One of the primary concerns associated with a multiple-cathode discharge chamber (MCDC) is the effect of an operating cathode on the dormant units. Results with the SPT-100 indicate that an operational cathode can cause significant erosion (destruction) of the dormant cathode.[77,78] In order to investigate the possibility of this phenomenon in a MCDC, diagnostic cylinders (DCs) are designed and fabricated to appear similar in size and shape to the active discharge cathode assembly (DCA), but are outfitted with plasma diagnostics. DCs are placed at the dormant cathode locations during MCDC test article (TA) operation to investigate the plasma properties at those locations. The following sections describe the experimental setup and results obtained with the DCs.

6.1 Experimental Setup

The DCs described in Chapter 3 are utilized to determine the plasma properties at the dormant cathode locations while the TA is operated as a simulated ion thruster without high-voltage beam extraction.[92] TA operation is accomplished with the 5PLP-DCs, 7PLP-DCs, APLP-DCs, ACLP-DCs, RPA-DCs, and 5PLPF-DCs attached. Only two DCs are utilized at any given time and data are acquired for electromagnet currents of 0 A, +5 A, and +10 A, as well as with the DCs electrically connected and electrically isolated from the TA. During electrically connected operation the “keeper” is connected

to the anode through a 10 kΩ resistor and the "cathode" electrode (where applicable) is connected to cathode common. The Langmuir probes associated with the DCs are connected to a Keithley 2410 sourcemeter or a voltage-controlled Sorenson DLM 60-10 power supply through 10 kΩ resistors. The voltage drop across each resistor is measured utilizing the data logger. The ion-retarding grid of the RPA-DC is operated with the Keithley 2410 sourcemeter and the collector current is monitored with a Keithley 486 picoammeter. All data are acquired through a LabView interface.

6.2 Results and Analysis

6.2.1 5PLP-DC

The following section describes the results obtained utilizing the 5PLP-DCs for left, middle, and right DCA TA operation. Results are shown from the perspective of a viewer looking downstream from behind the TA, following the coordinate system in Figure 2-17 and Figure 2-18. In the following figures, three different TA configurations are shown and for each configuration the three circles represent the three cathodes, one active cathode (DCA) and two DCs. Each colored dot inside the circles represents one of the planar Langmuir probes. The configuration nomenclature for each figure is described in APPENDIX B. All voltages are referenced with respect to cathode common. Figures of special interest are shown below and all data are shown in APPENDIX C.

Typical measured floating voltages are between 2-14 V above cathode potential with floating voltage increasing with electromagnet current. For the nominal operating condition of 0 A electromagnet current, floating voltages are on average 5 V above cathode potential. Connecting or disconnecting the 5PLP-DCs has no noticeable effect on

floating voltage. No noticeable trend between DCA activity and measured floating potential is determined. Typical results for floating voltage are shown in Figure 6-1.

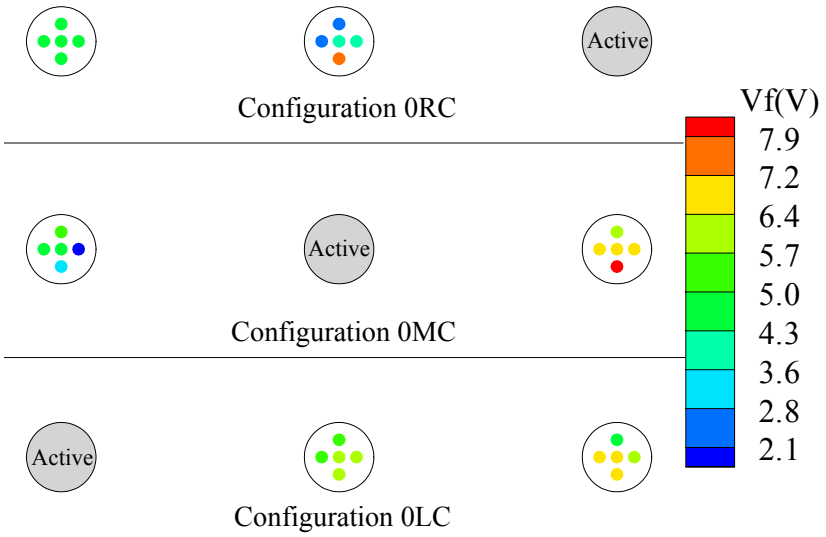

Figure 6-1: 5PLP-DC floating potential results for the 0RC, 0MC, and 0LC TA configurations.

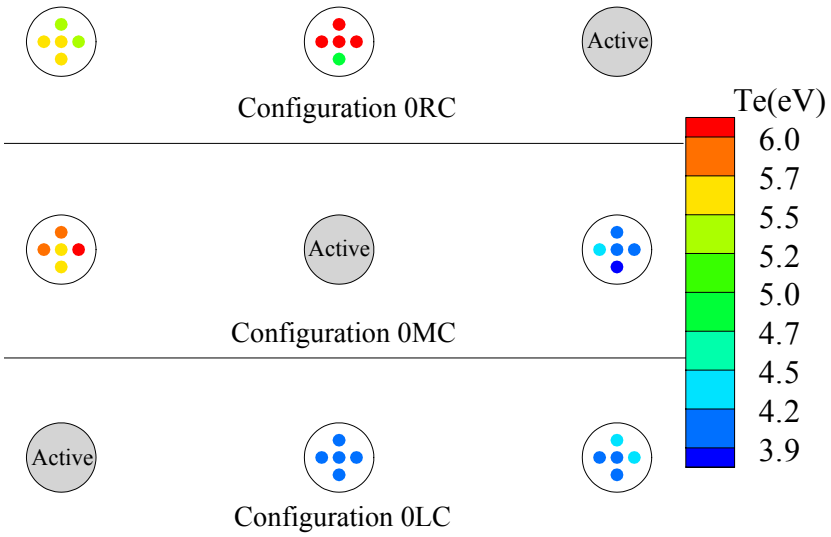

Figure 6-2: 5PLP-DC electron temperature results for the 0RC, 0MC, and 0LC TA configurations.

Measured electron temperatures are typically within 3-6 eV with electron temperature decreasing with increasing electromagnet current. The nominal operating

condition shows electron temperatures between 4-6 eV. Operation with the DCs connected shows slightly lower electron temperatures than disconnected operation. However, these differences are only on the order of 3% and could be accounted for by probe and analysis error. Right and middle DCA configurations show higher electron temperatures on the left side of the TA, and this difference decreases with increasing electromagnet current. Typical results for electron temperature are shown in Figure 6-2.

Plasma potentials are measured between 27-33 V with plasma potential increasing with increasing electromagnet current. The nominal operating condition of 0 A electromagnet current shows plasma potentials approximately 2-5 V above the discharge voltage of ~24.5 V. Measured plasma potential is typically higher for the right DCA active configurations, specifically configuration 10RC and 10RI. No noticeable difference is apparent when the DCs are electrically connected to or isolated from the TA. Typical results for plasma potential are shown in Figure 6-3.

Measured number densities are between $8.9 \times 10^{10} - 2.5 \times 10^{11}$ cm^{-3} with number density decreasing with increasing electromagnet current. For the nominal configuration number densities are consistently $1.3 \times 10^{11} - 2.5 \times 10^{11}$ cm^{-3}. No noticeable difference is apparent when the DCs are electrically connected to or isolated from the TA. Typical results for number density are shown in Figure 6-4.

Although the configurations with the middle DCA active (0MC, 5MC, 10MC, 0MI, 5MI, 10MI) are physically symmetric, plasma properties measured on the right and left side of the DCA differ. Specifically, number densities on the left side are approximately 50% larger than the right side for a 0 A electromagnet current. This result can be seen in Figure 6-4. The difference between the left and right side decreases with

increasing electromagnet current. A similar result is found for the electron temperature, Figure 6-2.

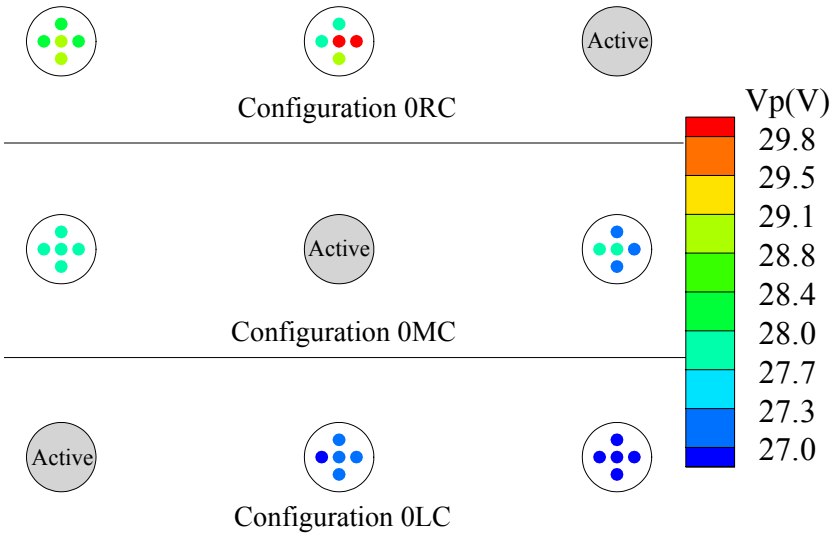

Figure 6-3: 5PLP-DC plasma potential results for the 0RC, 0MC, and 0LC TA configurations.

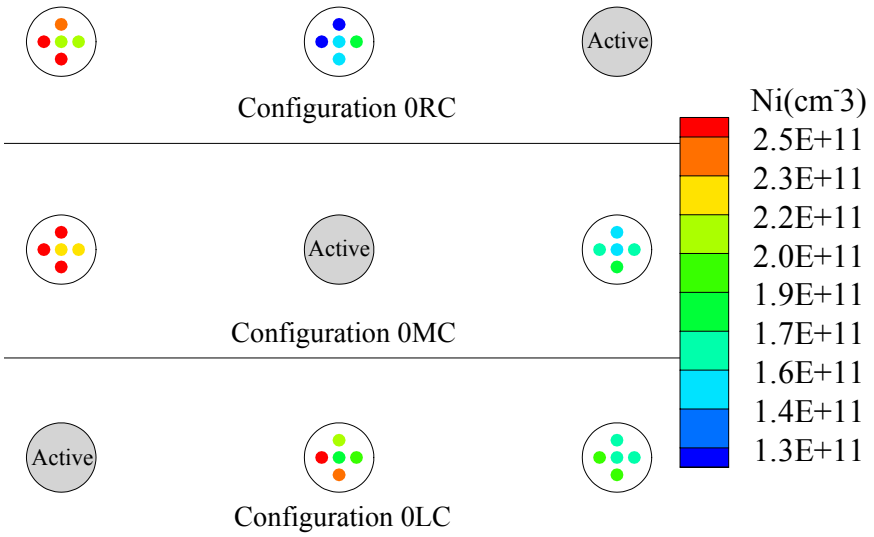

Figure 6-4: 5PLP-DC number density results for the 0RC, 0MC, and 0LC TA configurations.

The discrepancies described above are within the error of the number density measurements, which are expected to be ~50%,[44,79,134] but they may also be explained if

the plasma is coupling unevenly inside the TA. Asymmetries in the magnetic field may cause the plasma to be non-uniform and subsequently denser in regions of lower magnetic field strength. This may explain the dependence of these results on electromagnet current and subsequently the magnetic field. As electromagnet current increases the magnetic field increases causing one or both of the following to occur. 1) Increasing the magnetic field strength causes it to become more uniform making the relative difference between the left and right 5PLP-DCs to decrease; or 2) as the backplate magnetic field increases the plasma is pushed downstream, a trend that has been documented by other researchers[39,40] and the present investigation (see Chapter 5), causing the relative difference between the left and right 5PLP-DCs to decrease. Magnetic field mapping of the TA prior to experimental testing did not show any differences from the MagNet™ simulation results. However, symmetry was assumed and only one quadrant of the TA was mapped.

Another interesting result is that configurations with the left DCA active and those with the right DCA active are not symmetrical as expected (see Figure 6-4). Results have maximum differences on the order of ~50%, ~50%, and ~10% for number density, electron temperature, and plasma potential, respectively. The right DCA active configurations have larger values of plasma potential and electron temperature. These discrepancies are expected to be within the error of the methods applied here and the explanations developed above regarding the magnetic field may apply for these configurations as well. Another explanation may be the increased discharge voltage for right DCA activity configurations (~1 V larger). An increase in discharge voltage may

explain the increase in plasma potential, as well as the increased number density and electron temperature.

6.2.2 7PLP-DC

The following section describes the results obtained utilizing the 7PLP-DCs for left, middle, and right DCA operation. 7PLP-DC floating voltage, electron temperature, plasma potential, and number density values are typically on the order of 2-15 V above cathode potential, 3-6 eV, 27-35 V above cathode potential, and $5.0x10^{10} – 2.0x10^{11}$ cm^{-3}, respectively. General trends are identical to those described for the 5PLP-DC. An explanation for these results is analogous to those described in the 5PLP-DC section and is not repeated here. The 7PLP-DCs are designed and utilized in an attempt to determine if plasma properties vary with radial location on the DC. However, the error associated with the probes and the analysis procedure does not allow these types of trends to be determined.

6.2.3 APLP-DC

The APLP-DC is utilized for a left active and middle active DCA. APLP-DC data are not obtained for the right active DCA configuration. Typical raw data profiles are shown in Figure 6-5. When the probe is external to the DC (positive axial positions) the I-V characteristic appears as expected. As the probe moves internal to the DC, the collected current significantly decreases leading to an almost linear I-V characteristic with small slope. The decrease in probe signal leads to a smaller signal-to-noise ratio and, as a result, the thin-sheath analysis procedure (Chapter 4) is unable to calculate the plasma parameters. Specifically, internal to the DC, I-V characteristic derivatives become

quite noisy and the log-linear current versus voltage plot can no longer be used to obtain the electron temperature. Furthermore, magnetic field strength increases as the probe moves internal to the DC causing further perturbation to the I-V characteristic.

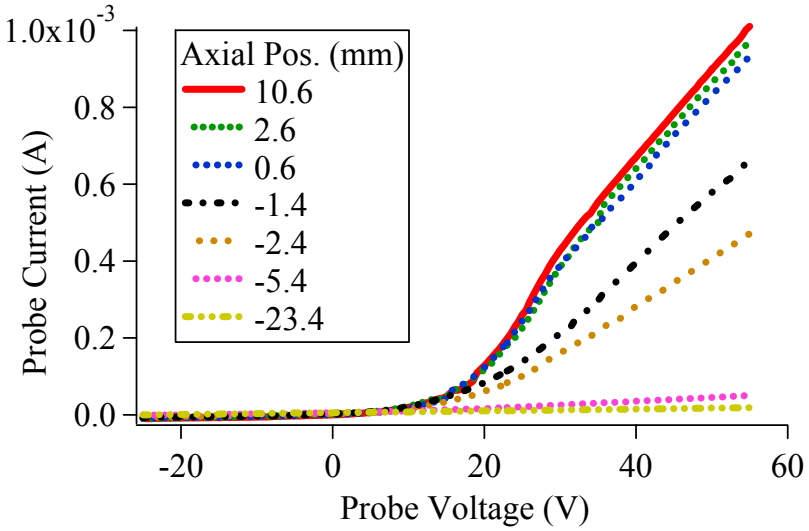

Figure 6-5: Typical APLP-DC raw data I-V characteristics as a function of axial position. As the probe moves inside the DC the probe current significantly decreases.

Figure 6-6 through Figure 6-8 show axial plasma properties for the APLP-DC for various TA operational configurations. All voltages are referenced with respect to cathode common. An axial position of zero on the plots corresponds to the external side of the "cathode" orifice. As shown by the figures, as the probe moves internal to the DC (negative axial positions) the data become much noisier and general trends are difficult to establish. Data are taken at smaller axial increments closer to the "cathode" and "keeper" orifices in an attempt to visualize the sheath structure; however, no clear structure is seen.

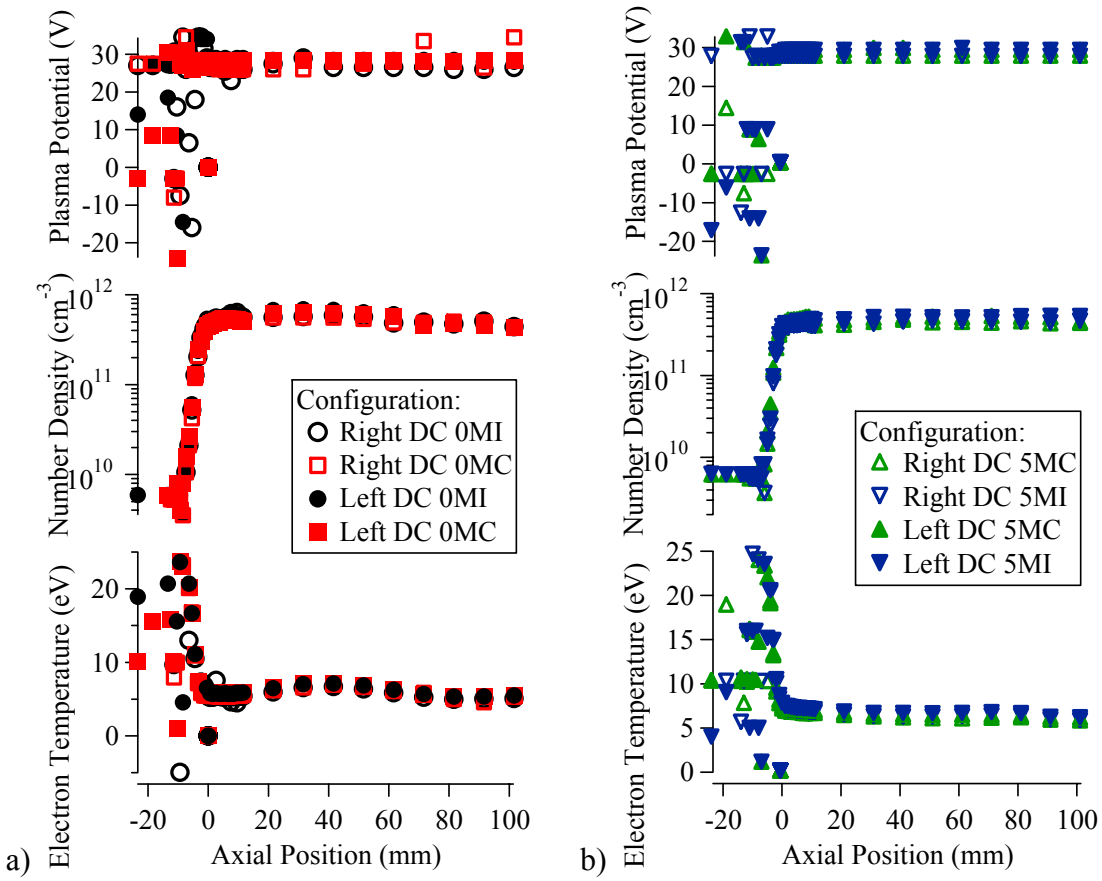

Figure 6-6: APLP-DC plasma property axial profiles for the a) 0MI and 0MC and b) 5MI and 5MC TA operational configurations.

Electron temperature values are typically between 5-8 eV external to the DC and appear to increase internal to the DC. As the electromagnet current increases, electron temperature decreases and this trend becomes more apparent at the "cathode" exit-plane (0 mm). Electrical connectivity of the DCs does not have a noticeable affect on the axial electron temperature profile. Data obtained at the right and left locations during middle DCA operation and at the middle and right locations during left DCA operation do not show significant differences and are typically within 0.5 eV of each other. For the nominal 0 A electromagnet configuration, electron temperatures are typically 5 eV, which is consistent with data obtained by the 5PLP-DCs and 7PLP-DCs.

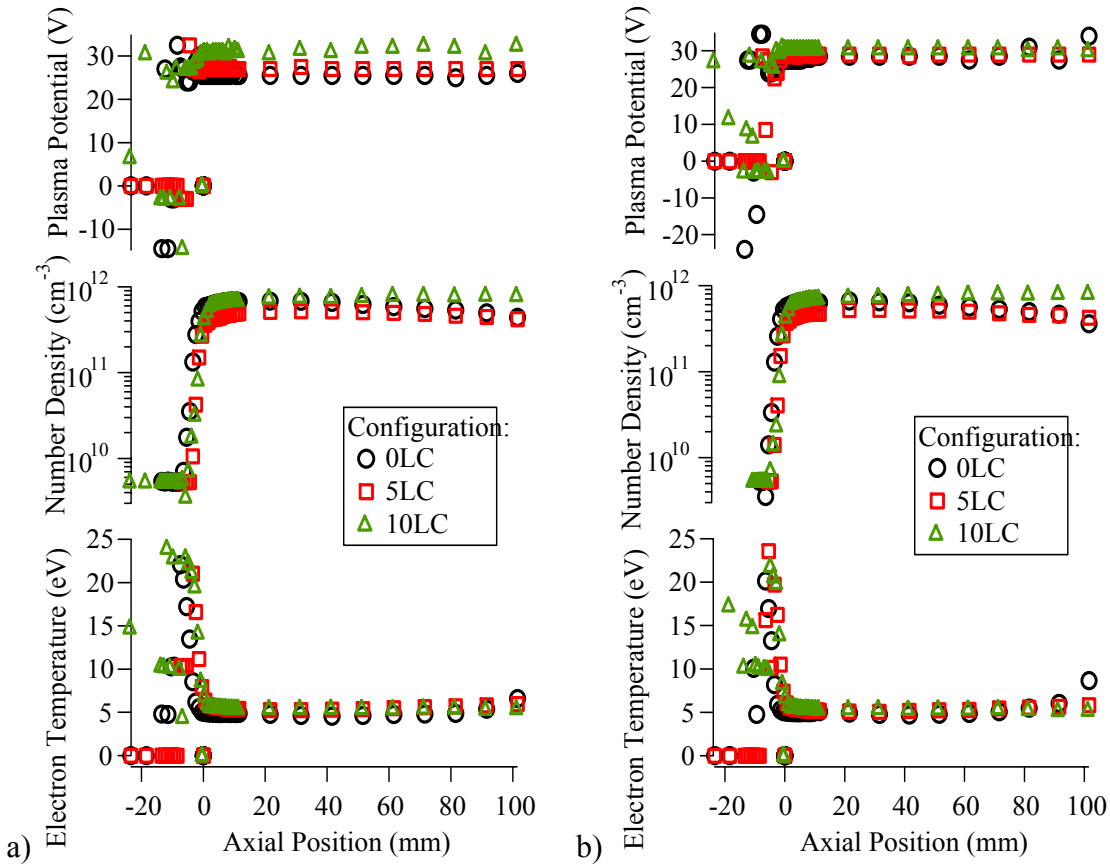

Figure 6-7: APLP-DC plasma property axial profiles for the a) middle DC and b) right DC for the 0LC, 5LC, and 10LC TA operational configurations.

Plasma potential values are typically between 28-32 V external to the DC, but internal to the DC the plasma potential data become extremely noisy. No noticeable trend is determinable internal to the DC because of the linear I-V characteristic phenomena described above. External to the DC the plasma potential remains relatively constant and tends to increase with electromagnet current. Electrical connectivity of the DC has no noticeable affect on the axial plasma potential profile. Data obtained at the right and left locations during middle DCA operation and at the middle and right locations during left DCA operation do not show significant differences and are typically within ~1 V of each other.

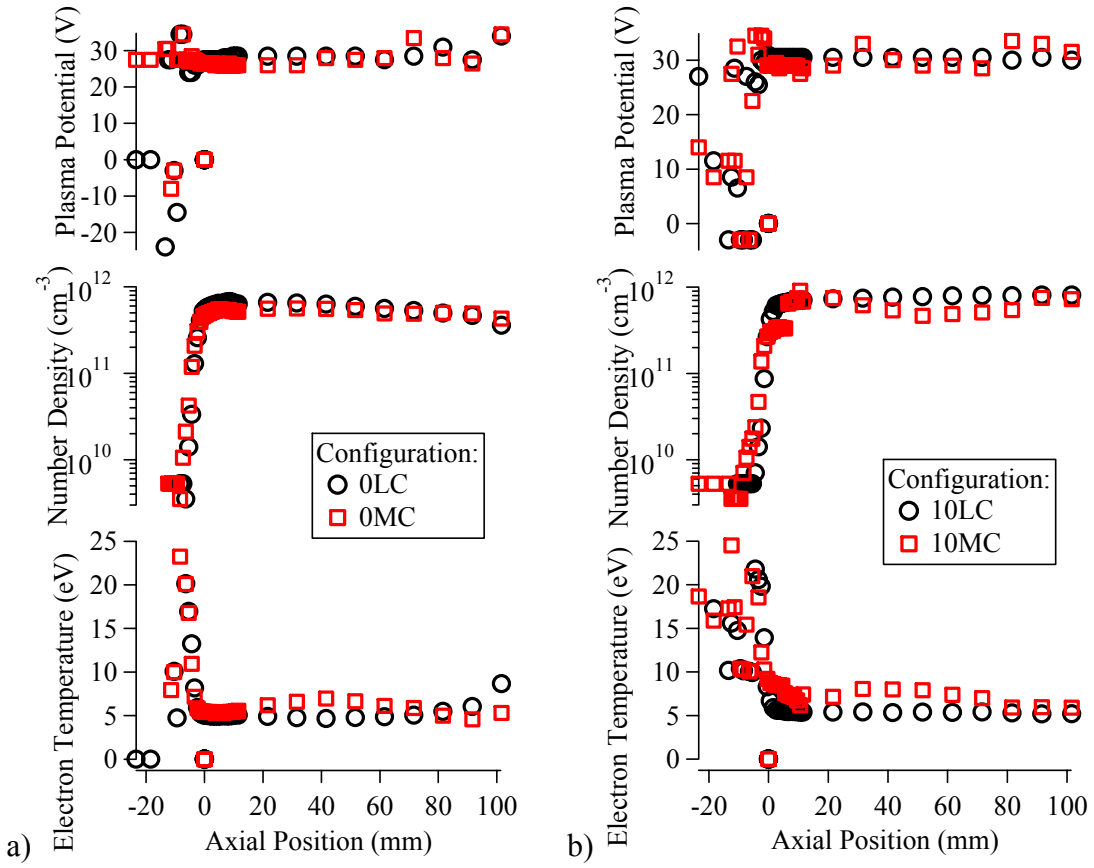

Figure 6-8: APLP-DC plasma property axial profiles for the right DC for the a) 0LC and 0MC and b) 10LC and 10MC TA operational configurations.

Number densities are typically on the order of 5.5×10^{11} cm^{-3}, which is slightly larger than data obtained with the 5PLP-DCs and 7PLP-DCs, but within ~45%. As electromagnet current increases, number density values decrease and this trend is especially apparent near the "cathode" exit plane (0 mm). DC electrical connectivity does not have a noticeable affect on axial number density profiles. When the middle DCA is active, the left APLP-DC typically measures number densities ~10% larger than the right APLP-DC. This trend is consistent with the 5PLP-DC and 7PLP-DC data. However, when the left DCA is active, the middle and right APLP-DCs measure approximately the

same number densities. Finally as the probe moves internal to the DC the number density decreases by two orders of magnitude within 5 mm.

Floating potentials are measured to be lower than expected and are on the order of -2.5 – 5 V relative to cathode common, a result inconsistent with the 5PLP-DC and 7PLP-DC data. However, as will be described in the next section, the ACLP-DC measures floating potentials in the range of 3-12 V above cathode potential, as expected. The lower floating potentials may be related to the increased electron temperature internal to the DC. Specifically, internal to the DC the floating potential must be more negative to repel the more-energetic higher-temperature electrons. This result is also obtained for the plasma potential mapping portion of this work, Chapter 7.

General trends associated with the APLP-DC are as follows: 1) Electrical connectivity of the DCs does not affect axial plasma property profiles; 2) as the electromagnet current increases (backplate magnetic field increases) plasma potential increases, while electron temperature and number density decrease; 3) number density falls off two orders of magnitude within 5 mm internal to the DC; and 4) data obtained internal to the DC are more difficult to analyze due to a decreased signal-to-noise ratio.

6.2.4 ACLP-DC

Only one ACLP-DC is utilized for a left active and middle active DCA. Axial profiles are obtained at the left location during middle DCA operation and at the middle location during left DCA operation. The right DC location is never investigated due to time constraints. Typical raw data profiles for the ACLP-DC appear similar to the APLP-DC profiles shown in Figure 6-5. Again, as the probe moves internal to the DC, the magnitude of the current collected decreases and the I-V characteristics becomes linear

with small slope. However, because the ACLP-DC has a larger collection area than the APLP-DC the signal-to-noise ratio does not deteriorate as much and slightly better trends are able to be determined.

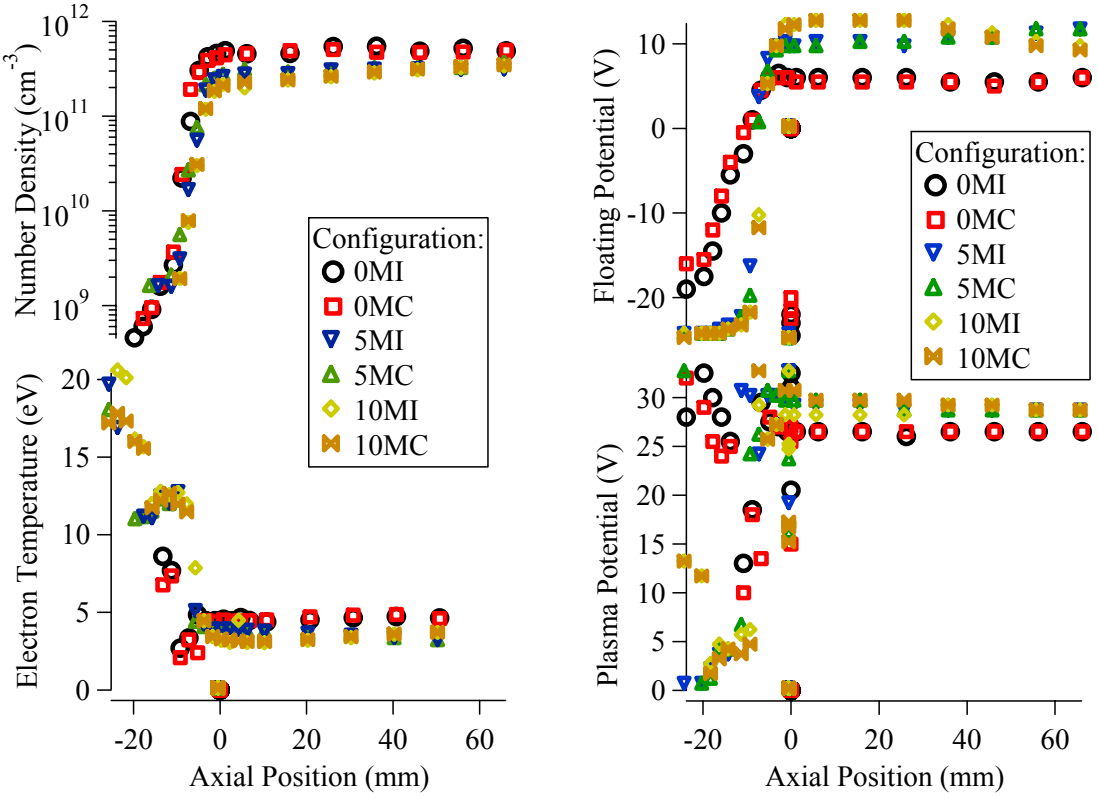

Figure 6-9: ACLP-DC plasma property axial profiles for the right DC for the investigated TA operational configurations.

Figure 6-9 shows the axial plasma properties for the ACLP-DC. All voltages are referenced with respect to cathode common. An axial position of zero on the plots corresponds to the external side of the "cathode" orifice and positions are measured from the tungsten wire–alumina sleeve interface on the probe. Because the probe is cylindrical, certainty in axial position is compromised and determined to be ~3 mm. Number density decreases as the probe moves internal to the DC, so an OML analysis becomes important. Transition to the OML regime is determined to occur at ~3 mm internal to the DC. At this

location the thin-sheath number density calculation is aborted and an OML calculation utilized.

Plasma potential values external to the DC are typically on the order of 26-30 V above cathode potential (2-4 V above the discharge voltage) and plasma potential increases with electromagnet current. Operation with the DC electrically connected or isolated does not produce a noticeable result. Internal to the DC plasma potential values fluctuate considerably due to the increased noise when taking the derivative of the I-V curve. Trends and magnitudes for ACLP-DC plasma potential profiles are very similar to those obtained with the APLP-DC.

Electron temperature is typically 3-5 eV for the ACLP-DC, which is slightly lower than results obtained with the APLP-DC. As the probe moves internal to the DC, electron temperature appears to increase. This result suggests that only the most energetic electrons are capable of entering the DC. However, as mentioned previously these results are difficult to obtain because the log-linear I-V characteristic fit becomes increasingly worse internal to the DC. Furthermore, the magnetic field increases as the probe moves in the negative axial direction further perturbing characteristic. The electron temperature profiles decrease with increasing electromagnet current, a trend noticed with the 5PLP-DC, 7PLP-DC, and APLP-DC.

The ACLP-DC makes floating potential measurements within the expected range of 3-12 V external to the DC. As the probe moves internal to the DC, floating potential drops to -25 V with respect to cathode common; i.e., ground. This result is explained by the measured increase in electron temperature internal to the DC. A lower floating potential is required to repel the higher-temperature electrons inside the DC. This

decrease occurs over a shorter length scale (10 mm) for the 5 A and 10 A electromagnet settings, but requires approximately 25 mm for the 0 A setting. Electrical connectivity of the DC does not affect these results.

Number density is on the order of 5.0×10^{11} cm^{-3}, which is similar to the results obtained by the APLP-DC. As mentioned above, at ~3 mm internal to the DC an OML analysis is substituted for the thin-sheath analysis. As electromagnet current increases, number density decreases. Within approximately 5 mm internal to the DC the number density has dropped two orders of magnitude and by 20 mm the ion current has become undetectable with the sourcemeter. These results are similar to those obtained with the APLP-DC.

In general, the trends determined with the ACLP-DC are similar to those obtained with the 5PLP-DC, 7PLP-DC and APLP-DC, further increasing the confidence in these measurements. Axial profiles for the ACLP-DC are very similar to those obtained with the APLP-DC.

6.2.5 RPA-DC

The RPA-DC is utilized for a left active and middle active DCA. RPA-DC data are not obtained for the right active DCA configuration. A voltage sweep of 70 V is utilized because increasing the sweep to larger voltages does not reveal any interesting structures. Figure 6-10 shows the peak E/q in the distribution function (most-probable-voltage) as a function of the TA configuration. All voltages are referenced with respect to cathode common. Typical trends show the most-probable-voltage increasing with increasing electromagnet current. Most-probable-voltage values range from 18 – 32 V above cathode common. No trends with the ion voltage distribution function other than

most-probable-voltage are noticed. This may be a result of the noise in the RPA-DC raw data that becomes amplified when taking a derivative.

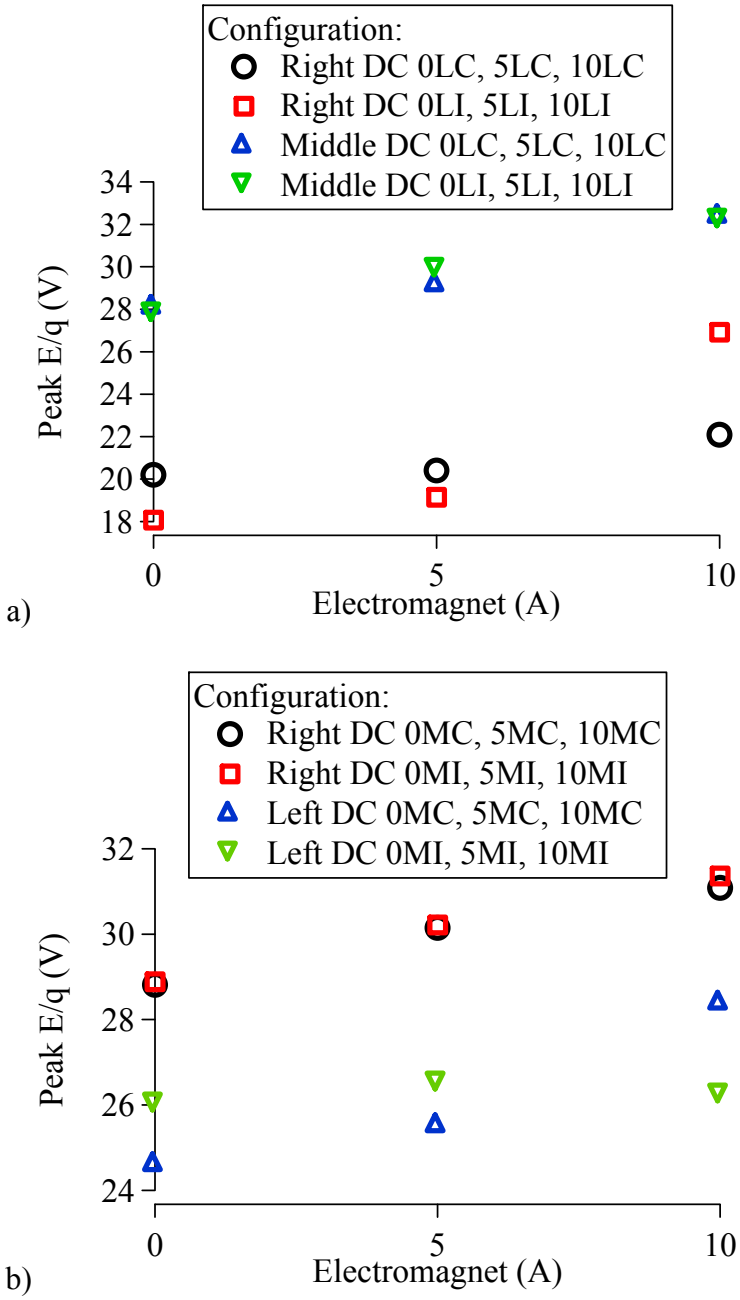

Figure 6-10: Peak E/q voltages (most-probable-voltage) obtained with the RPA-DC for the a) left and b) middle active DCA TA configurations.

Except for the right DC during left DCA operation, measured most-probable-voltages are larger than the discharge voltage (~24.5 V for the 0 A electromagnet configuration) and are similar to the plasma potential. As mentioned above, the plasma potential at the DC locations increases with increasing electromagnet current, a trend also noticed with the RPA-DC most-probable-voltage. These results are consistent with ions falling through the plasma potential to reach the RPA collector. Some of these results show voltages greater than or equal to 30 V, which is cause for concern, especially if there is a significant population of doubly-charged ions present. Some of these ions can be expected to impact the dormant cathode and, if a significant doubly-charged ion population exists, cause erosion of the dormant cathode. Furthermore, doubly-charged ions may also be impacting the active DCA and causing the familiar erosion patterns seen during wear-testing.[7,8,66,69]

6.2.6 5PLPF-DC

Results for the 5PLPF-DC are consistent with the 5PLP-DC and 7PLP-DC results described above. Trends due to adjustment of the magnetic field, DCA location, and DC connectivity are consistent with the previous investigations. Of primary interest for the experiments presented here is the effect of DC propellant flow on plasma properties at the DC "keeper" faceplate. As the 5PLPF-DC propellant flow is increased, the main plenum flow is decreased such that the total flow rate into the MCDC TA remains constant. A schematic of the 5PLPF-DC "keeper" faceplate with the probe numbering is shown in Figure 6-11. Probe 12 obtains results inconsistent with the other probes for all investigated TA configurations and is not presented. Results obtained with the probe located in the "keeper" orifice (probe 14) are discussed first. Results reported in Figure

6-12 are for probe 14, which is located in the "keeper" orifice of the DC on the right side of the TA for all experiments.

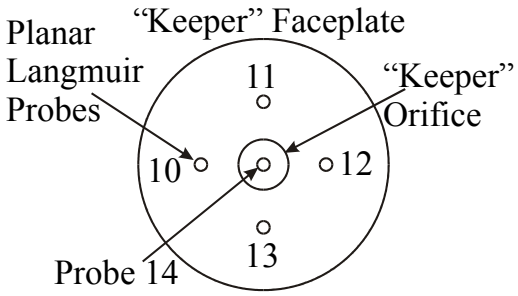

Figure 6-11: Schematic of the 5PLPF-DC "keeper" faceplate showing the 5 probes and the numbering used throughout the discussion.

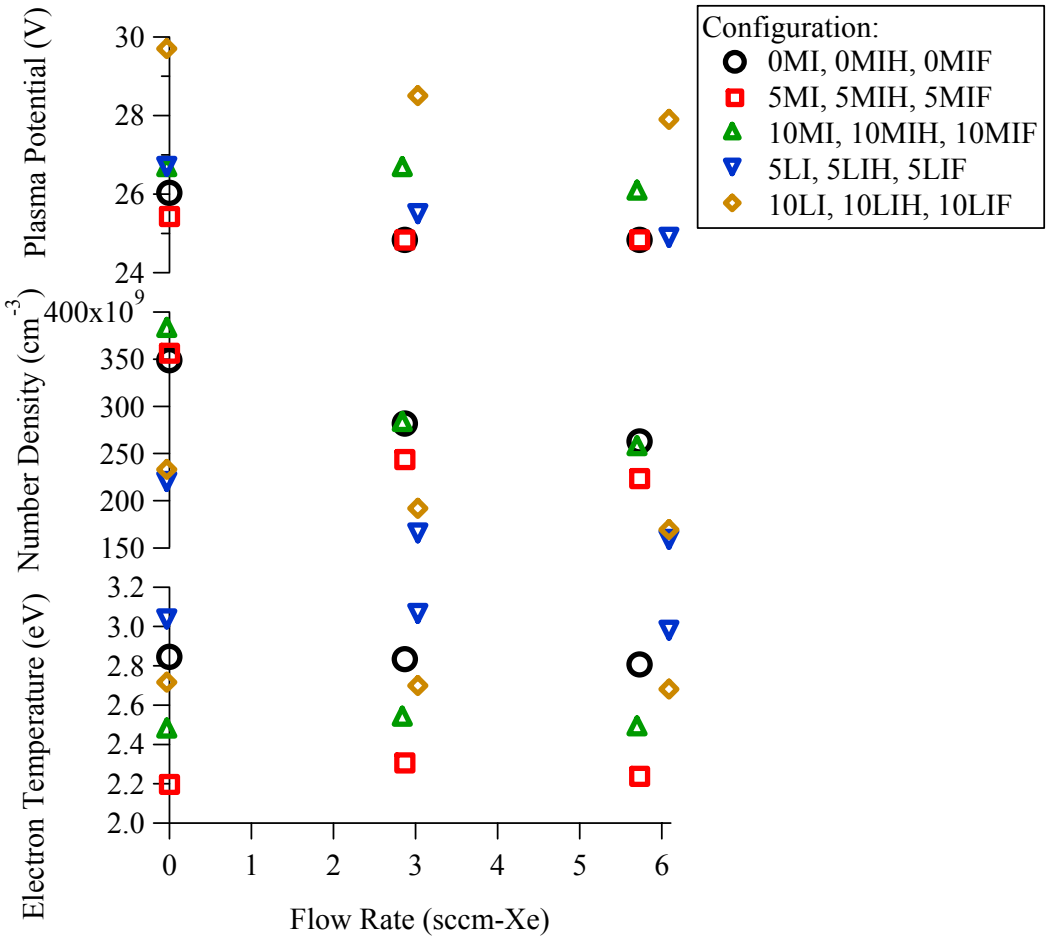

Figure 6-12: 5PLPF-DC "keeper" orifice (probe 14) plasma properties as a function of DC flow rate for various TA operational configurations.

Results indicate that the number density at the DC orifice decreases approximately 20%, electron temperature remains approximately constant, and plasma potential decreases slightly (only ~0.5-1.0 V) as the flow is increased from zero to the full DCA flow rate. The number density results are of particular interest because the flow appears to be shielding the DC from bombarding ions. Therefore dormant cathodes should be operated with propellant flow in order to reduce the number of ions bombarding those units and causing pre-operation erosion. Results from Chapter 5 show that dormant cathode propellant flow rate does not affect TA performance or flatness. Furthermore, as dormant cathode flow rate increases, the main plenum flow is reduced such that the total flow rate remains constant and thruster specific impulse is therefore not affected. The pre-operation wear of the dormant cathodes may be significantly reduced by operating the units with flow. These results also have implications on the operation of the active DCA as well. Specifically, operating the active DCA with an increased flow rate may reduce the number of keeper orifice bombarding ions. More suggestions about the effect of flow rate on the active DCA are discussed in Chapter 8.

Results from the probes located at different locations on the DC "keeper" faceplate (probe 10, 11, and 13, see Figure 6-11) do not show the same trend in ion number density as the "keeper" orifice probe (probe 14). These results are shown in Figure 6-13.

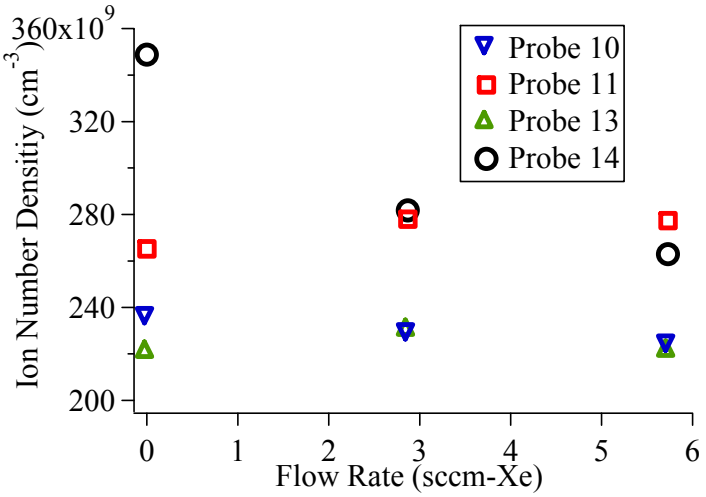

Figure 6-13: 5PLPF results for probes with different locations on the right DC for 0MI, 0MIH, and 0MIF TA configurations.

Because the results with the other probes do not show a consistent trend and the ion number density does not increase or decrease as significantly as the "keeper" orifice probe, the effects of the propellant flow are assumed to become negligible at the radial location of these probes. Therefore, at ~50% "keeper" radius from the DC centerline, propellant flow no longer has a noticeable effect on ion number density.

The decrease in DC "keeper" orifice number density may be attributed to elastic and charge-exchange (CEX) collisions, where the latter is known to cause changes in near-DCA ion energy distributions when external flow is present.[140,141] Elastic collisions have a similar collision cross-section,[142,143] but are not included in this analysis. Ions that may be collected by the probe and keeper suffer CEX collisions with neutral atoms being expelled from the keeper orifice. In a CEX collision, the neutral atom becomes a CEX-ion and the ion becomes a neutral. Both particles retain approximately their pre-CEX energy and direction. Because neutral atoms are expanding out of the orifice and moving in the downstream direction, the CEX-ions are also directed away from the probe and

keeper. The post-CEX neutral atoms may still impact the probe or keeper. However, they are not charged particles and do not register current upon impact with the probe. Furthermore, they are not accelerated through the sheath and therefore have less bombarding energy than impacting ions. A schematic of the process is shown in Figure 6-14.

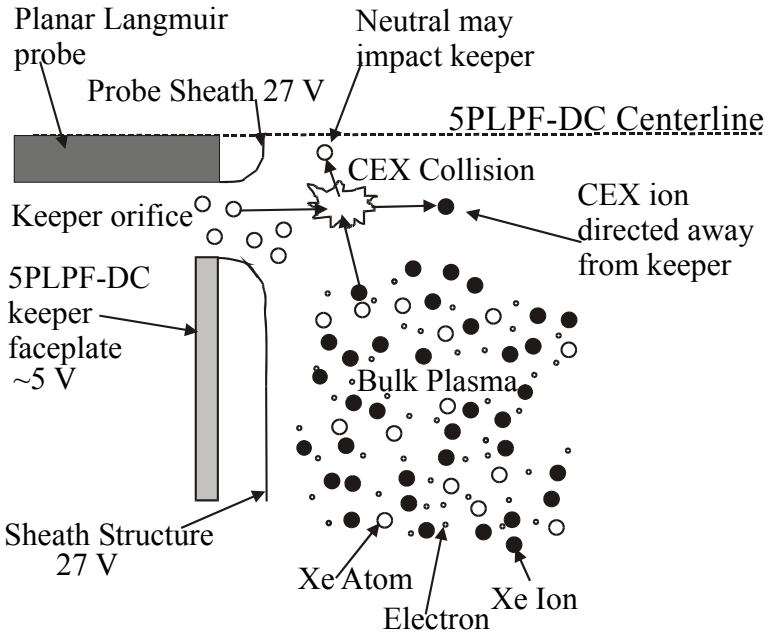

Figure 6-14: Schematic of the CEX process through which the dormant cathode shields itself from bombarding ions. If neutral xenon is not present more ions impact the dormant cathode keeper.

Considering the "keeper" orifice bombarding ions as an ion beam with initial current density, j, a first order estimation of the attenuation due to CEX collisions is obtained by considering the ion continuity equation in one dimension. The ratio of the ion current density at some position, j_z, to the initial ion current density is obtained by integrating over the pathlength, z. The result is Eqn. 6-1,[144]

$$\frac{j_z}{j} = \exp(-n_n \sigma_{ce} z) \qquad \textbf{Eqn. 6-1}$$

where j_z is the ion current density after the beam has suffered CEX attenuation over a pathlength z, j is the ion current density measured if CEX collisions are not present, n_n is the neutral density, and σ_{ce} is the CEX collision cross-section. Ion current density is related to ion number density through Eqn. 6-2,

$$j = qn_i v_i \qquad \textbf{Eqn. 6-2}$$

where q is the charge of the ions, n_i is the ion number density, and v_i is the average ion velocity. Assuming the mass flow rate through the DC, $\dot{m}_{sccm}$, is proportional to the neutral density, n_n, the experimental number density data in Figure 6-12 can be fit using a slightly modified form of Eqn. 6-1. The form of the equation fit to the data is shown in Eqn. 6-3,

$$n_i = K_0 + K_1 \exp(-K_2 \dot{m}_{sccm}) \qquad \textbf{Eqn. 6-3}$$

where K_o, K_1, and K_2 are the fit coefficients and $\dot{m}_{sccm}$ is the flow rate in sccm. The fit coefficients for the three curves shown in Figure 6-15 are given in Table 6-1.

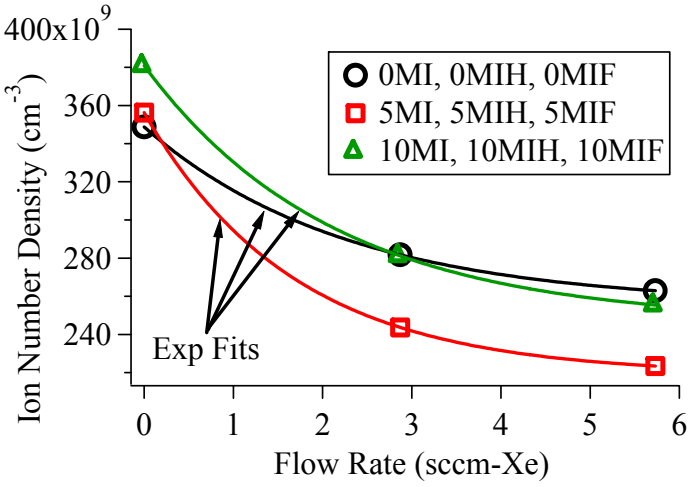

Figure 6-15: Exponential fit to the "keeper" orifice probe (probe 14) number density for various TA operational configurations.

These fits strongly suggest that CEX collisions are causing the observed trends. However, the pathlength, z, should be greater than the mean free path (MFP) of a CEX collision to ensure that multiple CEX collisions are occurring over the integrated pathlength.

Configuration	K_o	K_1	K_2	z/λ_{CEX} $\dot{m}_{sccm} = 3$	z/λ_{CEX} $\dot{m}_{sccm} = 6$
0MI, 0MIH, 0MIF	2.56E+11	9.33E+10	0.442	1.87	3.75
5MI, 5MIH, 5MIF	2.19E+11	1.37E+11	0.597	2.53	5.07
10MI, 10MIH, 10MIF	2.46E+11	1.35E+11	0.471	2.00	4.00

Table 6-1: Exponential fit parameters and ratio of the pathlength to the CEX mean free path.

The approximate relationship for the CEX MFP is given in Eqn. 6-4,

$$\lambda_{CEX} = \frac{1}{\sqrt{2} n_n \sigma_{ce}} \qquad \textbf{Eqn. 6-4}$$

where λ_{CEX} is the CEX MFP, σ_{ce} is the CEX collision cross-section, and n_n is the neutral density. By setting the exponential of Eqn. 6-1 and Eqn. 6-3 equal, a relationship between the theoretical attenuation equation and the experimental data can be determined. This result is shown in Eqn. 6-5.

$$n_n \sigma_{ce} z = K_2 \dot{m}_{sccm} \qquad \textbf{Eqn. 6-5}$$

$$\frac{z}{\lambda_{CEX}} = \sqrt{2} K_2 \dot{m}_{sccm} \qquad \textbf{Eqn. 6-6}$$

Combining Eqn. 6-4 and Eqn. 6-5 allows the ratio of the pathlength to the CEX MFP to be determined. The result is shown as Eqn. 6-6. For the flow rates presented here (~3 and 6 sccm) and for the experimentally determined K_2 values, the ratio is typically between 2-5, and the results for the data in Figure 6-15 are shown in Table 6-1. These results show that the pathlength is larger than the CEX MFP, suggesting that CEX collisions are

responsible for the observed decrease in ion number density with increasing propellant flow rate.

An estimation of the neutral pressure at the DC "keeper" orifice is obtained by considering the continuity equation and the ideal gas law. The result is Eqn. 6-7,

$$p = \frac{\dot{m}RT}{uA} \qquad \textbf{Eqn. 6-7}$$

where p is neutral pressure, u is the neutral velocity at the orifice, A is the orifice area, T is the neutral temperature, $\dot{m}$ is the mass flow rate, and R is the specific gas constant for xenon. Assuming T is 300 K and the velocity is equal to the sound speed, the pressure is calculated to be ~30 mTorr for the maximum flow rate, which yields a neutral density of 1.0×10^{21} m^{-3}. Furthermore, if the bombarding ions are assumed to have energy equal to the plasma potential (~30 V, consistent with the RPA-DC results), σ_{ce} is equal to 45 $Å^2$ [143,145] and the CEX MFP (Eqn. 6-4) and corresponding pathlength, z, are calculated to be 1.6 mm and 7.8 mm, respectively. These values are quite small and on the same order as the DC orifice, suggesting that CEX collisions are indeed occurring.

6.3 Dormant Cathode Plasma Property Conclusions

Dormant cathode plasma properties are analyzed using DCs designed to appear similar to the active DCA. Each DC is equipped with plasma probes such as Langmuir probes and a retarding potential analyzer. Six different DCs are utilized: a 5PLP-DC, 7PLP-DC, APLP-DC, ACLP-DC, RPA-DC, and 5PLPF-DC. Each DC is mounted at a dormant cathode location in the MCDC TA.

Results show no noticeable difference between operating the dormant cathodes electrically connected or electrically isolated from the TA. As the electromagnet current

increases, the backplate magnetic field increases causing the near dormant cathode electron temperature and number density to decrease, while the plasma potential increases. For the nominal 0 A electromagnet configuration, typical number density, electron temperature, and plasma potential values are on the order of 5.0×10^{11} cm^{-3}, 5 eV, and 27 V with respect to cathode common, respectively. Plasma potentials are typically 2-4 V above the discharge voltage, which is nominally 24.5 V. Results with the RPA suggest that ion energy-per-charge ratio is as large as 29 V with respect to the cathode, which is consistent with an ion falling from the plasma potential.

Results with the 5PLPF-DC indicate that dormant cathode "keeper" orifice number density decreases as propellant flow rate through the DC increases. Based on this result, the dormant cathodes in a MCDC should be operated with propellant flow to decrease the number of pre-operation erosion-causing ions. Operation with dormant cathode propellant flow may decrease the pre-operation erosion of the dormant units as much as 20%. Finally, CEX collisions are suggested as the cause for decreasing ion number density with increasing propellant flow. As the flow rate increases, the neutral density at the "keeper" orifice increases, causing more CEX collisions with bombarding ions and decreasing the orifice number density.

CHAPTER 7:

INTERNAL PLASMA PROPERTY MAPPING

A study of the internal plasma properties of the test article (TA) is completed by utilizing a single-Langmuir probe mounted to the high-speed axial reciprocating probe (HARP) positioning system. Using the HARP to sweep the probe in the axial (Z-axis) direction and moving the TA in the radial direction (X-axis) provides two-dimensional maps of the internal plasma properties. The following sections describe the experimental setup and results from this series of experiments.

7.1 Experimental Setup

For the experiments presented here the TA is outfitted with the 5PLPF-DCs to supply propellant flow at the dormant cathode locations. The plasma mapping Langmuir probe is utilized to map the internal plasma properties of the TA and the HARP provides accurate direct linear probe motion while minimizing probe residence time. The probe is mounted to the HARP and the zero or resting position places the exposed tungsten electrode at the TA grid plane. During plasma mapping the HARP moves the probe in the negative (in-sweep) and then positive (out-sweep) axial (Z-axis) direction to complete one sweep. Residence times of the probe inside the discharge chamber are on the order of 750 msec, however, the probe is stationary inside the discharge chamber for less than 100 msec. Small residence times minimize probe heating and discharge plasma perturbation.

The Power DAQ is used to record HARP position, probe voltage, probe current, discharge voltage, and discharge current. The DAQ triggers off the HARP position signal and subsequently records the 5 channels. During a single probe sweep 25,000 points are obtained at 70 kHz per channel. Only the in-sweep of the probe motion is recorded. This method of data acquisition provides approximately 125 I-V pairs for each I-V curve and a total of approximately 180 I-V curves are recorded during one sweep.

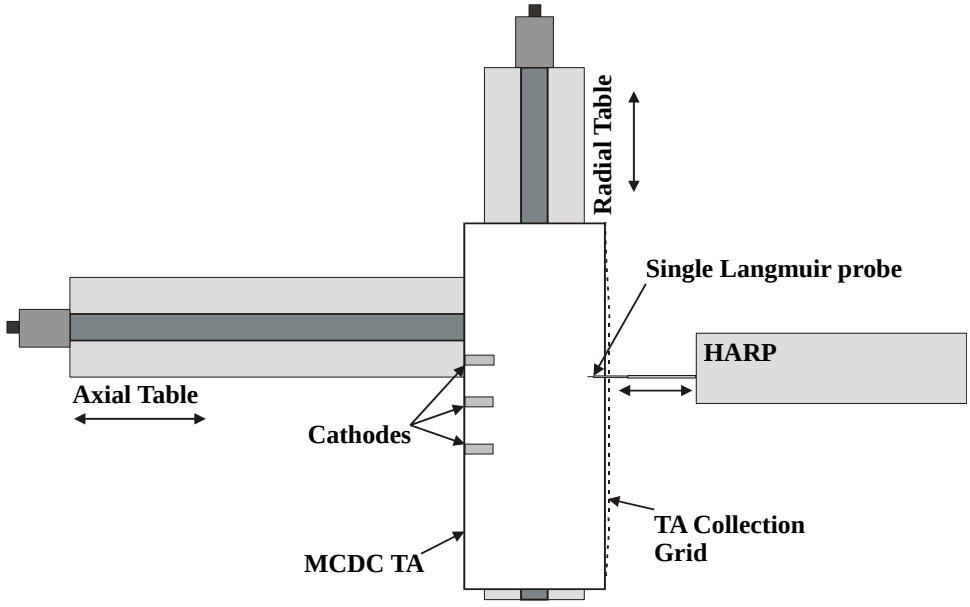

Figure 7-1: Internal TA plasma property mapping experimental setup.

A schematic of the experimental setup is shown in Figure 7-1.The data acquisition procedure is as follows. First, the TA radial and axial position is set with the translation stages. Then the HARP is triggered with the data logger and the probe begins to move. As the HARP position passes through the DAQ trigger point, data are recorded and saved. This process is then repeated at a new radial location. Two separate computers are utilized for this setup. The first computer moves the TA and triggers the HARP, and the second computer is dedicated to the DAQ. A total of 549 radial (X-axis) positions are recorded and one map requires 20 min. to complete. A total of 62 maps are completed

over two horizontal planes (Y = 0 cm and Y = 11.1 cm), which requires over 20 hours of data collection and over 50,000 HARP sweeps.

7.2 Mapping Results

In order to analyze the 6 million I-V characteristics obtained during plasma structure mapping, the IGOR analysis routine described in Chapter 4 is utilized. Initially, the saved data must be broken up into individual I-V characteristics, since a single raw data file contains approximately 180 I-V curves. IGOR is used to 1) determine inflection points in the probe voltage signal; 2) remove the data between inflection points (i.e., take out a single I-V curve); 3) reorganize the data if required ("flip" a decreasing voltage ramp into an increasing ramp); 4) send the data to the I-V curve analysis routine. This procedure is shown on the raw data in Figure 7-2.

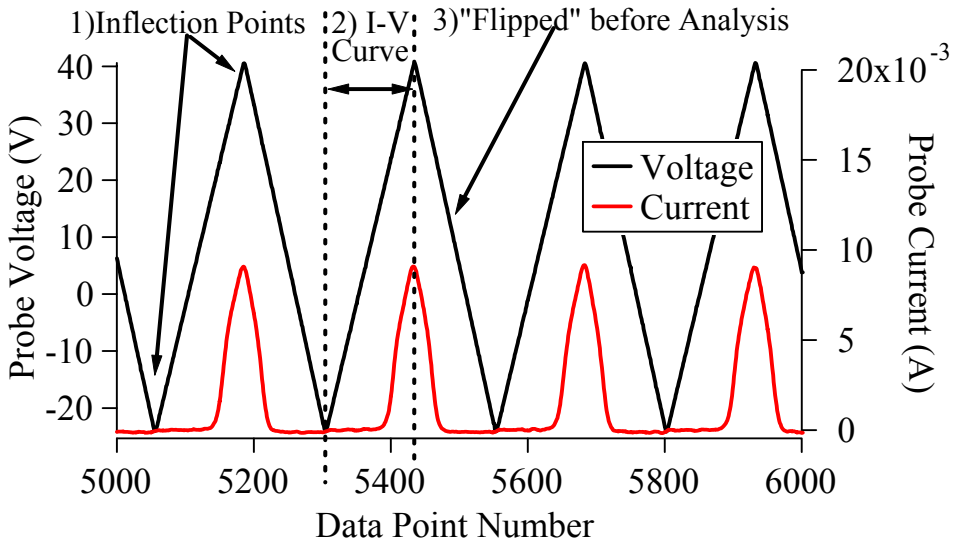

Figure 7-2: Raw data before the IGOR analysis routine is applied.

The spatial location at which each I-V curve is acquired can be computed using the recorded HARP position. Analysis of a single map consists of approximately 100,000

I-V curves and requires approximately 10 min. to complete. The analysis of the recorded discharge current and voltage during probe insertion shows minimal perturbation. Specifically, discharge current does not show any appreciable fluctuation and discharge voltage increases a maximum of 0.3 V when the probe is inserted along the DCA centerline.

The following plots show the internal plasma structure of the TA for two horizontal (X-Z) planes (Y = 0 cm and Y = 11.1 cm) as determined by the analysis routine described above. Plane 1 (Y = 0 cm) corresponds to the mid-plane of the TA where the active DCA and two dormant units are located, whereas plane 2 (Y = 11.1 cm) is 11.1 cm above plane 1 and does not contain the active DCA and dormant units. Trends associated with number density, electron temperature, floating potential, and plasma potential are discussed in the following sections.

In each figure the plasma property map is displayed with notional magnetic field lines and some of the plots also show notional DCAs. Spatial units are normalized by the DCA cathode orifice radius. The origin of all plots corresponds with the DCA cathode orifice. Acquired data for all configurations are displayed in APPENDIX D.

An example plot showing regions of interest in plane 1 is given in Figure 7-3. Note the magnetic cusps formed by the permanent magnet field lines and the intercusp region. Cusps are located around the DCAs and at radial positions of +250 and -250.

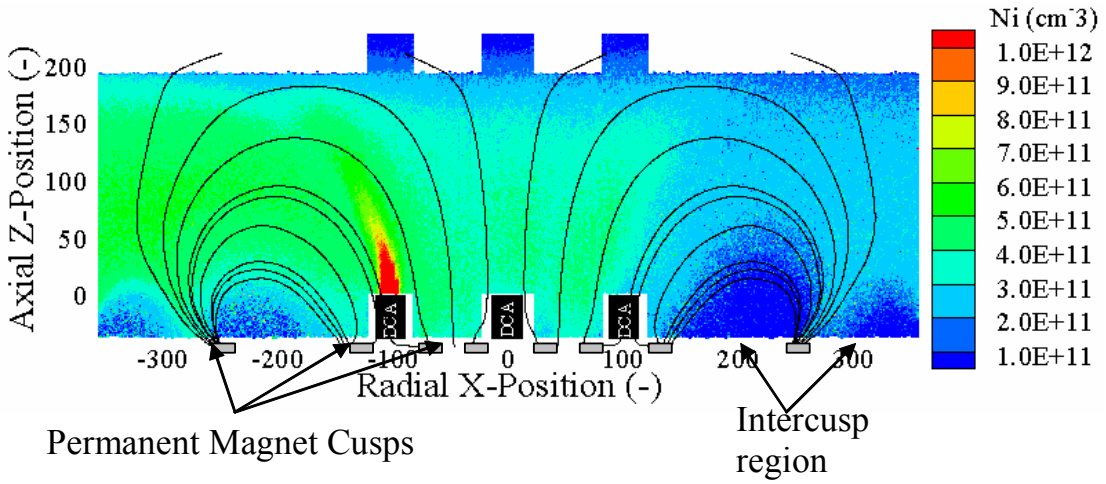

Figure 7-3: Example plane 1 figure showing regions of interest.

7.2.1 Plane 1 (Y = 0 cm) - Electron Temperature

The effects of DCA location and magnetic field strength on electron temperature structures are shown in Figure 7-4 and Figure 7-5, respectively. The cathode plume shows larger electron temperatures than the bulk discharge plasma and this higher temperature plume is consistently directly downstream of the DCA. Bulk discharge electron temperature is on the order of 2-4 eV with the cathode plume at temperatures between 5-10 eV. During left DCA operation for the 0 A electromagnet configuration (Figure 7-4a), the higher temperature plume appears to couple with the left side of the TA along the magnetic field lines. The left high temperature region is also apparent during middle DCA operation (Figure 7-4b).

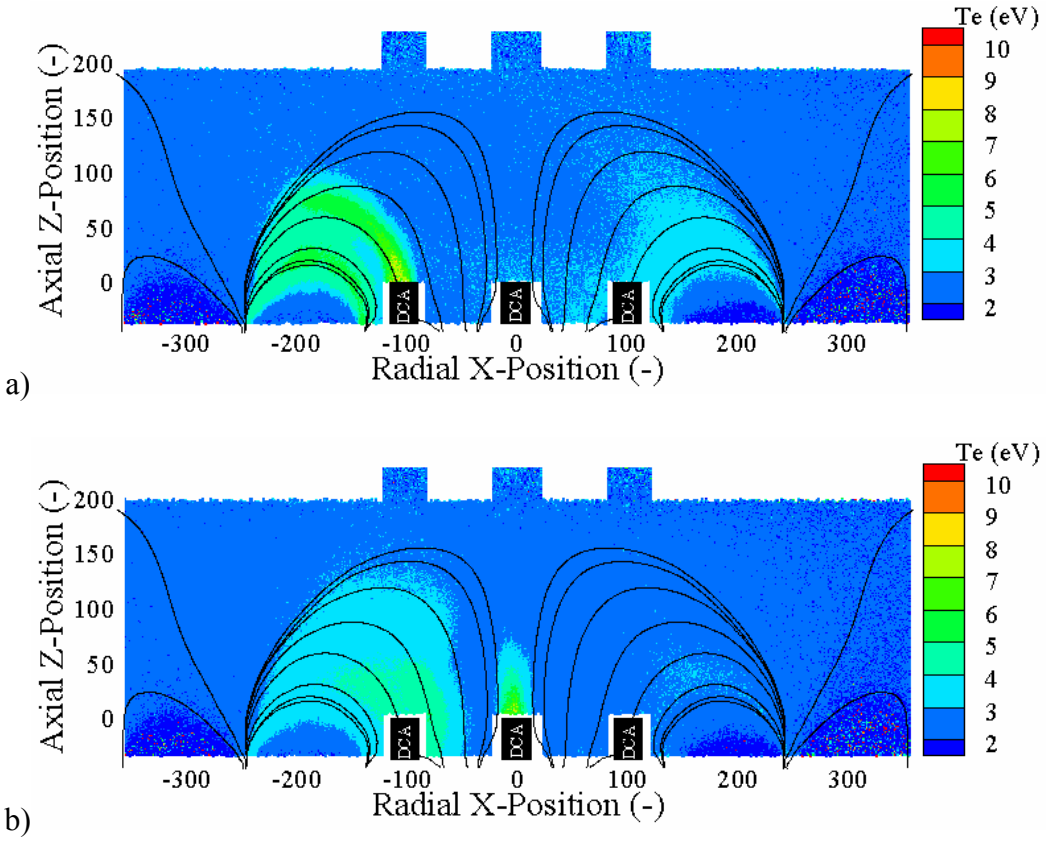

Figure 7-4: Effect of DCA location on electron temperature structure for the a) 0LI and b) 0MI configurations.

As the electromagnet current increases, the axial magnetic field increases and Figure 7-5 shows that 1) the higher temperature plume becomes elongated; and 2) the electron temperature increases. The electron temperature results are consistent with the fact that electrons are confined to spiral along the magnetic field lines.[23,38,146,147] Increasing the magnetic field confines more electrons to the center of the TA and decreases the electron cyclotron radius so that higher-temperature electrons traverse farther into the TA.

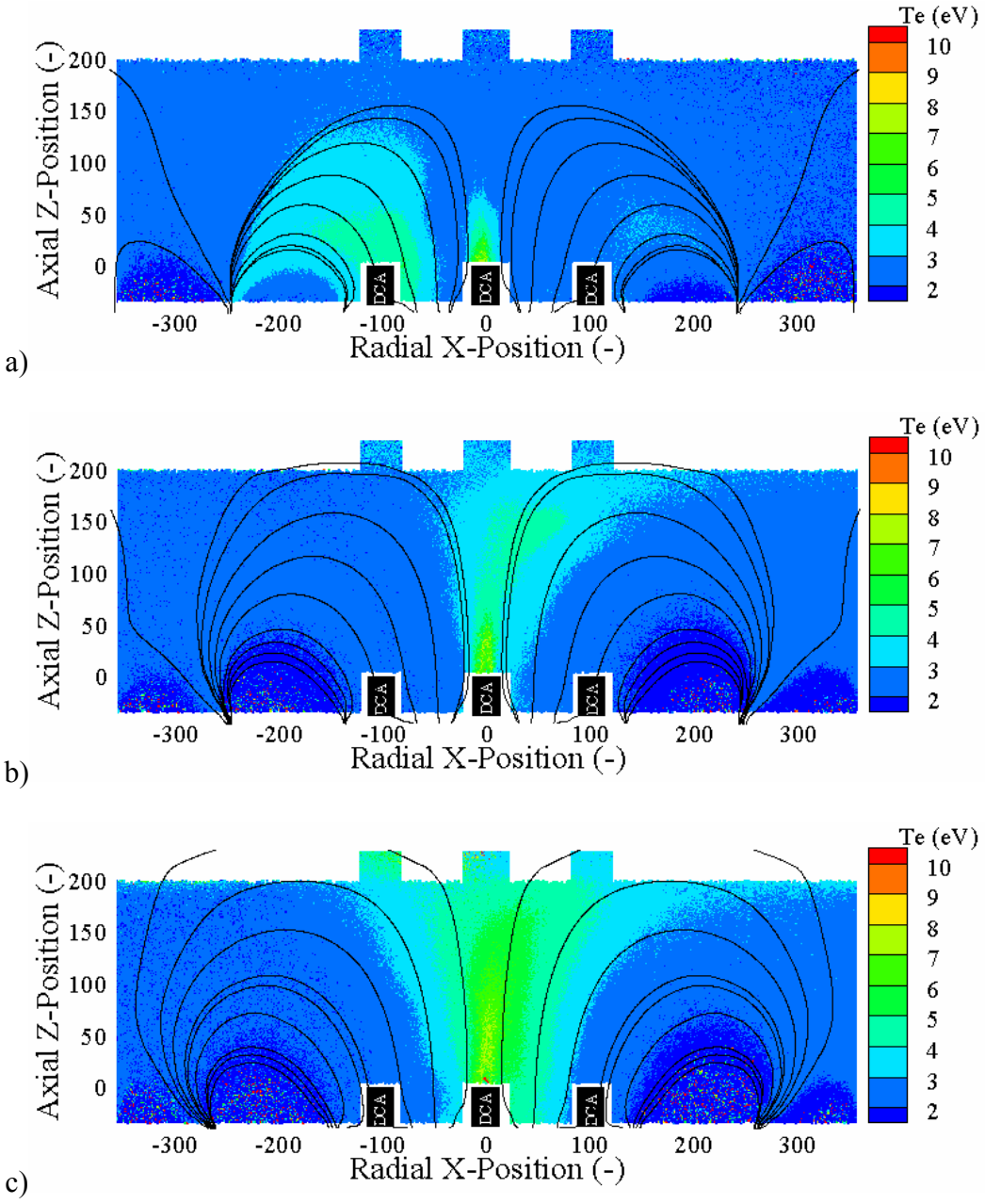

Figure 7-5: Effect of magnetic field on electron temperature for a) 0MC, b) 5MC, and c) 10MC configurations.

Although a few high-temperature "spots" are shown due to noise in the data, the intercusp regions typically show lower electron temperatures than the bulk discharge. Therefore these regions have lower-energy electrons that may have suffered inelastic collisions that caused them to move transverse to the field lines. Electron motion across

field lines to the intercusp region is governed by classical diffusion, which is proportional to $1/B^2$.[44] Therefore, increasing the magnetic field decreases the number of electrons that can diffuse into the intercusp region, decreasing ion production in that region. Furthermore, as the axial magnetic field increases, electrons are incapable of reaching off-axis regions. Higher-energy electrons are confined to the field lines and are therefore found along the field lines and in the cusps. Finally, electron temperature profiles do not change with dormant cathode flow rate or connectivity.

7.2.2 Plane 1 (Y = 0 cm) - Number Density

The effects of DCA location and magnetic field strength on TA number density structure are shown in Figure 7-6 and Figure 7-7, respectively. The dense cathode plume is consistently directly downstream of the DCA. During left DCA operation for the 0 A electromagnet configuration (Figure 7-6a), the higher density plume appears to couple with the left side of the TA and the density is larger on the left side of the TA. Even during middle DCA operation for the 0 A electromagnet configuration (Figure 7-6b), the density appears larger on the left side of the TA. This is a result that has also been noted with the diagnostic cylinder (DC) experiments. Number densities presented here are consistent with previous results obtained with the grid-plane Langmuir probe and the DCs.

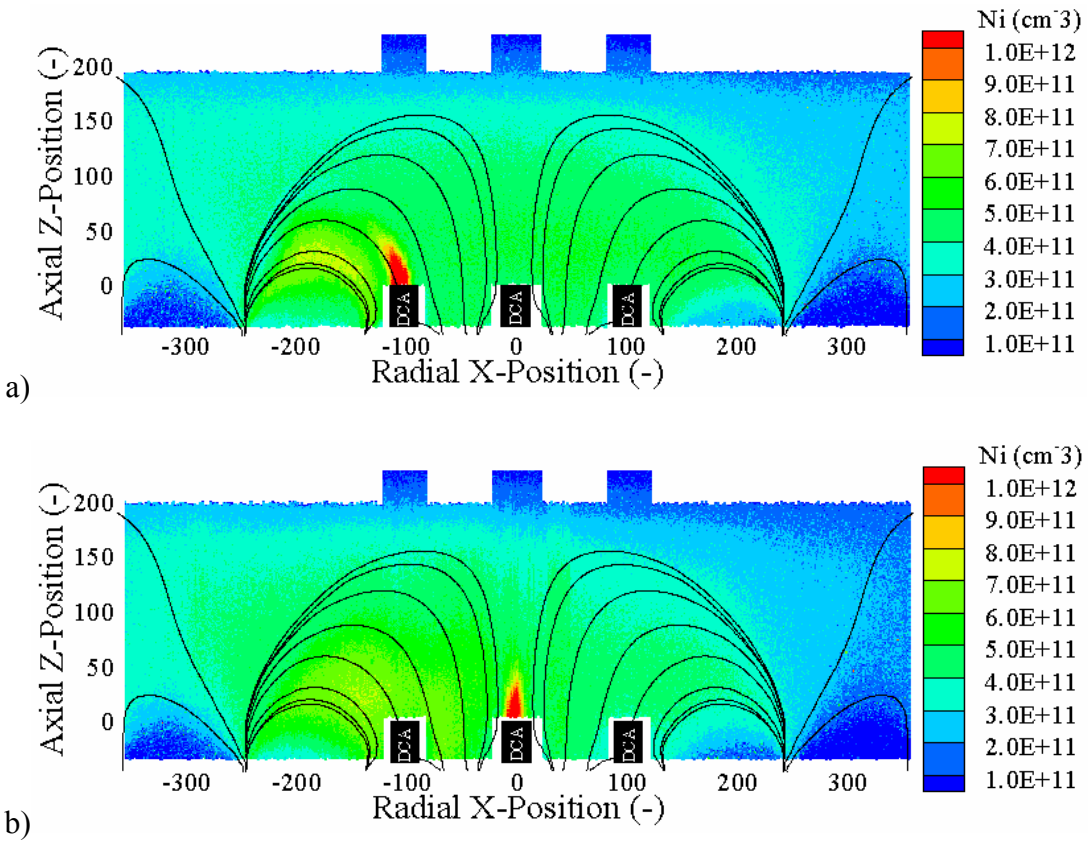

Figure 7-6: Effect of DCA location on number density for a) 0LI and b) 0MI configurations.

As the electromagnet current increases, the axial magnetic field increases and Figure 7-7 shows that 1) the discharge plasma becomes more collimated; 2) the high-density cathode plume becomes elongated and denser; and 3) the intercusp number density decreases. This suggests that more ion production occurs along the field lines and in the cusps, consistent with the fact that more-energetic higher-temperature electrons are present in these regions. Finally, variations in the dormant cathode propellant flow rate and electrical connectivity do not affect the number density structures.

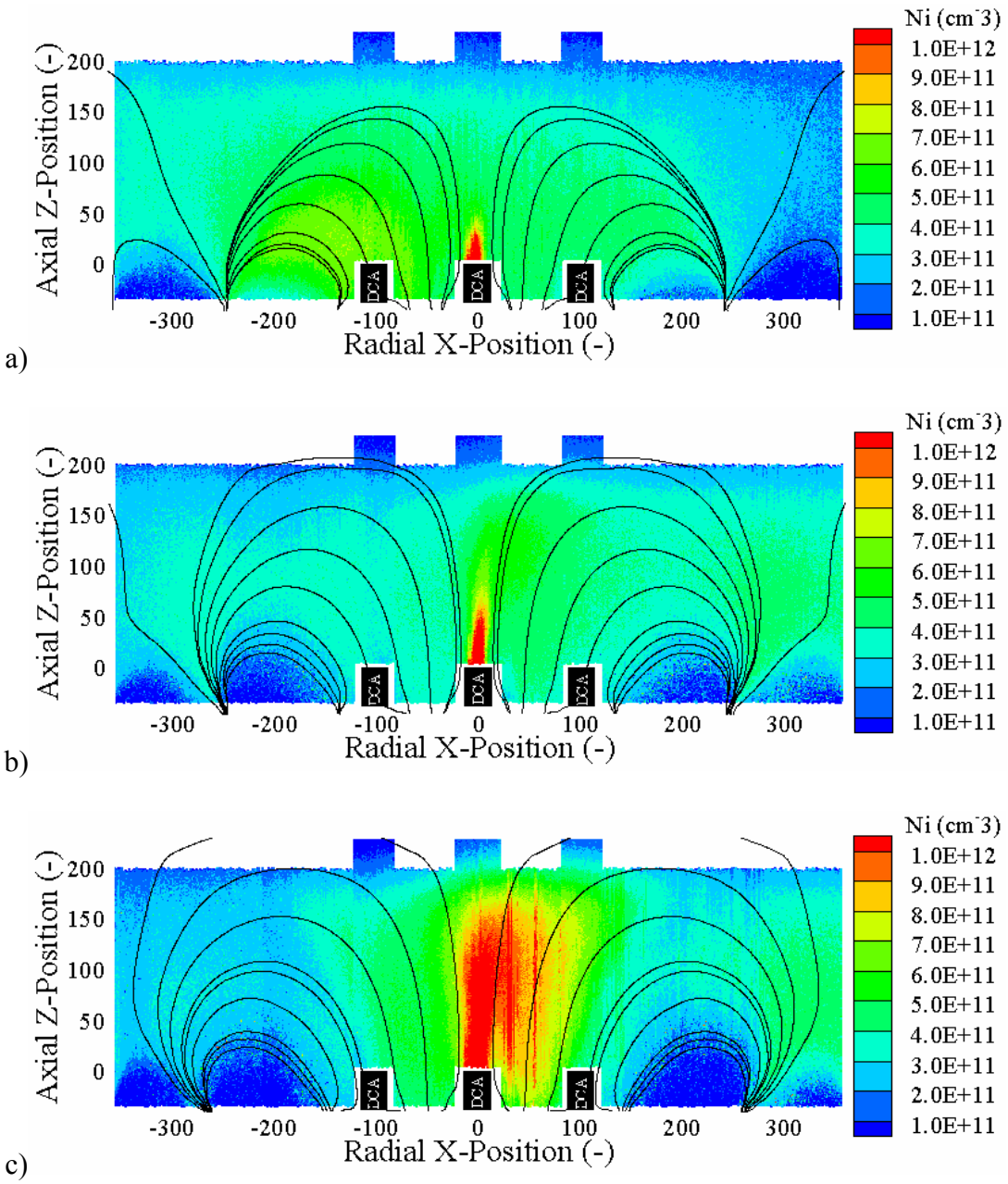

Figure 7-7: Effect of magnetic field on number density for a) 0MC, b) 5MC, and c) 10MC configurations.

7.2.3 Plane 1 (Y = 0 cm) - Floating Potential

The effects of DCA location and magnetic field strength on floating potential structures are shown in Figure 7-8 and Figure 7-9, respectively. DCA plume floating potential is lower than the bulk discharge, which is on the order of 10 V. The lower

floating potential DCA plume is consistently directly downstream of the DCA. During left DCA operation the low floating potential plume couples with the left side of the TA, consistent with the results presented for electron temperature and number density.

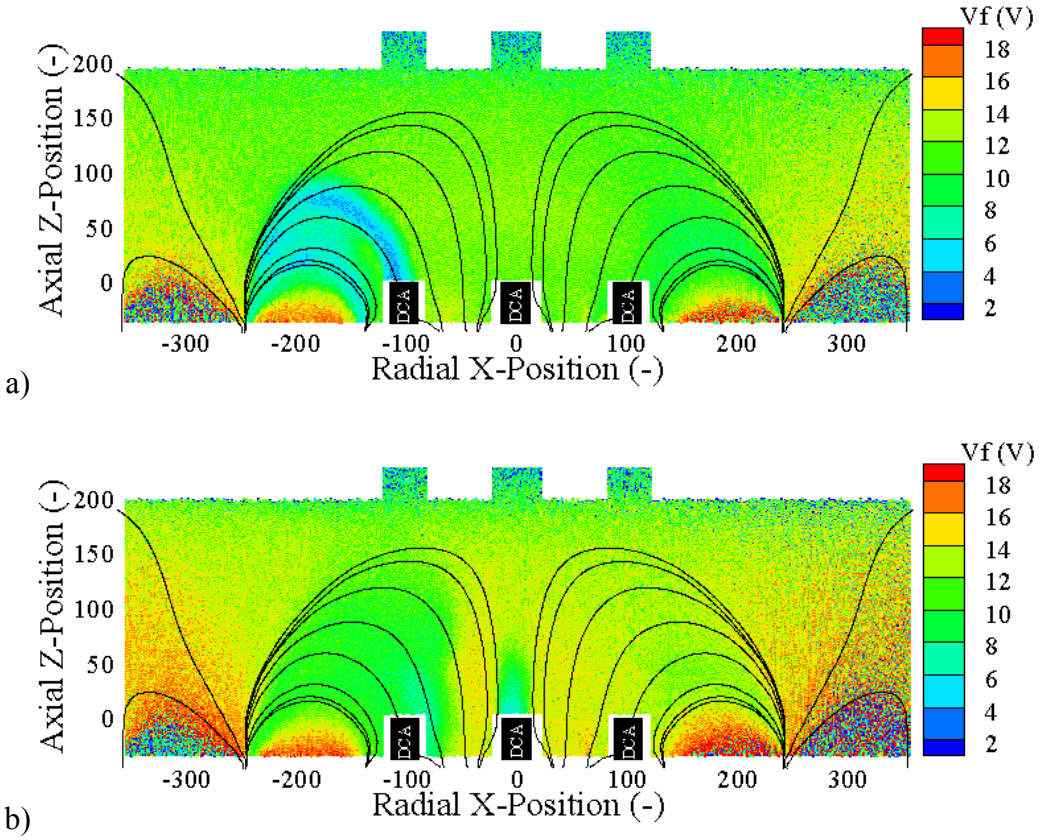

Figure 7-8: Effect of DCA location on floating potential for a) 0LIH and b) 0MIH configurations.

As the electromagnet current increases, the axial magnetic field increases and the lower floating potential plume structure becomes elongated. The floating potential results are consistent with the results displayed for electron temperature. Because more-energetic higher-temperature electrons are located in the DCA plume, the floating potential must be lower in order to repel those electrons during an I-V curve sweep. Floating potential profiles do not change with dormant cathode flow rate or electrical connectivity.

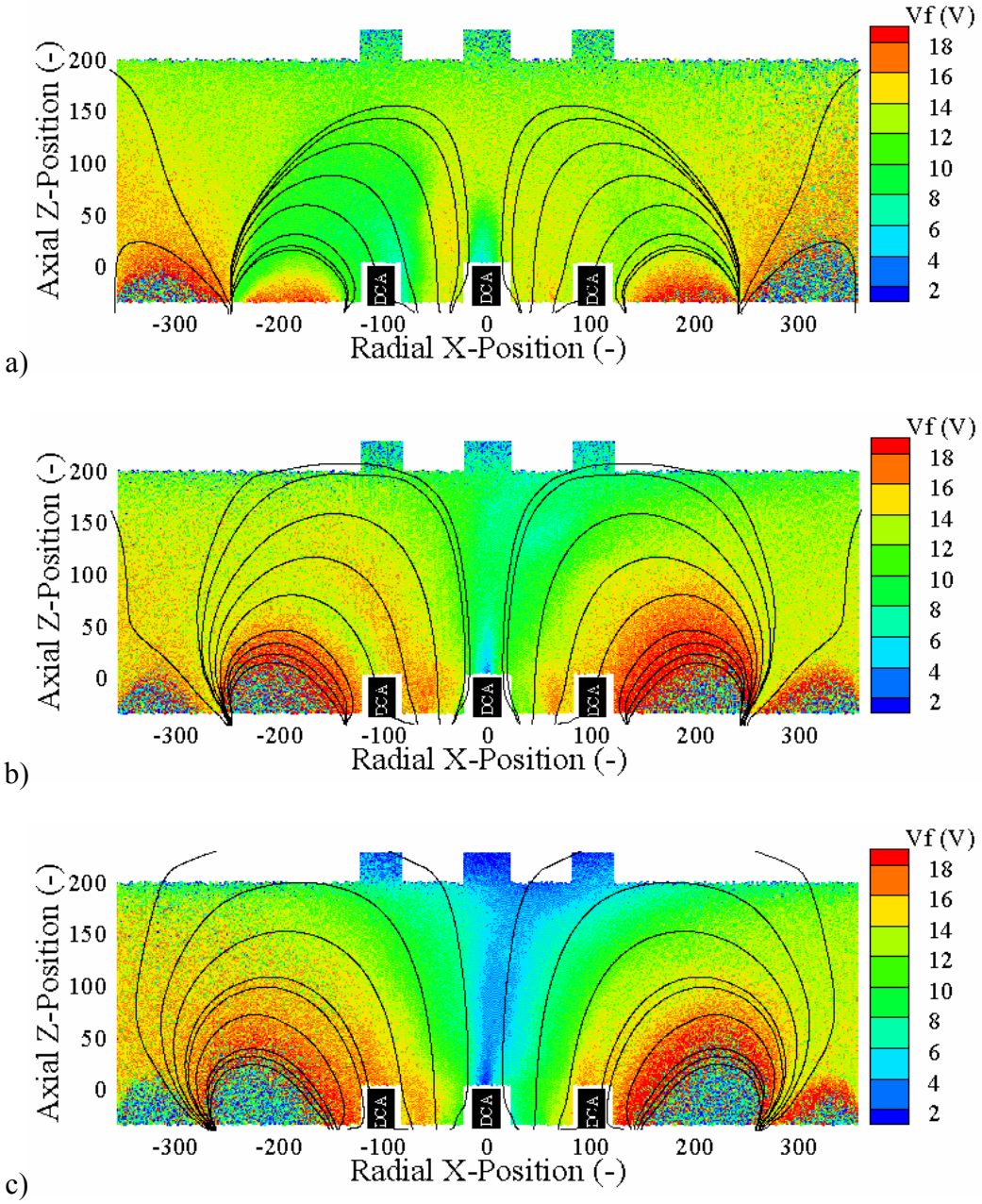

Figure 7-9: Effect of magnetic field on floating potential for a) 0MCH, b) 5MCH, and c) 10MCH configurations

7.2.4 Plane 1 (Y = 0 cm) - Plasma Potential

The effects of DCA location and magnetic field strength on plasma potential structures are shown in Figure 7-10 and Figure 7-11, respectively.

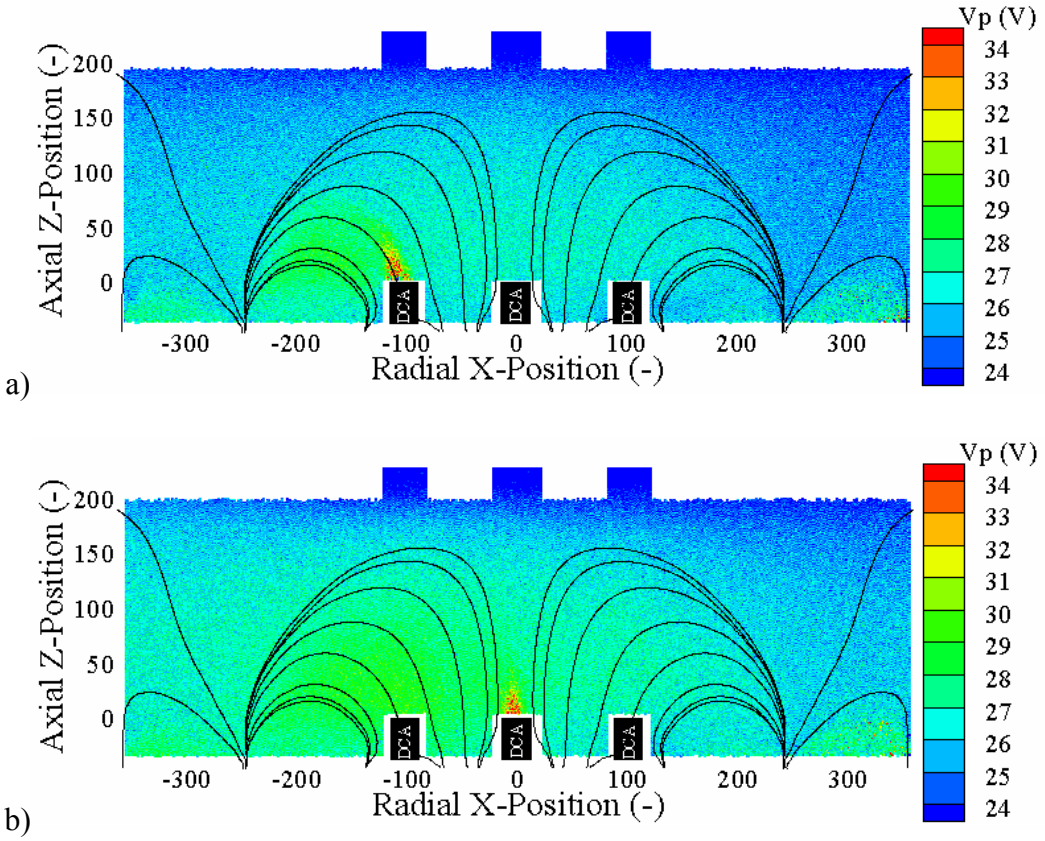

Figure 7-10: Effect of DCA location on plasma potential for a) 0LIF and b) 0MCF configurations.

DCA plume plasma potential structure shows a low-potential region (< ~25 V) near the DCA surrounded by a high-potential region (~35 V). This structure is consistently directly downstream of the DCA. The bulk plasma potential is typically a few volts above the discharge voltage, consistent with previous TA results for the grid-plane Langmuir probe and DCs. During left DCA operation the DCA plume plasma potential structure couples with the left side of the TA, consistent with the results for the other measurements.

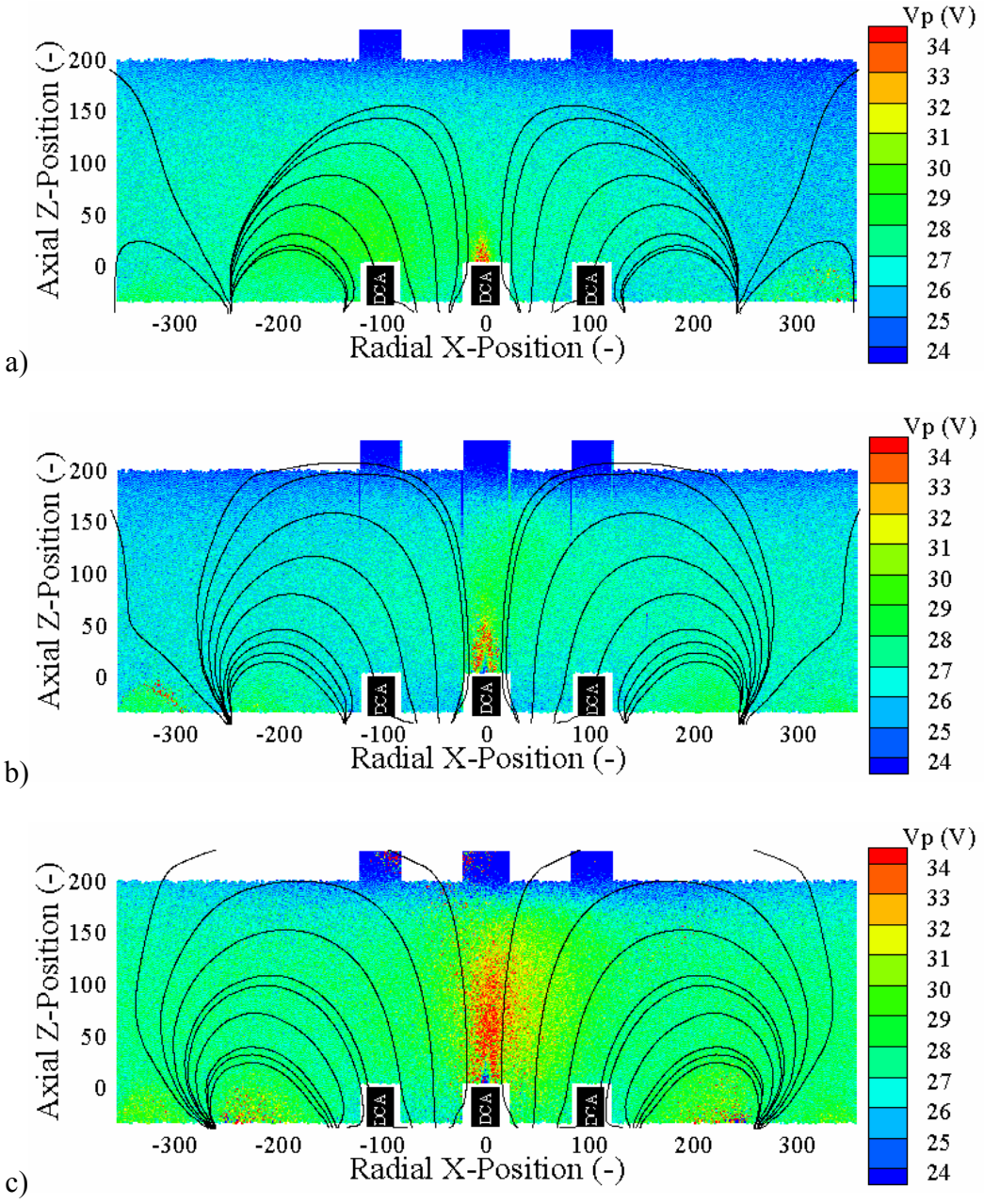

Figure 7-11: Effect of magnetic field on plasma potential for a) 0MCF, b) 5MCF, and c) 10MCF.

As the electromagnet current increases, the axial magnetic field increases and the plasma potential structure becomes elongated. Also, the near-DCA potential structure becomes more visible and shows a high-potential surrounding a lower-potential region. This type of profile is indicative of the potential-hill model described by previous

researchers and shown in Figure 7-12.[140,148-151] Investigation of the cusp and intercusp region shows results consistent with the other plasma properties. Plasma potential is higher in the intercusp region, consistent with a lower density in this region. Lastly, the plasma potential profiles do not change with dormant cathode flow rate or connectivity.

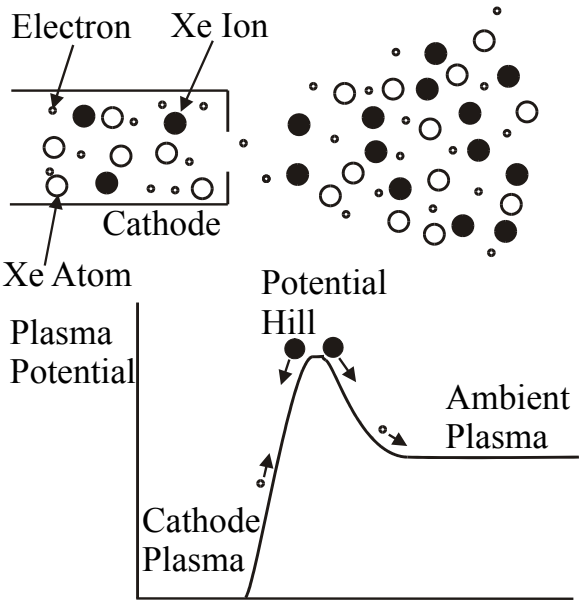

Figure 7-12: Schematic representation of a near-DCA downstream potential-hill structure.

A potential-hill model for high-energy, backstreaming, cathode-impinging ions has been suggested as a primary cause of DCA erosion in ion thruster discharge chambers.[140,148-151] In this model, a near-DCA potential-hill is created due to extensive electron-impact ionization. High-energy electrons ejected from the cathode ionize neutral atoms near the DCA exit-plane. Secondary electrons created by the ionization events readily thermalize and escape the near-DCA region due to their low mass. The more massive ions are traveling at much lower speeds and tend to accumulate, thereby inducing the electric fields in this region that lead to the formation of the potential-hill.

DCA erosion is then caused by ions accelerated upstream by the potential-hill that impact the DCA.

The existence of a potential-hill downstream of an ion thruster DCA is debatable because of the contradiction in experimental results. Sengupta, *et.al.*, have shown an increase in plasma potential on DCA centerline by calculating the plasma potential from the derivative of a single-Langmuir probe I-V curve.[122,152] However, results obtained by Herman with an emissive probe show a decrease in plasma potential near the DCA and no potential-hill.[79,97] Jameson, *et al.*, have used an emissive probe to obtain results similar to Herman's using variable anode geometries with and without a magnetic field.[153,154] Also, Goebel has obtained measurements internal and downstream of an operating DCA (not operating inside an ion thruster) that negate the potential-hill theory.[155] Using a cathode with a ring anode and a single-Langmuir probe, Martin, *et al.*, have reported a potential well directly downstream of a cathode orifice.[156] However, this last experiment was conducted without a magnetic field, which can significantly alter the near-DCA plasma potential structure.[155] Obviously there is still some debate about the existence of a near-DCA potential-hill in an operating ion thruster.

The reported near-DCA plasma potential-hill structures may be a product of the data analysis and probe technique. Figure 7-13 shows how the probe characteristic changes from the bulk plasma (away from the DCA) to the near-DCA region.

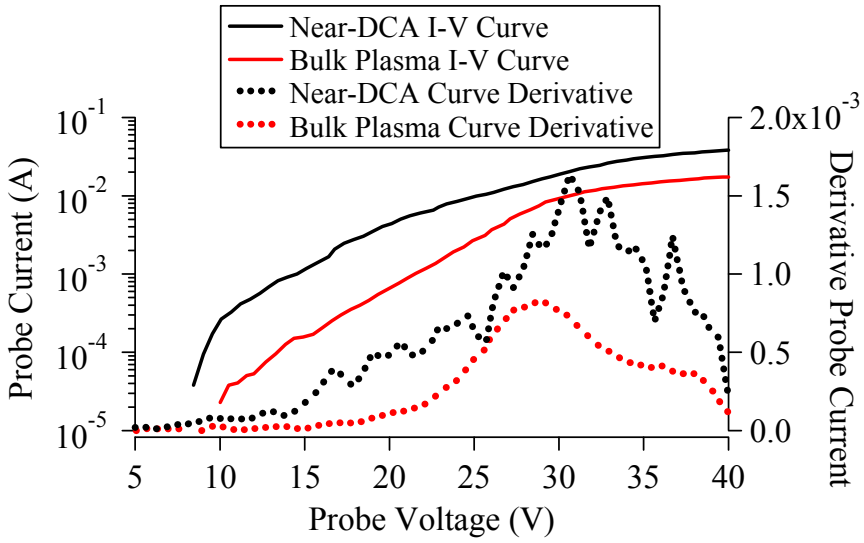

Figure 7-13: Near-DCA and bulk plasma I-V characteristics and their associated derivatives. Using a single-Langmuir probe I-V characteristic and its derivative to determine plasma potential becomes more difficult in the near-DCA region.

Specifically, near the DCA the transition from the electron retarding to the electron saturation region of the probe trace becomes more rounded and difficult to determine. Therefore the derivative becomes noisier and the maximum (i.e., the plasma potential) is more difficult to accurately obtain. Martin, *et al.*, have also reported this phenomenon in near-cathode plume measurements.[156] Excessive rounding is indicative of a noisy or turbulent plasma[124] and excessive noise may be indicative of plasma conditions that cause heating of ions or production of multiply-charged ions that can cause sputter erosion of surfaces.[157] Furthermore, the rounding may be due to a high-frequency component of the plasma potential. Jameson, *et al.*, have reported plasma potential fluctuations of 12-45 V at frequencies between 100-500 kHz.[153] More information regarding a possible high-frequency plasma component is discussed in section 7.3 below. In general, results in the near-DCA region suggest that plasma potential structures within that region are best captured using emissive probes instead of single-Langmuir probes.

Further study of the near-DCA plasma potential is completed utilizing a different method for calculating plasma potential. Internal Hall-effect thruster (HET) plasma potential is typically calculated using the floating potential and electron temperature measured with a single-Langmuir probe.[114,158,159] In an unmagnetized, quiescent, Maxwellian plasma, the floating potential (V_f) is related to the plasma potential (V_p) by Eqn. 7-1.[108,114]

$$V_p = V_f + \frac{T_e}{2}\left[1 - \ln\left(\frac{2\pi m_e}{M_i}\right)\right] \qquad \textbf{Eqn. 7-1}$$

In this equation, T_e is electron temperature, m_e is electron mass, and M_i is ion mass. The presence of a magnetic field, streaming ions and electrons, and the possible presence of a non-Maxwellian velocity distribution near the DCA complicate the relationship between the floating and plasma potential, such that Eqn. 7-1 is not strictly valid. However, the error is on the order of the electron temperature (~10 eV in the near-DCA region and ~5 eV in the bulk discharge) so the floating potential profile is still a useful, albeit inexact, representation of the plasma potential.[160] Results presented here are only meant to be a first-order approximation.

Utilizing Eqn. 7-1, along with the floating potential and electron temperature results presented above, new plasma potential plots are constructed. The results are compared with the original plasma potential profiles obtained by finding the maximum in the derivative of the I-V curve trace. The differences in results between the two methods are shown in Figure 7-14 and Figure 7-15.

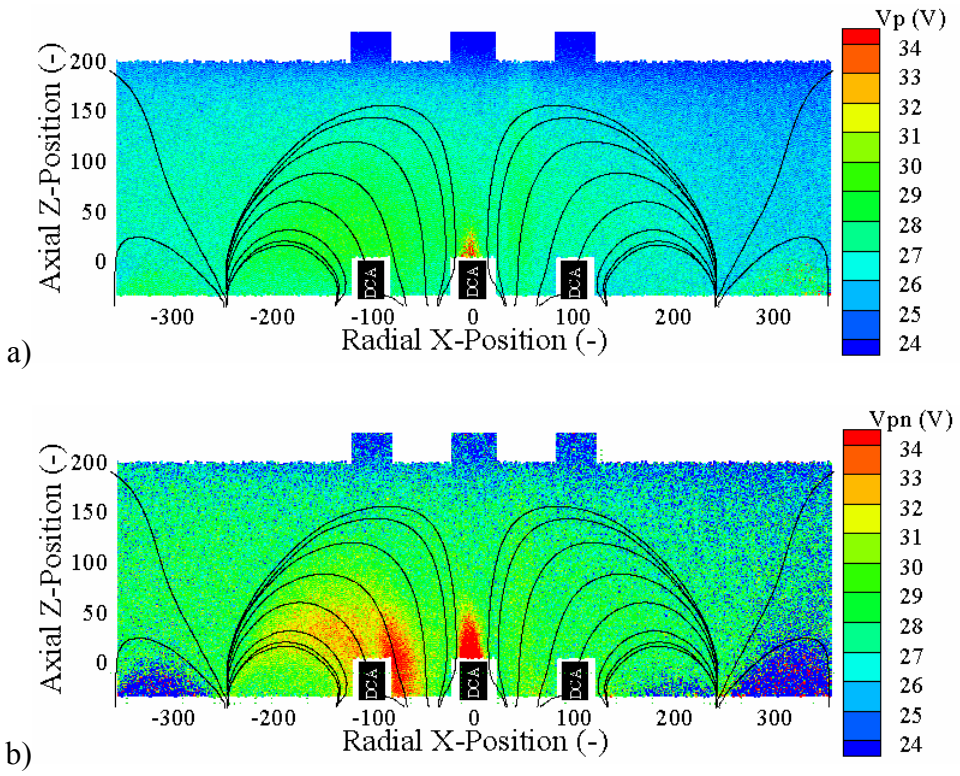

Figure 7-14: Comparison of the 0MI configuration plasma potential profiles obtained by a) finding the maximum of the derivative of the I-V curve and b) utilizing floating potential and electron temperature in Eqn. 7-1.

Results obtained by utilizing Eqn. 7-1 show both similar and different trends compared to the derivative approach. Specifically, both methods predict a larger plasma potential near the DCA with the plasma potential following the magnetic field lines. However, utilizing Eqn. 7-1 tends to predict larger bulk plasma potentials by ~1-2 V and the size of the near-DCA high-potential plume increases. No near-DCA potential-hill structure is evident with the Eqn. 7-1 method. Results in the intercusp regions are also inconsistent. Taking the derivative of the I-V curve predicts an increase in plasma potential in the intercusp region, while the opposite trend is obtained when using Eqn. 7-1. Physically, the results with the derivative method appear to be consistent with the fact that intercusp number density is reduced causing the plasma potential to increase.

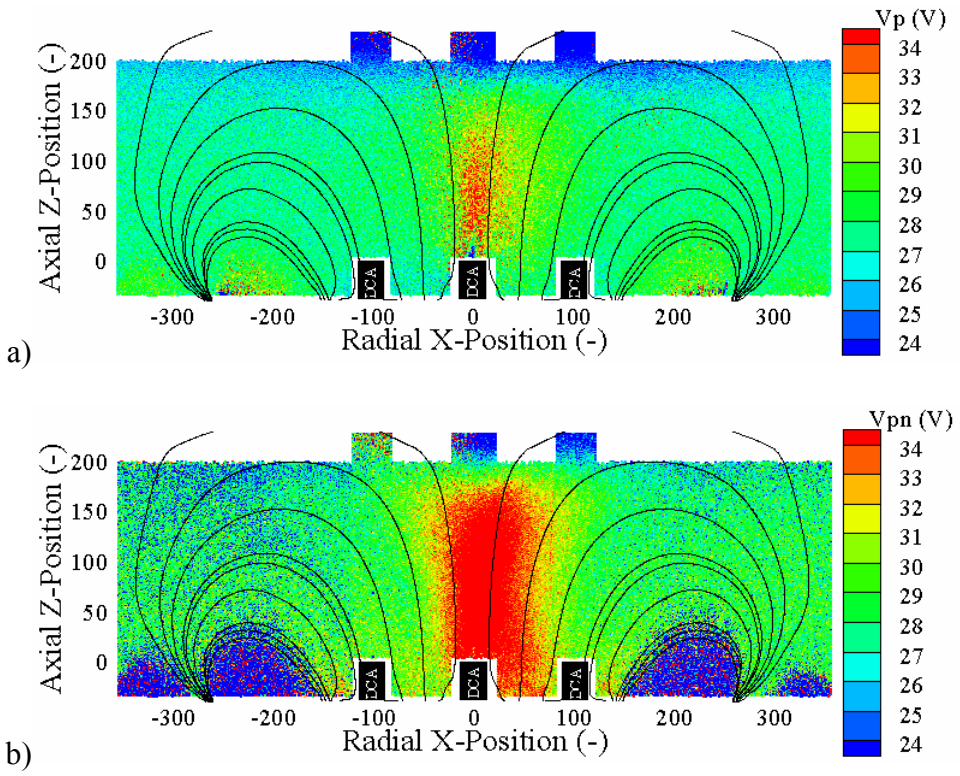

Figure 7-15: Comparison of the 10MI configuration plasma potential profiles obtained by a) finding the maximum of the derivative of the I-V curve and b) utilizing floating potential and electron temperature in Eqn. 7-1.

The discrepancy in results between the two methods, particularly near the DCA, cusp, and intercusp regions, is attributed to the presence of magnetic fields and error in the measurements. The magnetic field is stronger in these regions and therefore Eqn. 7-1 provides less accurate results. In the bulk discharge, where the magnetic field is negligible, the two methods are more closely matched. Error in the electron temperature calculation also contributes to the discrepancies between the methods. Based on this comparison the derivative of the I-V curve provides the most consistent and physically insightful results. The method utilizing Eqn. 7-1 only provides approximate magnitudes and trends, and should only be used if electron saturation of the I-V curve trace can not be achieved (i.e, the probe trace can not be extended past the plasma potential).

7.2.5 Plane 2 (Y = 11.1 cm)

Plane 2 is located 11.1 cm above plane 1 and does not contain the active DCA and dormant units. This plane is located along one of the backplate rectangular permanent magnet cusps. An example plot with important regions labeled is shown in Figure 7-16.

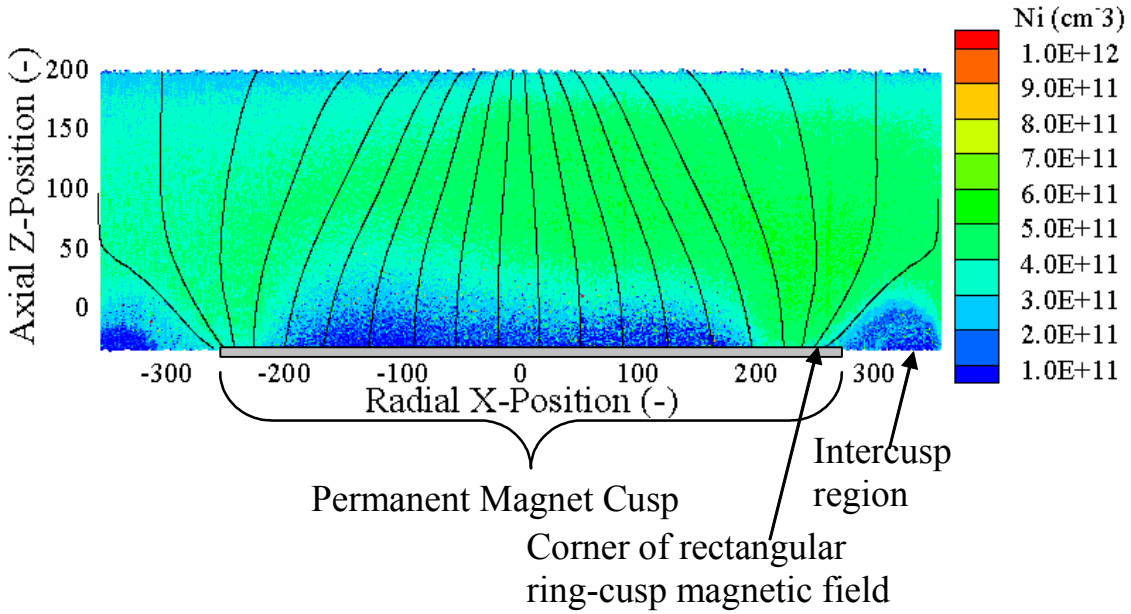

Figure 7-16: Example plane 2 figure showing regions of interest.

Note that the permanent magnet cusp extends from a radial position of -250 to +250. The intercusp region extends from approximately +250 to +375 and -250 to -375. Figures important for the discussion are presented below and profiles for all investigated configurations are shown in APPENDIX D.

Electron temperature at plane 2 shows evidence of the DCA plume for the middle active DCA configurations and those configurations with electromagnet current. Specifically, during middle DCA operation a higher-temperature spot is visible on the left side of the DCA. However, as the electromagnet current increases the higher-temperature region becomes larger and couples with the left and both sides of the TA during left and

middle DCA operation, respectively. This result is shown in Figure 7-17. Higher electron temperatures are always present in the corners of the rectangular ring-cusp TA, consistent with results presented for plane 1. For the +10 A electromagnet configurations, the largest electron temperatures are found at the grid-plane. This result is consistent with the results displayed for plane 1, which show the plasma becoming more collimated and pushed farther downstream for larger electromagnet currents.

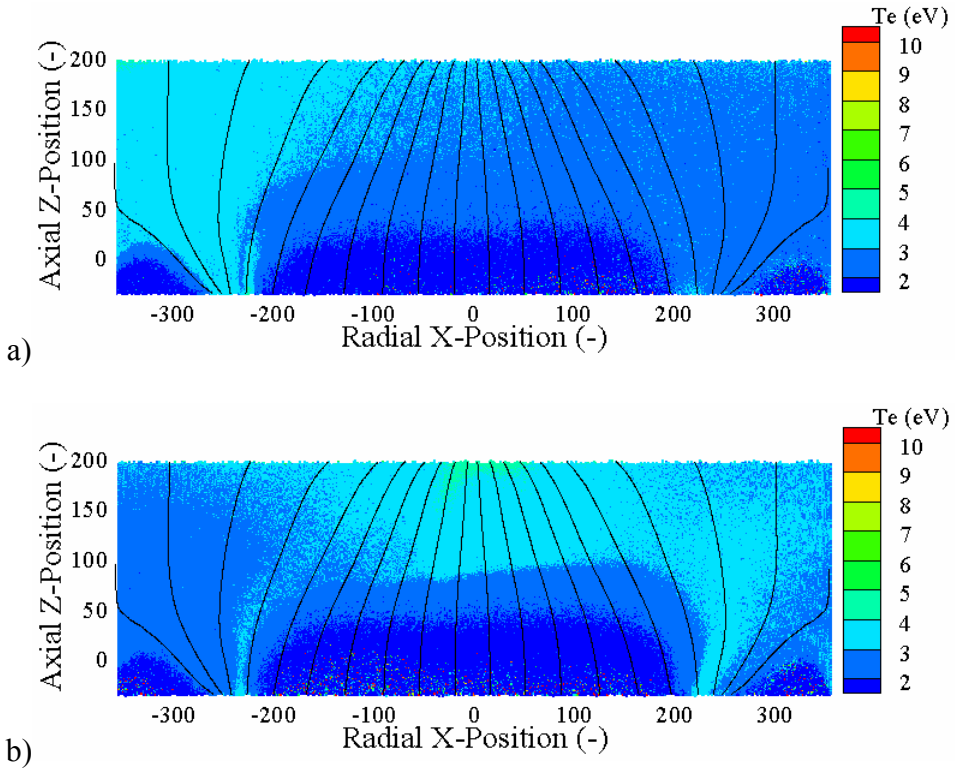

Figure 7-17: Plane 2 electron temperature for a) 5LIH and b) 5MIH configurations.

Plane 2 number density plots show typical values on the order of 5.0×10^{11} cm^{-3} and no evidence of the high-density DCA plume structure. For this reason the number density profiles appear much more uniform than results obtained at plane 1. As the electromagnet current increases, the axial magnetic field increases and the plasma is pushed downstream toward the collection grid. Also, as the electromagnet increases the

number density increases on the left side for left DCA operation and on the right side for middle DCA operation. Furthermore, the corners of the magnetic cusps continue to collect the bulk of the discharge current, a result consistent with the backplate button probe investigation (Chapter 5). These results are shown in Figure 7-18.

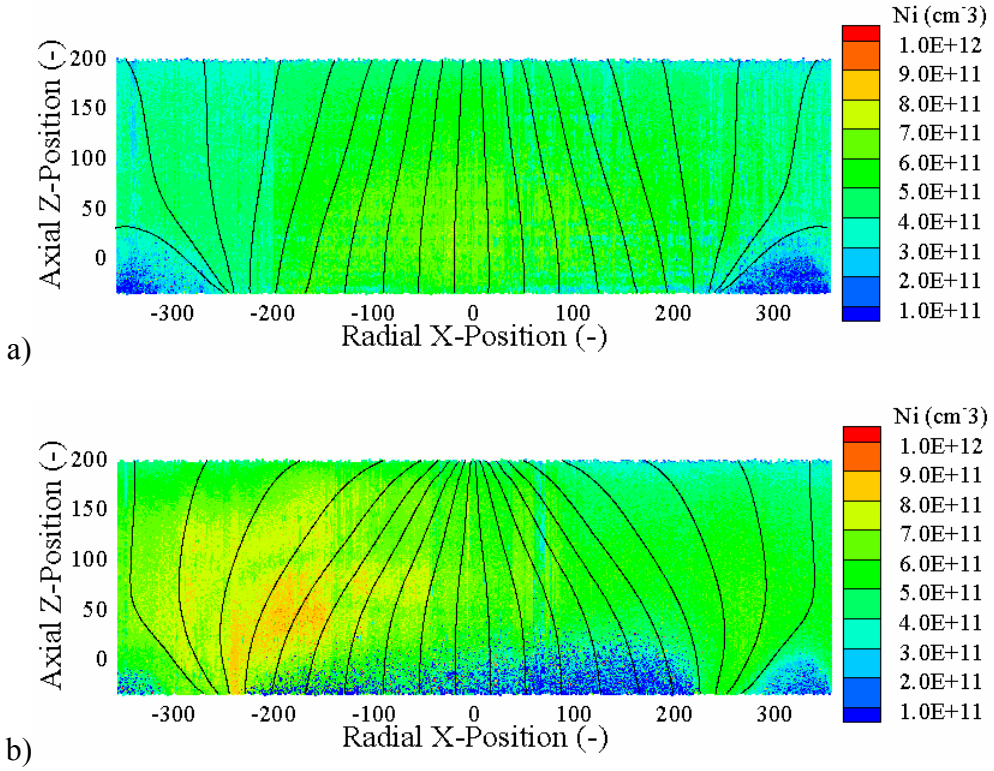

Figure 7-18: Plane 2 number density for the a) 0LI and b) 10LI configurations. As the electromagnet increases the plasma density increases and moves downstream.

Plane 2 floating potential results are consistent with the electron temperature measurements and the explanation given above for plane 1 results. More-energetic higher-temperature electrons cause the floating potential to decreases because the probe must be more negative to repel these electrons. Therefore the floating potential behaves similar to, and shows opposite trends as, the electron temperature. This result is shown in Figure 7-19.

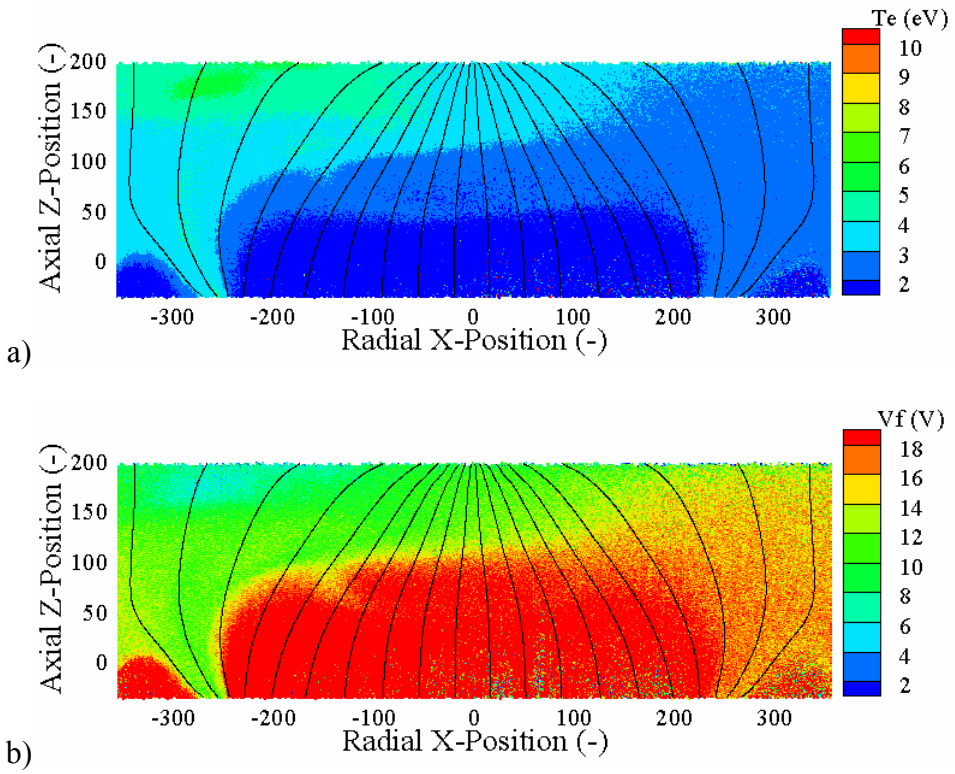

Figure 7-19: Comparison of a) electron temperature and b) floating potential profiles at for the 10LI configuration at plane 2.

Finally, plasma potential at plane 2 is quite uniform and is typically a few volts above the discharge voltage. Increasing the magnetic field with the electromagnet causes the plasma potential to increase ~3-4 V. The intercusp regions have slightly higher potentials than the cusps, consistent with the plane 1 results presented above. The corners of the rectangular cusps show slightly lower potential, which is consistent with the increased number density at those locations. These results are shown in Figure 7-20.

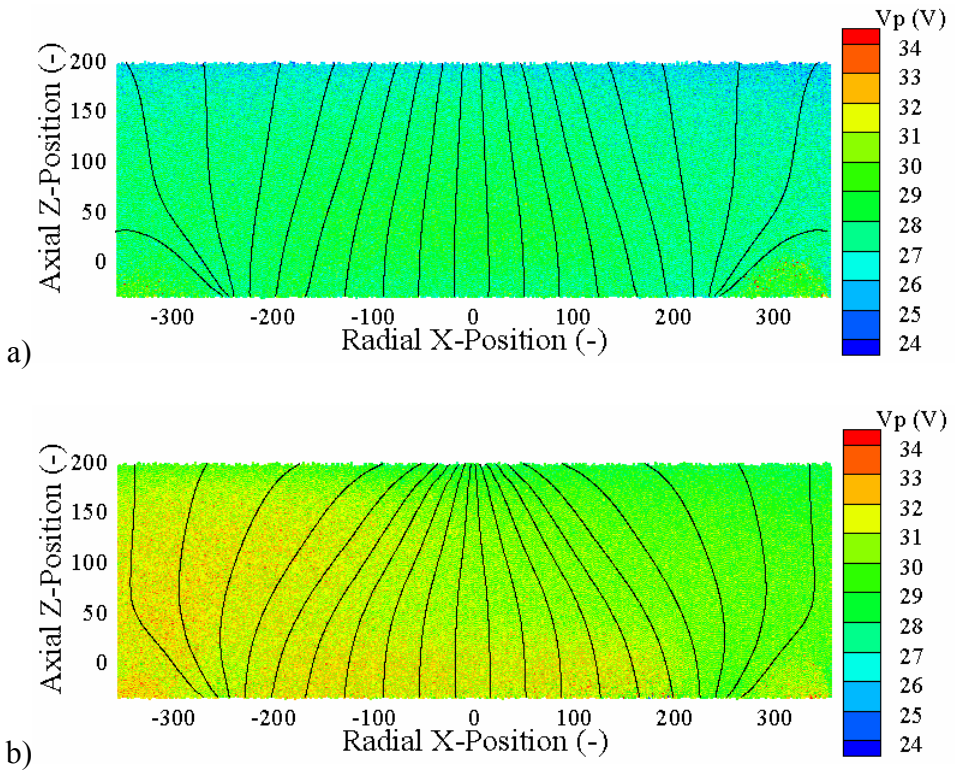

Figure 7-20: Effect of electromagnet on plasma potential for the a) 0LIF and b) 10LIF configurations at plane 2.

7.3 Time-Resolved Floating Potential

Previous researchers have suggested that one possible mechanism for DCA erosion is high-frequency plasma oscillations, which cause bombarding ions to momentarily significantly increase their energy. Jameson, *et al.,* have measured plasma potential fluctuations on the order of 12-45 V at frequencies between 100-500 kHz using a 1MHz sampling frequency.[153] In order to investigate this phenomenon in the TA, time-resolved floating potential measurements are obtained by connecting the mapping Langmuir probe directly to the Power DAQ (no probe circuit). HARP position and probe floating potential are monitored as the probe is inserted into the TA. A total of 90,000 points at 400 kHz are obtained for each of the two channels. This allows floating

potential fluctuations at high frequencies to be investigated. Results presented here utilize the difference between the maximum and minimum floating potential values. Typical results are shown in Figure 7-21.

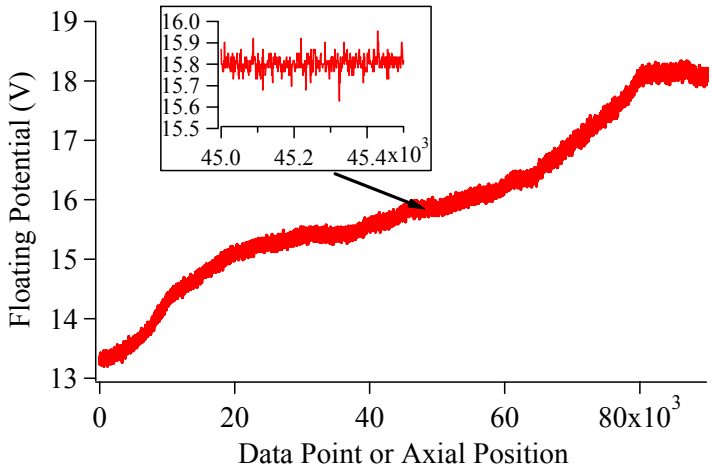

Figure 7-21: Floating potential as a function of axial position. Data acquired at 400 kHz per channel.

No noticeable high-frequency large-amplitude component is noticed in the signal. Specifically, the difference between the maximum and minimum voltage over a 1000 point range is typically only 0.4 V, suggesting these fluctuations are caused by noise in the signal and not TA plasma related phenomena.

The absence of a high-frequency large-fluctuation component in these data is not conclusive that this type of phenomenon is not present. The results presented by Jameson[153] were obtained with radial sweeps in front of the DCA keeper faceplate, whereas most of the results presented here are obtained in the bulk discharge, away from the DCA. For the few cases where the probe is located near the DCA a small increase in the magnitude of the fluctuations is observed, however, the fluctuations are still less than 0.6 V peak-to-peak. The probe electrode is never closer than 4 mm to the DCA keeper. A DAQ with a larger sampling frequency may be required. Also, floating potential is

presented in these results, whereas Jameson[153] measured plasma potential oscillations. Finally, the use of a high-frequency filter between the thruster and the discharge power supply may also be preventing these fluctuations from being measured.

7.4 Plasma Property Mapping Conclusions

Plasma property mapping of the TA is completed using a single-Langmuir probe mounted to the HARP. Axial HARP sweeps as the TA is moved in the radial direction allows two-dimensional plasma property profiles to be obtained. Data are acquired at two different horizontal planes. Plane 1 is at Y = 0 cm and contains the active and dormant cathodes, while plane 2 is above plane 1 (Y = 11.1 cm) and does not contain the cathodes. Time-resolved floating potential measurements are also obtained to analyze any high-frequency large-amplitude plasma oscillations.

Results indicate that the near-DCA plume contains higher-temperature electrons than the bulk discharge and electrons are confined to the magnetic field lines. Specifically, the magnetic cusps contain higher electron temperatures than the intercusp regions. As the electromagnet current increases (axial magnetic field increases), electrons are more confined to the center of the TA and the DCA plume elongates, increases temperature, and becomes more collimated.

Using the results for electron temperature, all other plasma properties can be explained. Number density is dependent on the electron temperature because more-energetic higher-temperature electrons ionize more neutral propellant. So regions of higher electron temperature also contain larger number densities. Specifically, the cusps and near-DCA region contain larger number densities. Regions with higher electron temperature have a lower floating potential because the probe must repel more-energetic

electrons. Finally, since quasi-neutral plasma is assumed, regions with larger number density have lower plasma potential because of the presence of more electrons.

Near-DCA plasma potential structures measured with the single-Langmuir probe show a low-potential region at the DCA orifice surrounded by a higher-potential region, characteristic of a potential-hill structure. Other researchers have also suggested the presence of a potential-hill downstream of an operational ion thruster DCA.[140,148-151] However, there is still much debate regarding this phenomenon due to the contradiction in reported results. Reported near-DCA plasma potential results may be dependent on the probe and data analysis techniques. Specifically, I-V characteristics near the DCA tend to have a rounded electron retarding-to-electron saturation region (knee) that makes determining the plasma potential difficult and less reliable than other probe methods. An emissive probe may provide better near-DCA plasma potential results than a single-Langmuir probe.

Jameson, *et al.*, have measured the presence of a large-amplitude high-frequency component in the plasma potential,[153] however, time-resolved floating potential results in the TA do not show this result. Measured oscillations have peak-to-peak values on the order of 0.4 V, which is only 3-5% of the signal and is attributed to signal noise. The inability to resolve any high-frequency large-amplitude oscillations may be due to the measurement of floating potential instead of plasma potential or the need for a faster sampling rate.

CHAPTER 8:
ION TRAJECTORY – EROSION PROFILE SIMULATION

The following sections describe an ion trajectory – erosion profile simulation that is applied to the multiple-cathode discharge chamber (MCDC) test article (TA) plasma potential results described in Chapter 7 and the Functional Model Thruster (FMT)-2 plasma potential results obtained by Herman.[79,117] The FMT-2 is a NASA Solar Technology and Applications Readiness (NSTAR)-derivative 30-cm-diameter ring-cusp xenon ion thruster and more detailed information regarding this thruster can be found in Ref. 79, 94, 95, 116-118, 149, 150, 161 and 162. The primary goals of the simulations are: 1) to determine how the NSTAR near-discharge cathode assembly (DCA) plasma potential structures (measured by Herman[79,117]) are contributing to the known DCA keeper erosion; and 2) to determine if the internal MCDC TA plasma potential structures cause DCA erosion and pre-operation erosion of the dormant cathodes.

8.1 Model Description

Previous researchers have developed models to numerically investigate the transport of charged and neutral particles in different types of plasma and plasma processing systems, including tokomaks and ionized vapor deposition systems.[163,164] In many models the path of incident projectiles is followed until a collision with the amorphous or polycrystalline target occurs. The original projectile and all of the target atoms it knocks are then followed by the model. If the initial projectile or any of the

impacted atoms gain energy beyond the surface binding energy of the material, they are considered removed from the target.[165] Because real surfaces of target materials are not flat or smoothly varying, they are approximated as fractals.[166] The model described and utilized in this analysis is a simplified form of this basic algorithm, but does not consider the interaction of the projectile and target atoms on a molecular scale. Instead, experimentally measured target material sputter yields for known bombarding ion energy and incidence angle are utilized.

Ion trajectory – erosion profile simulations are completed to determine how the discharge chamber internal plasma potential structures are contributing to the known DCA erosion and if the MCDC TA potential structures cause dormant cathode erosion. Specifically, the trajectories of ions are computed utilizing simple force equations and experimental plasma potential maps. The following sections describe the two main components of the simulation: 1) calculation of the ion trajectory to determine if an ion impacts the DCA or dormant cathode keepers and, if so, determine the ion impact velocity components and location on the keeper downstream face; and 2) an erosion calculation (i.e., how many atoms are sputtered per incident ion) using the calculated impact angle and known bombarding ion energy. Combining these two steps allows the trajectories of ions within the discharge chamber to be calculated and a simulated keeper erosion profile to be determined.

8.1.1 Ion Trajectory Simulation

An ion trajectory calculation compiled using MatLab is utilized to determine the path of ions within the discharge chamber and the angle and location of those ions that impact the DCA or dormant cathode keeper downstream face. The trajectory simulation

procedure is similar to that used by Beal[111] and is divided into five main steps: 1) load the plasma potential maps (either those provided by Herman for the FMT-2 or the MCDC TA maps shown in Chapter 7); 2) calculate the electric field produced by the variation of plasma potential with spatial location; 3) determine initial conditions for a simulation ion; 4) iteratively calculate the ion trajectory based on the initial conditions; and 5) determine if the ion impacts the keeper and, if so, determine the impact location and velocity components.

Initially, the plasma potential structures are loaded. The investigated FMT-2 plasma potential structures are shown in sections 8.2 below. MCDC TA plane 1 plasma potential data are utilized and shown in Chapter 7 and APPENDIX D. The 2-D area over which data are plotted is initially reduced to create a rectangular region shown in Figure 8-1 and Figure 8-2 for the FMT-2 and the MCDC TA, respectively.

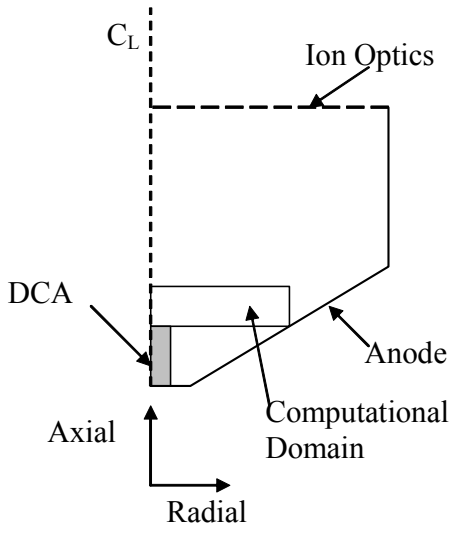

Figure 8-1: Schematic of the NSTAR-derivative FMT-2 showing the computational domain over which the ion trajectories are computed. Not to scale.

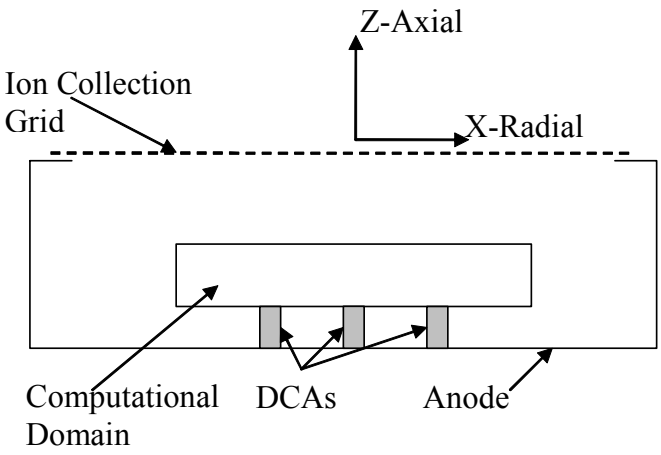

Figure 8-2: Schematic of the MCDC TA showing the computational domain over which the ion trajectories are computed. Not to scale.

This domain size is chosen because plasma potential data for the FMT-2 are only available in this region and computationally the analysis is simplified and more time efficient for a smaller rectangular domain. Next, the data are interpolated onto a 1 mm by 1 mm grid. Because a certain amount of noise is present in the raw plasma potential data, the built-in MatLab cubic smoothing spline algorithm is used to smooth the data. An example of the raw and smoothed data for the FMT-2 and the MCDC TA is shown in Figure 8-3 and Figure 8-4, respectively. Next, the electric field is calculated within the computational domain. The electric field at a given point is determined using the plasma potentials at the six adjacent points and Eqn. 8-1,[167] where V_p is plasma potential, $\vec{E}$ is electric field, and $\vec{x}$ is the relative position between grid points.

$$\vec{E} = -\frac{dV_p}{d\vec{x}} \qquad \textbf{Eqn. 8-1}$$

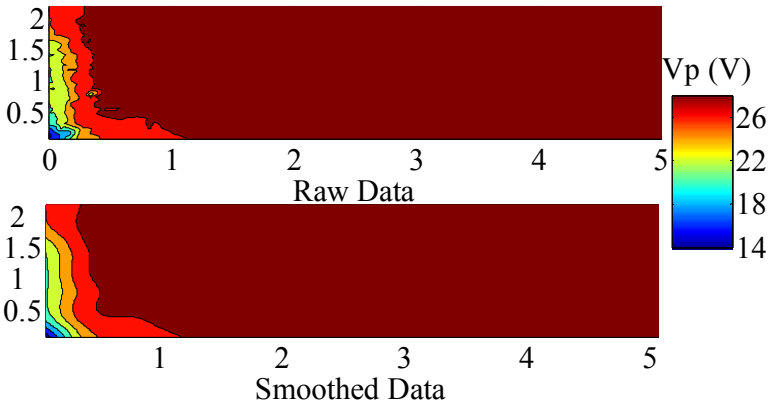

Figure 8-3: Comparison of raw and smoothed data for the TH15 FMT-2 operating condition. Spatial locations are non-dimensionalized by the discharge cathode keeper diameter.

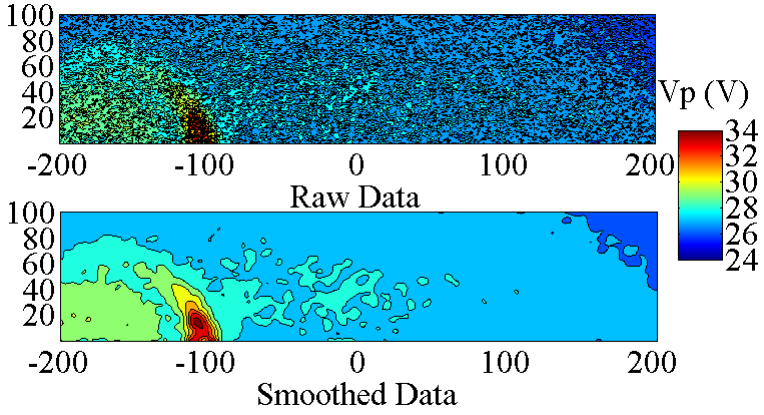

Figure 8-4: Comparison of raw and smoothed data for the MCDC TA 0LI configuration. Spatial locations are non-dimensionalized by the discharge cathode orifice radius.

Table 8-1 shows the ion initial conditions investigated. A single FMT-2 simulation has 35,200 ions with 4,400 initial positions (an ion starts from each of the computational domain grid points) and 8 initial angular orientations. TA simulations have 10,100 ions with 2,525 initial positions and 4 angular orientations. Fewer positions and orientations are used for the TA because its larger domain size requires more iteration and is therefore more time consuming. Angular orientations of 0 degrees and 90 degrees

correspond to an initial velocity in the positive radial and positive axial directions, respectively. Simulations are completed for both warm and cold ions, as well as singly- and doubly-charged ions. The doubles-to-singles current ratio in the NSTAR thruster is a function of the operating condition and is expected to be within 20-25%.[168] For this analysis, the ratio is assumed to be a constant equal to 20% for both the FMT-2 and the TA. Therefore the number of singly- and doubly-charged ions is equal to 83% and 8.5% of the total number density, respectively. These values do not sum to 100% because the doubly-charged ions account for two times the ion current as the singly-charged ions. Warm and cold ions are assumed to have energies of 5 eV and 0.05 eV, respectively.[9] A warm temperature of 5 eV is chosen to straddle the various ion energy measurements.[148,161,169,170] Also, ions are assumed to translate in only the axial and radial directions; i.e., along the TA X-axis and Z-axis. This assumption is valid for the axisymmetric FMT-2 thruster, but may not strictly apply for the TA because ions are also expected to move in the Y-direction. In order to fully simulate the TA, three-dimensional plasma potential profiles are required.

	FMT-2 Simulations	MCDC TA Simulations
Locations	4400 points (Δx = 1.0 mm)	2525 points (Δx = 3.0 mm)
Charge-state	Singly, Doubly	Singly, Doubly
Initial Energy (eV) (velocity)	Warm (5 eV) Cold (0.05 eV)	Warm (5 eV) Cold (0.05 eV)
Angular Orientation (deg.)	0, 45, 90, 135, 180, 225, 270, 315	0, 90, 180, 270

Table 8-1: Ion trajectory – erosion profile simulation ion initial conditions.

Utilizing the provided initial conditions, the ion trajectory is calculated by iterating through the familiar Lorentz force equation, Eqn. 8-2.

$$\vec{F} = q(\vec{E} + \vec{v} \times \vec{B}) \qquad \textbf{Eqn. 8-2}$$

In this equation, $\vec{F}$ is the force on the ion, $\vec{E}$ is the electric field, $\vec{v}$ is the ion velocity, q is the ion charge, and $\vec{B}$ is the magnetic field. A collisionless analysis is appropriate because the Knudsen number (Eqn. 4-1), which relates the charged particle mean free path to the dimensions of the discharge chamber, is much greater than 1. For the simulations presented here, the magnetic field inside the ion thruster is assumed to have a negligible impact on ion motion. This assumption is justified because the ion cyclotron radius is an order of magnitude larger than the discharge chamber dimensions. Therefore the Lorentz equation can be reduced and divided into axial and radial components as shown in Eqn. 8-3, where Newton's relation for force and acceleration has also been used.[167]

$$\left(\frac{dv}{dt}\right)_a = \frac{qE_a}{M_i}$$
$$\left(\frac{dv}{dt}\right)_r = \frac{qE_r}{M_i} \qquad \textbf{Eqn. 8-3}$$

In these equations, v_a and v_r are the ion velocity in the axial and radial directions, respectively, t is time, E_a and E_r are the axial and radial electric field, respectively, and M_i is the ion mass. Lastly, Eqn. 8-4 is utilized as the relation between spatial location and velocity, where x_a and x_r are the axial and radial position, respectively.[167]

$$v_a = \left(\frac{dx}{dt}\right)_a$$
$$v_r = \left(\frac{dx}{dt}\right)_r \qquad \textbf{Eqn. 8-4}$$

Utilizing the equations described above, the trajectory calculation iterative procedure loop is as follows: 1) interpolate the electric field at the ion position (Because the ion position is rarely directly on one of the grid points, the electric field values are

linearly interpolated from the 4 nearest grid points. A more accurate method of calculating the electric field accounts for the variation of volume with distance from the centerline axis,[171] but is not utilized in this study.); 2) calculate the new velocity components using Eqn. 8-3; 3) determine the new spatial location by assuming the new velocity components are constant over the time step; and 4) repeat. This procedure loop is iterated until the ion exits the computational domain (Figure 8-1 and Figure 8-2). If the ion exit position is at the DCA or dormant cathode keepers, then the ion location is recorded. The outputs of the trajectory simulator are the initial location, initial velocity components, pre-sheath velocity components, and pre-sheath location of ions striking a keeper.

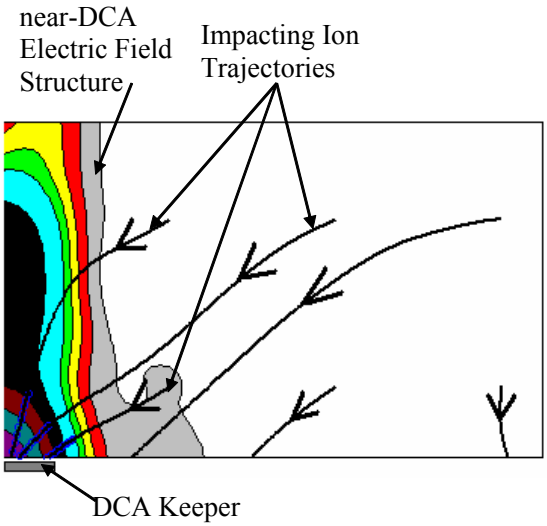

Figure 8-5: Example ion trajectories through the calculated FMT-2 electric field profile within the computational domain.

Initial simulations are completed to determine the required time step that provides accurate and timely results. Simulations are completed for values greater than or equal to $1x10^{-9}$ s. Comparison of the output results show that time steps of $1x10^{-7}$ s and smaller yield identical trajectories. Therefore a time step of $1x10^{-7}$ s is used for all simulations

reported here. Examples of ion trajectories through the calculated electric field profile for the FMT-2 are shown in Figure 8-5. Note that three of the six ions impact the DCA keeper.

8.1.2 Erosion Calculation

The results of the trajectory simulations provide the pre-sheath velocity components and pre-sheath impact location of ions striking the DCA or dormant cathode keepers. However, ions first pass through the keeper sheath before impacting, so the through-sheath impact location, angle, and energy must be determined. An ion is assumed to only translate axially through the sheath, so the through-sheath impact location is equivalent to the pre-sheath location. This assumption is justified by the small thickness of the sheath and small radial electric fields expected within the sheath. Pre-sheath radial velocity is assumed constant through the sheath and the axial velocity component is assumed to increase corresponding with the gain in energy through the keeper sheath potential drop. The angle of the sum of these two velocity components is the through-sheath impact angle. A schematic of this procedure is shown in Figure 8-6.

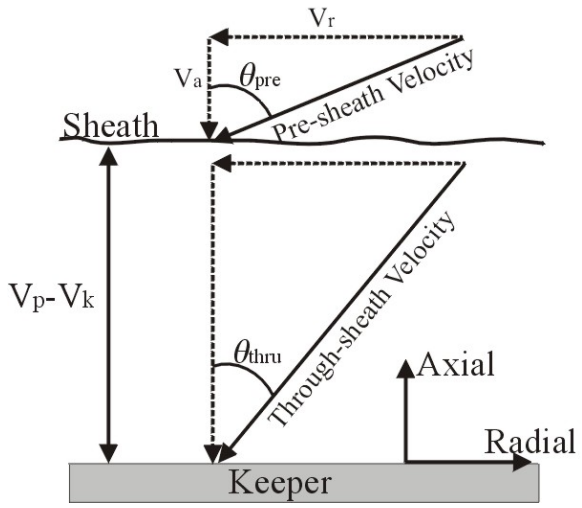

Figure 8-6: Schematic of the through-sheath velocity calculation.

The near-DCA plasma potential (~14 V) and floating keeper potential (~5 V) are used to determine the DCA keeper sheath potential drop of ~9 V. The near dormant cathode plasma potential is assumed to be ~27 V and a keeper floating potential of ~7 V yields the dormant cathode keeper sheath potential drop of ~20 V. Bombarding ion energy is calculated as the ion kinetic energy using the through-sheath velocity components.

The keeper erosion profile is predicted utilizing the through-sheath impact angle, location, and velocity components. Calculation of an erosion profile requires either an accurate sputtering yield model or, in this case, experimental sputtering yield data. Sputtering yield, Y, is a statistical variable defined as the mean number of atoms removed from a solid target per incident particle. In this application, the sputtering yield indicates the mean number of molybdenum (Mo) atoms removed from the keeper face per incident xenon ion.

Doerner, *et al.*, measured Mo sputtering yields during xenon ion bombardment in the energy range of 10 to 200 eV utilizing the standard weight loss and spectroscopic techniques.[172,173] These results compare nicely to each other and to existing low-energy Xe^{+}-Mo data taken by other researchers.[173] These experimental data are the low-energy normal-incidence sputtering yields that are utilized as the basis for the erosion calculations. The Doerner data are log-log plotted and a sixth order polynomial fit to the resulting graph provides an empirical relation for sputtering yield (Y) and normal-incident bombarding ion energy (E_i), Eqn. 8-5.

$$Y_{Doerner}(E_i) = \exp\{-0.372304[\ln(E_i)]^6 + 9.48041[\ln(E_i)]^5 - 100.046[\ln(E_i)]^4 + 560.276[\ln(E_i)]^3 - 1758.24[\ln(E_i)]^2 + 2940.48[\ln(E_i)] - 2064.3\} \quad \textbf{Eqn. 8-5}$$

$$\left(\frac{Y(\theta)}{Y(0)}\right) = \cos^{-19.96}(\theta)\cdot\exp[-13.55(\cos^{-1}(\theta)-1)] \quad \textbf{Eqn. 8-6}$$

Numerous sputtering yield investigations have demonstrated that sputtering yield has a definite angular dependence.[165,174-182] An empirical formula for the angular dependence of the sputtering is given by Yamamura, *et al.*, as Eqn. 8-6.[177,183] The numeric factors are energy-dependent fit parameters determined from 100 eV xenon ions impacting a Mo target and Y(0) is the sputtering yield at normal incidence; i.e., Eqn. 8-5.[183] Previous use of this erosion analysis algorithm has been applied with success by Herman.[79,97]

8.2 FMT-2 Simulation Results

The NSTAR-derivative FMT-2 near-DCA plasma potential profiles measured by Herman[79,117] are utilized in the simulation routine. Specifically, the TH15 and TH8 operating condition plasma potential profiles are utilized. Nominal operating conditions for the NSTAR thruster are shown in Table 8-2.

Operating Point	Input Power[a] (kW)	Beam Current[b] (A)	Beam Voltage[b] (V)	Accelerator Voltage (V)	Main Flow (mg/s)	Discharge Cathode Flow (mg/s)
TH0[c]	0.5	0.51	650	-150	0.58	0.24
TH4[c]	1.0	0.71	1100	-150	0.81	0.24
TH8[c]	1.4	1.10	1100	-180	1.40	0.24
TH10[c]	1.7	1.30	1100	-180	1.67	0.25
TH12[c]	1.8	1.49	1100	-180	1.79	0.26
TH15[c]	2.3	1.76	1100	-180	2.27	0.36

[a]Nominal values. [b]Power supply current or voltage. [c]Nominal NSTAR operating condition.

Table 8-2: Selected NSTAR ion thruster nominal operating parameters.

The TH8 and TH15 conditions are of primary interest due to the NSTAR extended life test (ELT) results, which showed a change in the DCA keeper erosion when the thruster operating point was changed from TH15 to TH8. Specifically, the 1,000-h and 8,200-h

wear tests showed erosion of the DCA keeper occurring primarily from the downstream keeper face at approximately the 50% keeper radius, as shown in Figure 8-7.[67]

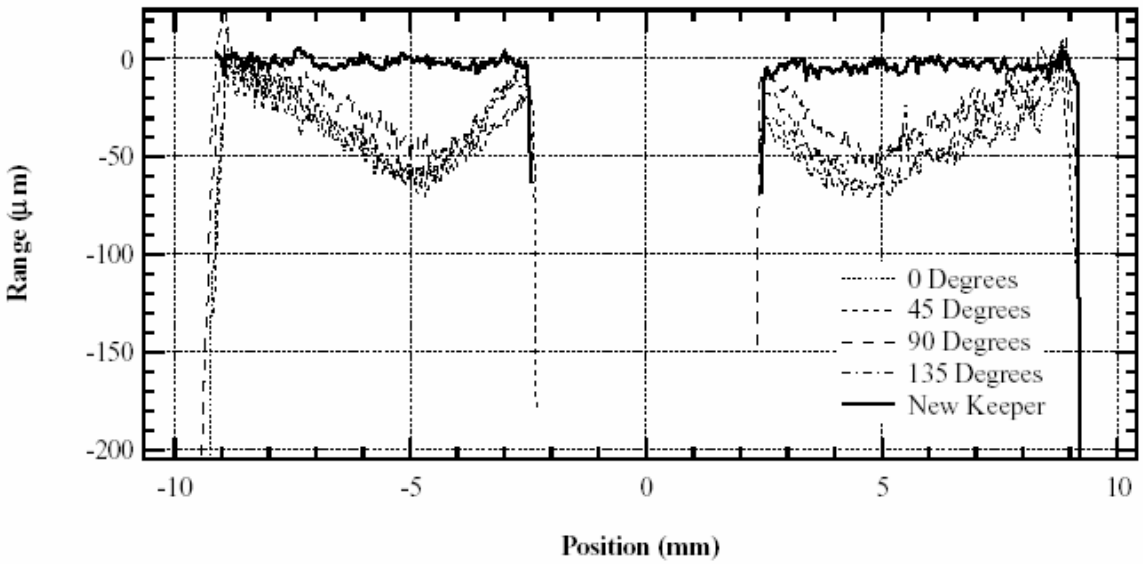

Figure 8-7: Measured profiles of NSTAR DCA keeper downstream face for the 1,000-h wear test, conducted primarily at TH15. Note that the maximum erosion occurs at ~50% keeper radius.[67]

However, during the ELT, the primary erosion location changed from the keeper downstream face to the keeper orifice. An experimental investigation by Kolasinski found evidence that the erosion location shifted when the thruster was operated at a reduced beam current condition; i.e., when the thruster was adjusted from the nominal high-power TH15 condition to the lower-power TH8 operating point.[139,184]

The plasma potential structures for TH15 and TH8 utilized in the simulations are shown in Figure 8-8. The DCA keeper orifice is located at (0,0) and the DCA plume extends in the axial direction. More information regarding the structures can be found in Ref. 79 and 117.

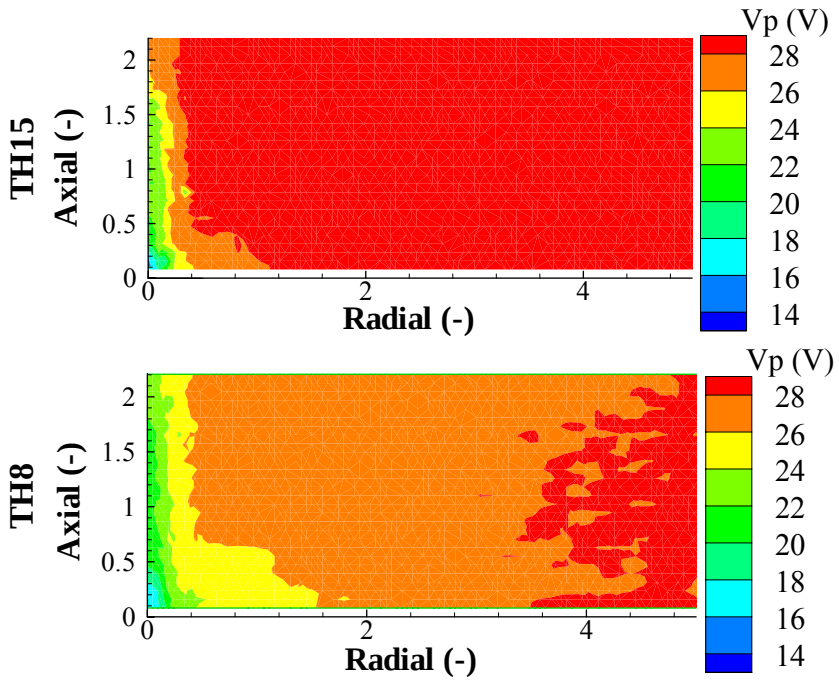

Figure 8-8: Experimentally measured plasma potential profiles in the near-DCA region of the FMT-2 NSTAR-derivative ion thruster for TH15 and TH8. Spatial locations are non-dimensionalized with respect to discharge cathode keeper outer diameter.

Figure 8-9 shows simulated erosion profiles for the TH15 and TH8 NSTAR thruster operating conditions. Uniform ion number density is assumed, but Herman has shown that number density varies in the near-DCA region.[79,118] Doubly-charged ions tend to increase the magnitude of the profile, but have no affect on the shape. The warm ion assumption predicts less erosion of the keeper than the cold profile because higher-energy warm ions are capable of escaping from the near-DCA low plasma potential region, while less-energetic cold ions are more easily pulled into the keeper by the potential field. Because the discharge chamber plasma contains a distribution of ions, the true erosion profile is assumed to be some combination of the warm and cold ion results.

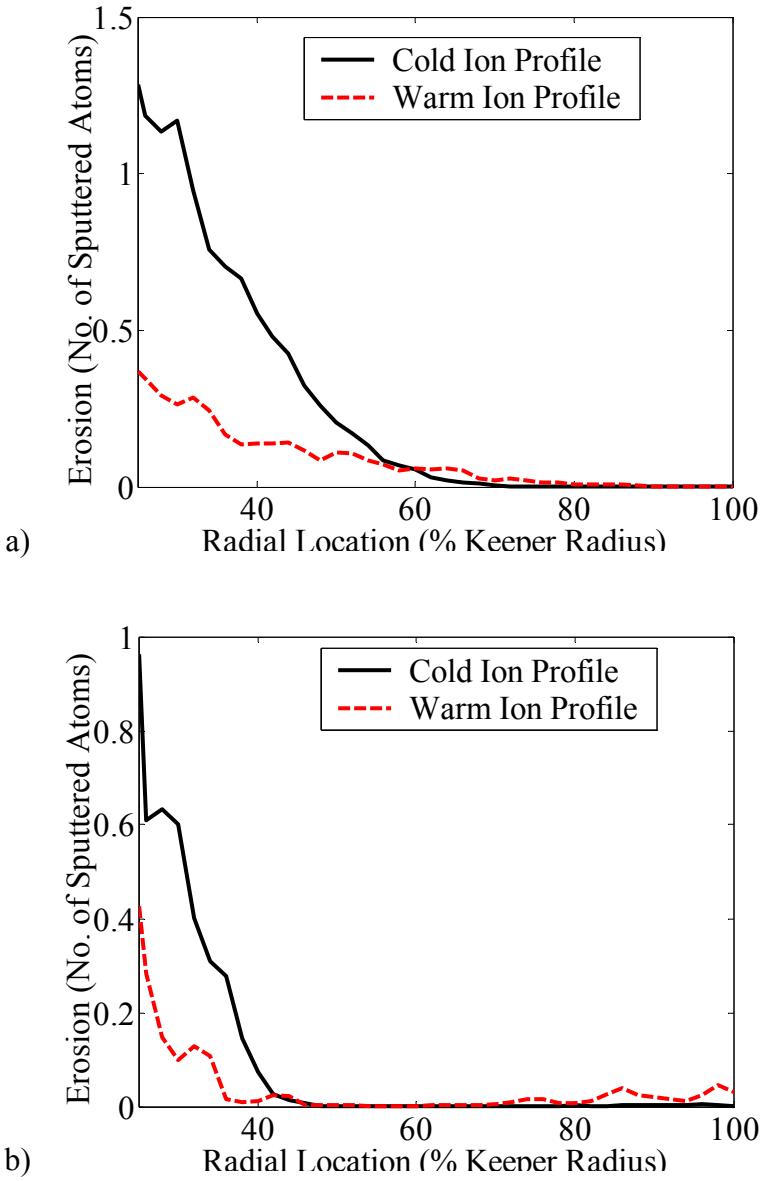

Figure 8-9: Simulated erosion profiles for the warm and cold ion assumptions for a) TH15 and b) TH8 NSTAR FMT-2 plasma potential maps.

The "bump" in the erosion profiles at approximately 30% keeper radius is attributed to the computational domain grid size. Using a slightly smaller or larger grid causes the erosion profile to become noisier or smoother, respectively, but the general shape and trend are not affected. Both the TH15 and TH8 results predict an erosion profile with maximum erosion occurring at the keeper orifice that leads to chamfering of

the orifice. The increase in erosion at the keeper orifice (~25% keeper radius) causes the orifice diameter to increase until the entire keeper faceplate is eroded. This analysis suggests that the plasma potential structure, produced by the double-layer coupling the DCA and bulk plasma,[79] causes the primary erosion location to be at the DCA keeper orifice. Results from the 1,000-h and 8,200-h wear-tests show the dominant erosion location to be at approximately the 50% keeper radius location (Figure 8-7), not the keeper orifice. Therefore the plasma potential structure alone can not be causing the known erosion results.

8.3 DCA Erosion Theory

A DCA erosion theory is developed that combines the ion trajectory – erosion profile simulations (Section 8.2) and the 5 planar Langmuir probe with propellant flow (5PLPF) diagnostic cylinder (DC) results (Section 6.2.6). The following sections use the results previously presented to qualitatively predict erosion profiles for the TH15 and TH8 NSTAR operating conditions (Table 8-2), as well as explain the change in the maximum erosion location between operating points. The theory is then used to explain the ELT erosion results.

One of the key assumptions is that the propellant flow rate results obtained with the 5PLPF-DCs are applicable to the active DCA. The 5PLPF-DCs are not electron emitting devices and are therefore not producing the familiar near-DCA plasma potential structures. The active DCA keeper may have a different ion number density distribution. However, the goal of this analysis is to develop physical insight into possible erosion producing and erosion mitigating mechanisms using known results. Further investigation and validation of this theory requires determining the effects of propellant flow rate on

the active DCA keeper ion number density. Therefore the theory presented is purely qualitative, but based on quantitative results from the ion trajectory – erosion profile simulations and the 5PLPF-DCs.

The DCA erosion theory couples the near-DCA plasma potential structures with charge-exchange (CEX) collisions to explain the known keeper wear test results and erosion profiles. This theory is illustrated in Figure 8-10.

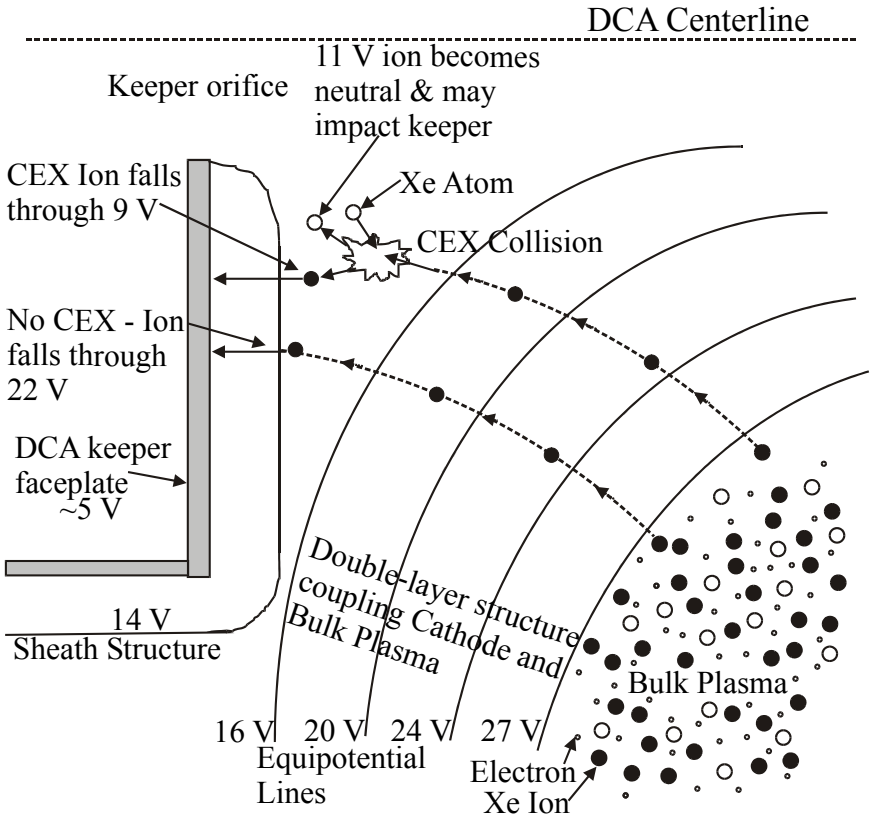

Figure 8-10: Schematic illustrating the DCA erosion theory processes. The double-layer structure coupling the bulk and cathode plasmas pulls and focuses ions toward the DCA. CEX collisions decrease the bombarding energy of ions.

The double-layer plasma potential structure coupling the bulk and cathode plasmas focuses and pulls ions into the DCA. Some bombarding ions suffer CEX collisions with the neutral xenon atoms being expelled from the DCA, the product of which is a "slow"

CEX-ion and "fast" neutral. The CEX-ion is easily pulled into the DCA keeper. However, CEX-ions are created at a lower potential than ions originating in the bulk plasma and therefore have lower bombarding energy (~9 V, Note that voltages in parenthesis are based on Figure 8-10 above and are only meant to assist with the explanation. CEX collisions may occur at higher or lower potential locations, in which case the referenced voltages would change). The neutral xenon atom resulting from the CEX collision may also impact the keeper and cause erosion. However, neutral xenon is not accelerated through the plasma potential structure and therefore impacts the keeper with the pre-CEX ion energy (~11 V). Therefore the presence of CEX collisions decreases keeper erosion because a single high-energy bombarding ion from the bulk plasma (~22 V) is substituted with two lower-energy particles, a CEX-ion (~9 V) and a neutral atom (~11 V). Each of the two resulting particles has lower energy than the initial ion and therefore causes less erosion. In fact, the energy of each of the post-CEX particles may be lower than the threshold energy of the target material, in which case no sputtering erosion occurs.

For this theory to be applicable, the CEX mean free path (MFP) at the DCA keeper orifice must be small and on the order of the orifice diameter (mm). Assuming the neutral temperature at the DCA keeper orifice is 1000 K[136] and the velocity is equal to the sound speed, the keeper orifice neutral pressure is calculated using Eqn. 6-7 to be 111.8 mTorr and 167.3 mTorr for the TH8 and TH15 operating conditions, respectively. Furthermore, if the bombarding ions are assumed to have energy equal to the plasma potential (~27 V), σ_{ce} is equal to 45 Å^2 [143,145] and the CEX MFP (Eqn. 6-4) is 1.5 mm and 1.0 mm for the TH8 and TH15 operating conditions, respectively. These results are

summarized in Table 8-3 and suggest that CEX collisions at the DCA keeper orifice are occurring, with a smaller CEX MFP during operation at the TH15 condition.

Operating Condition	TH8	TH15
$\dot{m}$ (mg/s)	0.24	0.36
p (Pa)	14.9	22.3
p (mTorr)	111.8	167.3
n_n (m^{-3})	$1.1x10^{21}$	$1.6x10^{21}$
λ_{CEX} (mm)	1.5	1.0

Table 8-3: NSTAR DCA keeper orifice neutral pressure, number density, and CEX MFP calculation results.

The keeper orifice neutral density and CEX MFP for both TH8 and TH15 are similar to 5PLPF-DC values of $1.0x10^{21}$ m^{-3} and 1.6 mm, respectively (Section 6.2.6). The following sections apply the DCA erosion theory to the TH15 and TH8 operating conditions to develop qualitative erosion profiles that explain the ELT results.

8.3.1 TH-15

The NSTAR operating condition TH15 is the high-power higher-flow rate condition (Table 8-2). Figure 8-11 shows the predicted erosion profile for TH15 and Figure 8-7 shows the measured erosion profile of the DCA keeper downstream face after the 1,000-h wear test, which operated primarily at TH15.[67] Propellant flow rate results with the 5PLPF-DCs suggest that near the DCA keeper orifice, bombarding ion number density is reduced due to CEX collisions. Therefore the erosion at the keeper orifice predicted by the ion trajectory – erosion profile simulation is reduced. As radial distance from the orifice increases, the neutral density and corresponding number of CEX collisions decreases, leading to an increase in erosion. At approximately the 50% keeper radius, the 5PLPF-DC results suggest that the effects of propellant flow rate are no longer

present. Therefore the 50% keeper radius corresponds with the maximum erosion point. Note that in the 1,000-h wear test results (Figure 8-7) the maximum erosion occurs at approximately the 50% keeper radius.[67] At larger radial locations the erosion profile corresponds with the ion trajectory simulation results because propellant flow rate effects are no longer present.

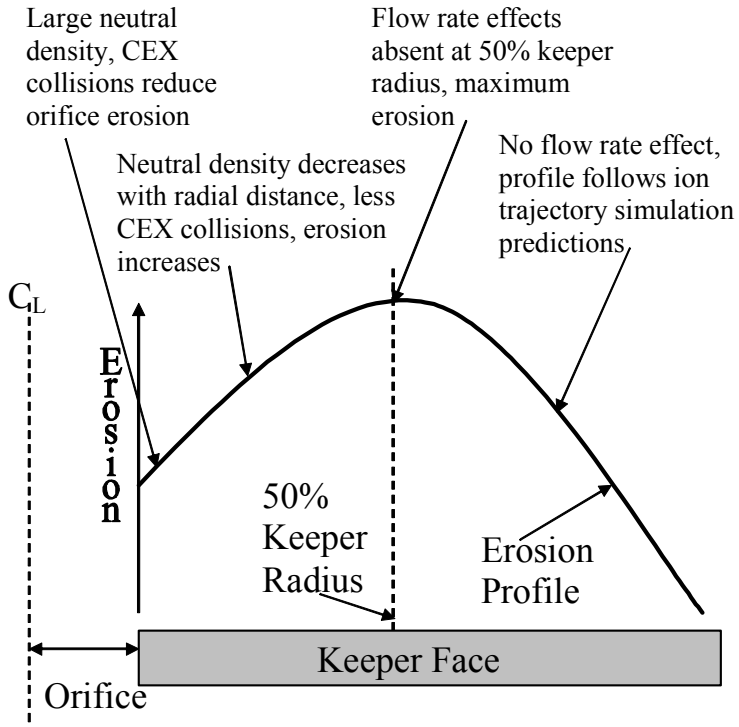

Figure 8-11: Qualitative erosion profile prediction for TH15.

8.3.2 TH-8

The TH8 NSTAR operating point is lower-power and lower-flow rate than the TH15 point (Table 8-2). The reduction in DCA flow rate reduces the keeper orifice neutral density and therefore the ability of the DCA to protect itself from bombarding ions through CEX collisions. The TH8 erosion profile is therefore identical to the ion trajectory simulation predicted profiles (Figure 8-9) because flow rate effects and CEX

collisions are either not present or significantly reduced. This result is shown in Figure 8-12.

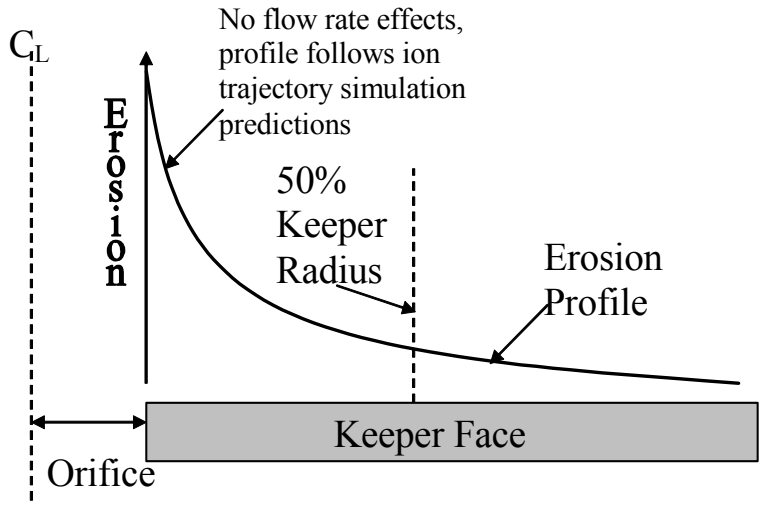

Figure 8-12: Qualitative erosion profile prediction for TH8.

8.3.3 ELT Results Explanation

During the ELT, the NSTAR flight spare engine was operated at various power levels and operating points.[7,8,71] Erosion of the DCA keeper orifice began during TH8 after ~6,400-h of operation. The sudden and significant increase in keeper orifice erosion also corresponded with a short between the cathode and the keeper.[8] Herman has shown that the potential structure of the near-DCA plasma does not change when the cathode is shorted to the keeper.[79,117] However, bombarding ions gain more energy through the keeper sheath (the keeper-to-cathode floating potential, 5-7 V) when the cathode is shorted to the keeper, which increases the sputter yield and the erosion rate. The following section uses the DCA erosion theory to explain the ELT results.

At the onset of the ELT, the thruster is operated at TH12 and then TH15, where it suffers erosion at the 50% keeper radius point on the keeper downstream face (TH15

erosion profile, Figure 8-11). At ~4,500-h into the test, the thruster is adjusted to the lower-power lower-flow rate TH8 operating point. The erosion profile then shifts due to the change in DCA flow rate and the erosion now occurs at the keeper orifice, leading to a chamfering profile (Figure 8-12). The cathode-to-keeper short at ~6,400-h only increases the erosion rate, the erosion profile is not affected. At ~10,500 hours the thruster is returned to TH15, but the keeper orifice has been eroded to two times its initial diameter. Although the DCA flow rate is increased upon returning to TH15, the keeper orifice is larger so the neutral number density does not return to the pre-TH8 value. Because of the enlarged orifice and corresponding reduced neutral density, the orifice cannot protect itself with CEX collisions and the erosion continues with the TH8 profile even though the thruster is operating at TH15. This erosion profile remains the same throughout the remainder of the ELT, eventually eroding away the entire keeper faceplate.

8.4 MCDC TA Simulation Results

The plane 1 plasma potential structures for the TA are shown in Chapter 7 and APPENDIX D. Plane 1 is used for the ion trajectory-erosion profile simulations. Because these simulations are completed over a larger computational domain, fewer grid points and initial angular orientations are utilized to decrease the computational time. Furthermore, only axial and radial (Z-axis and X-axis) ion motion is considered. Ion motion in the Y-direction is not included because plasma potential data are only available within the mapped plane.

MCDC TA simulation results show different trends than the FMT-2 simulations. Specifically, ions are no longer pulled and focused into the active DCA, but are repelled

due to the potential-hill structure. In fact, only ion initial positions directly in front of the DCA, upstream of the potential-hill, have a chance to impact. However, depending on the ion initial energy and angular orientation, some of these ions have enough directed energy to climb the potential-hill and escape the near-DCA region. All ions created at initial positions within the bulk of the discharge, downstream of the potential-hill, migrate in the axial (positive-Z) direction toward the ion beam extraction plane, not toward the DCA. This result is different from the FMT-2, which shows ions are focused into the active DCA. These results are independent of the active DCA location in the TA. Because very few ions actually impact the active DCA and cause erosion, an erosion profile is unable to be determined.

Simulation results for the dormant cathodes show that ions randomly enter the sheath structure and impact the dormant cathode keeper. Because a noticeable potential structure is not present near the dormant cathodes, ions are not pulled and focused into those units. Instead, only ions that randomly enter the dormant cathode sheath become accelerated and impact. Due to the random nature of ion collection, very few dormant cathode impacting ions are recorded and an erosion profile is unable to be calculated. However, uniform wear and random pre-sheath impact angles are expected at the keeper faceplate since no focusing potential structures are present.

Since there is no preferred pre-sheath angle and ions enter the dormant cathode sheath at thermal velocity, then the maximum through-sheath impact angle is determined by considering an ion with purely radial velocity entering the sheath. Assuming the ion enters the sheath at ~90 degrees with respect to keeper normal at thermal velocity, it is then accelerated axially by the plasma-to-keeper potential difference, such that its impact

angle with respect to keeper normal is given by Eqn. 8-7. A schematic of the pre- and through-sheath velocities is shown in Figure 8-6.

$$\tan(\theta_{thru}) = \frac{v_r}{v_a} = \frac{v_{therm}}{\sqrt{\frac{2E}{M_i}}} = \frac{\sqrt{\frac{8eT_i}{\pi M_i}}}{\sqrt{\frac{2e(V_p - V_k)}{M_i}}} \qquad \textbf{Eqn. 8-7}$$

The ion velocity distribution is assumed to be Maxwellian with the average velocity utilized as the thermal velocity.[185] During spot-mode operation, ion temperature in the plume of a DCA is on the order of 0.5 – 1.5 eV.[148] Ions outside of the DCA and near the dormant cathodes may have slightly lower temperatures, so a value of 0.5 eV is assumed for this analysis.

Utilizing this assumption and Eqn. 8-7, dormant cathode impacting ions have through-sheath angles of 10 degrees or less with respect to keeper normal. Ions that enter the sheath at the thermal velocity with pre-sheath angles less than 90 degrees have through-sheath bombarding angles less than 10 degrees. This result has a profound impact on dormant cathode keeper sputtering erosion phenomenon because the sputter yield is known to be dependent on ion impact angle (Eqn. 8-6, Section 8.1.2). Specifically, lower impact angles have lower sputter yields, so ion bombardment at 10 degrees causes less erosion than larger angles. Consideration of doubly-charged ions at similar temperatures results in smaller bombarding angles because doubles gain more axial velocity passing through the sheath. Further discussion of dormant cathode erosion is provided in Chapter 9.

CHAPTER 9:

EROSION AND LIFETIME PREDICTIONS

The primary goal of the multiple-cathode discharge chamber (MCDC) is to increase ion thruster lifetime by operating multiple discharge cathodes sequentially. However, previous multiple-cathode electric propulsion devices have shown erosion of the dormant cathode to be a significant affect. Specifically, results with the SPT-100 indicate that an operational cathode can cause significant erosion (destruction) of the dormant cathode.[77,78] This chapter uses ion bombardment sputtering erosion theory to quantify the pre-operation erosion of the MCDC dormant cathodes. Based on these results a lifetime prediction and example MCDC mission timeline is determined.

9.1 Dormant Cathode Erosion Analysis

In the following sections the measured dormant cathode plasma properties are utilized to predict the possible pre-operation erosion of those units for both Molybdenum (Mo) and Carbon graphite discharge cathode assembly (DCA) keeper materials. Currently, most DCA keepers are constructed of Mo, but different materials with lower sputtering yields, such as Carbon graphite, are being investigated.[10,56,61] In order to predict the erosion of the dormant cathodes, an accurate sputtering yield model for low-energy xenon ions bombarding the keeper is required. Many models have been developed, but unfortunately no one model appears to be superior. Both Duchemin[183] and

Nakles[186] have summarized sputtering yield and theory at low bombarding energies near threshold, illustrating the uncertainty in sputter yields near threshold.

For the analysis that follows, two erosion models are developed based on experimental sputter data and sputtering theory. The output of the models is sputter yield calculated as a function of bombarding ion energy and ion incidence angle. Erosion rate is then determined based on the output sputter yield. The first model is developed for both Mo and graphite, while the second model is only applicable to Mo.

9.1.1 Mo and Graphite Model

For the first model, sputtering energy threshold as a function of incidence angle is assumed to be of the form described by Yamamura.[178] For small angles, the sputtering process dominates and Yamamura suggests the following relation.

$$E_{th}(\theta) = E_s\left[4.4 - 1.3\log\left(m_2/m_1\right)\right]\cos^2(\theta) \qquad \textbf{Eqn. 9-1}$$

In this equation, E_s is sublimation energy, m_1 and m_2 are the incident and target atom mass, respectively, and θ is the angle of incidence. Herman[79] and Williams[162] suggest ions bombarding the active DCA have pre-sheath angles on the order of 60 degrees, resulting in through-sheath impacting angles of ~35 degrees or less with respect to keeper normal. However, the dormant cathodes do not show the same potential structure as the active DCA. Specifically, results with the ion trajectory – erosion profile simulator show that ions enter the dormant cathode sheath with no preferred pre-sheath angle. Ions bombarding the dormant cathodes are anticipated to have through-sheath impact angles between 0 - 10 degrees with respect to keeper normal (Section 8.4).

Eqn. 9-1 is used to determine Mo and graphite sputtering threshold energy as a function of angle of incidence for angles less than 40 degrees. These results are presented in Figure 9-1.

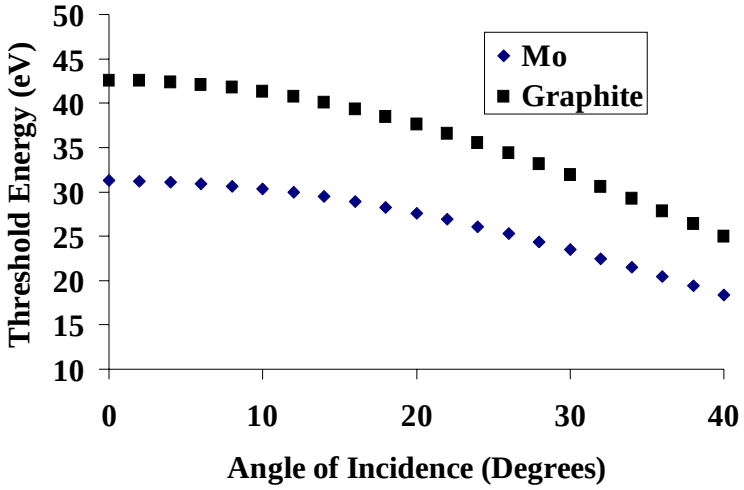

Figure 9-1: Graphite and molybdenum threshold energy as a function of angle of incidence.

Sputtering yields are calculated by adjusting the equation developed by Wilhelm[187] to account for both bombarding ion energy and incidence angle as illustrated in Eqn. 9-2.

$$Y(E_i,\theta) = K(E_i - E_{th}(\theta))^2 \qquad \textbf{Eqn. 9-2}$$

In this equation, E_i is the ion energy and K is a constant. Doerner, *et al.,*[173] have measured sputter yields for normal incident xenon bombarding graphite and Mo using a weight loss detection scheme. A curve fit of Eqn. 9-2, assuming normal incident ions, to the measured Mo and graphite sputter yield data is shown in Figure 9-2. The fits yield K values of $3.7\text{x}10^{-6}$ and $1.0\text{x}10^{-5}$ for the graphite and Mo data, respectively. Although data used to obtain these K-values are for normal incident ions, these results are also utilized for off-normal incidence. Each fit is made to have better agreement with the low-energy data because low-energy sputtering is of primary interest for this analysis.

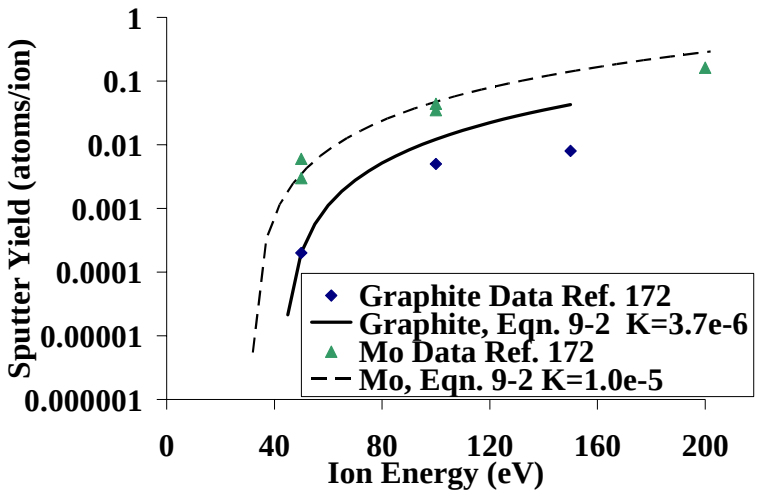

Figure 9-2: Equation 9-2 fit to Doerner, *et al.*, molybdenum and graphite sputter yield weight loss data for normal ion incidence.[173]

Ion energy is calculated assuming an initially stationary ion falling through the potential difference between the plasma and keeper, as illustrated by Eqn. 9-3. In this equation, V_p is the plasma potential and V_k is the keeper potential. Keeper potential is assumed constant for this analysis. Eqn. 9-4 represents the flux of ions required to produce a given rate of erosion.

$$E_i = (V_p - V_k) \qquad \textbf{Eqn. 9-3}$$

$$\Gamma_i = 2.78x10^{-13}\frac{S\rho_2}{Ym_2} \qquad \textbf{Eqn. 9-4}$$

In Eqn. 9-4, S is the erosion rate (mm/khr), ρ_2 is the density of the keeper material, m_2 is the mass of the material, and the constant is used to correct mm/khr to m/s. Finally, the flux required to produce a given erosion rate (Eqn. 9-4) is equated with the directed flux of ions to the keeper surface, where the velocity of the ions is calculated from the ion energy in Eqn. 9-3. Eqn. 9-5 illustrates the erosion rate as a function of ion number

density and energy for xenon bombardment. Input parameters for the model are summarized in Table 9-1.

$$S = \frac{1}{2.78x10^{-13}} \sqrt{\frac{2eE}{m_1}} \frac{m_2}{\rho_2} Yn_i \qquad \textbf{Eqn. 9-5}$$

	Xenon	Molybdenum	Graphite
ρ_2 (kg/m^3)	N/A	10280	2274
m_1 (kg/atom)	2.18E-25	N/A	N/A
m_2 (kg/atom)	N/A	1.59E-25	2.00E-26
E_s (eV)[188,189]	N/A	6.83	7.41
K in Eqn. 9-2	N/A	1.0E-5	3.7E-6

Table 9-1: Erosion model input parameters.

Doubly-charged ions have been shown to be an important factor for erosion calculations[79] and are considered in this analysis. The doubles-to-singles current ratio in the ion beam of the 30-cm NSTAR thruster and 40-cm NEXT is a function of the operating condition and is expected to be within 18-25%.[168] For this analysis, the doubles-to-singles ratio is assumed equivalent to the downstream ion beam ratio and is also assumed to be a constant equal to 20%. Therefore, the number of singly- and doubly-charged ions is equal to 83% and 8.5% of the total number density, respectively. These values do not sum to 100% because the doubly-charged ions account for two times the ion current as the singly-charged ions. The equations listed below are used to convert the total number density measurement into doubly- and singly-charged ion number density components for the erosion calculations.[79]

$$n_{total} = n_{sngl} + n_{dbl} \qquad \textbf{Eqn. 9-6}$$

$$j_{total} = j_{sngl} + j_{dbl} \qquad \textbf{Eqn. 9-7}$$

$$n_{sngl} = \left(\frac{j_{sngl}}{j_{total}} \right) n_{total} \qquad \textbf{Eqn. 9-8}$$

$$n_{dbl} = \frac{1}{2} \left(\frac{j_{dbl}}{j_{total}} \right) n_{total} \qquad \textbf{Eqn. 9-9}$$

In order to calculate the anticipated erosion rate of the dormant cathodes, representative inputs for plasma potential, keeper potential, and number density are required. Results from the plasma property mapping, diagnostic cylinders (DCs), and the stability, performance, and uniformity analysis are used to determine plasma potential, number density and keeper potential values for the four extreme operational cases. The input values are shown in Table 9-2.

	Case 1	Case 2	Case 3	Case 4
DC Flow	No Flow	No Flow	DCA Flow	DCA Flow
I_{emag}	0	10	0	10
V_k (V)	6	6	9	9
n_i (cm^{-3})	5.5E+11	5.0E+10	4.4E+11	4.0E+10
V_p (V)	27	35	27	35

Table 9-2: Input plasma properties for the 4 cases investigated.

Case 1 and 2 are for the dormant cathodes operated without propellant flow and the TA operated with electromagnet currents of 0 A and +10 A. Case 3 and 4 represent the dormant cathodes operated with the full DCA propellant flow rate and the TA operated with electromagnet currents of 0 A and +10 A. Results with the DCs and the stability, performance, and uniformity analysis (Chapter 5 and 6) indicate that propellant flow causes the dormant cathode ion number density to decrease and the keeper floating potential to increase. These trends are represented in the 4 investigated cases. The values in Table 9-2 are utilized in the model to calculate the erosion rates shown in Figure 9-3 and Figure 9-4.

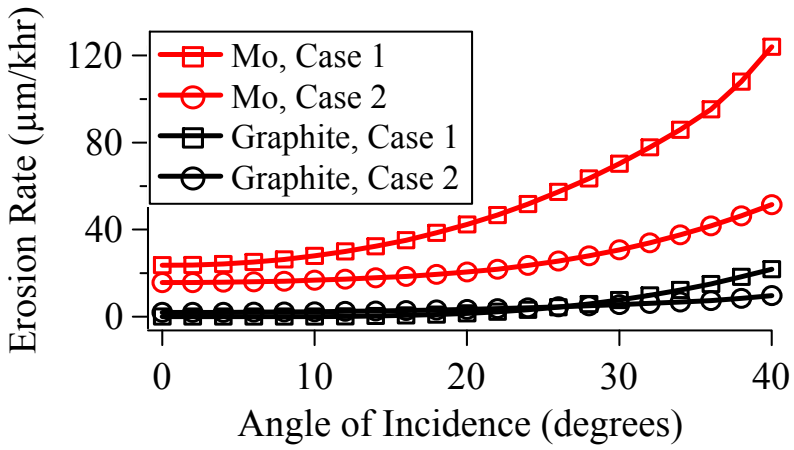

Figure 9-3: Dormant cathode erosion rate as a function of bombarding ion incidence angle for Mo and graphite keeper materials for case 1 and 2.

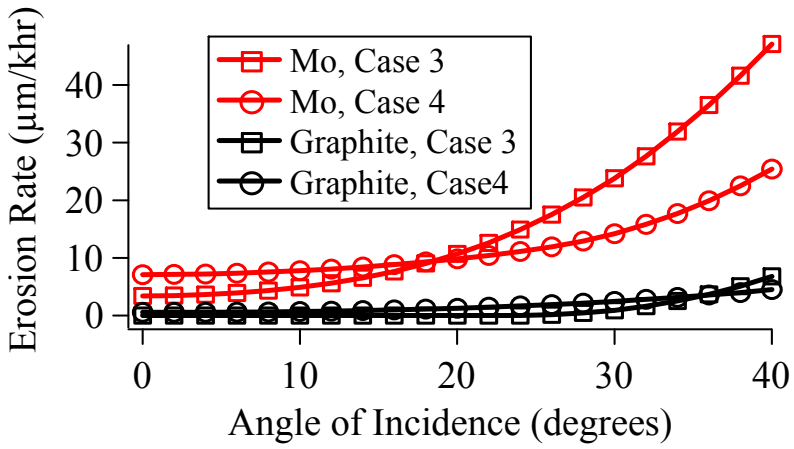

Figure 9-4: Dormant cathode erosion rate as a function of bombarding ion incidence angle for Mo and graphite keeper materials for case 3 and 4.

Calculations resulting in an erosion rate of 0 are due to ion bombarding energies below the sputtering threshold energy. Erosion calculation results show Mo has the highest erosion rate. These results suggest that if the dormant cathode keepers are constructed of Mo, they may suffer pre-operation erosion. However, pre-operation dormant cathode erosion can be significantly reduced if those units are operated with the full DCA propellant flow rate. The erosion rate results also reinforce the conclusion that optimum TA operation is obtained with the electromagnet at 0 A.

The maximum measured DCA erosion rate during wear testing is 70 μm/khr.[9,69] At the anticipated maximum bombardment angle of 10 degrees (Section 8.4) for no dormant cathode propellant flow (case 1), an erosion rate of 25 μm/khr is calculated. This suggests that a dormant cathode Mo keeper erodes through its thickness after only 38,000 hours (~4.4 years). Operating the dormant cathodes with propellant flow (case 3) reduces the erosion rate to 5 μm/khr and the Mo keeper erodes through its thickness after 304,000 hours (~34.7 years). This is a decrease of a factor of 5 in erosion rate and corresponding increase in anticipated lifetime. It should also be noted that graphite has a calculated erosion rate of ~0 μm/khr for the nominal case 3.

Although this model provides insight into dormant cathode erosion, multiple approximations have been made. The following list describes and justifies some of the shortcomings of this particular erosion model. 1) Limited low-energy sputter data for graphite and Mo at normal and off-normal incidence is available; 2) Sputter threshold and yield data have large discrepancies ($7<E_{th}<62$ eV);[186] 3) Utilizing a directed flux overestimates the erosion rate; and 4) Normal incidence sputter data is used for off-normal ion bombardment erosion predictions.

In general, these erosion prediction results suggest graphite is the best choice to reduce dormant cathode and possibly discharge cathode assembly (DCA) keeper erosion. Recent results from 2,000-h wear tests of graphite DCA keepers in both the Nuclear Electric Xenon Ion System (NEXIS) and High-Power Electric Propulsion (HiPEP) thrusters indicate negligible keeper erosion,[56,61] suggesting graphite eliminates keeper erosion. However, other phenomena may plague graphite keepers. Specifically, residual amounts of oxygen impurity ions may strike the surface along with the xenon plasma

ions. The sputter yield of high-energy oxygen ions on carbon is orders of magnitude larger than low-energy xenon ion bombardment.[173] This effect must be better understood or eliminated, and further investigation into xenon-graphite sputtering behavior must be completed in order to validate graphite as an erosion-reducing lifetime-increasing design solution.

9.1.2 Mo Only Model

The second model is a modified form of the first and is developed for Mo only, utilizing the sputter yield analysis presented in Chapter 8. This model uses Eqn. 9-5, with the sputter yield, Y, determined from Eqn. 8-5 and Eqn. 8-6. Furthermore, this model assumes the same doubles-to-singles ratio as the Mo and graphite model, 20%. Calculations are completed for the 4 cases described in Table 9-2 and the results are presented in Figure 9-5 and Figure 9-6.

The effect of doubly-charged ions on the erosion rate is shown in Figure 9-5. The addition of doubly-charged ions significantly increases the erosion rate and becomes the dominant erosion mechanism. Doubly-charged ions gain 2 times more energy and cause exponentially more sputtering erosion. Results for the 4 investigated cases are shown in Figure 9-6.

Results for the Mo only model predict erosion rates similar to the Mo and graphite model presented above and show that a Mo keeper may suffer pre-operation erosion. Specifically, the dormant cathodes should be operated with propellant flow to reduce the number of bombarding ions. However, even with propellant flow, the dormant cathodes may still suffer an erosion rate of ~15 μm/khr at the anticipated 0-10 degree ion bombardment.

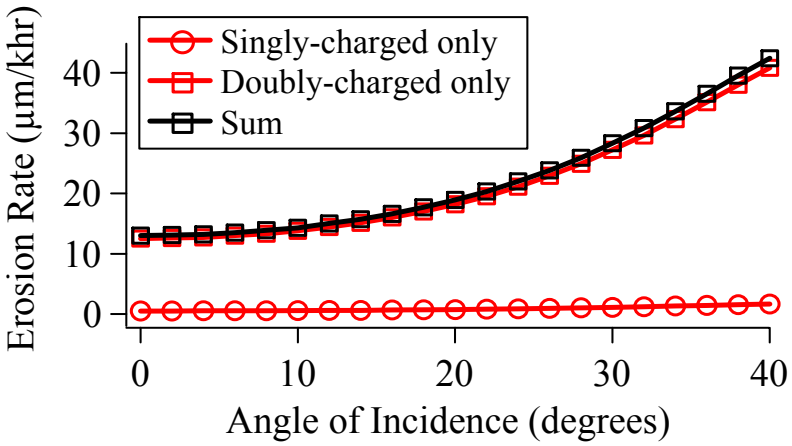

Figure 9-5: Dormant cathode erosion rate as a function of bombarding ion incidence angle for case 3. The effect of doubly-charged ions significantly increases the erosion rate.

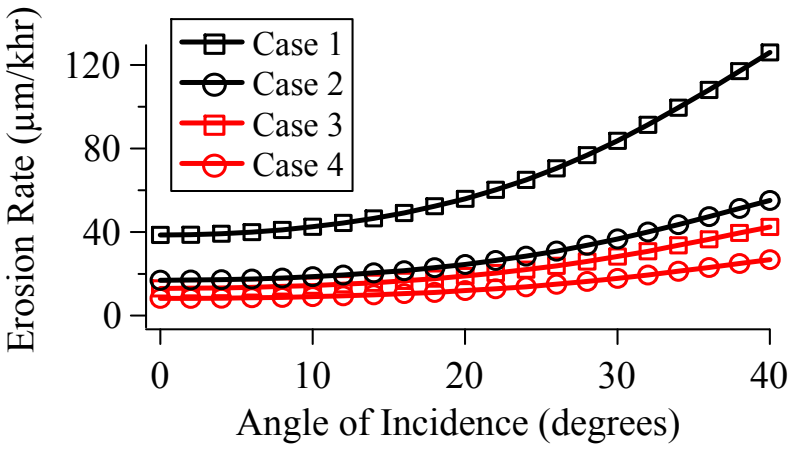

Figure 9-6: Dormant cathode erosion rate including doubly-charged ions as a function of bombarding ion incidence angle for the 4 investigated cases.

The presented erosion rate results suggest that Mo-keeper dormant cathodes suffer pre-operation erosion. Therefore Mo atoms are being released from the keeper into the discharge chamber. Furthermore, ion optics erosion is also present in ion thrusters and releasing particles into the discharge chamber. Therefore, there exists a finite possibility that these particles will become deposited onto the insert of the dormant hollow cathodes, preventing those units from being operated or deteriorating their performance. However,

this type of analysis is beyond the scope of this work. Plus, operating the dormant cathodes with the preferred full propellant flow rate may reduce or eliminate any type of deposition onto the insert.

9.2 MCDC Lifetime Prediction

Utilizing the erosion rates predicted by the erosion models, a MCDC ion thruster mission timeline can be determined. Two mission timelines are presented by using the maximum and minimum calculated dormant cathode erosion rates. First, maximum dormant DCA Mo keeper erosion is assumed to be the average of the Mo/graphite and Mo-only models for case 1 presented above and is equal to 35 μm/khr. Based on the ELT and wear test results, active DCA Mo keepers are assumed to erode at 50 μm/khr, and a DCA is assumed terminated upon erosion through the keeper thickness at ~30,000-h (however, keeper erosion is not necessarily a DCA failure mechanism, so this analysis represents a worst-case scenario). Table 9-3 shows an example mission timeline for a Mo-keeper triple-DCA MCDC ion thruster with the dormant cathodes operated electrically isolated (floating) and with no propellant flow rate.

	DCA # 1		DCA # 2		DCA # 3	
Mission Time (hrs):	Status	Keeper (% left)	Status	Keeper (% left)	Status	Keeper (% left)
0	Active	100	Dormant	100	Dormant	100
15,000	Active	50	Dormant	65	Dormant	65
30,000	Eroded	0	Active	30	Dormant	30
39,000	Eroded	0	Eroded	0	Active	9
41,700	Eroded	0	Eroded	0	Eroded	0

Table 9-3: Predicted Mo-keeper triple-DCA MCDC ion thruster mission timeline when the dormant cathodes are operated electrically isolated (floating) and with no propellant flow rate. Predicted lifetime is only 1.4 times longer than a single-DCA thruster.

At 30,000 hours, the first DCA keeper erodes and the second DCA is activated. However, at this point the second DCA keeper is already eroded through 35% of its thickness and is therefore only operational for 9,000 hours. When the third DCA is ignited, only 9% of its keeper thickness remains so it's only operational for 2,700 hours. In this scenario, pre-operation erosion of the dormant cathodes significantly limits the lifetime provided by multiple cathodes and total thruster lifetime is only 1.4 times longer than a single-DCA engine.

The second analysis is for the minimum calculated dormant DCA Mo keeper erosion, based on the average of the Mo/graphite and Mo-only models for case 3 presented above, and is equal to 10 μm/khr. Table 9-4 shows an example mission timeline for a Mo-keeper triple-DCA MCDC ion thruster with the dormant cathodes operated electrically isolated (floating) and with full propellant flow rate.

	DCA # 1		DCA # 2		DCA # 3	
Mission Time (hrs):	Status	Keeper (% left)	Status	Keeper (% left)	Status	Keeper (% left)
0	Active	100	Dormant	100	Dormant	100
15,000	Active	50	Dormant	90	Dormant	90
30,000	Eroded	0	Active	80	Dormant	80
54,400	Eroded	0	Eroded	0	Active	64
73,900	Eroded	0	Eroded	0	Eroded	0

Table 9-4: Predicted Mo-keeper triple-DCA MCDC ion thruster mission timeline when the dormant cathodes are operated electrically isolated (floating) and with full propellant flow rate. Predicted lifetime is 2.5 times longer than a single-DCA thruster.

At 30,000 hours, the first DCA keeper erodes and the second DCA is activated. However, at this point the second DCA keeper is already eroded through 20% of its thickness and is therefore only operational for 24,400 hours. When the third DCA is ignited, only 64% of its keeper thickness remains so it's only operational for 19,500 hours.

Although these analyses involve some simplifications, clearly a triple-DCA MCDC with Mo keepers does not provide a threefold increase in lifetime. Pre-operation erosion of the dormant DCA keepers limits the lifetime increase provided by the addition of extra DCAs. Comparison of Table 9-3 and Table 9-4 illustrates the importance of operating the dormant cathodes with maximum propellant flow rate. Although the dormant cathodes have propellant flow, the total flow rate into the discharge chamber is constant because the main plenum flow is reduced. Also, Chapter 5 results indicate that MCDC performance and flatness are not affected by dormant cathode flow rate. Finally, this analysis suggests that utilizing three DCAs can increase discharge chamber life by a factor of ~2.5 over that of a single-DCA thruster.

Utilization of graphite keepers should provide a significantly larger increase in thruster lifetime because the active-DCA erosion rate, as well as the dormant cathode pre-operation erosion rate, decreases for graphite. Recent wear test results for the NEXIS and HiPEP thrusters utilizing graphite DCA keepers showed no erosion.[56,61] Therefore graphite keepers may increase DCA life such that keeper erosion and subsequent DCA failure is no longer the primary thruster failure mode. Furthermore, if graphite keepers are successful in increasing thruster life for Prometheus-class long-duration missions, the use of multiple cathodes may not be required.

CHAPTER 10:

CONCLUSIONS

The following sections describe the important conclusions developed throughout this thesis. Conclusions based on the design and general operation of the multiple-cathode discharge chamber (MCDC) test article (TA) are discussed first, followed by a discussion of the ability of the MCDC to increase thruster lifetime. The presented discharge cathode assembly (DCA) erosion theory is summarized and compared with another recent theory developed at the NASA Jet Propulsion Laboratory (JPL). Finally, suggestions for future work include development of a new cylindrical/conical MCDC and design of a new DCA to eliminate or reduce erosion.

10.1 MCDC Design and Operation

Experimental testing of the TA was conducted in the LVTF at operating pressures on the order of 4×10^{-6} Torr and the TA was operated as a simulated ion thruster.[92] A NASA Evolutionary Xenon Thruster (NEXT) DCA was used and two dormant cathode units (DCUs) were also mounted in the TA. Magnetic field configuration, DCU electrical connectivity, and DCU flow rate were adjusted, while performance, uniformity, DCU floating voltages, DCU currents, and backplate electron current ratio were monitored. Furthermore, other experimental investigations involved using diagnostic cylinders (DCs) to measure the dormant cathode plasma properties and completing two-dimensional

plasma property profiles within the TA internal volume. The following sections describe the conclusions drawn from these various investigations.

Both centerline (center) and off-centerline (left) DCA operation within the TA was accomplished. Simulated performance curves and calculated flatness parameters showed the optimal TA configuration performs within the same operational regimes as contemporary ion thruster discharge chambers. Adjustment of the DCA location changes TA performance only a few percent (~5%) and the maximum grid-plane current density shifts to directly downstream of the DCA location. DCU connectivity and flow rate have no effect on TA performance or grid-plane uniformity (flatness). Also, as dormant cathode flow rate increases, the main plenum flow is reduced such that the total flow rate remains constant and therefore thruster specific impulse should not be affected. The TA magnetic field profoundly affects both performance and uniformity. Specifically, as the magnetic field increases, the discharge plasma is pushed downstream and becomes more collimated. As will be discussed in a following section, this result is due to better confinement of electrons in the center of the TA. The optimum magnetic field configuration is determined to be the 0 A electromagnet configuration. Enclosure of the 50 G line is not required for optimum performance of the rectangular MCDC. Other configurations have lower losses; however, the 0 A configuration balances both performance and uniformity.

The TA is a rectangular discharge chamber, so the ratio of corner to mid-plane anode electron deposition was monitored. Calculated backplate current ratios are on average 10, suggesting that considerably more discharge current is deposited in the corners of the rectangular TA than at the mid-plane. This ratio decreases with DCU flow

rate. Furthermore, this result suggests that a discharge chamber utilizing a point-source for electrons (i.e., a hollow cathode) should have an axisymmetric design and not a fully three-dimensional rectangular geometry. More uniform plasma production and current collection may be obtained with an axisymmetric (cylindrical or partial-conic) MCDC design.

Internal discharge chamber plasma property mapping results indicate that the near-DCA plume contains higher-temperature electrons than the bulk discharge and electrons are confined to the magnetic field lines. Specifically, the magnetic cusps contain higher electron temperatures than the intercusp regions. Cross-field diffusion to the intercusp regions in ion thrusters is known to be governed by classical diffusion and has a $1/B^2$ dependence.[44] Therefore, as the electromagnet current increases (axial magnetic field increases), electrons are more confined to the center of the TA because electron mobility to off-axis regions is reduced. Furthermore, electrons spiral more tightly along the magnetic field lines. Other types of electron motion, such as grad-B, curvature, magnetic-mirror, and $\vec{E} \times \vec{B}$ drift,[43] may also be present. The combination of these effects is to elongate, collimate, and increase the temperature of the DCA plume.

Using the results for electron temperature, all other plasma properties within the TA can be explained. Number density is dependent on the electron temperature because more-energetic higher-temperature electrons ionize more neutral propellant. Therefore, regions of higher electron temperature also contain larger number densities. Specifically, the cusps and near-DCA region contain larger number densities. As the axial magnetic field increases, the electron temperature profile becomes more collimated at the center of the TA causing the number density distribution to also become collimated. This result is

consistent with measurements of the grid-plane current density uniformity. Regions with higher electron temperature have a more negative floating potential because the probe must repel more-energetic electrons. Finally, since a quasi-neutral plasma is assumed, regions with larger number density have lower plasma potential because of the presence of more electrons. Therefore, the cusps show lower plasma potential than the intercusp regions.

Plasma potential structures show a low-potential region at the DCA orifice surrounded by a higher-potential region, characteristic of the potential-hill structure documented by other researchers.[140,148-151] However, the existence of a potential-hill downstream of an ion thruster DCA is debatable because of the contradiction in experimental results. In fact, data presented here suggest that time-averaged single-Langmuir probe plasma potential results are less accurate than results obtained by an emissive probe. Specifically, the electron retarding-to-electron saturation region of the single-Langmuir probe trace (or knee) becomes rounded, making the plasma potential calculation difficult and less accurate. Martin, *et al.*, have reported a similar result for a cathode operating with a ring anode.[156] The rounded knee may be a product of high-frequency large-amplitude plasma potential oscillations, similar to those measured by Jameson, *et al.*[153] However, time-resolved floating potential results in the TA do not show this result.

Plasma properties at the dormant cathode locations and throughout the MCDC show no noticeable difference when operating the dormant cathodes electrically connected or electrically isolated from the TA. However, dormant cathode propellant flow rate does affect the plasma number density at the dormant cathode locations.

Specifically, results with the 5 planar Langmuir probe with propellant flow diagnostic cylinder (5PLPF-DC) indicate that dormant cathode "keeper" orifice number density decreases as propellant flow rate through the DC increases. Based on this result, the dormant cathodes in a MCDC should be operated with propellant flow to decrease the number of pre-operation erosion-causing ions. Operation with dormant cathode propellant flow may decrease the pre-operation erosion of the dormant units significantly. Finally, the decrease in number density with increasing propellant flow is suggested to be caused by charge-exchange (CEX) collisions. As the flow rate increases, the neutral density at the "keeper" orifice increases, causing more CEX collisions with bombarding ions and decreasing the orifice number density.

10.2 MCDC Ability to Increase Thruster Lifetime

Ion trajectory – erosion profile simulations with the MCDC TA internal plasma potential maps do not show ions bombarding the dormant cathodes. This result is due to the lack of a potential structure near the dormant cathodes and therefore ions must randomly enter the keeper sheath. A geometric model is used for the ion acceleration through the keeper sheath and ions are assumed to enter the sheath at their thermal velocity. Based on these assumptions, bombarding ions impact the dormant cathode keeper with an angle less than 10 degrees with respect to normal. This result has profound impacts on erosion because lower angles typically cause less erosion than larger angles.

The use of multiple sequentially operated ion thruster discharge cathodes is expected to increase thruster lifetime. Molybdenum (Mo)-keeper dormant cathodes suffer pre-operation erosion, but at significantly smaller erosion rates than the active Mo-keeper

DCA (~10 μm/khr compared to ~65 μm/khr). Therefore, a Mo-keeper triple-DCA ion thruster does not provide a three-fold increase in lifetime, but can increase lifetime by a factor of ~2.5 over a Mo-keeper single-DCA thruster. Utilization of Carbon graphite for the keeper material may significantly reduce both active DCA and dormant cathode keeper erosion. In fact, erosion calculations suggest a graphite dormant cathode keeper suffers no pre-operation erosion.

Dormant cathode pre-operation erosion phenomenon in an MCDC is mitigated by operating those units electrically isolated (floating) and with propellant flow. Propellant flow reduces the collected keeper current and decreases the orifice ion number density through CEX collisions, so fewer erosion-causing ions impact the keeper. Based on the retarding potential analyzer diagnostic cylinder (RPA-DC) results, ions bombarding the dormant cathodes are falling from the plasma potential and therefore gain energy equivalent to the plasma-to-keeper potential difference. Propellant flow increases the keeper floating potential so ions gain less bombarding energy. Furthermore, Kolasinski has shown that increased keeper potentials reduce erosion because the plasma-to-keeper potential difference is reduced.[139]

A rectangular MCDC design also has benefits for increasing thruster lifetime. In a MCDC, the maximum grid-plane current density is consistently located directly downstream of the active DCA. This result has important consequences for ion optics grid-erosion and lifetime. Specifically, the maximum grid-erosion is known to occur at the maximum current density location, which is directly downstream of the centerline DCA in a single-DCA ion thruster.[62,81-87] During MCDC off-centerline DCA operation, the maximum grid-erosion location is also off-centerline. Therefore, throughout the life

of the thruster, the maximum grid-erosion occurs at multiple locations and no one location suffers prolonged exposure to maximum grid-erosion.

During off-centerline DCA operation the maximum current density is also off-centerline and, as a result, a moment exists on the thruster. Although mission planners typically prefer an electric propulsion device that produces a purely axial centerline thrust, this adverse effect can be eliminated through slight gimballing of the thruster. Plus, future deep-space spacecraft are being designed to utilize clusters of thrusters divided into pods.[5,6] For instance, the Jupiter Icy-Moons Orbiter (JIMO) mission through NASA's project Prometheus is designed to have two thruster pods, one on each side of the spacecraft, each containing clusters of ion thrusters and Hall-effect thrusters (HETs).[5,6] Operating an ion thruster with its mirror image on the opposite side of the spacecraft can eliminate the moment on the spacecraft.

10.3 DCA Erosion

10.3.1 Potential Structure and Propellant Flow Rate Theory

The DCA erosion theory developed for this work is based on ion trajectory – erosion profile simulation results and propellant flow rate effects. Ion trajectories are simulated using plasma potential structure measurements obtained by Herman[79,117] and simple force equations. Results indicate that the plasma potential structures cause a chamfering erosion of the DCA keeper orifice, which eventually causes the orifice to enlarge and the keeper faceplate to be completely eroded. These results are identical for the NSTAR thruster TH15 and TH8 operating conditions. Results from the 1,000-h and 8,200-h NSTAR thruster wear-tests show maximum erosion occurring at approximately

the 50% keeper radius, not the keeper orifice. Therefore, the potential structure alone cannot be causing the known wear-test erosion results.

Propellant flow rate effects with the 5PLPF-DC in the MCDC TA suggest that increasing flow rate through the DCA may lead to a decrease in orifice bombarding ions due to CEX collisions. The erosion theory combines the erosion profiles caused by the near-DCA potential structure with the 5PLPF-DC flow rate effects. The theory suggests that CEX collisions between bombarding ions and expelled neutral atoms from the keeper orifice replace a single high-energy bombarding ion with two lower-energy particles, a CEX-ion and a neutral atom. Each of the two resulting particles has lower energy than the unperturbed initial ion would and therefore causes less erosion. In fact, the energy of each of the post-CEX particles may be lower than the threshold energy of the target material, in which case no sputtering erosion occurs.

The erosion theory is used to qualitatively predict erosion profiles for the TH8 and TH15 operating conditions. The lower-power lower-flow rate TH8 condition has an exponentially decreasing erosion profile that causes maximum erosion at the keeper orifice. This profile leads to chamfering of the orifice and eventual loss of the keeper faceplate. The high-power high-flow rate TH15 condition has a peaked erosion profile with less erosion at the orifice due to CEX collisions and a maximum erosion location at approximately the 50% keeper radius point. The theory is consistent with erosion profiles measured after the 1,000-h wear test[67] and results presented by Kolasinski that suggest the erosion profile changes from TH15 to TH8.[139,184]

Extended life test (ELT) erosion results are a product of the thruster operating point and the cathode-to-keeper short. Specifically, the change in ELT erosion location

from the downstream keeper face to the keeper orifice is caused by the decrease in propellant flow rate when the thruster is adjusted from TH15 to TH8. The increase in erosion rate is caused by the cathode-to-keeper short because bombarding ions gain more energy, the cathode-to-keeper potential. Initial ELT operation is at TH15, during which time the DCA keeper erodes primarily at the 50% keeper radius location. When the thruster is throttled down to TH8, the DCA flow rate is reduced and the primary erosion location shifts to the keeper orifice. While operating at TH8, the cathode-to-keeper short significantly increases the erosion rate and the keeper orifice begins to enlarge. When the thruster is returned to the higher-flow rate TH15, the keeper orifice is two times its initial diameter so that the neutral density at the orifice does not return to the original value. Because of the reduced orifice neutral density, the primary erosion location remains at the keeper orifice, eventually removing the entire keeper faceplate.

10.3.2 High-Energy Radially-Accelerated Ions Theory

Recent RPA and near-DCA emissive probe results obtained by Goebel, *et al.*, suggest that a high-energy radial ion component produced by large-amplitude high-frequency plasma potential oscillations is contributing to DCA keeper erosion.[190] Axial ion energies are on the order of the plasma potential, but radial ion energies as large as 100 V are measured. The high-energy radial ion energy distributions for TH15 and TH8 appear identical, suggesting that the keeper erosion during the ELT for TH8 operation should have been comparable to TH15 operation. However, comparable erosion rates were not observed.[7,139,184]

The high-frequency large-amplitude oscillations and resulting high-energy radially-accelerated ions are suggested to be primarily created in a “plasma ball” that

changes axial location dependent on the thruster operating condition. For the TH15 operating condition, the "plasma ball" is located downstream of the keeper and the high-energy radially-accelerated ions miss the keeper. As the thruster is throttled down and the DCA flow rate is reduced for TH8 operation, the "plasma ball" moves into the keeper orifice and the high-energy radially-accelerated ions bombard the front corner and inside diameter of the keeper orifice. The high-energy, radially-accelerated ions and the shift in "plasma ball" location with thruster operating point explain the change in erosion location associated with the ELT and Kolasinski's results.[139,184,190]

10.3.3 Erosion Reduction or Elimination

Although the DCA erosion theory put forth by Goebel, *et al.*,[190] is somewhat more complicated than that presented in this thesis, and a full understanding of the origin of the high-frequency large-amplitude plasma potentials that create radially-accelerated ions is not well understood, the two theories are not mutually exclusive. In fact, both theories suggest the same solution to DCA keeper erosion. Increasing DCA propellant flow rate may eliminate or reduce ion bombardment and erosion of the DCA keeper. Specifically, increasing the DCA flow rate for the lower-power TH8 condition may protect the keeper orifice from bombarding erosion-causing ions and this solution can be applied to other thruster operation conditions as well. Furthermore, external flow released through the keeper may also eliminate erosion.

Propellant flow expelled through the keeper at various radial locations may decrease keeper erosion through CEX collisions with bombarding ions. A schematic of how this type of device may be designed and constructed is shown in Figure 10-1. Each of the 8 secondary exhaust orifices on the keeper faceplate expels neutral propellant

injected upstream into the keeper tube. The expulsion of neutral particles through the holes effectively creates a shield around the keeper faceplate so that high-energy bombarding ions suffer CEX collisions with the neutral particles. As previously mentioned, CEX collisions are expected to replace a high-energy bombarding ion with two lower-energy particles, a CEX-ion and a neutral atom.

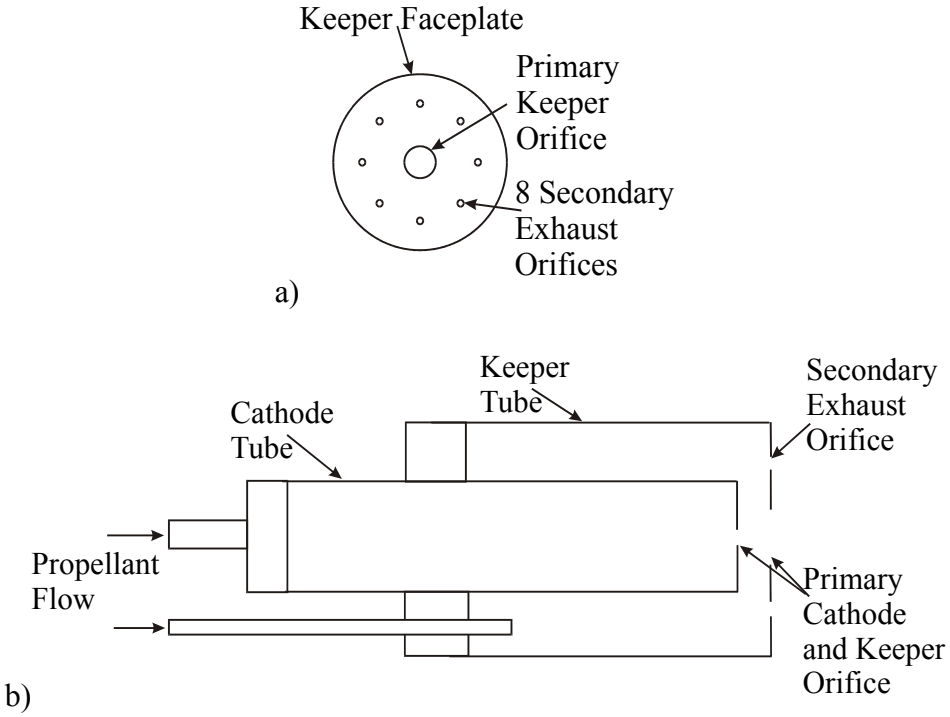

Figure 10-1: Schematic of a) keeper faceplate with primary orifice and 8 secondary exhaust orifices through which propellant is expelled and b) cross-sectional view of a DCA with keeper flow.

Using assumptions and an analysis similar to section 6.2.6 (Eqn. 6-7), the required flow rate for the device in Figure 10-1 to be effective can be determined. Specifically, if the 8 secondary orifices have a 1-mm-diameter, then 4.0 sccm-Xe is required to produce a secondary-orifice neutral number density of 1.6×10^{21} m^{-3} (identical to the NSTAR DCA keeper orifice for TH15 and similar to the 5PLPF-DC). Assuming a total thruster flow rate of 60 sccm-Xe and constant thrust, the specific impulse (I_{sp}) decreases ~6.6% if 4.0

sccm-Xe propellant is injected through the keeper. For Prometheus-class missions using high-power, high-specific impulse thrusters, this means a specific impulse decrease from ~8,000 seconds to ~7,500 seconds.

Another method for decreasing keeper erosion is use of an angled profile for the keeper faceplate. Herman[79] and Williams[162] suggest ions bombarding the active DCA have pre-sheath angles on the order of 60 degrees. Therefore, using a keeper faceplate with an angle of 60 degrees causes bombarding ions to impact at normal incidence. This type of design is shown in Figure 10-2. Ions striking at large radial distances from the orifice impact with normal incidence, causing significantly less sputter erosion. At smaller radial distances, ions either miss the keeper altogether or impact at glancing angles that cause less sputter erosion. Furthermore, with this type of design, more material is placed at the 50% keeper radius location where maximum erosion is known to occur. Also, the conical orifice shape increases the neutral density at the orifice and at axial locations downstream of the orifice so that more CEX collisions with bombarding ions occur.

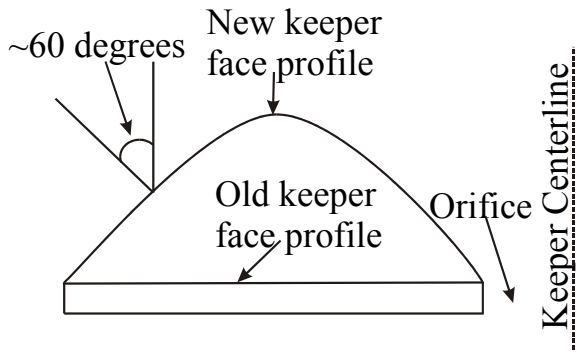

Figure 10-2: Example keeper faceplate profile designed to minimize erosion caused by ions with pre-sheath angular orientations of 60 degrees.

10.4 Suggestions for Future Work

Erosion rate calculations for both the ion trajectory – erosion profile simulations and the dormant cathode erosion analysis are based upon very little low-energy sputtering yield experimental data. Furthermore, the universal angular dependence corrections may differ significantly for low-energy sputter erosion. The accumulation of more low-energy heavy-particle sputtering yield data as a function of angle of incidence would be invaluable for calculating erosion rates. A large variation in bombarding ion energies and angular incidences should be investigated so that semi-empirical formulae and experimental data fitting become more reliable.

Calculated erosion rates are found to be extremely sensitive to the doubles-to-singles ion current ratio. Presented results assume the internal discharge chamber ratio is equivalent to the ratio measured in the ion beam of the NSTAR thruster and NEXT. While it is generally assumed that the plasma characteristics just upstream of the beam extraction optics remain constant as the plasma is accelerated and expelled, this assumption has never been experimentally justified and may not be valid in regions farther upstream near the DCA. Therefore characterization of the doubles-to-singles ratio near the DCA is an important and logical future step that could be accomplished either spectroscopically or perhaps with a miniature $\vec{E} \times \vec{B}$ probe (Wien filter).

Results presented here suggest that the dormant cathodes in the MCDC should be operated with propellant flow to increase keeper floating potential (thereby reducing ion bombarding energy) and reduce bombarding ion number density. However, it would also be interesting to study the effect of propellant flow on the ion energy distribution near the dormant cathodes. This could be achieved by developing a new RPA-DC with propellant

flow rate capabilities, similar to the 5PLPF-DC. Furthermore, laser-induced fluorescence measurements could also be utilized to measure ion energy distributions near the dormant cathodes.[191] These techniques would measure ion energy distributions with and without propellant flow present. The injection of relatively cold neutral gas (~300 K) may have a cooling effect through CEX collisions with the plasma near the dormant cathodes, further reducing bombarding ion energies.

The MCDC TA in the experimental investigations presented here has fixed cathode spacing. The three cathodes are spaced linearly across the backplate and their relative distances are not adjusted. Future experiments may consider the effect of moving the dormant cathodes closer or farther from the active DCA. Moving the left and right cathodes farther from the center of the TA will cause the internal plasma to shift farther from centerline to the new cathode location. Placing the dormant cathodes closer to the active DCA may be dangerous in terms of stable DCA operation and dormant cathode pre-operation erosion. Specifically, if the dormant cathodes are too close to the active DCA, they may interfere with the near-DCA potential structure and that potential structure may change the erosion of those units.

Another important aspect of MCDC operation that needs to be considered is the post-operation state of the cathodes. Results from the ELT indicate that relatively large tantalum flakes become removed from the heater radiation shield, presumably due to ion bombardment.[73] At beginning of life, the radiation shield is enclosed by the DCA keeper. However, if a cathode is significantly eroded during its active phase, then the heater radiation shield may become exposed and remain exposed when cathode operation is terminated. In an MCDC, the terminated cathode is still immersed in plasma and will

continue to suffer some ion bombardment. Flakes may be removed from the terminated cathode heater shield, migrate to the ion optics, and terminate thruster operation by shorting the accelerator and screen grids. This phenomenon may be cause for concern in an MCDC and should be investigated. It may be possible to use a different heater shield material to prevent large flakes from forming.

Another important phenomenon that needs investigation is surface contamination or coating of the hollow cathode insert due to eroded keeper and/or grid material. Presented results suggest that in a MCDC, Mo-keeper dormant cathodes suffer erosion, releasing Mo atoms into the discharge chamber. Furthermore, ion optics grid materials also erode during thruster operation. There exists a finite possibility that eroded keeper and/or grid materials may become deposited onto the dormant cathode insert, preventing cathode activated or deteriorating performance. However, insert deposition may be prevented or reduced by operating the dormant cathodes with the preferred full propellant flow rate. Although free-molecular flow still exists in this regime, the expulsion of neutral particles from the dormant cathode orifice may reduce insert deposition.

Using a point-source of electrons (i.e., a hollow cathode) in a rectangular, fully three-dimensional discharge chamber does not produce uniform plasma and an axisymmetric discharge chamber may be better suited. If the next generation MCDC will be operated with a hollow cathode, it should have an axisymmetric design, either entirely cylindrical (like the ring-cusp thrusters analyzed by Sovey[39]) or cylindrical/conical like the NSTAR thruster and NEXT. Specifically, the circular backplate should be enlarged to accommodate the three (or possibly more?) cathodes and each cathode should be surrounded by a circular permanent magnet ring. The new design should appear similar to

Figure 2-5 or Figure 2-7. One of the primary design criteria should be placing the dormant cathodes out of the active DCA plasma potential structure. Placing the cathodes too close to one another may interfere with the active DCA's ability to generate the plasma discharge. Canting of the cathodes may also be considered so that the peak beam current density remains at the same location throughout the thruster operational lifetime. However, as previously mentioned, extended operation with the same maximum current density location may cause ion optics grid failure.[62,81-87] Further magnetic field modeling and experimental investigation of the effect of cathode location should be completed for the next MCDC design.

Experimental investigation of a DCA with keeper flow rate (Figure 10-1) is needed to determine if the expulsion of neutral propellant at various keeper faceplate locations effectively shield the device from bombarding ions. Also, investigation of a new keeper faceplate design (Figure 10-2) should be completed to determine if that method also reduces erosion. The change in erosion rate and maximum erosion location for these two methods could easily be tested using surface layer activation.[139,184,192]

APPENDIX A: MAGNETIC FIELD COMPARISON

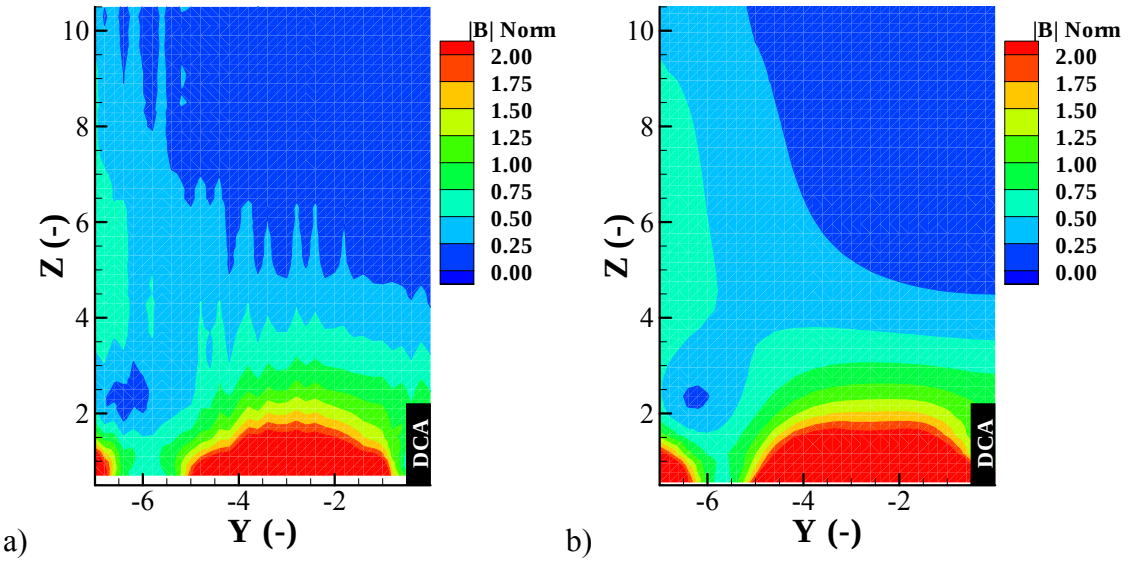

Figure A-1: Comparison of a) experimentally measured and b) simulated magnetic field for the X = 0 cm plane with 50 G line enclosed.

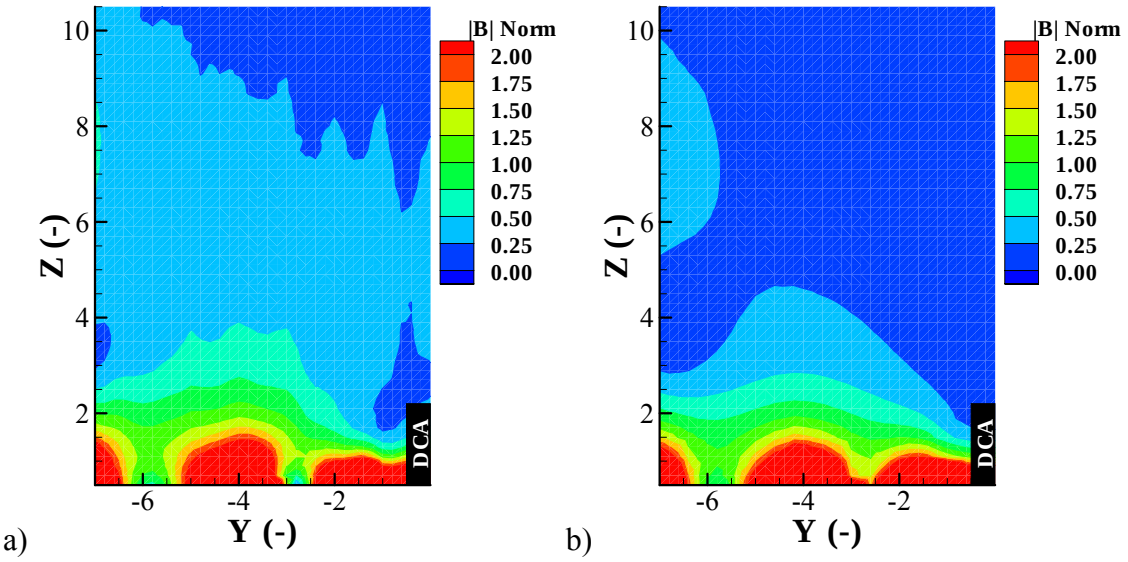

Figure A-2: Comparison of a) experimentally measured and b) simulated magnetic field for the X = 0 cm plane with I_{emag}= -10 A.

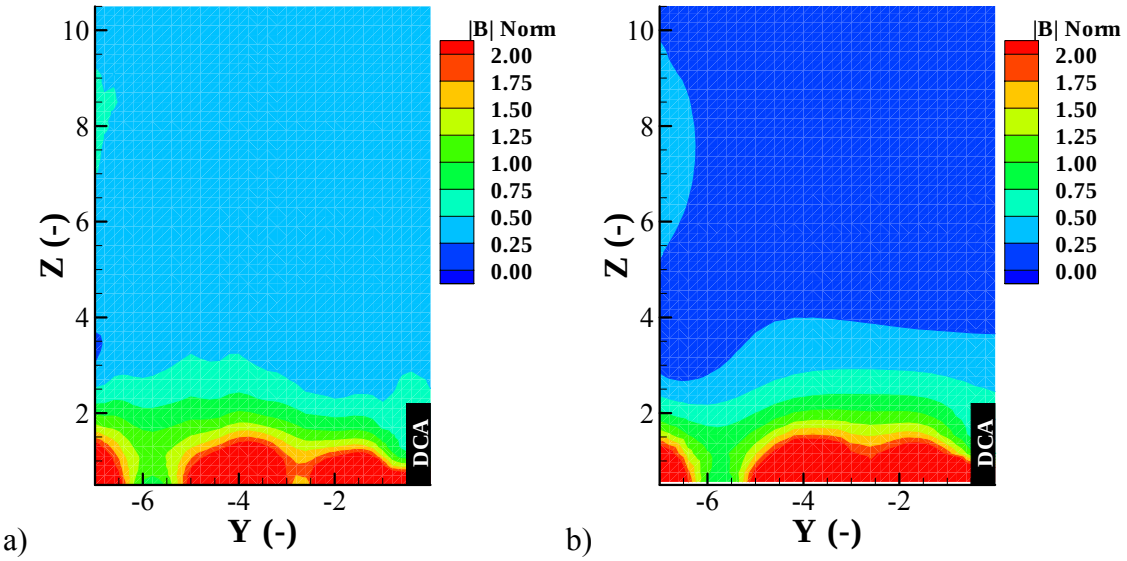

Figure A-3: Comparison of a) experimentally measured and b) simulated magnetic field for the X = 0 cm plane with I_{emag}= -5 A.

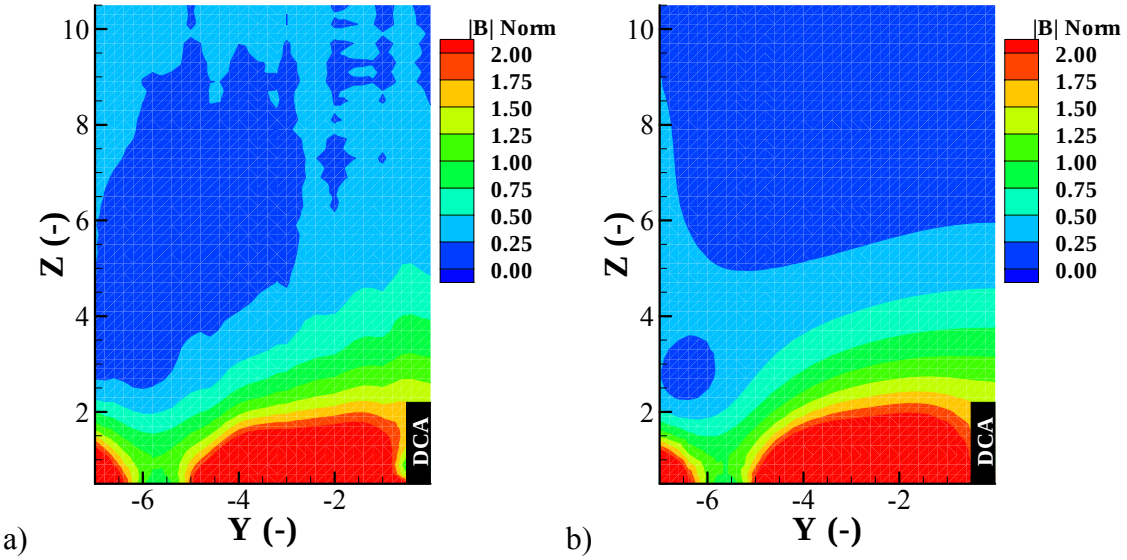

Figure A-4: Comparison of a) experimentally measured and b) simulated magnetic field for the X = 0 cm plane with I_{emag}= +5 A.

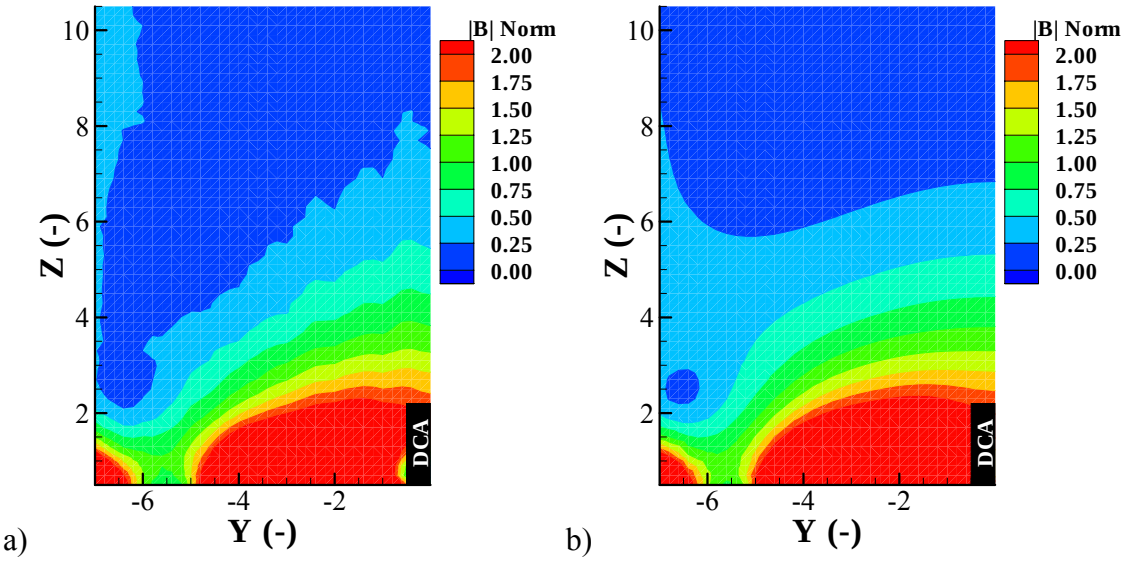

Figure A-5: Comparison of a) experimentally measured and b) simulated magnetic field for the X = 0 cm plane with I_{emag}= +10 A.

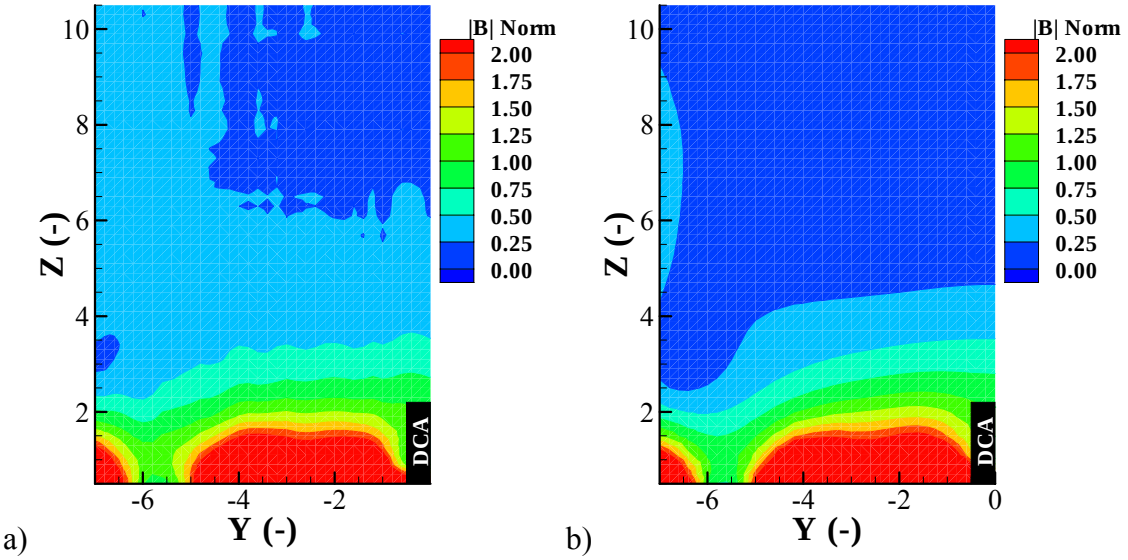

Figure A-6: Comparison of a) experimentally measured and b) simulated magnetic field for the X = 10.2 cm plane with I_{emag}= 0 A.

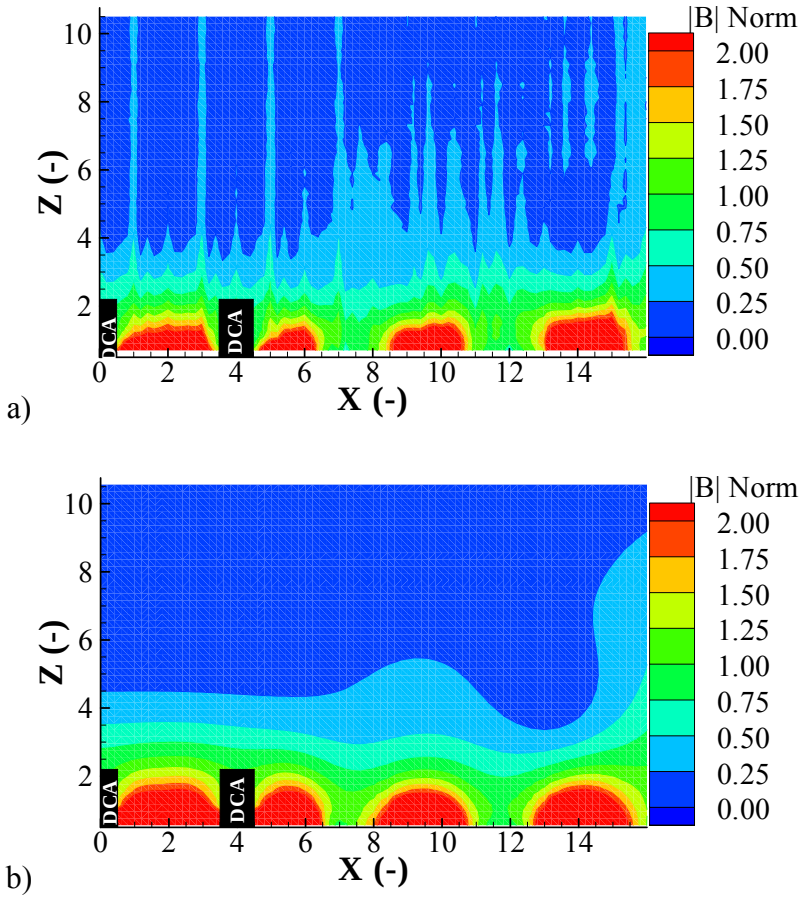

Figure A-7: Comparison of a) experimentally measured and b) simulated magnetic field for the Y = 0 cm plane with the 50 G line enclosed.

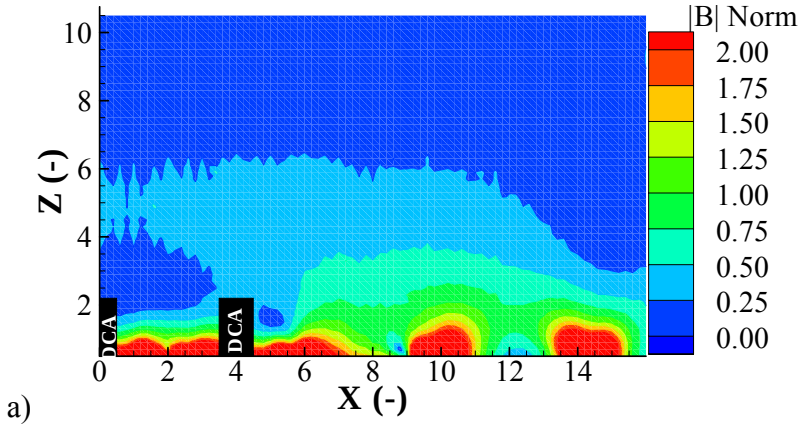

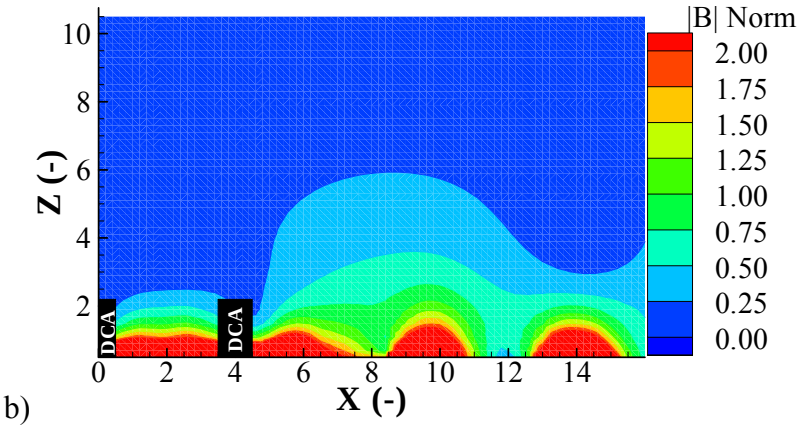

b)

Figure A-8: Comparison of a) experimentally measured and b) simulated magnetic field for the Y = 0 cm plane with I_{emag}= -10 A.

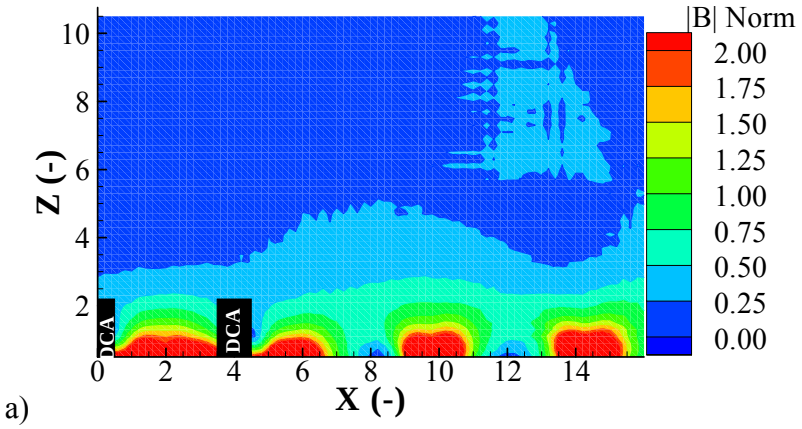

a)

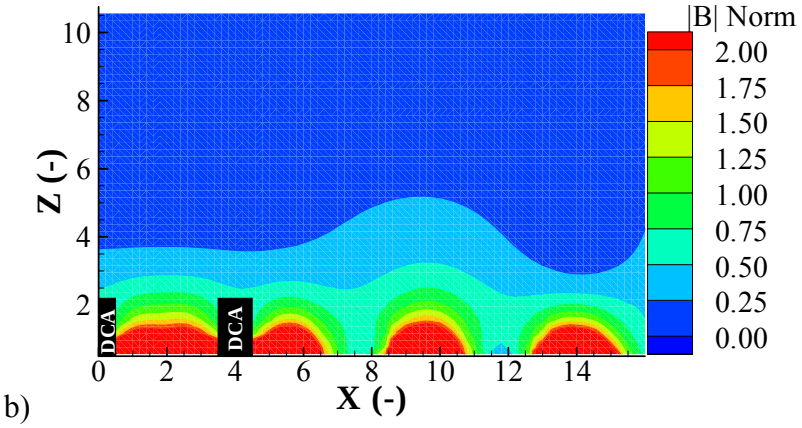

b)

Figure A-9: Comparison of a) experimentally measured and b) simulated magnetic field for the Y = 0 cm plane with I_{emag}= -5 A.

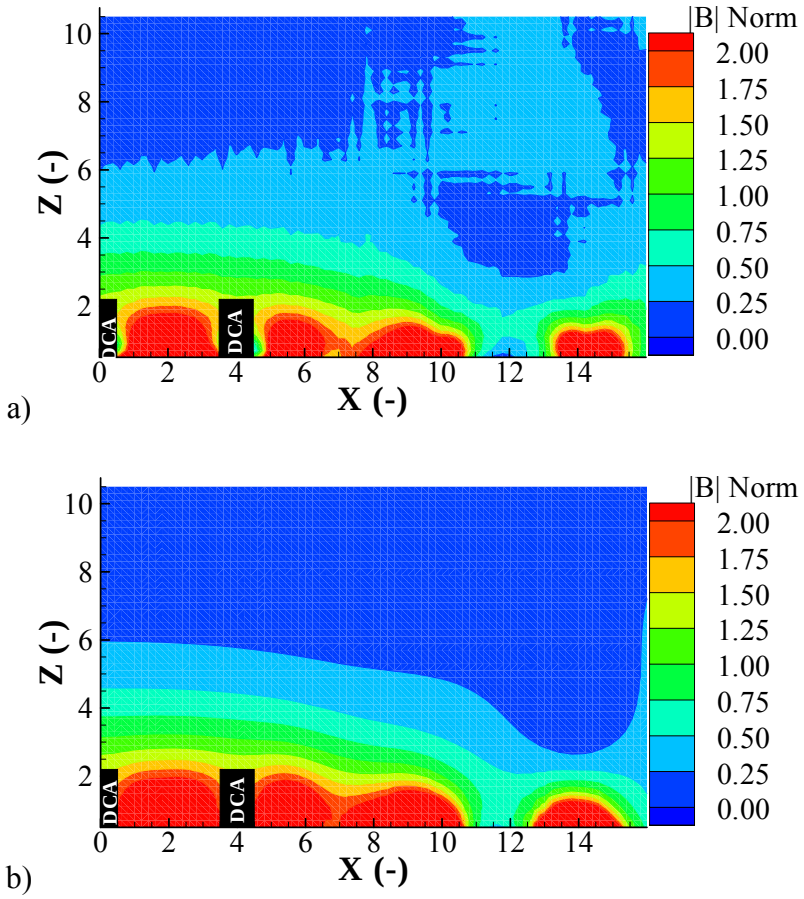

Figure A-10: Comparison of a) experimentally measured and b) simulated magnetic field for the Y = 0 cm plane with I_{emag}= +5 A.

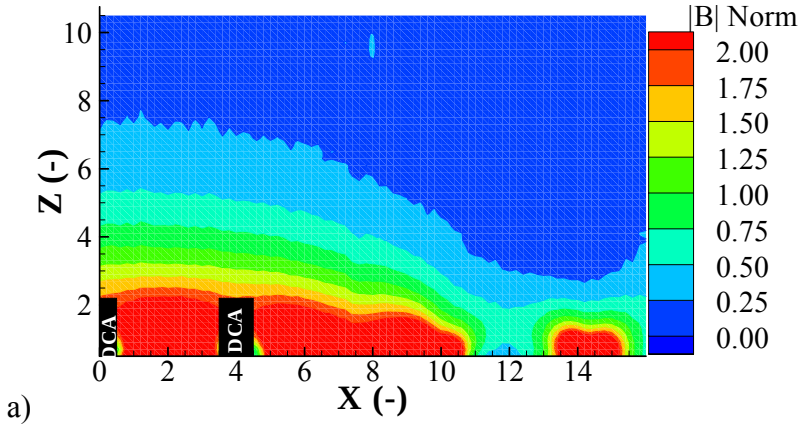

b)

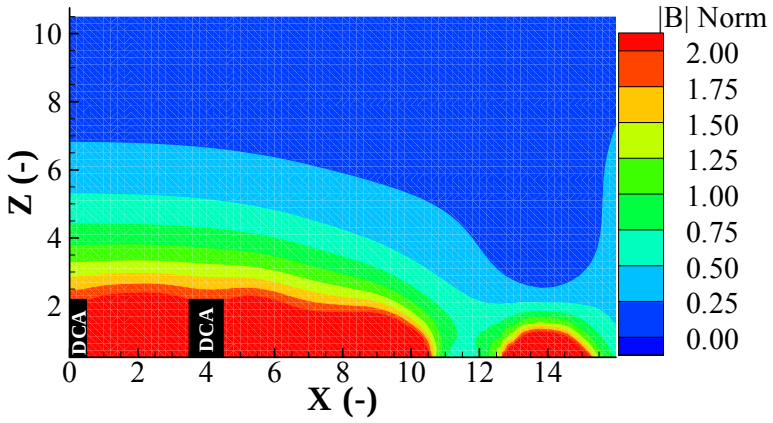

Figure A-11: Comparison of a) experimentally measured and b) simulated magnetic field for the Y = 0 cm plane with I_{emag}= +10 A.

APPENDIX B: TA OPERATIONAL CONFIGURATIONS

Configuration	DCA	I_{emag} (A) and/or Bfield Configuration	Dormant Cathode Electrical Connectivity	Dormant Cathode Mass Flow (sccm)
50LC	Left	50 G enclosed	Connected	No Flow
50MC	Center	50G enclosed	Connected	No Flow
50RC	Right	50G enclosed	Connected	No Flow
-10LC	Left	-10	Connected	No Flow
-10MC	Center	-10	Connected	No Flow
-10RC	Right	-10	Connected	No Flow
-5LC	Left	-5	Connected	No Flow
-5MC	Center	-5	Connected	No Flow
-5RC	Right	-5	Connected	No Flow
0LC	Left	0	Connected	No Flow
0MC	Center	0	Connected	No Flow
0RC	Right	0	Connected	No Flow
5LC	Left	5	Connected	No Flow
5MC	Center	5	Connected	No Flow
5RC	Right	5	Connected	No Flow
10LC	Left	10	Connected	No Flow
10MC	Center	10	Connected	No Flow
10RC	Right	10	Connected	No Flow
50LI	Left	50 G enclosed	Isolated	No Flow
50MI	Center	50 G enclosed	Isolated	No Flow
50RI	Right	50 G enclosed	Isolated	No Flow
-10LI	Left	-10	Isolated	No Flow
-10MI	Center	-10	Isolated	No Flow
-10RI	Right	-10	Isolated	No Flow
-5LI	Left	-5	Isolated	No Flow
-5MI	Center	-5	Isolated	No Flow
-5RI	Right	-5	Isolated	No Flow
0LI	Left	0	Isolated	No Flow
0MI	Center	0	Isolated	No Flow
0RI	Right	0	Isolated	No Flow
5LI	Left	5	Isolated	No Flow

5MI	Center	5	Isolated	No Flow
5RI	Right	5	Isolated	No Flow
10LI	Left	10	Isolated	No Flow
10MI	Center	10	Isolated	No Flow
10RI	Right	10	Isolated	No Flow
50LCH	Left	50 G enclosed	Connected	Half DCA Flow
50MCH	Center	50 G enclosed	Connected	Half DCA Flow
50RCH	Right	50 G enclosed	Connected	Half DCA Flow
-10LCH	Left	-10	Connected	Half DCA Flow
-10MCH	Center	-10	Connected	Half DCA Flow
-10RCH	Right	-10	Connected	Half DCA Flow
-5LCH	Left	-5	Connected	Half DCA Flow
-5MCH	Center	-5	Connected	Half DCA Flow
-5RCH	Right	-5	Connected	Half DCA Flow
0LCH	Left	0	Connected	Half DCA Flow
0MCH	Center	0	Connected	Half DCA Flow
0RCH	Right	0	Connected	Half DCA Flow
5LCH	Left	5	Connected	Half DCA Flow
5MCH	Center	5	Connected	Half DCA Flow
5RCH	Right	5	Connected	Half DCA Flow
10LCH	Left	10	Connected	Half DCA Flow
10MCH	Center	10	Connected	Half DCA Flow
10RCH	Right	10	Connected	Half DCA Flow
50LIH	Left	50 G enclosed	Isolated	Half DCA Flow
50MIH	Center	50 G enclosed	Isolated	Half DCA Flow
50RIH	Right	50 G enclosed	Isolated	Half DCA Flow
-10LIH	Left	-10	Isolated	Half DCA Flow
-10MIH	Center	-10	Isolated	Half DCA Flow
-10RIH	Right	-10	Isolated	Half DCA Flow
-5LIH	Left	-5	Isolated	Half DCA Flow
-5MIH	Center	-5	Isolated	Half DCA Flow
-5RIH	Right	-5	Isolated	Half DCA Flow
0LIH	Left	0	Isolated	Half DCA Flow
0MIH	Center	0	Isolated	Half DCA Flow
0RIH	Right	0	Isolated	Half DCA Flow
5LIH	Left	5	Isolated	Half DCA Flow
5MIH	Center	5	Isolated	Half DCA Flow
5RIH	Right	5	Isolated	Half DCA Flow
10LIH	Left	10	Isolated	Half DCA Flow

10MIH	Center	10	Isolated	Half DCA Flow
10RIH	Right	10	Isolated	Half DCA Flow
50LCF	Left	50 G enclosed	Connected	Full DCA Flow
50MCF	Center	50 G enclosed	Connected	Full DCA Flow
50RCF	Right	50 G enclosed	Connected	Full DCA Flow
-10LCF	Left	-10	Connected	Full DCA Flow
-10MCF	Center	-10	Connected	Full DCA Flow
-10RCF	Right	-10	Connected	Full DCA Flow
-5LCF	Left	-5	Connected	Full DCA Flow
-5MCF	Center	-5	Connected	Full DCA Flow
-5RCF	Right	-5	Connected	Full DCA Flow
0LCF	Left	0	Connected	Full DCA Flow
0MCF	Center	0	Connected	Full DCA Flow
0RCF	Right	0	Connected	Full DCA Flow
5LCF	Left	5	Connected	Full DCA Flow
5MCF	Center	5	Connected	Full DCA Flow
5RCF	Right	5	Connected	Full DCA Flow
10LCF	Left	10	Connected	Full DCA Flow
10MCF	Center	10	Connected	Full DCA Flow
10RCF	Right	10	Connected	Full DCA Flow
50LIF	Left	50 G enclosed	Isolated	Full DCA Flow
50MIF	Center	50 G enclosed	Isolated	Full DCA Flow
50RIF	Right	50 G enclosed	Isolated	Full DCA Flow
-10LIF	Left	-10	Isolated	Full DCA Flow
-10MIF	Center	-10	Isolated	Full DCA Flow
-10RIF	Right	-10	Isolated	Full DCA Flow
-5LIF	Left	-5	Isolated	Full DCA Flow
-5MIF	Center	-5	Isolated	Full DCA Flow
-5RIF	Right	-5	Isolated	Full DCA Flow
0LIF	Left	0	Isolated	Full DCA Flow
0MIF	Center	0	Isolated	Full DCA Flow
0RIF	Right	0	Isolated	Full DCA Flow
5LIF	Left	5	Isolated	Full DCA Flow
5MIF	Center	5	Isolated	Full DCA Flow
5RIF	Right	5	Isolated	Full DCA Flow
10LIF	Left	10	Isolated	Full DCA Flow
10MIF	Center	10	Isolated	Full DCA Flow
10RIF	Right	10	Isolated	Full DCA Flow

Table B-1: Possible TA operational configurations and nomenclature.

APPENDIX C: 5PLP-DC RESULTS

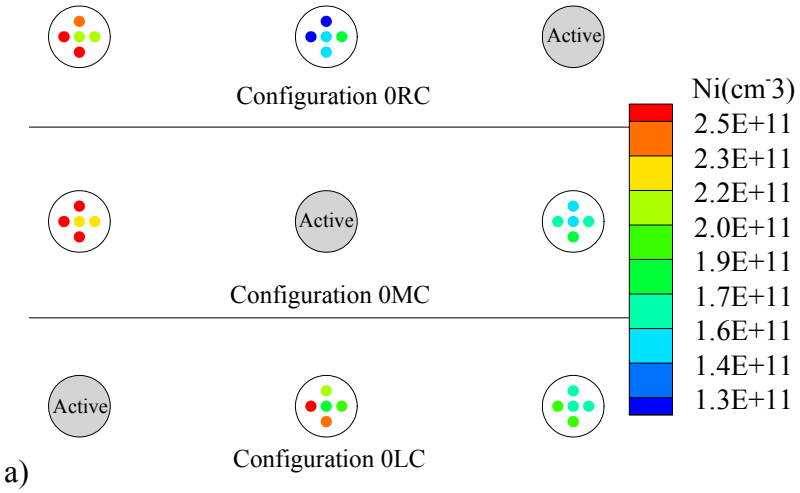

a)

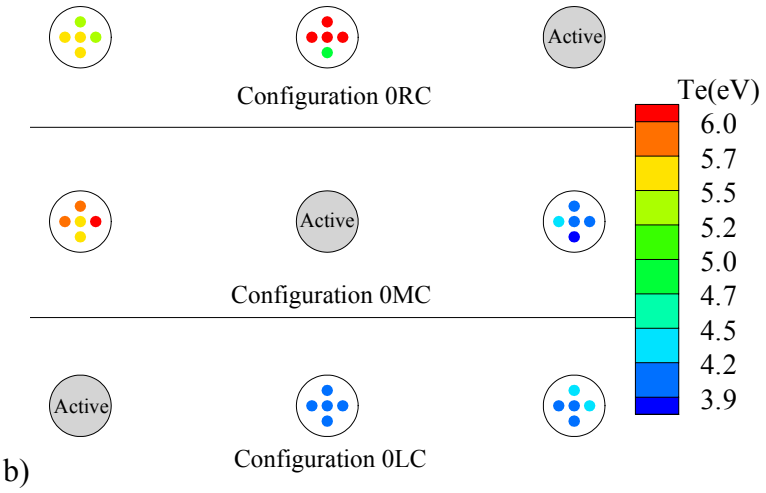

b)

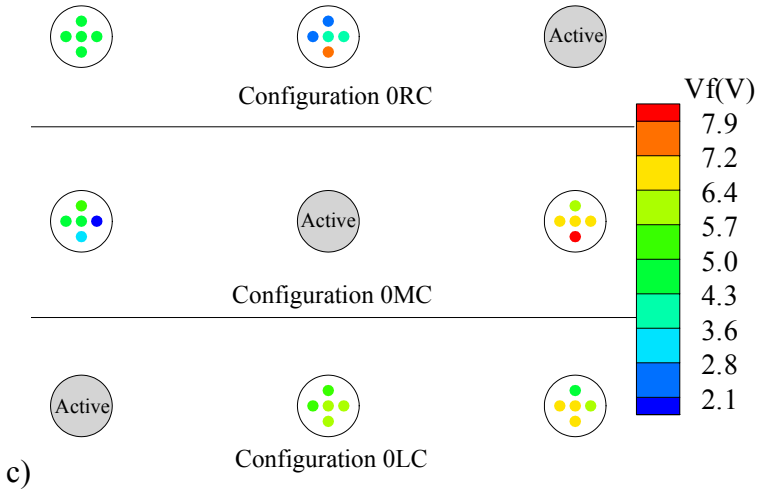

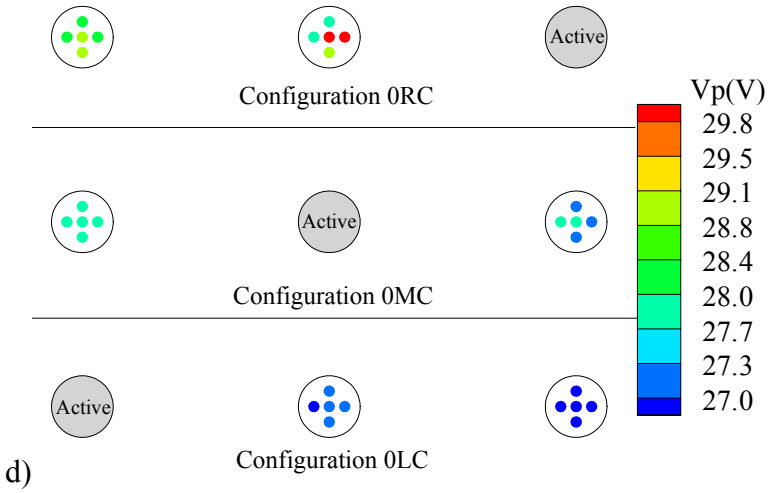

Figure C-1: a) Number density, b) electron temperature, c) floating potential, and d) plasma potential 5PLP-DC results for the 0RC, 0MC, and 0LC configurations.

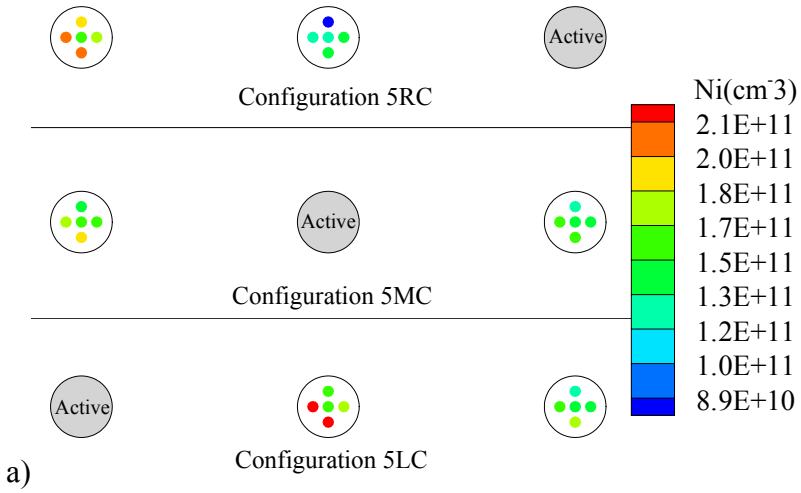

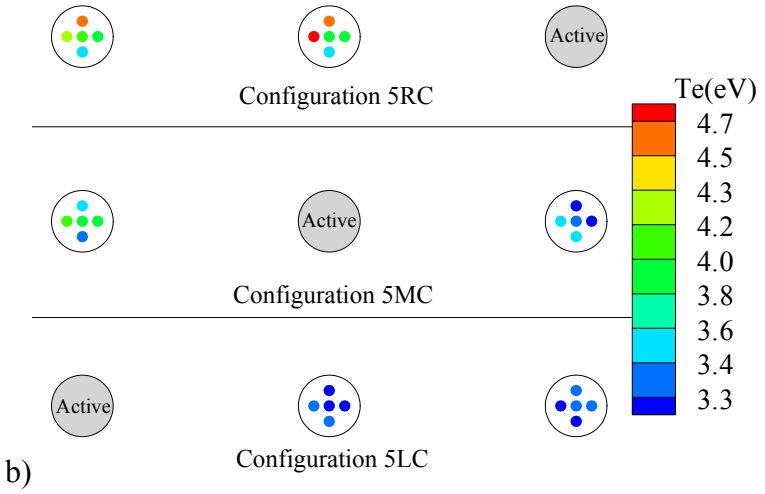

b)

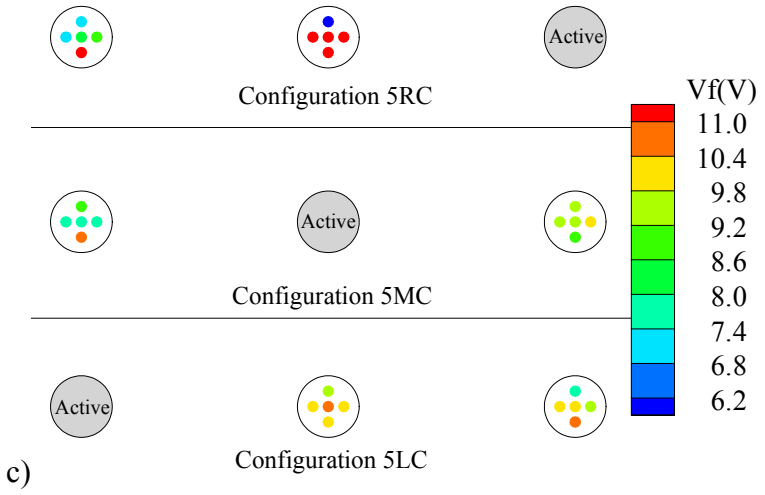

c)

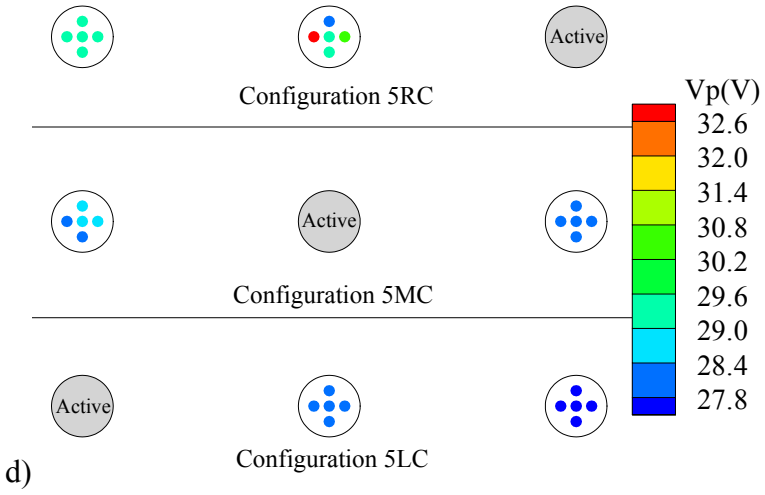

d)

Figure C-2: a) Number density, b) electron temperature, c) floating potential, and d) plasma potential 5PLP-DC results for the 5RC, 5MC, and 5LC configurations.

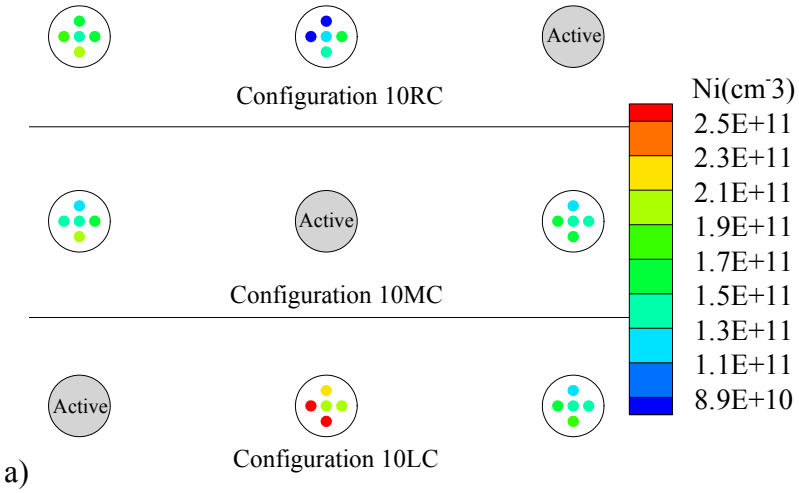
Active
Configuration 10RC
Active
Active
Configuration 10MC
Active
Configuration 10LC
Ni(cm-3)
2.5E+11
2.3E+11
2.1E+11
1.9E+11
1.7E+11
1.5E+11
1.3E+11
1.1E+11
8.9E+10

a)

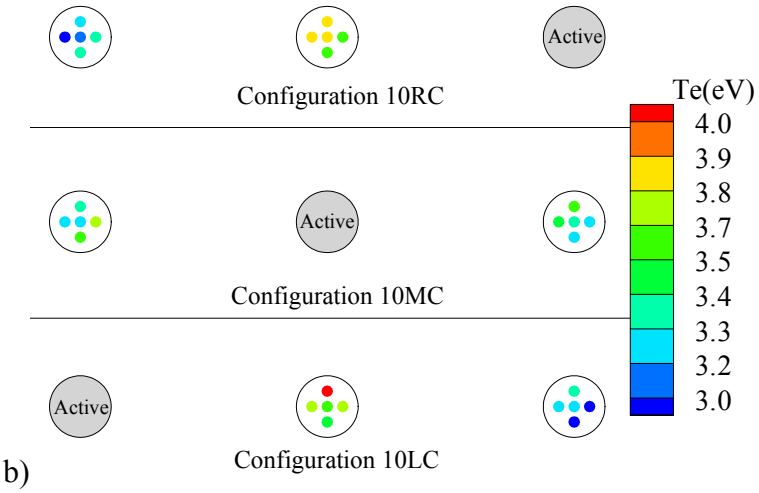
Active
Configuration 10RC
Active
Active
Configuration 10MC
Active
Configuration 10LC
Te(eV)
4.0
3.9
3.8
3.7
3.5
3.4
3.3
3.2
3.0

b)

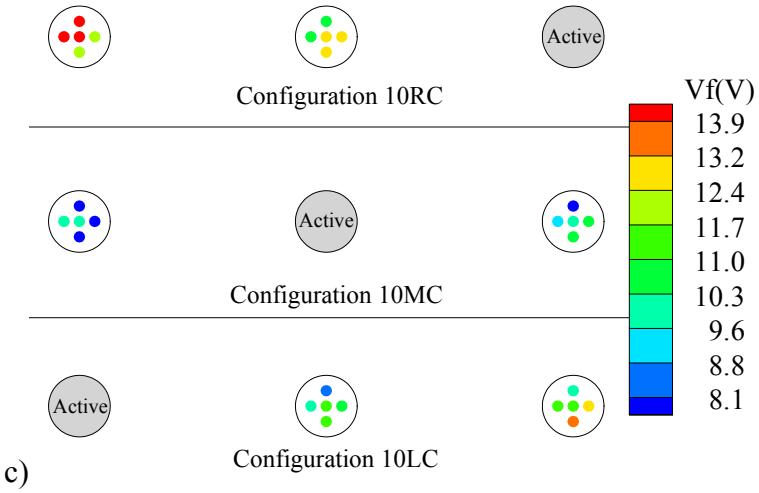
Active
Configuration 10RC
Active
Active
Configuration 10MC
Active
Configuration 10LC
Vf(V)
13.9
13.2
12.4
11.7
11.0
10.3
9.6
8.8
8.1

c)

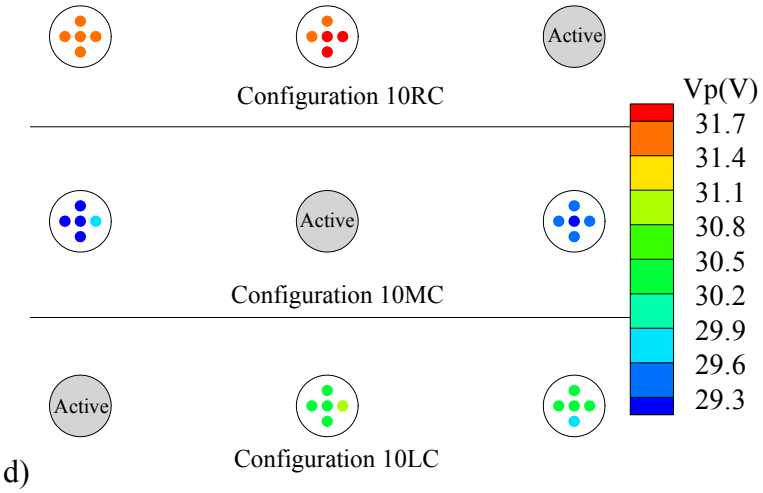

d)

Figure C-3: a) Number density, b) electron temperature, c) floating potential, and d) plasma potential 5PLP-DC results for the 10RC, 10MC, and 10LC configurations.

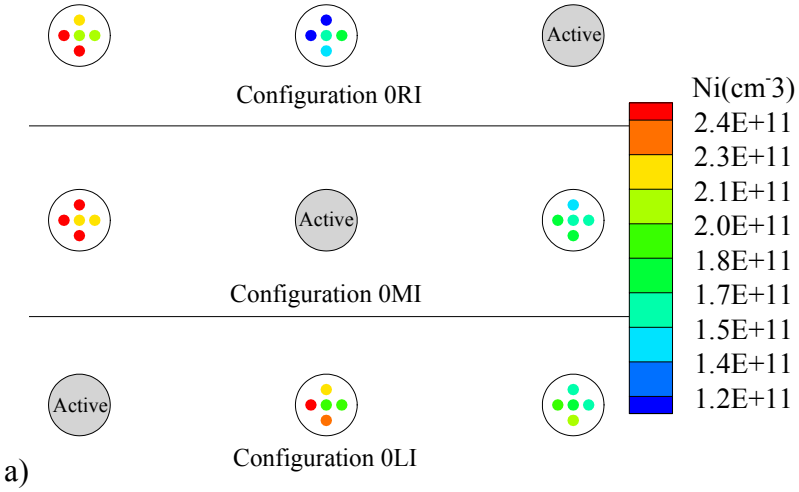

a)

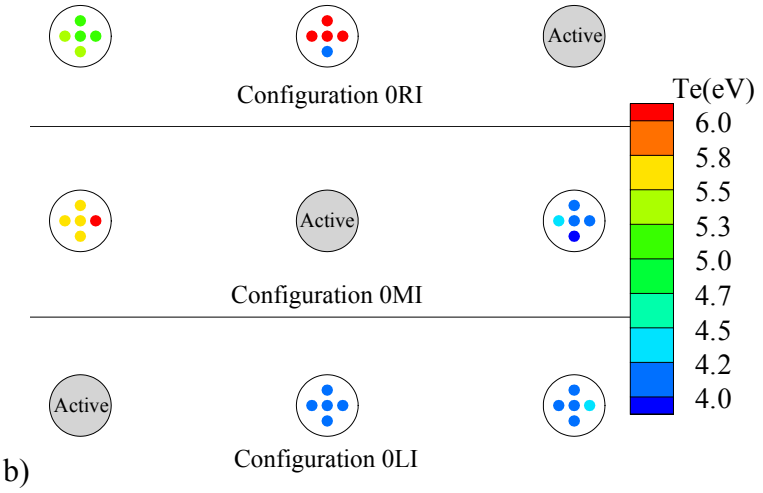

b)

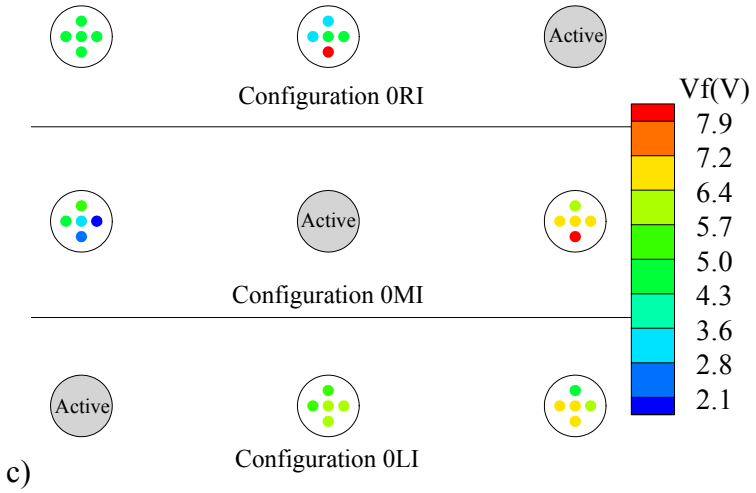

c)

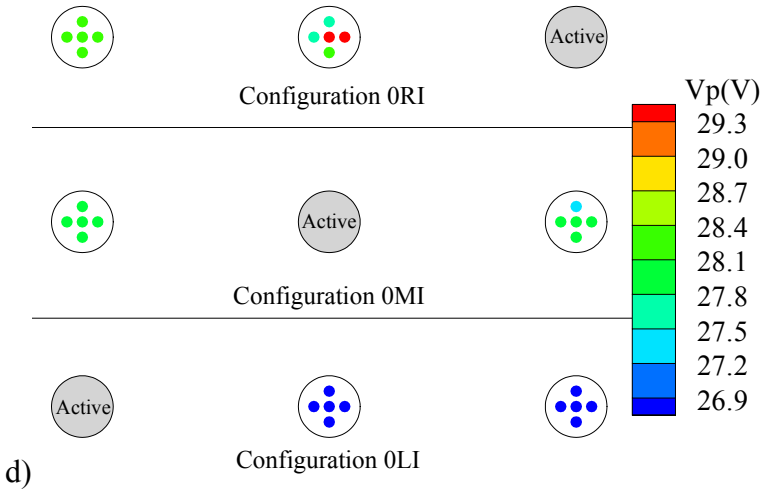

d)

Figure C-4: a) Number density, b) electron temperature, c) floating potential, and d) plasma potential 5PLP-DC results for the 0RI, 0MI, and 0LI configurations.

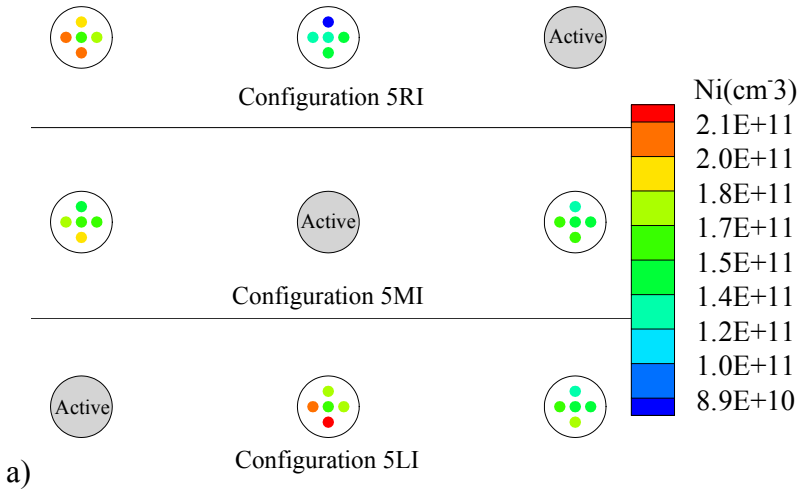

a)

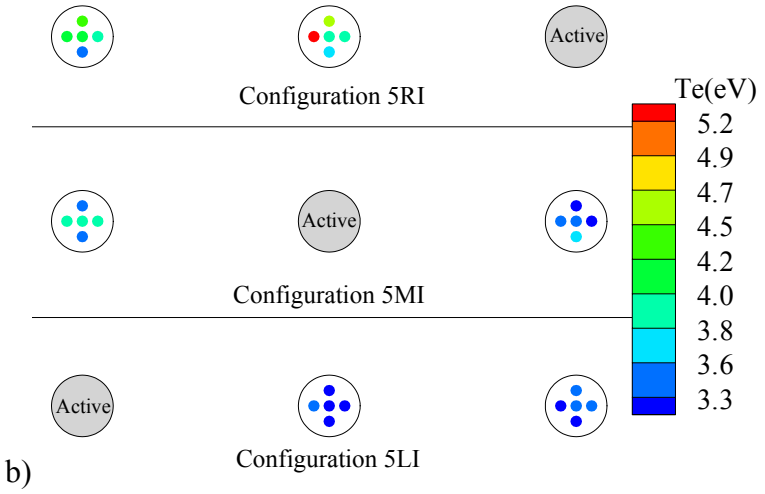

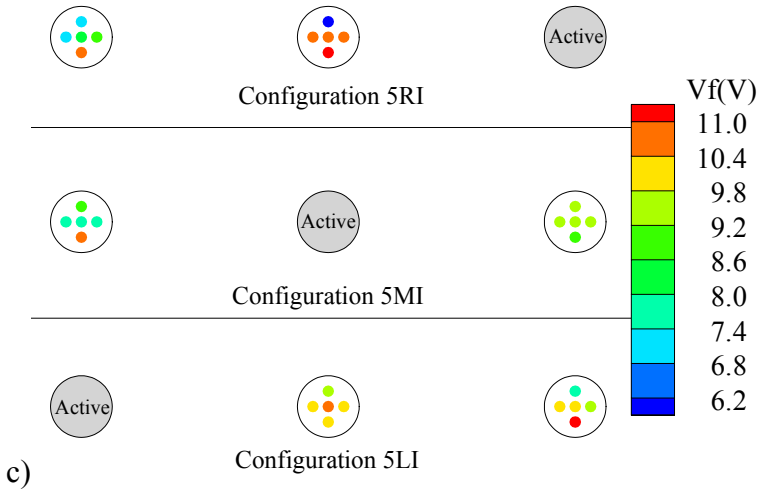

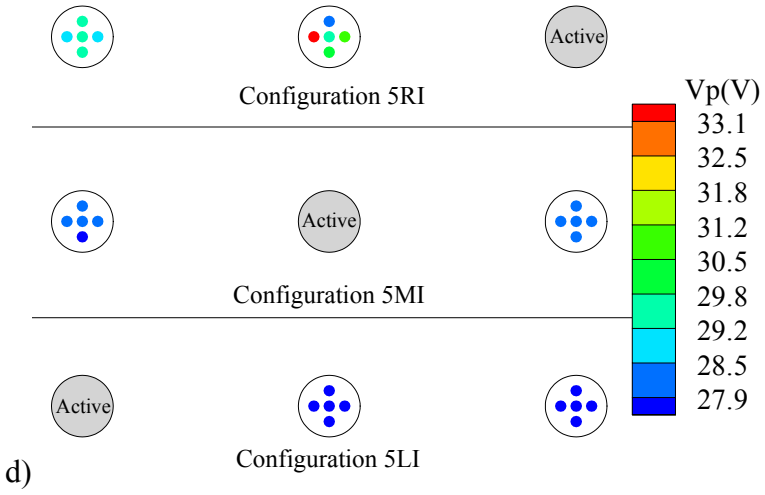

Figure C-5: a) Number density, b) electron temperature, c) floating potential, and d) plasma potential 5PLP-DC results for the 5RI, 5MI, and 5LI configurations.

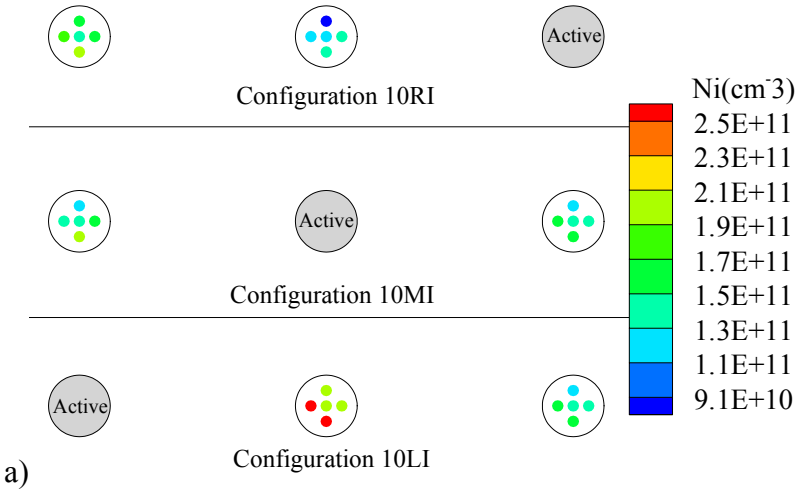
Active
Configuration 10RI
Ni(cm-3)
2.5E+11
2.3E+11
2.1E+11
1.9E+11
1.7E+11
1.5E+11
1.3E+11
1.1E+11
9.1E+10
Active
Active
Configuration 10MI
Active
Configuration 10LI

a)

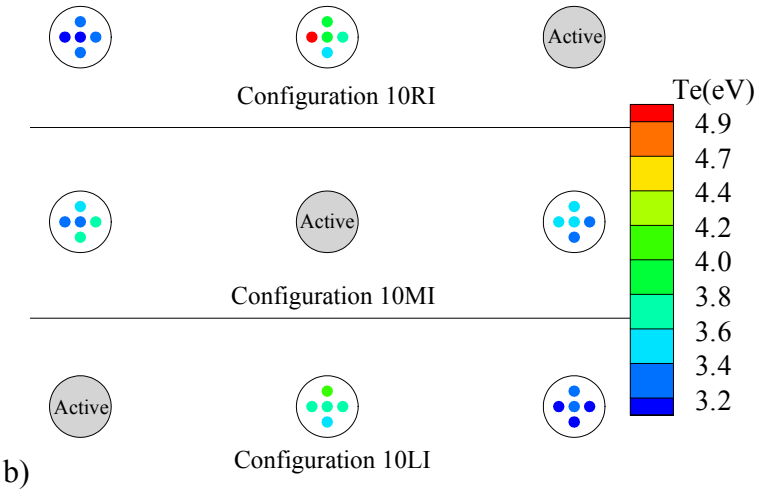
Active
Configuration 10RI
Te(eV)
4.9
4.7
4.4
4.2
4.0
3.8
3.6
3.4
3.2
Active
Active
Configuration 10MI
Active
Configuration 10LI

b)

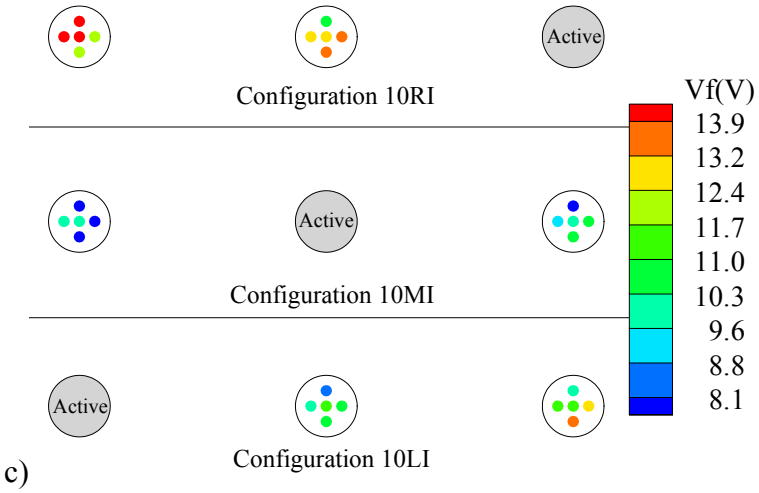
Active
Configuration 10RI
Vf(V)
13.9
13.2
12.4
11.7
11.0
10.3
9.6
8.8
8.1
Active
Active
Configuration 10MI
Active
Configuration 10LI

c)

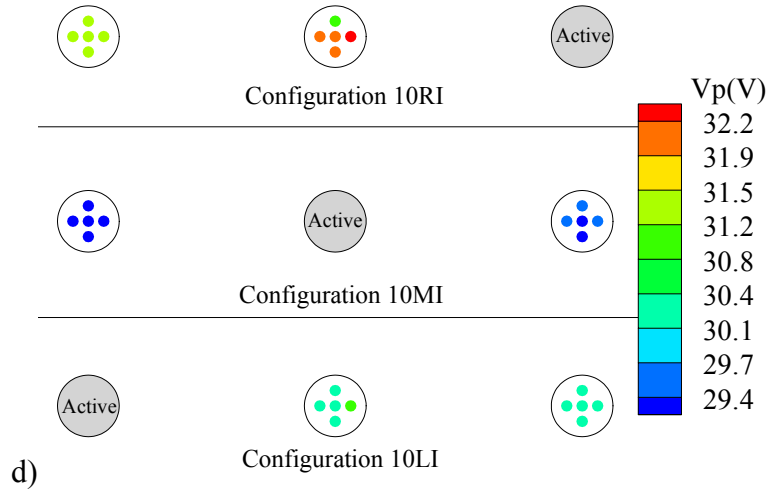

Figure C-6: a) Number density, b) electron temperature, c) floating potential, and d) plasma potential 5PLP-DC results for the 10RI, 10MI, and 10LI configurations.

APPENDIX D: INTERNAL PLASMA STRUCTURE

D.1 Plane 1 (Y = 0 cm)

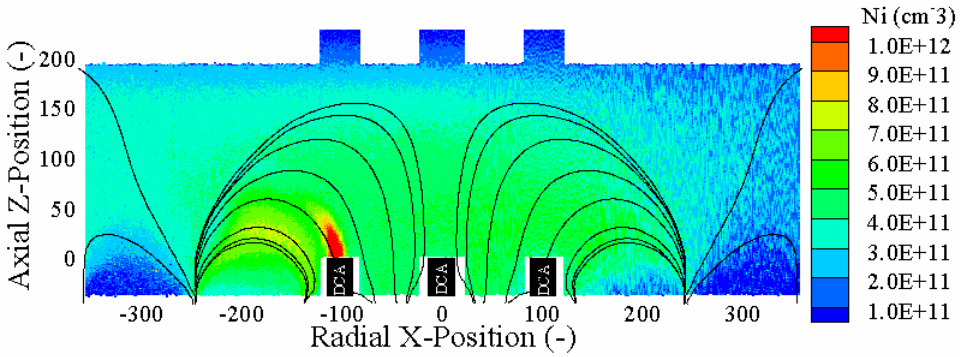

a)

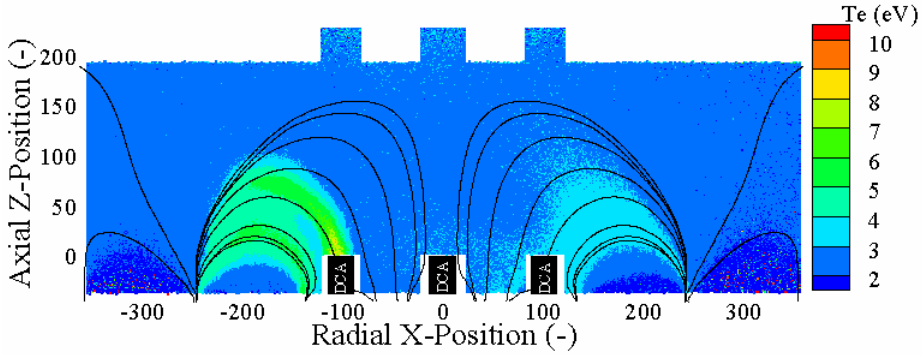

b)

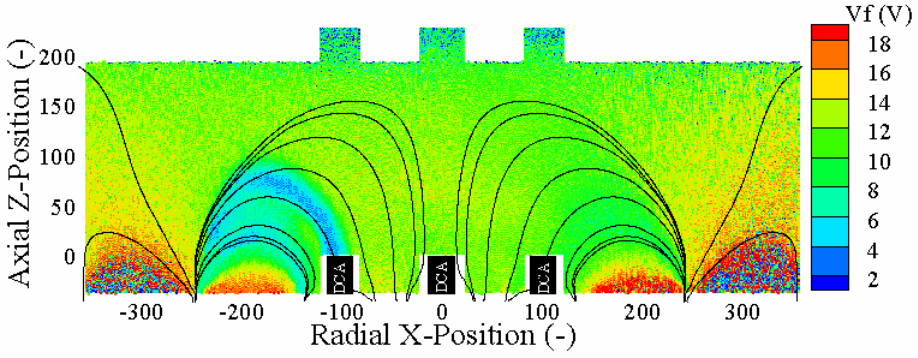

c)

d)

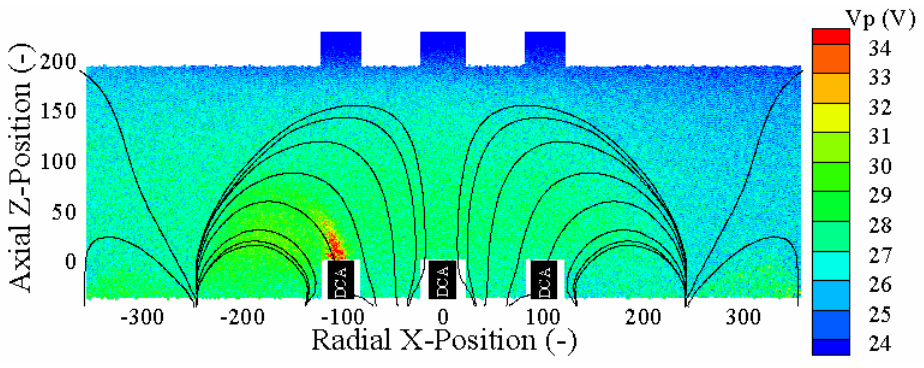

Figure D-1: a) Number density, b) electron temperature, c) floating potential, and d) plasma potential for configuration 0LC at plane 1.

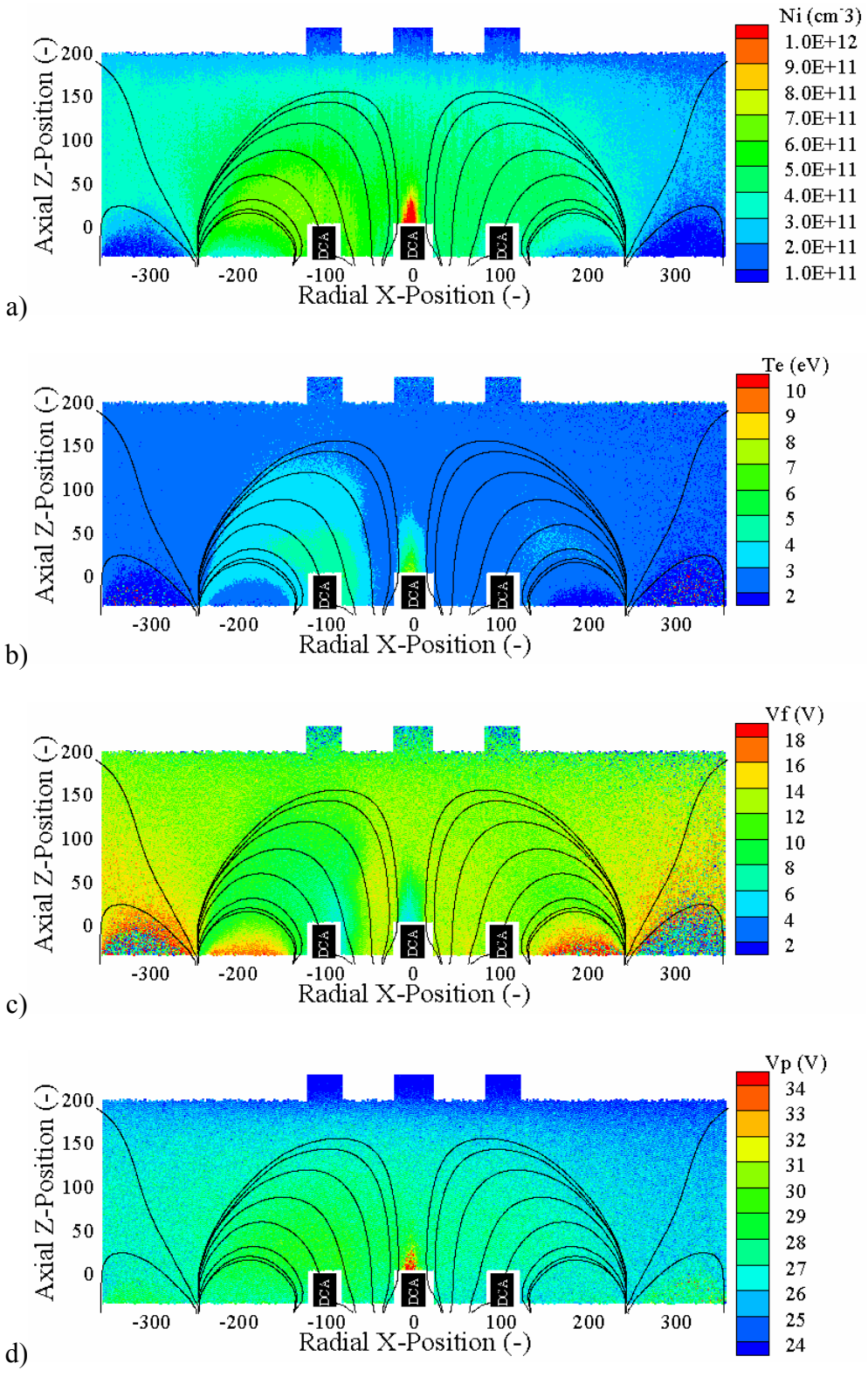

Figure D-2: a) Number density, b) electron temperature, c) floating potential, and d) plasma potential for configuration 0MC at plane 1.

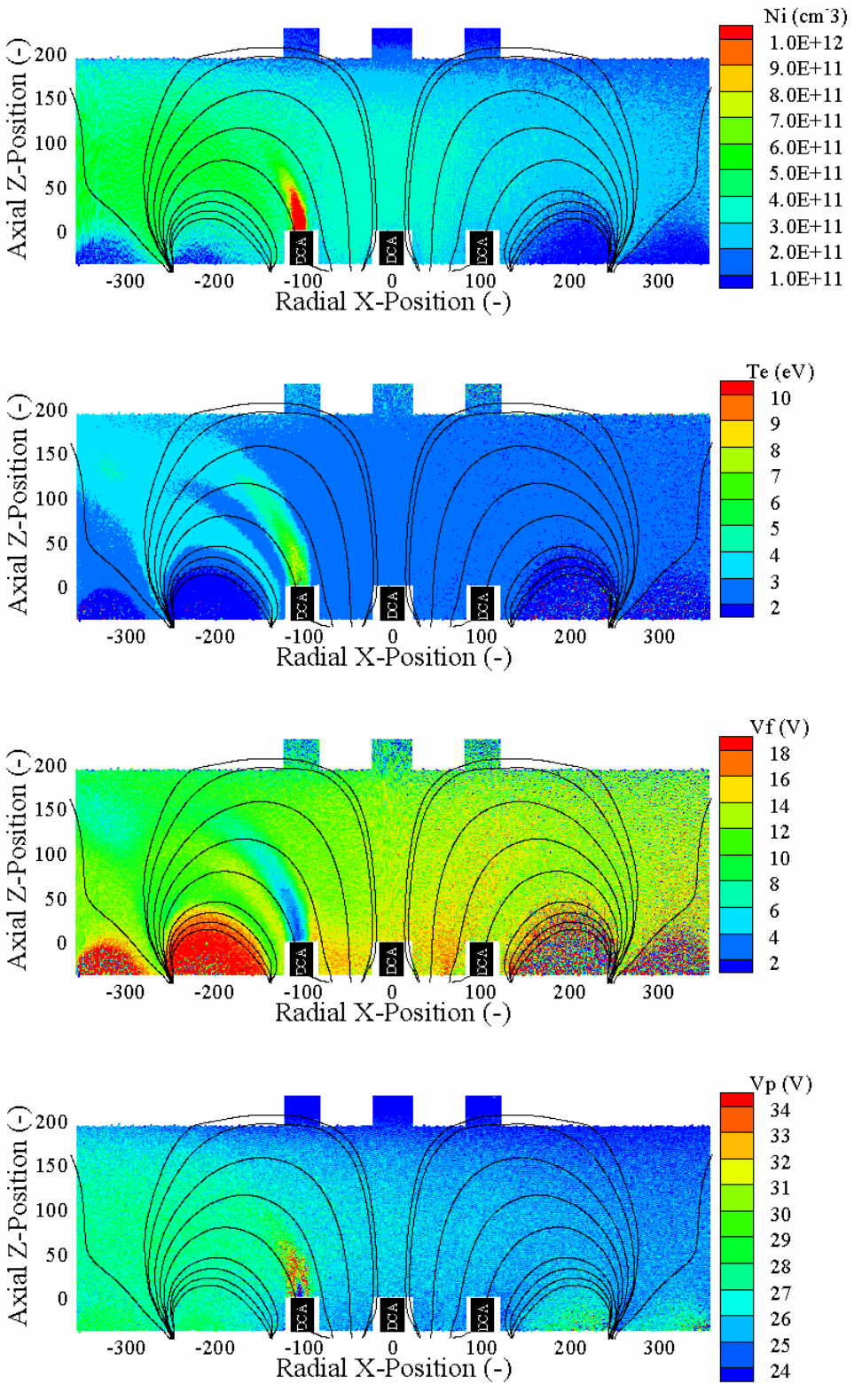

Figure D-3: a) Number density, b) electron temperature, c) floating potential, and d) plasma potential for configuration 5LC at plane 1.

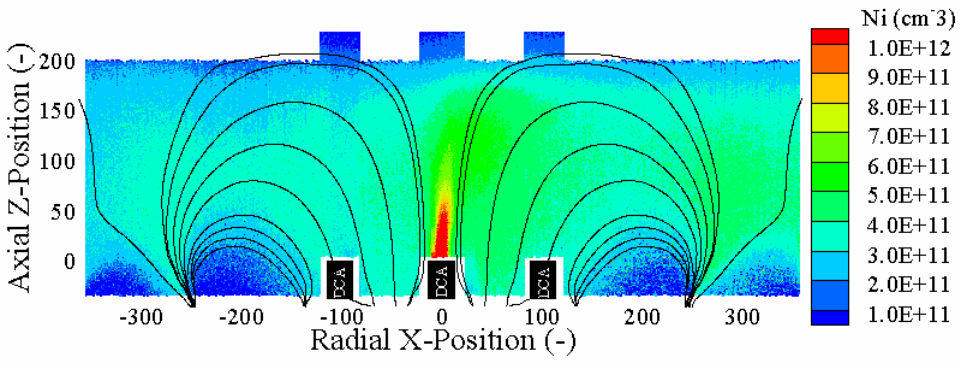

a)

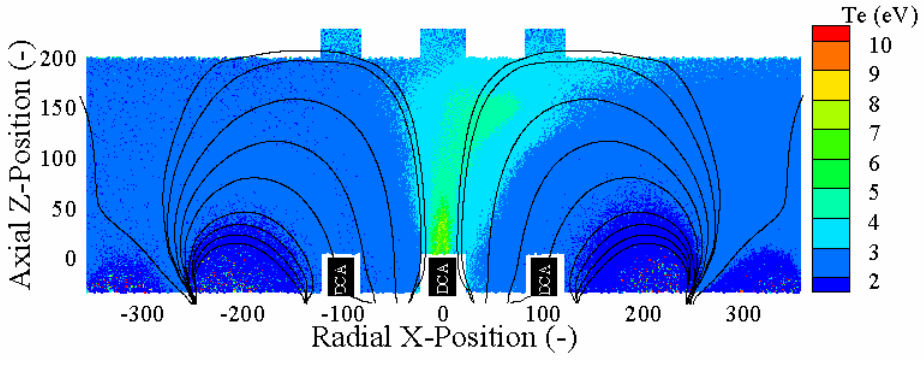

b)

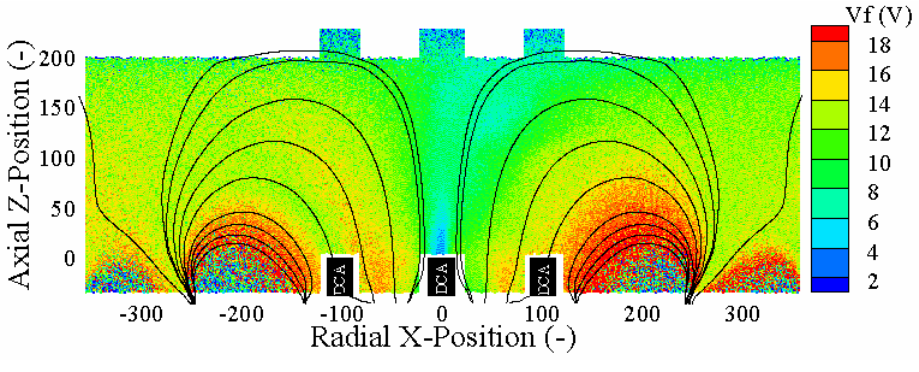

c)

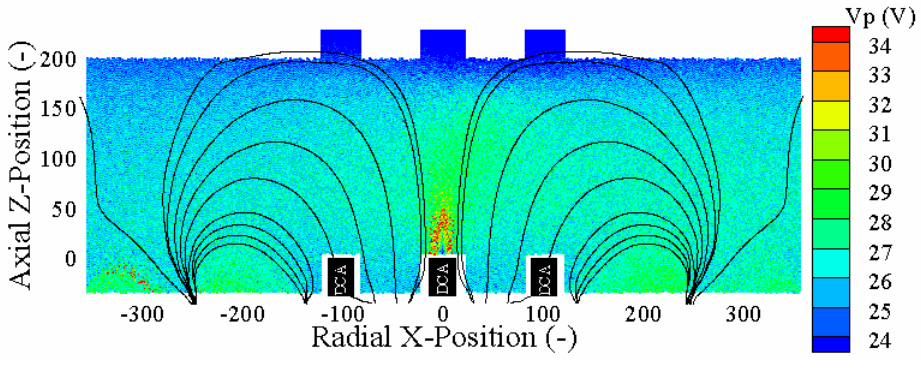

d)

Figure D-4: a) Number density, b) electron temperature, c) floating potential, and d) plasma potential for configuration 5MC at plane 1.

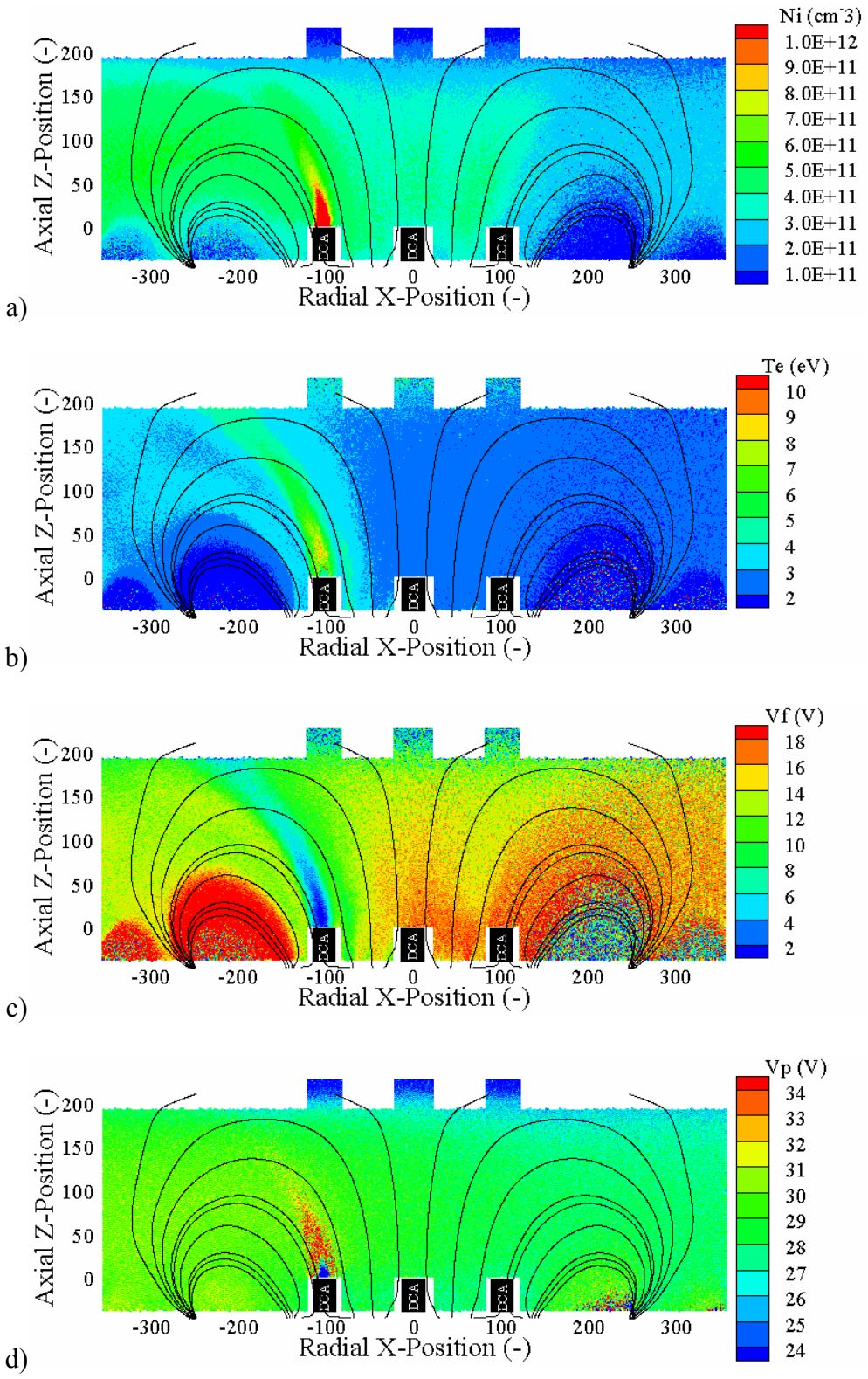

Figure D-5: a) Number density, b) electron temperature, c) floating potential, and d) plasma potential for configuration 10LC at plane 1.

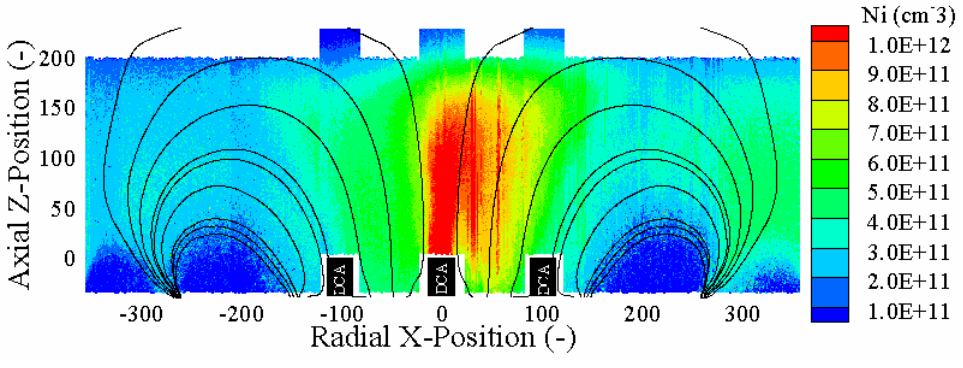

a)

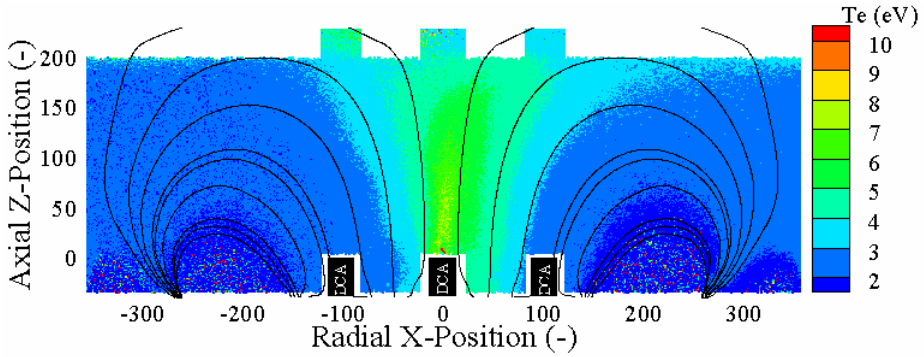

b)

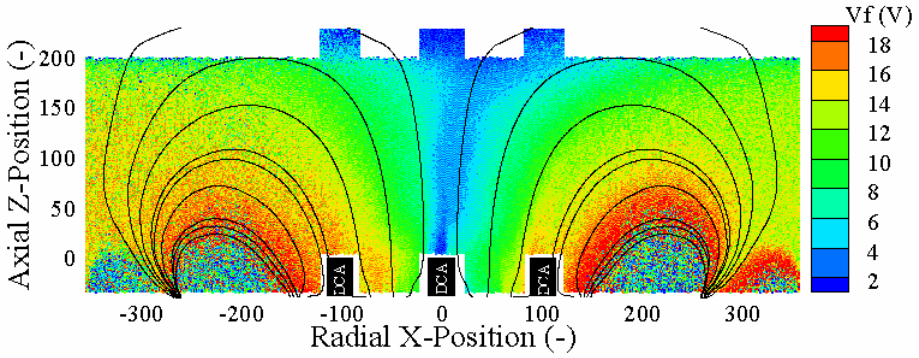

c)

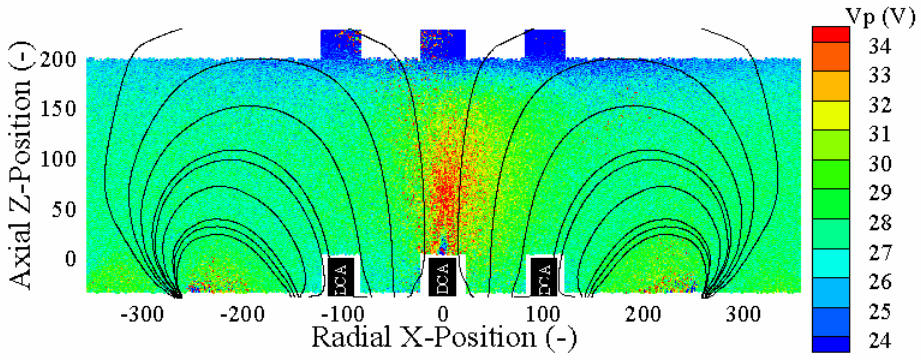

d)

Figure D-6: a) Number density, b) electron temperature, c) floating potential, and d) plasma potential for configuration 10MC at plane 1.

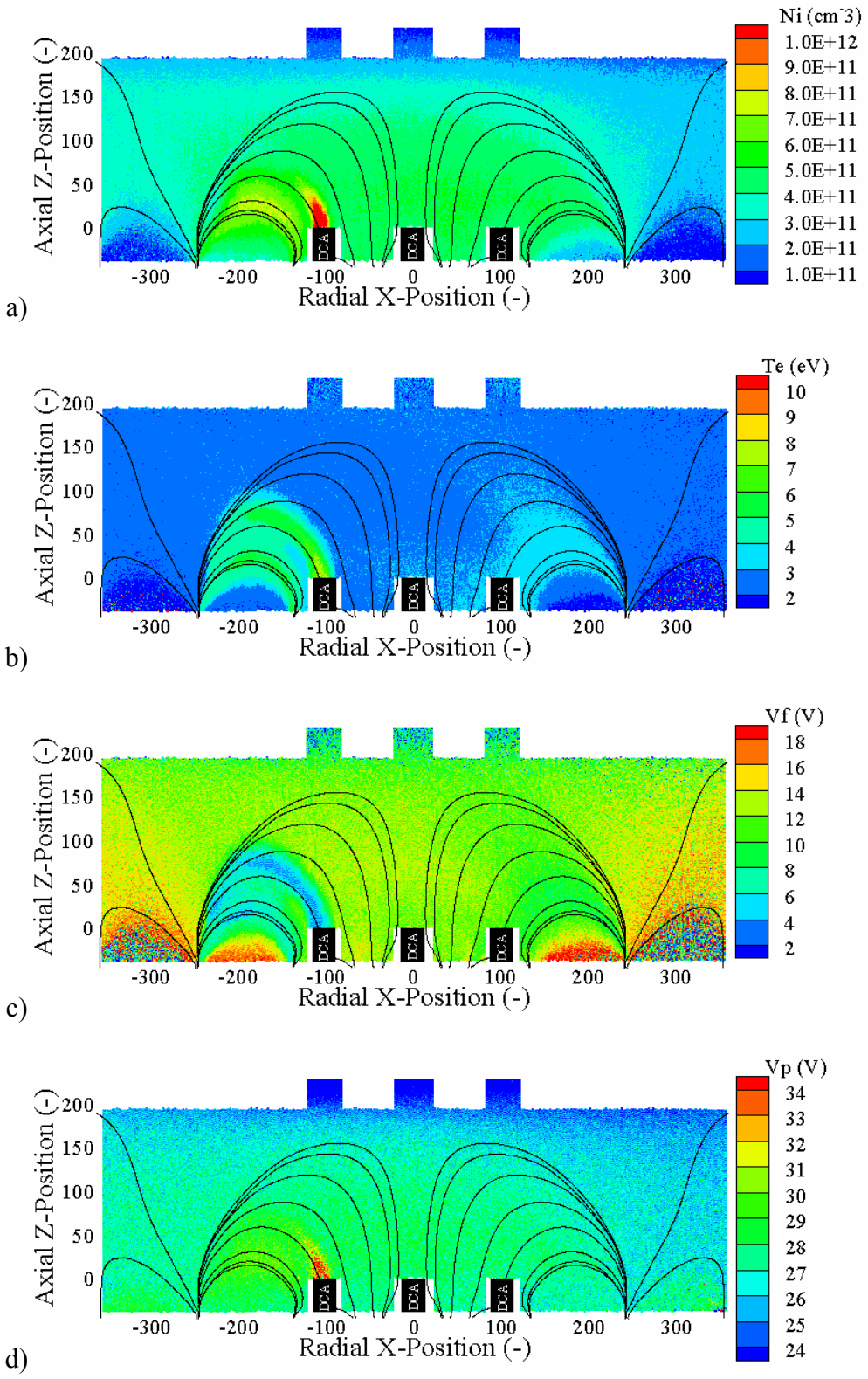

Figure D-7: a) Number density, b) electron temperature, c) floating potential, and d) plasma potential for configuration 0LI at plane 1.

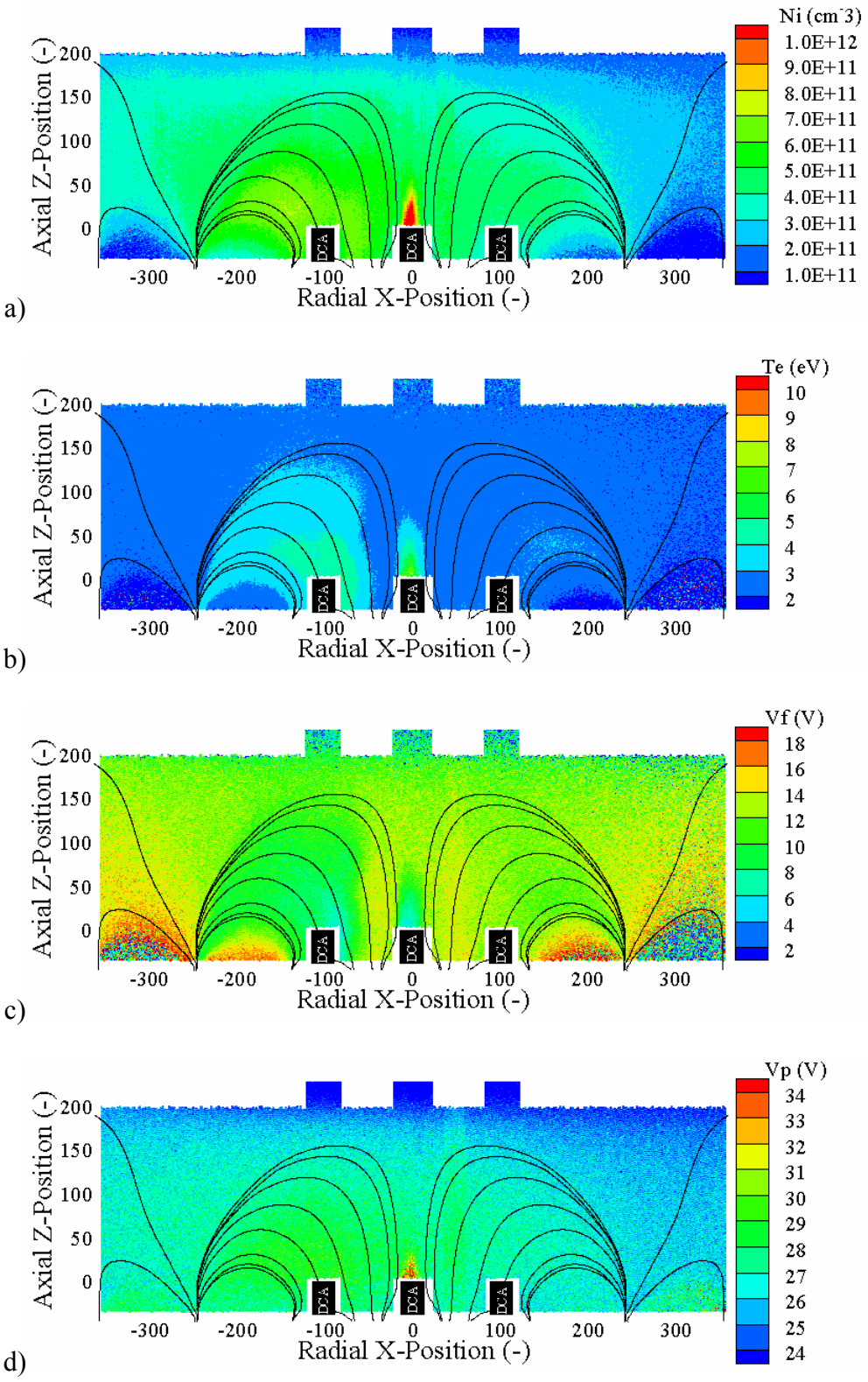

Figure D-8: a) Number density, b) electron temperature, c) floating potential, and d) plasma potential for configuration 0MI at plane 1.

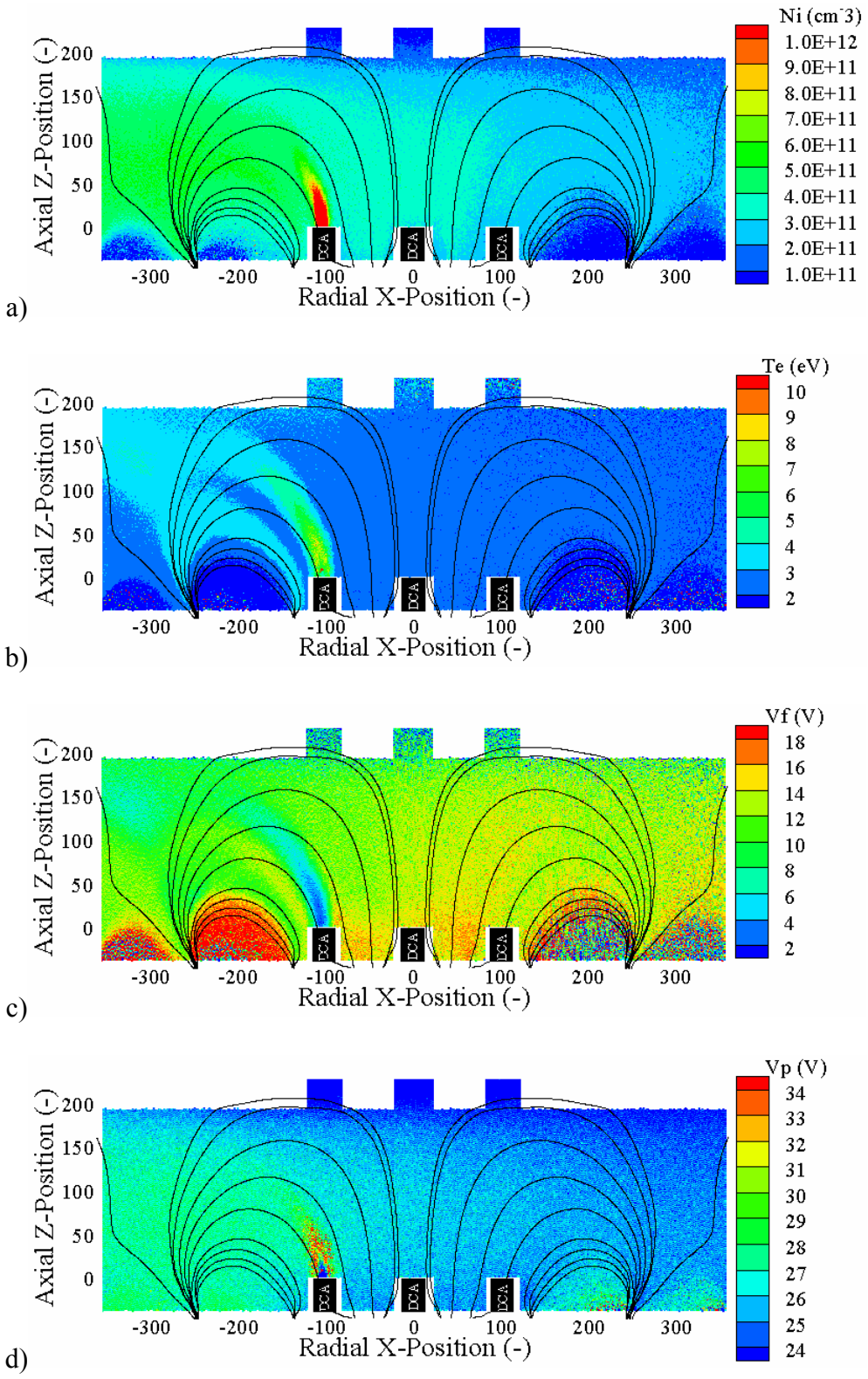

Figure D-9: a) Number density, b) electron temperature, c) floating potential, and d) plasma potential for configuration 5LI at plane 1.

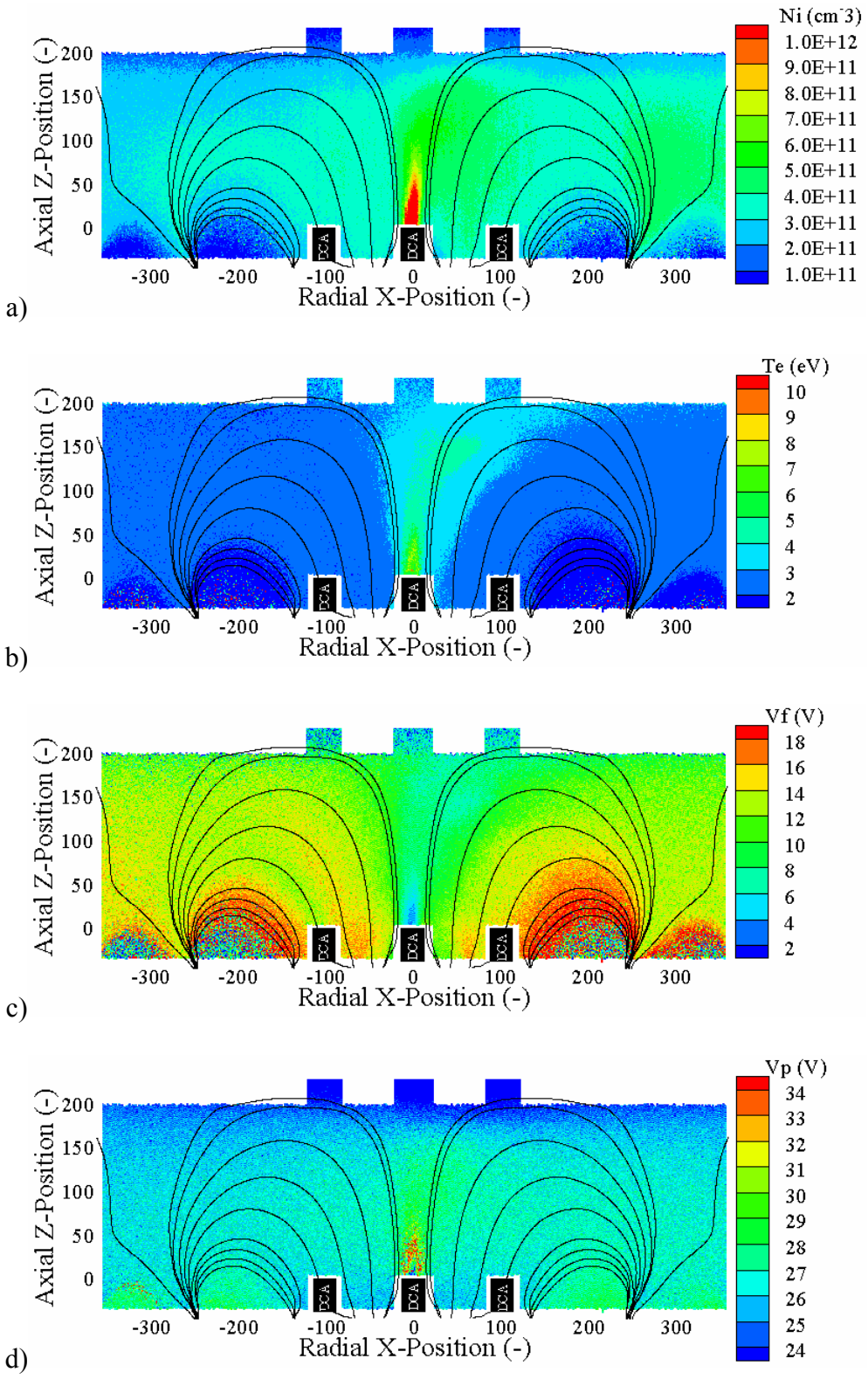

Figure D-10: a) Number density, b) electron temperature, c) floating potential, and d) plasma potential for configuration 5MI at plane 1.

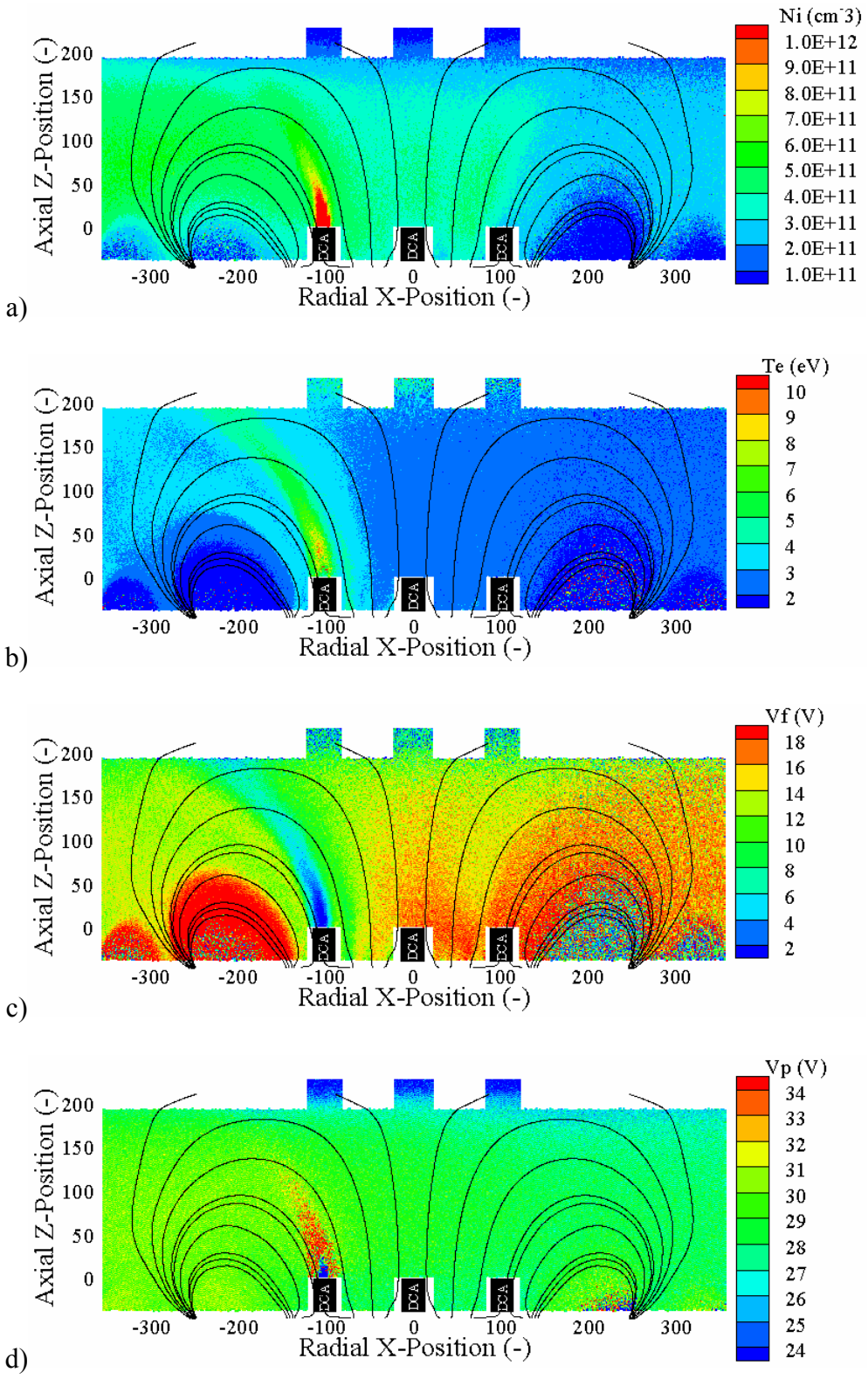

Figure D-11: a) Number density, b) electron temperature, c) floating potential, and d) plasma potential for configuration 10LI at plane 1.

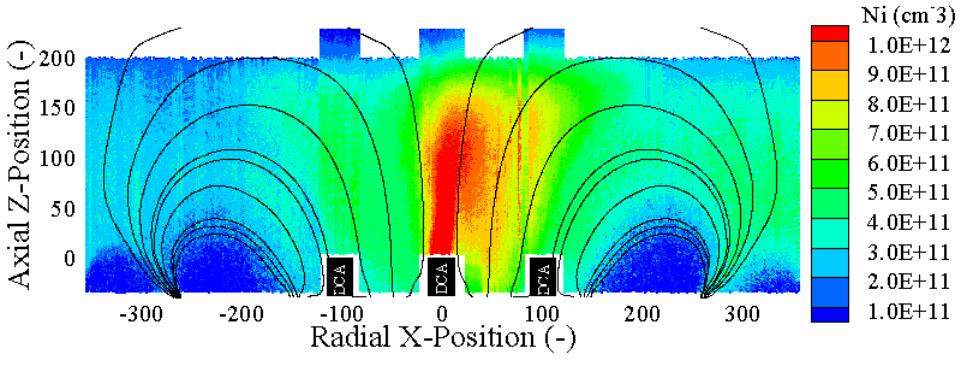

a)

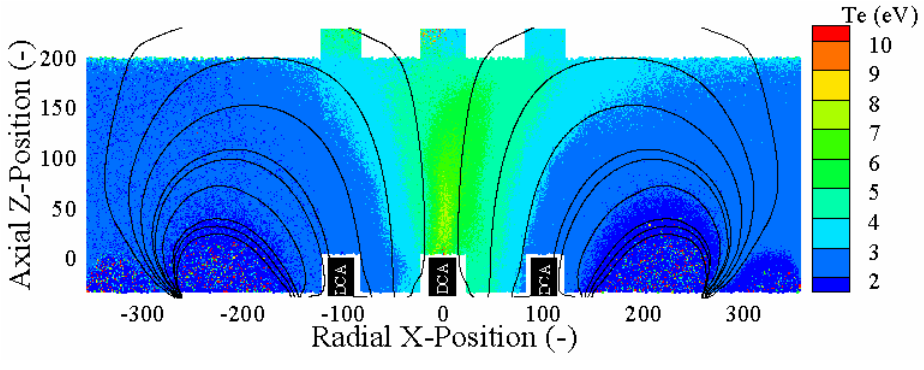

b)

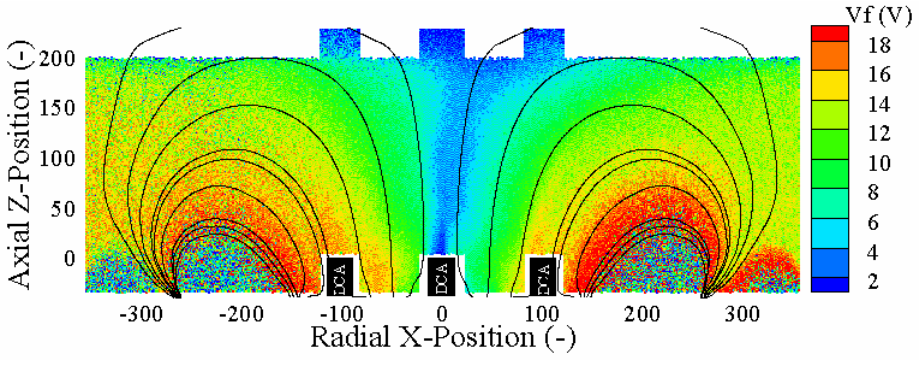

c)

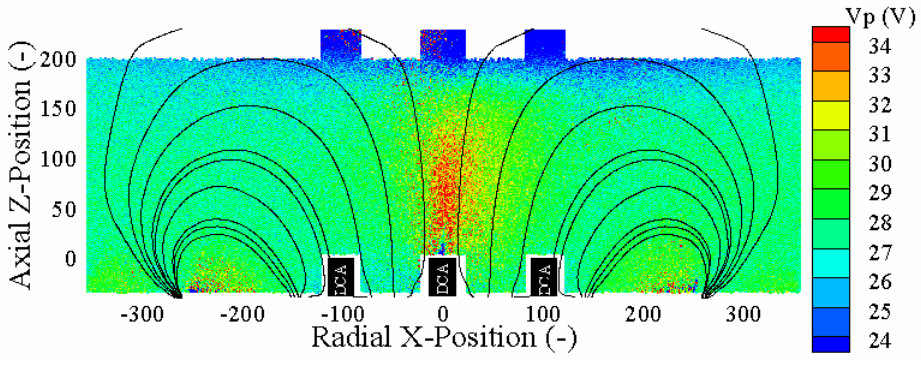

d)

Figure D-12: a) Number density, b) electron temperature, c) floating potential, and d) plasma potential for configuration 10MI at plane 1.

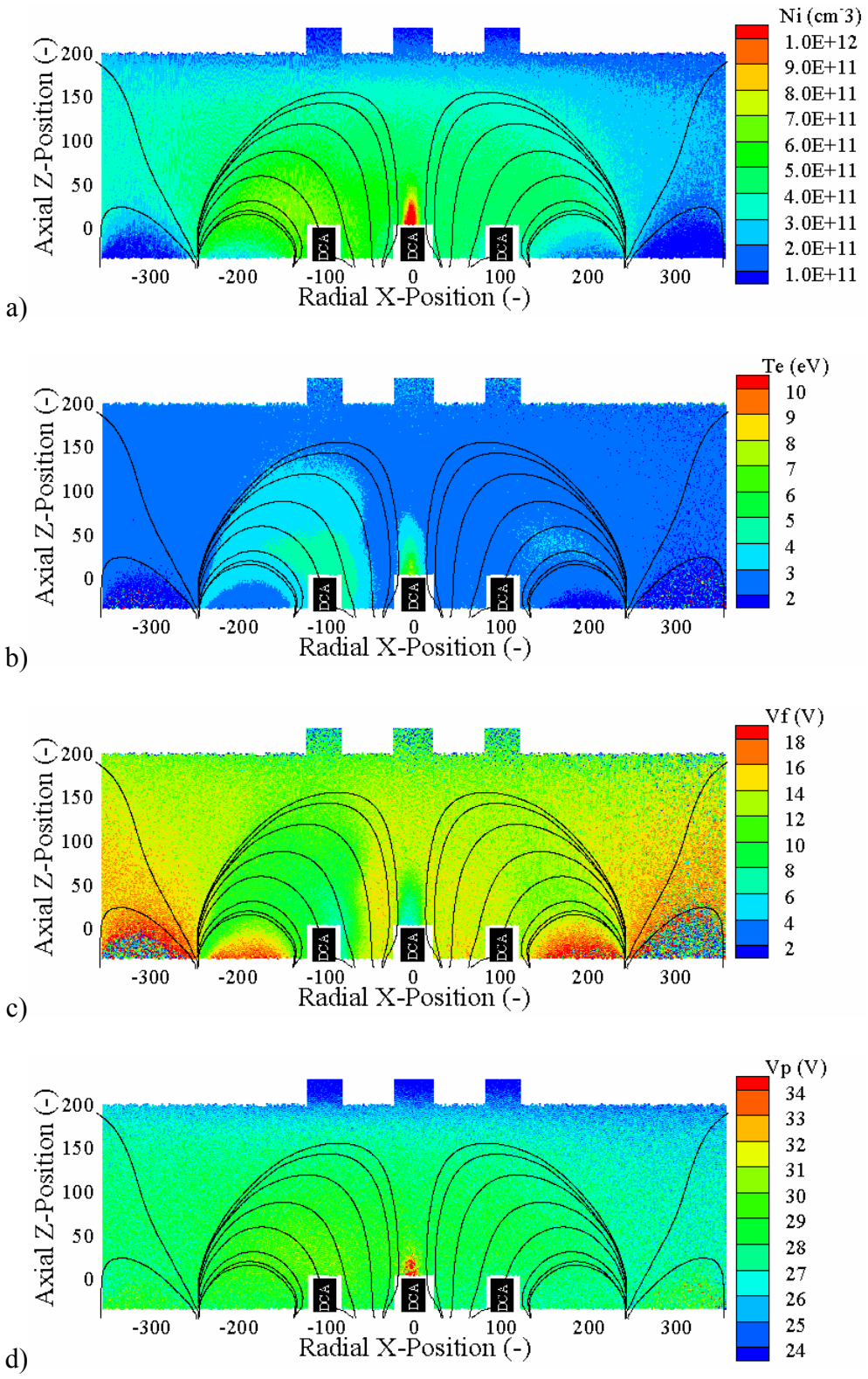

Figure D-13: a) Number density, b) electron temperature, c) floating potential, and d) plasma potential for configuration 0MCH at plane 1.

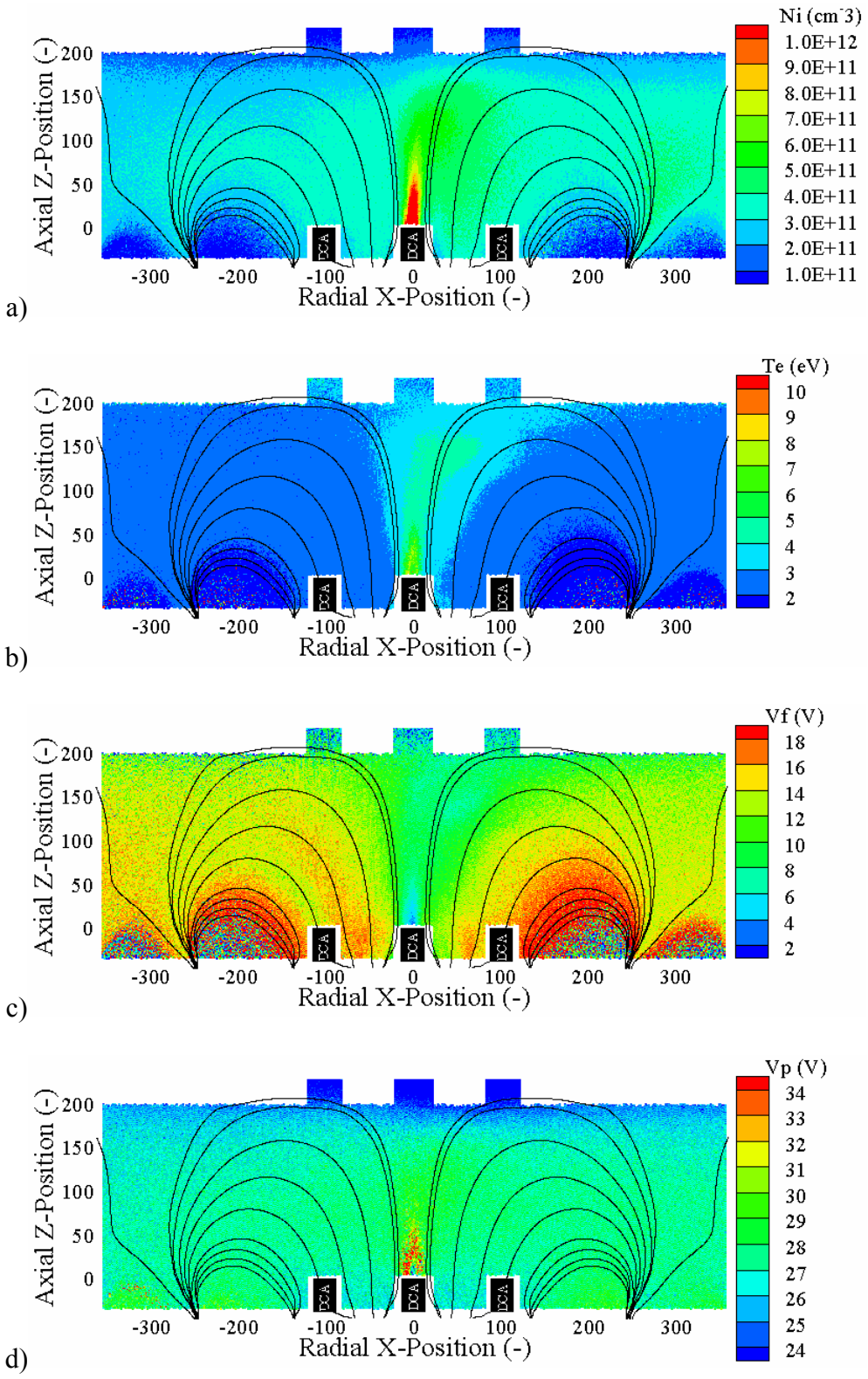

Figure D-14: a) Number density, b) electron temperature, c) floating potential, and d) plasma potential for configuration 5MCH at plane 1.

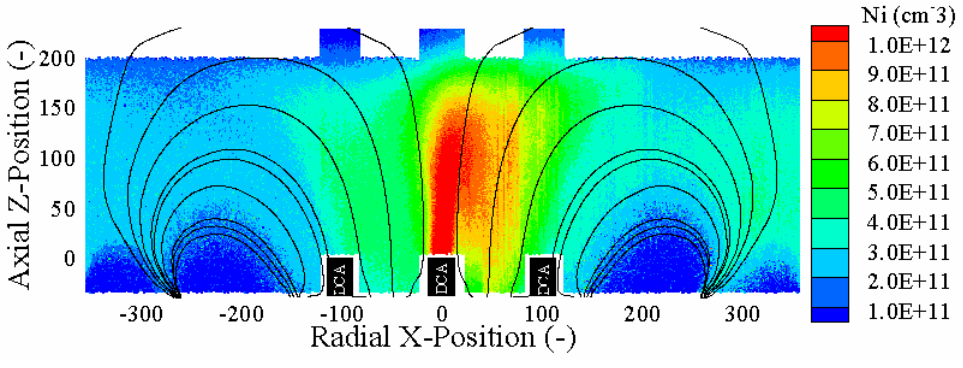

a)

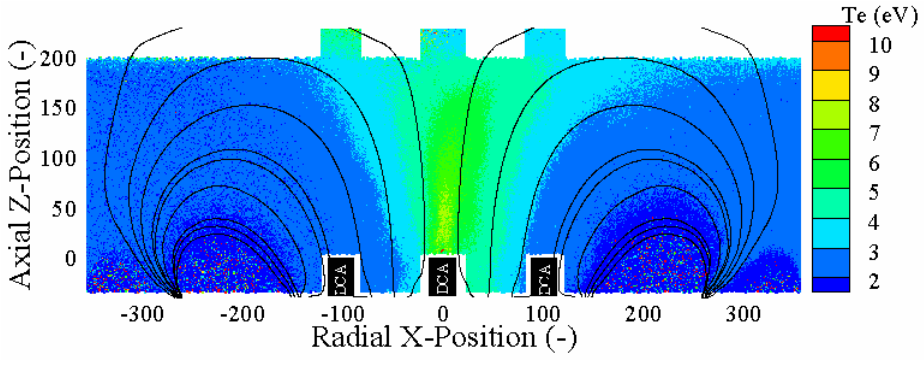

b)

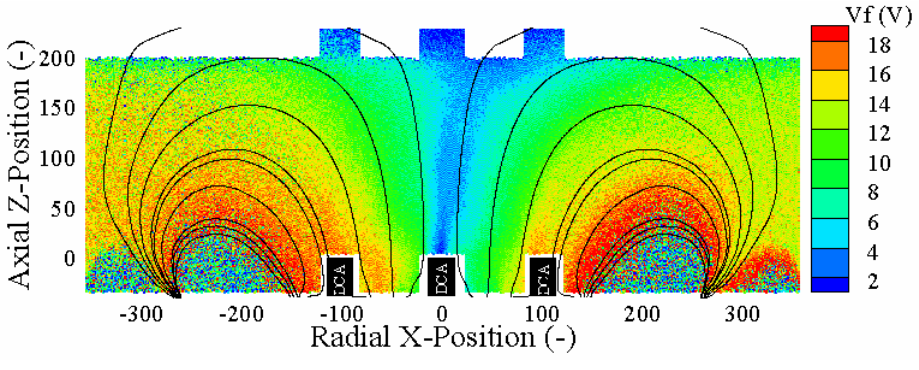

c)

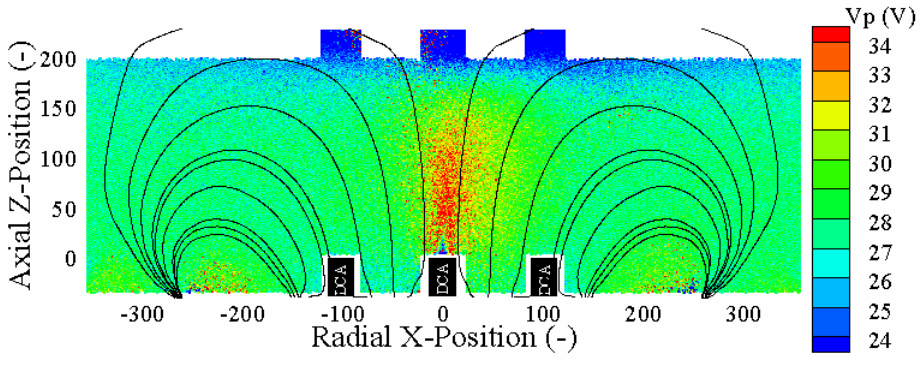

d)

Figure D-15: a) Number density, b) electron temperature, c) floating potential, and d) plasma potential for configuration 10MCH at plane 1.

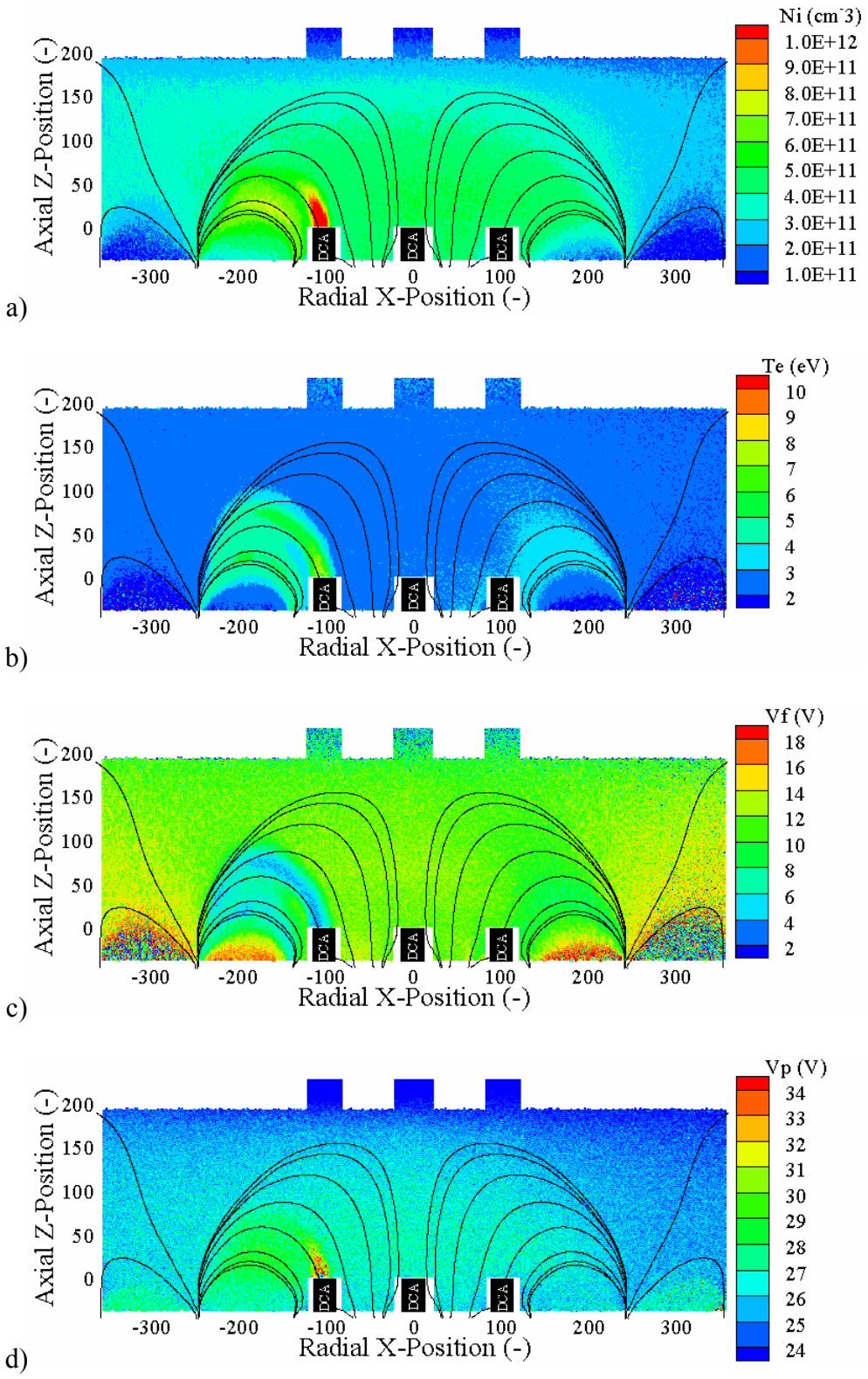

Figure D-16: a) Number density, b) electron temperature, c) floating potential, and d) plasma potential for configuration 0LIH at plane 1.

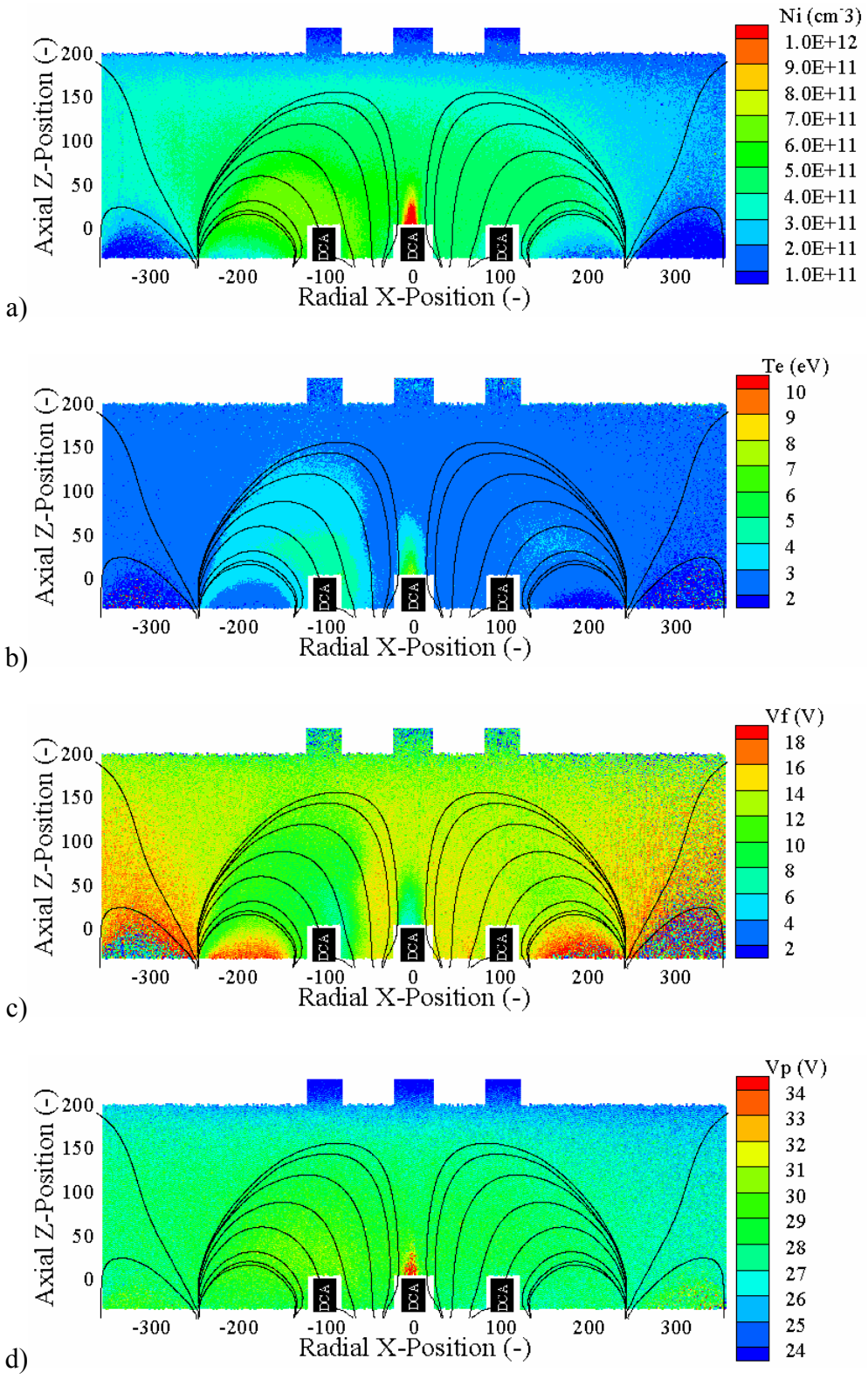

Figure D-17: a) Number density, b) electron temperature, c) floating potential, and d) plasma potential for configuration 0MIH at plane 1.

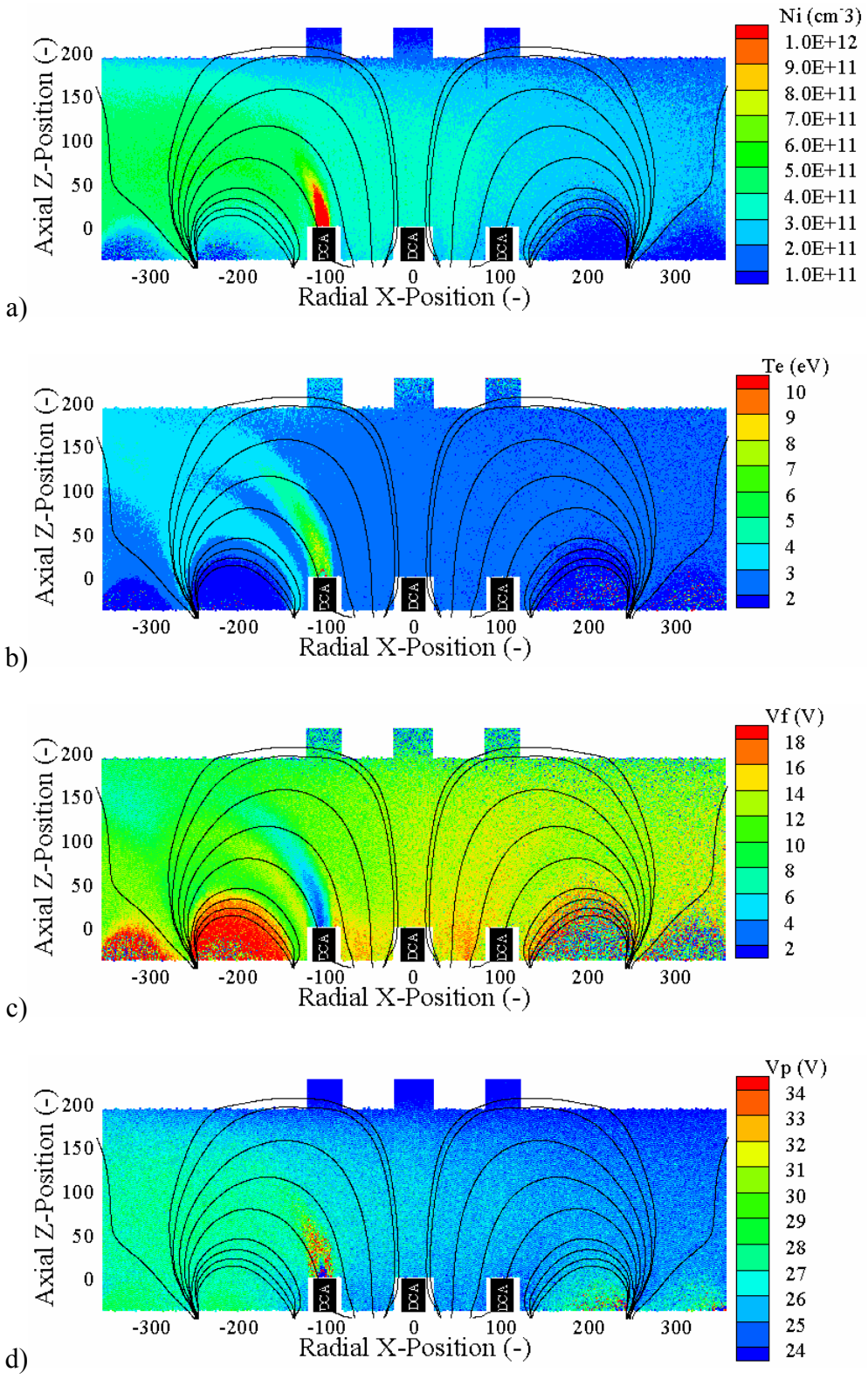

Figure D-18: a) Number density, b) electron temperature, c) floating potential, and d) plasma potential for configuration 5LIH at plane 1.

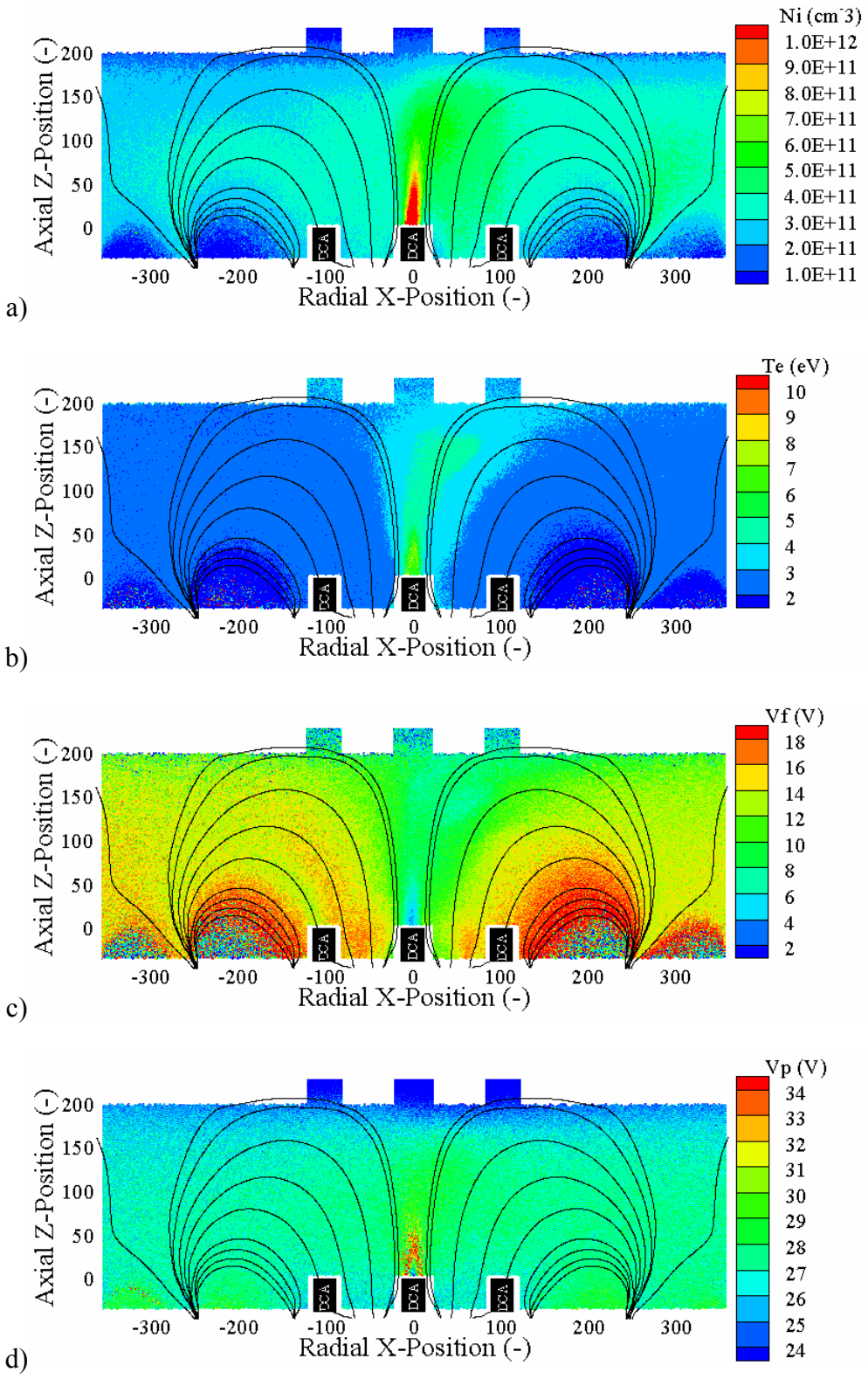

Figure D-19: a) Number density, b) electron temperature, c) floating potential, and d) plasma potential for configuration 5MIH at plane 1.

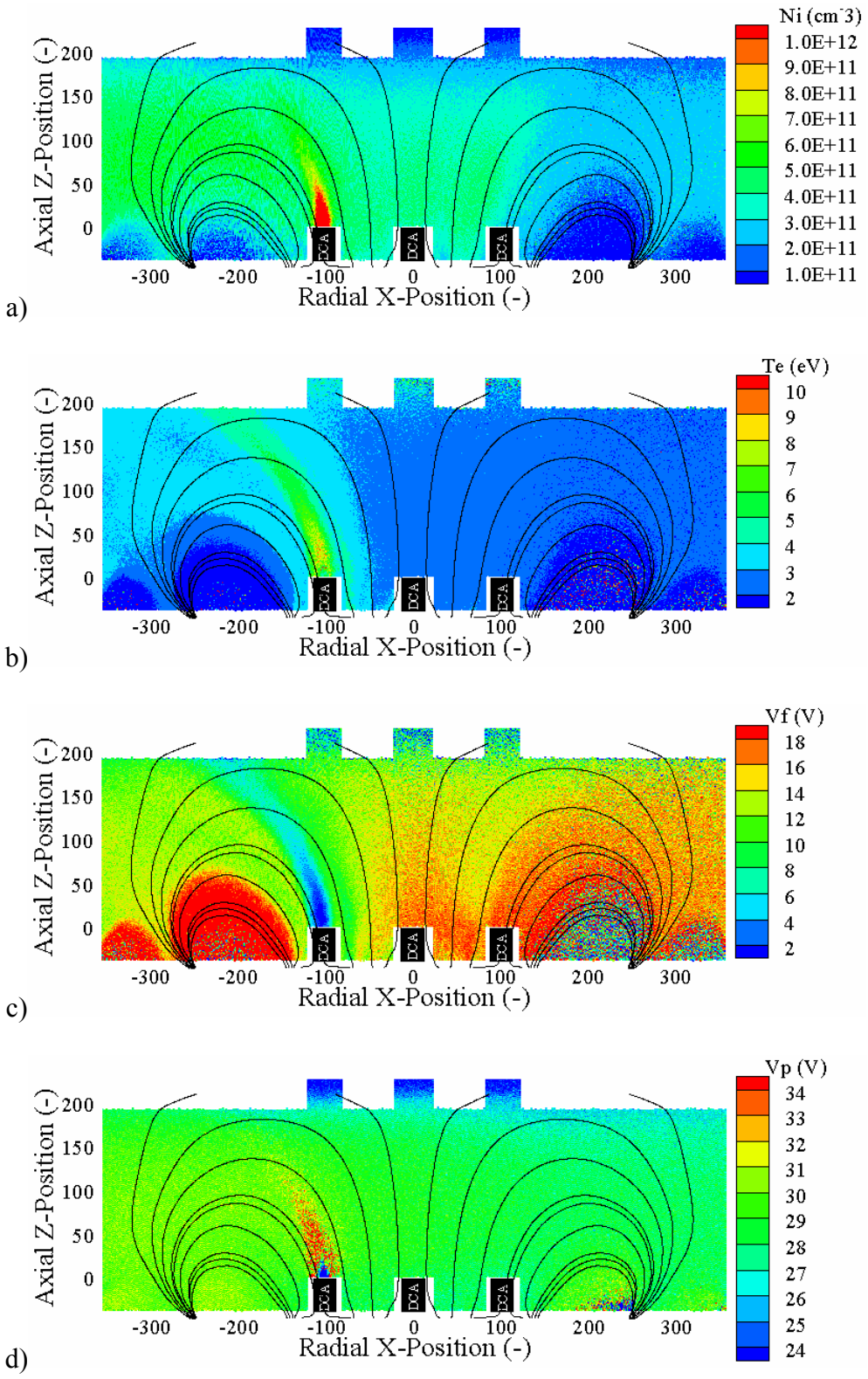

Figure D-20: a) Number density, b) electron temperature, c) floating potential, and d) plasma potential for configuration 10LIH at plane 1.

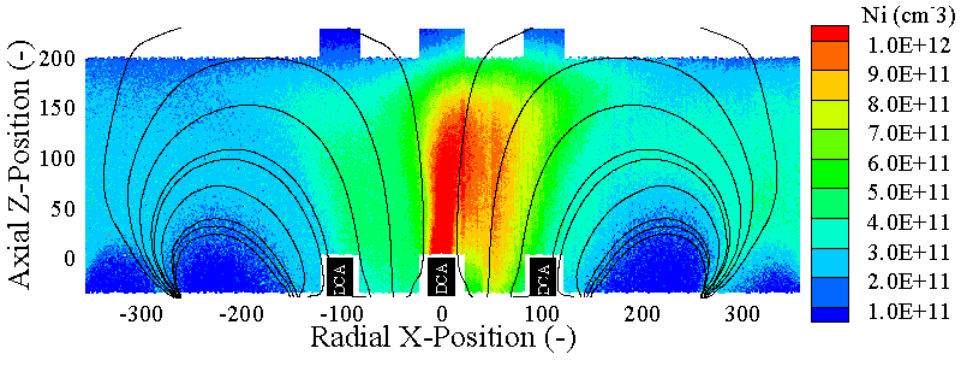

a)

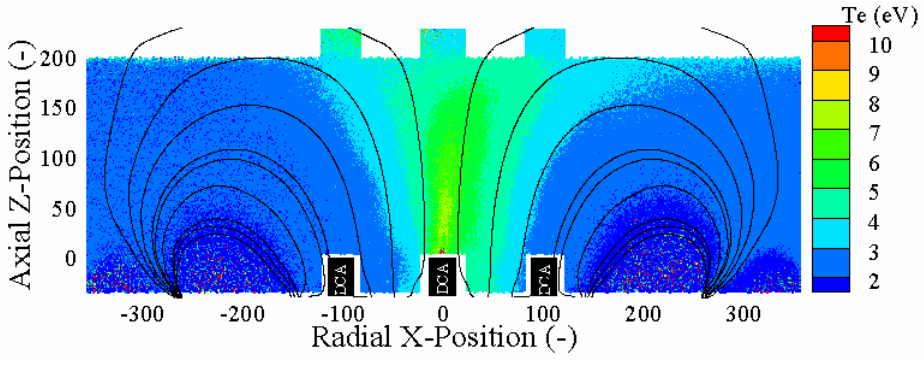

b)

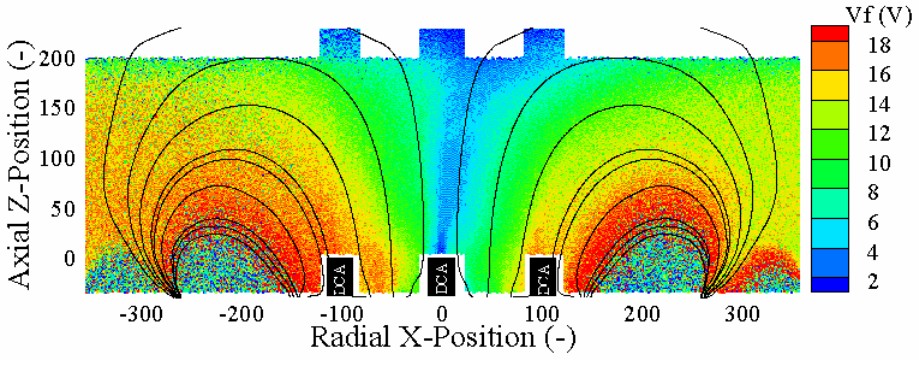

c)

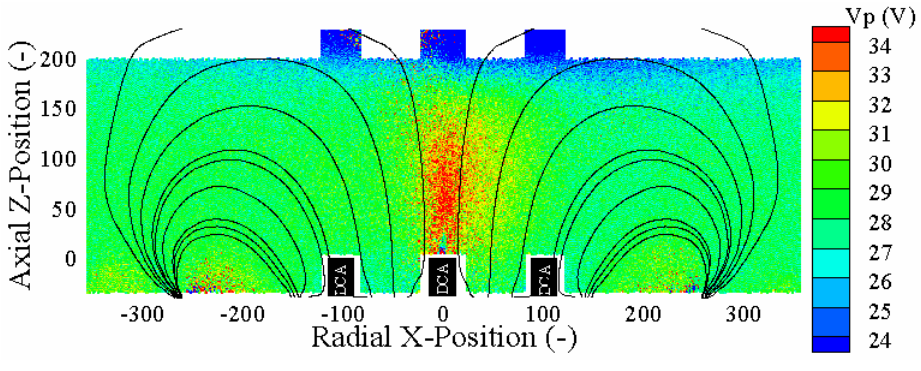

d)

Figure D-21: a) Number density, b) electron temperature, c) floating potential, and d) plasma potential for configuration 10MIH at plane 1.

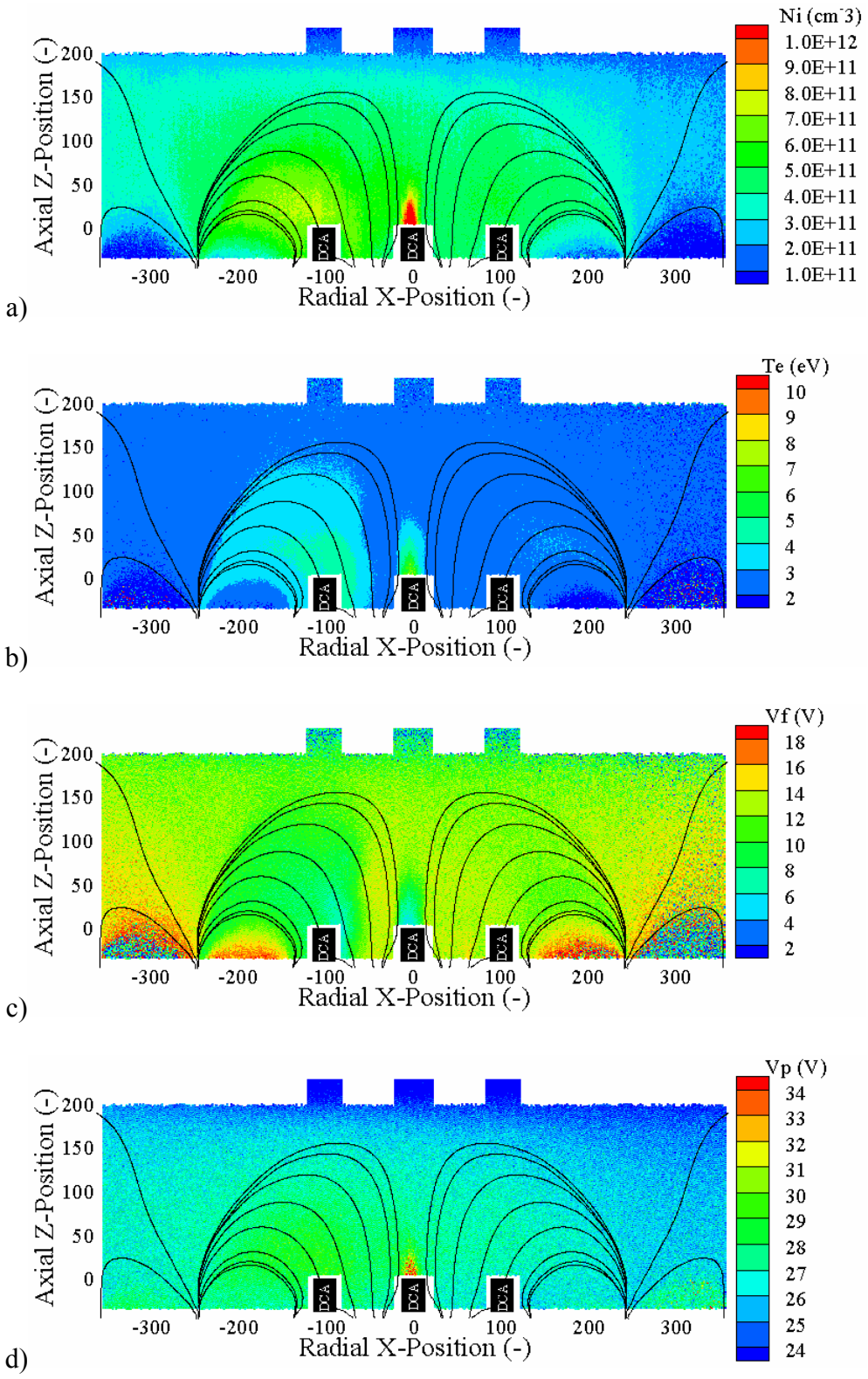

Figure D-22: a) Number density, b) electron temperature, c) floating potential, and d) plasma potential for configuration 0MCF at plane 1.

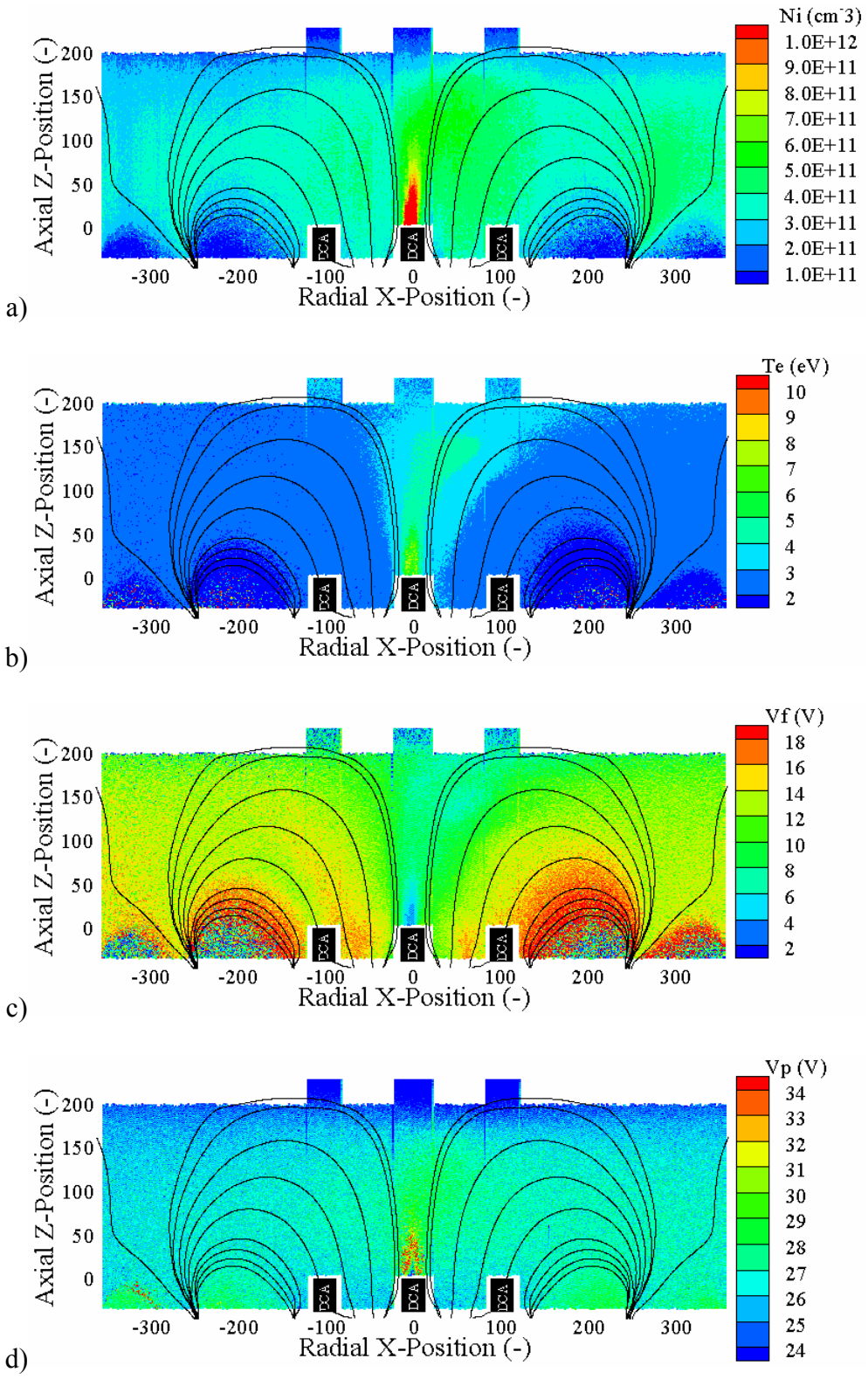

Figure D-23: a) Number density, b) electron temperature, c) floating potential, and d) plasma potential for configuration 5MCF at plane 1.

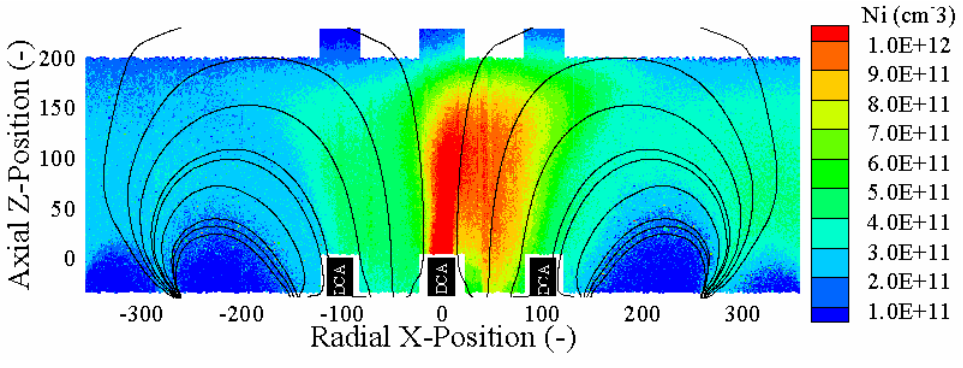

a)

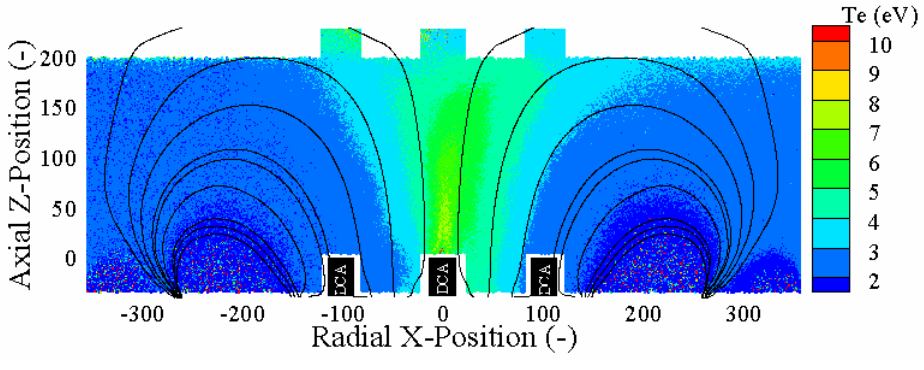

b)

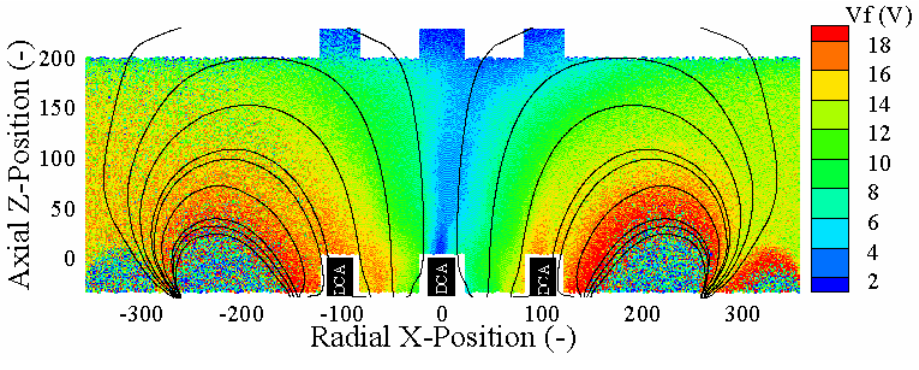

c)

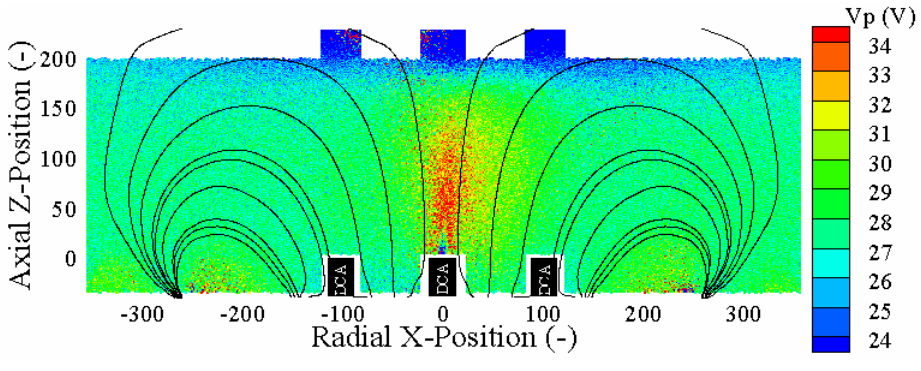

d)

Figure D-24: a) Number density, b) electron temperature, c) floating potential, and d) plasma potential for configuration 10MCF at plane 1.

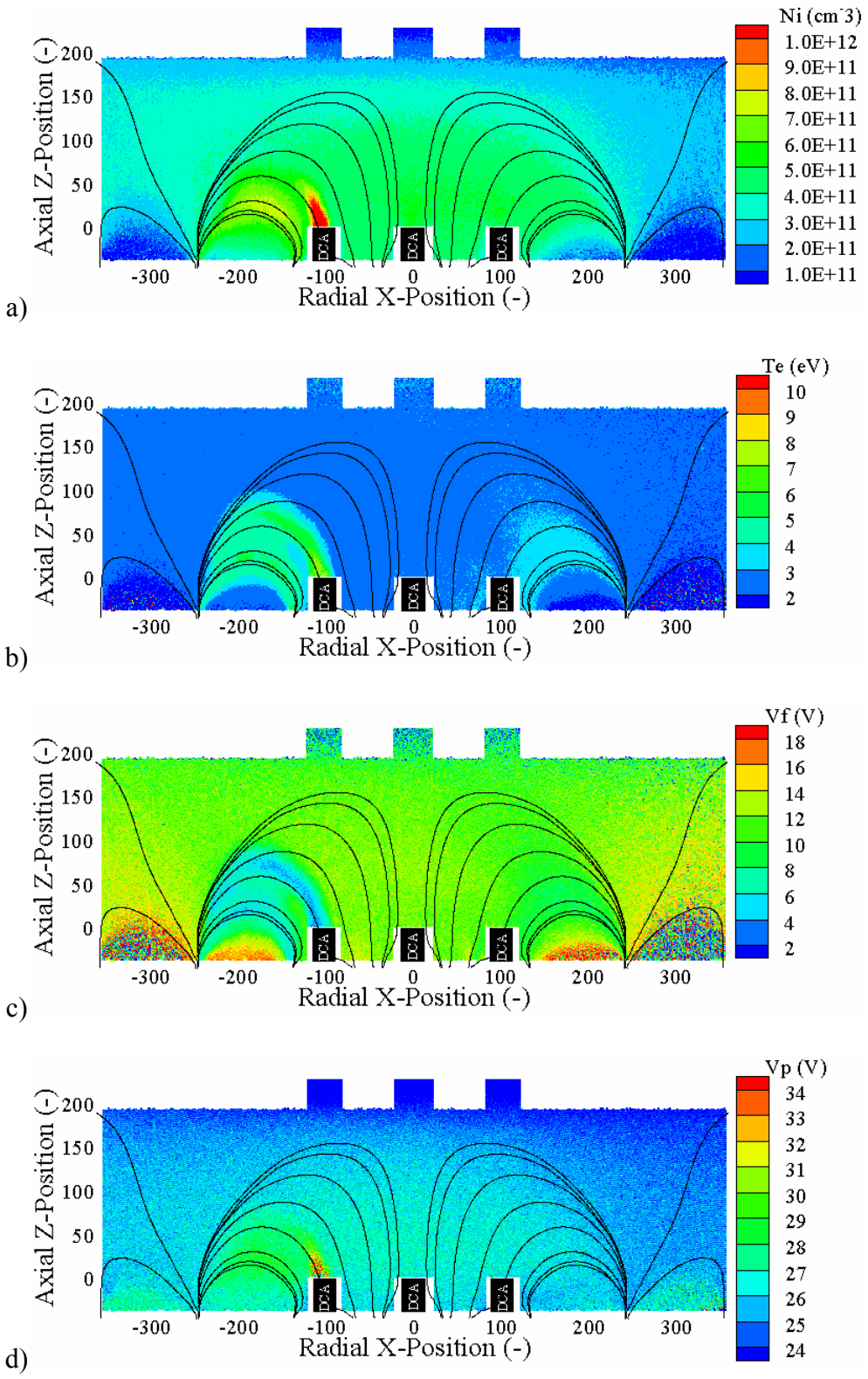

Figure D-25: a) Number density, b) electron temperature, c) floating potential, and d) plasma potential for configuration 0LIF at plane 1.

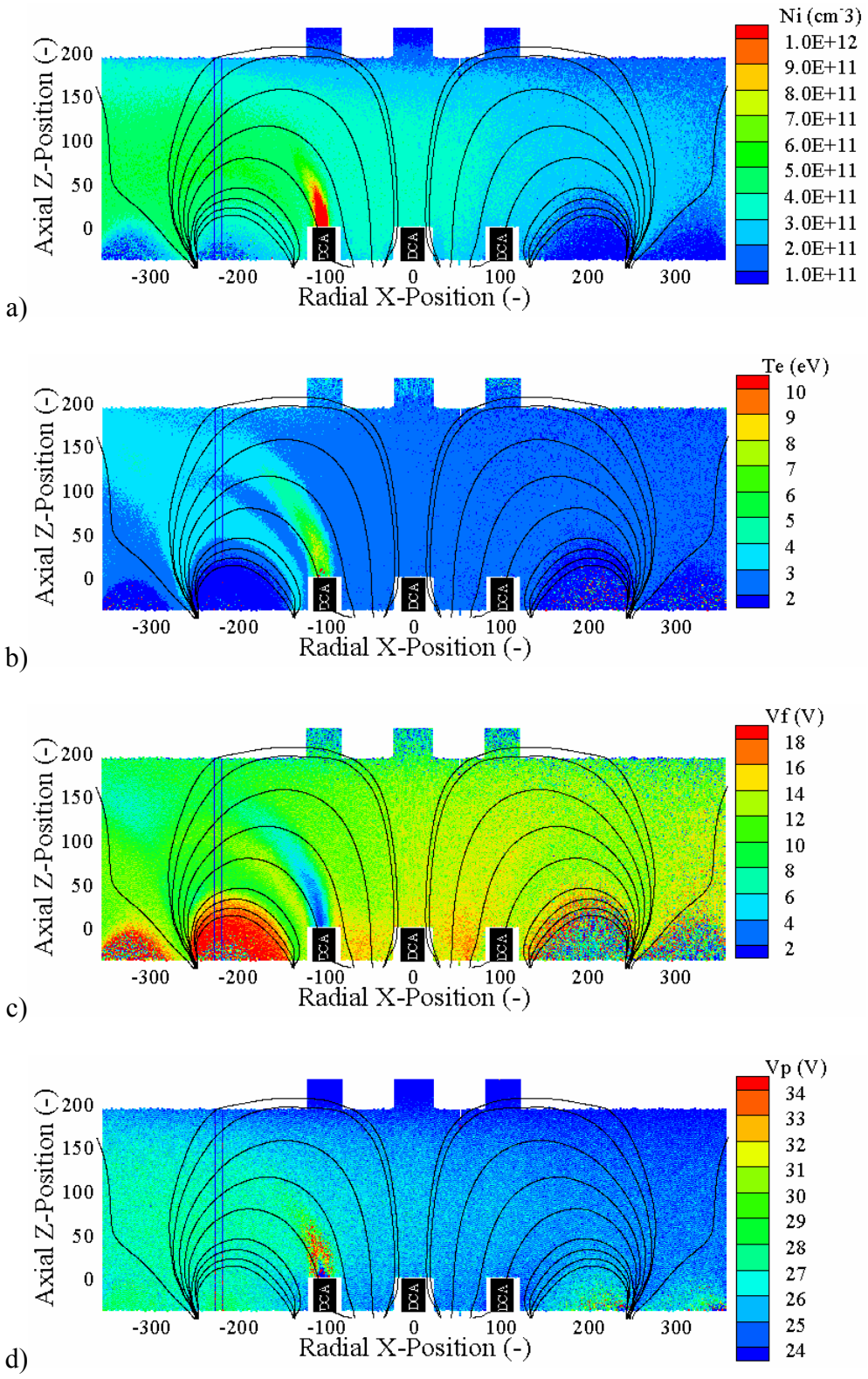

Figure D-26: a) Number density, b) electron temperature, c) floating potential, and d) plasma potential for configuration 5LIF at plane 1.

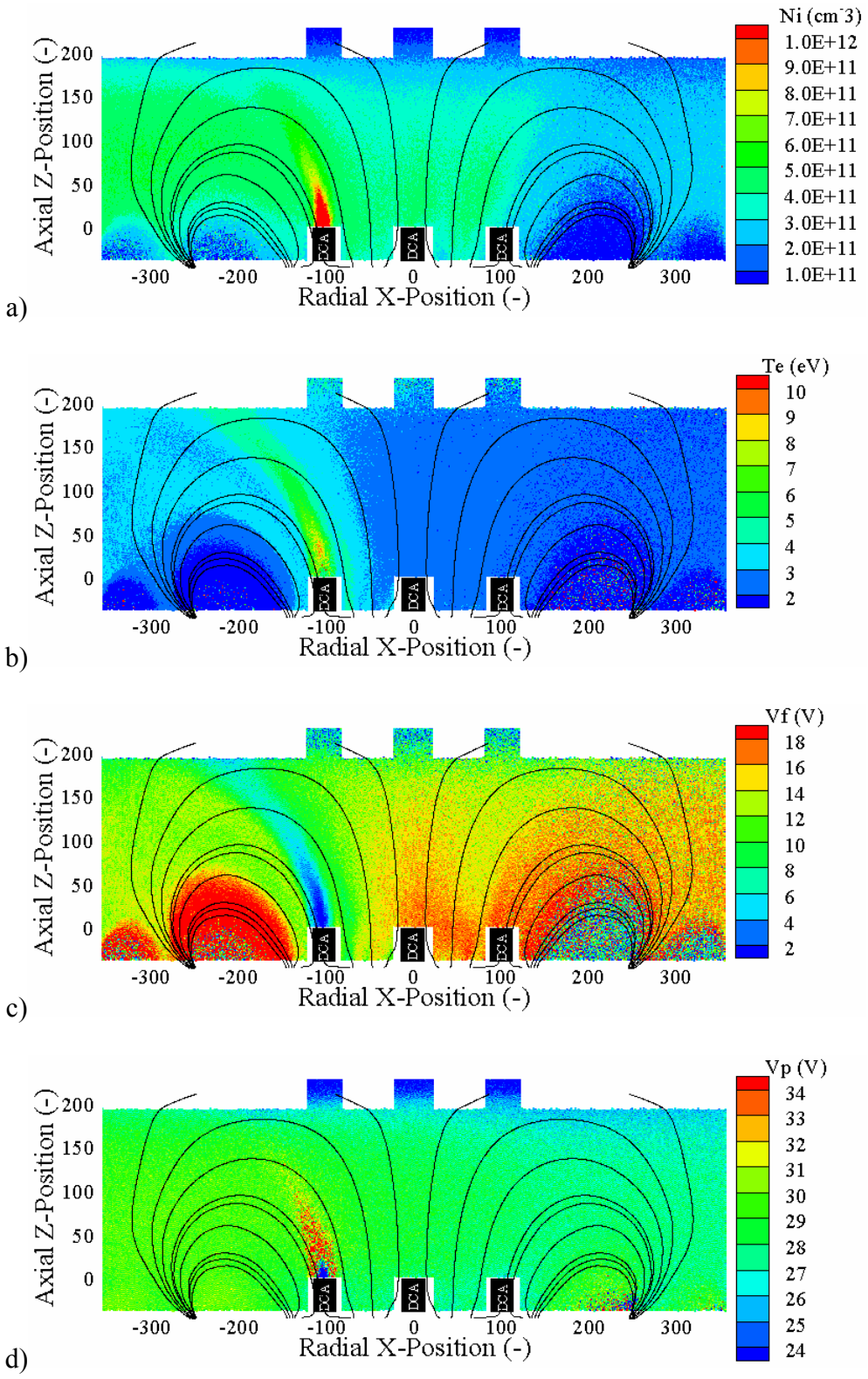

Figure D-27: a) Number density, b) electron temperature, c) floating potential, and d) plasma potential for configuration 10LIF at plane 1.

D.2 Plane 2 (Y = 11.1 cm)

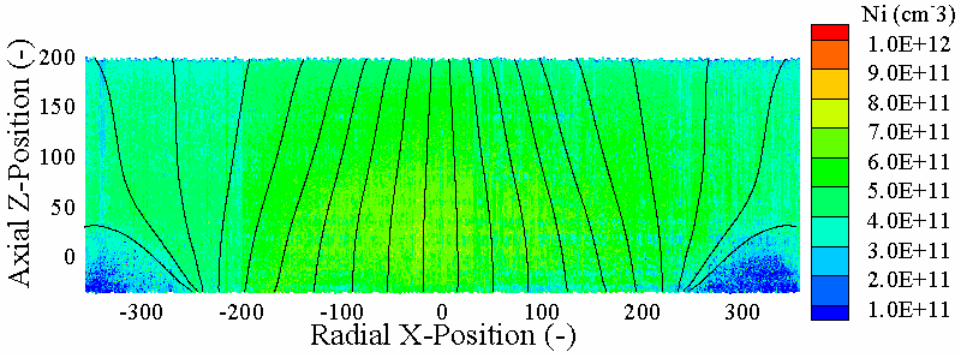

a)

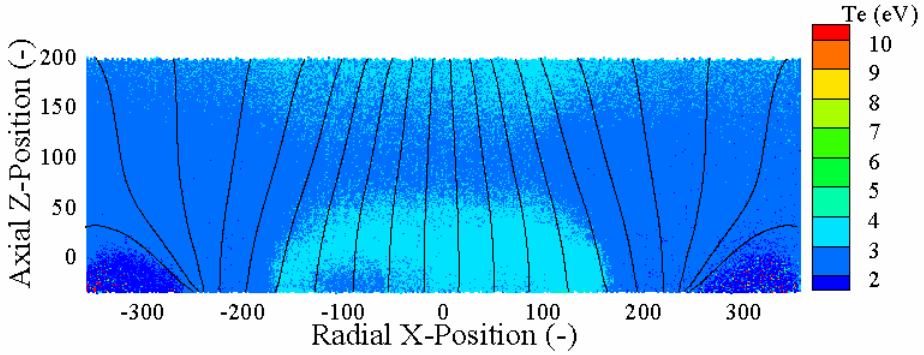

b)

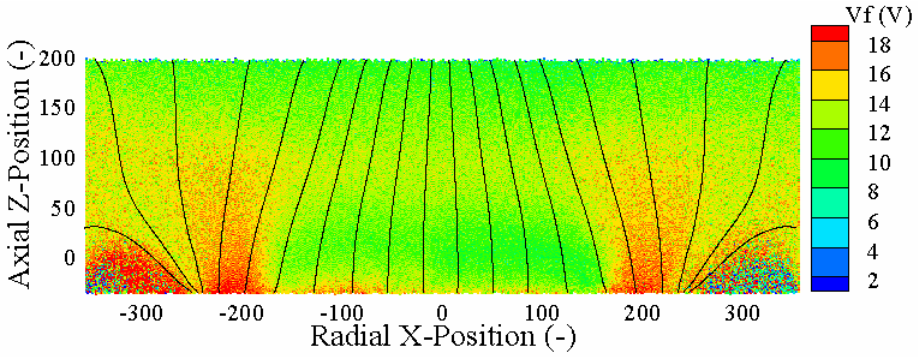

c)

d)

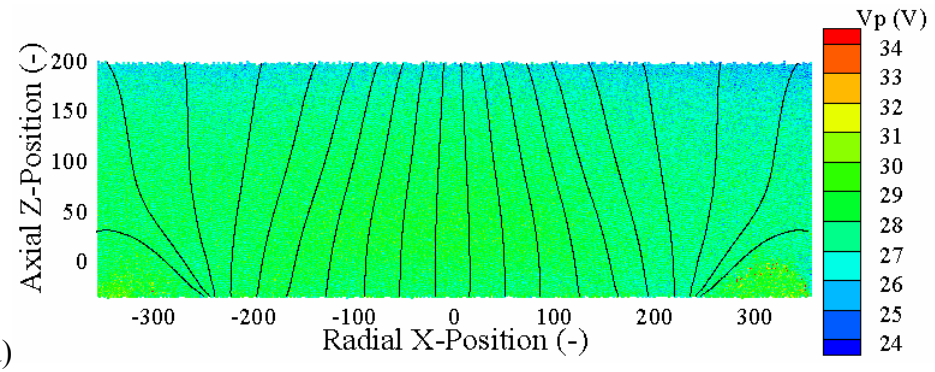

Figure D-28: a) Number density, b) electron temperature, c) floating potential, and d) plasma potential for configuration 0LI at plane 2.

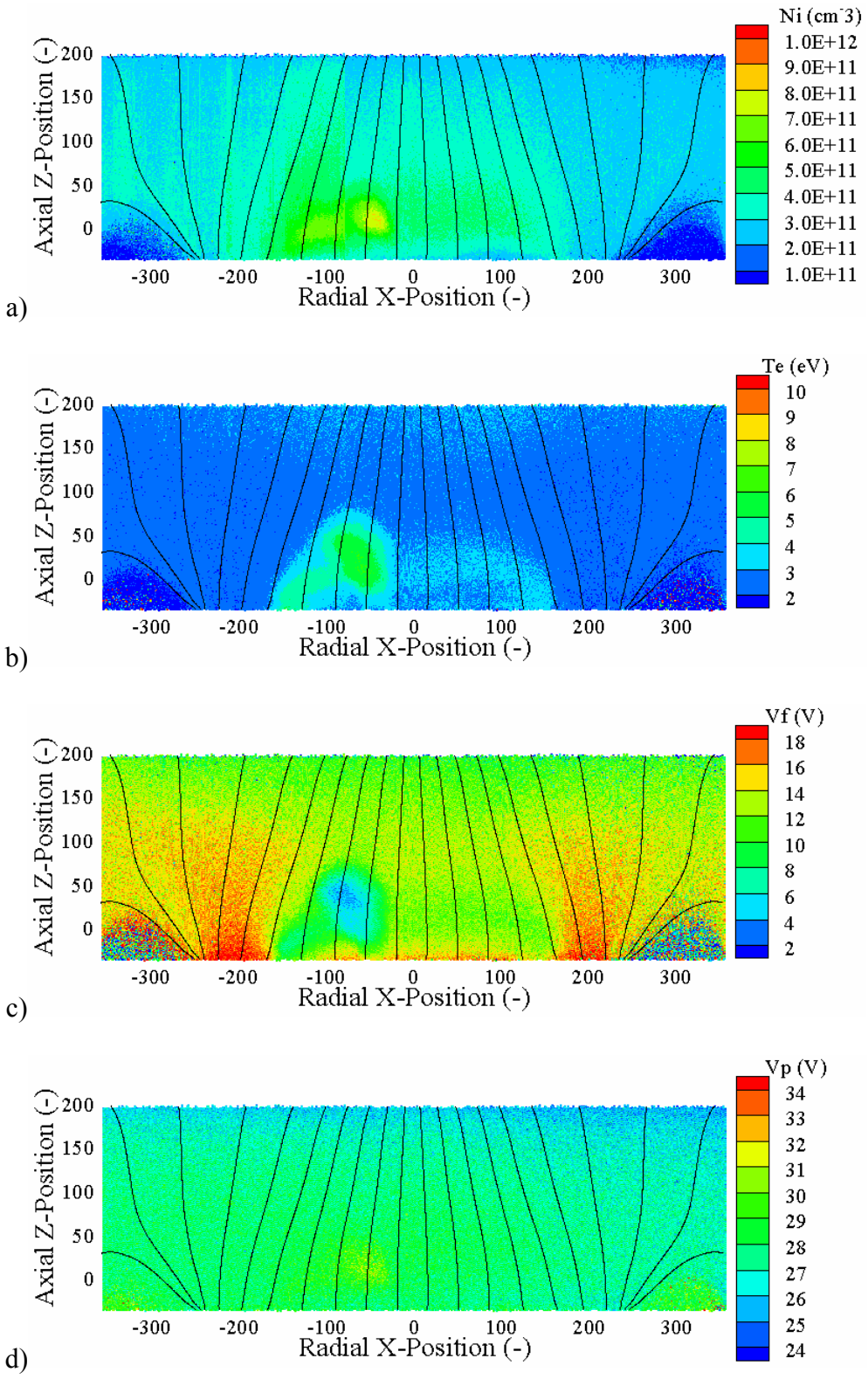

Figure D-29: a) Number density, b) electron temperature, c) floating potential, and d) plasma potential for configuration 0MI at plane 2.

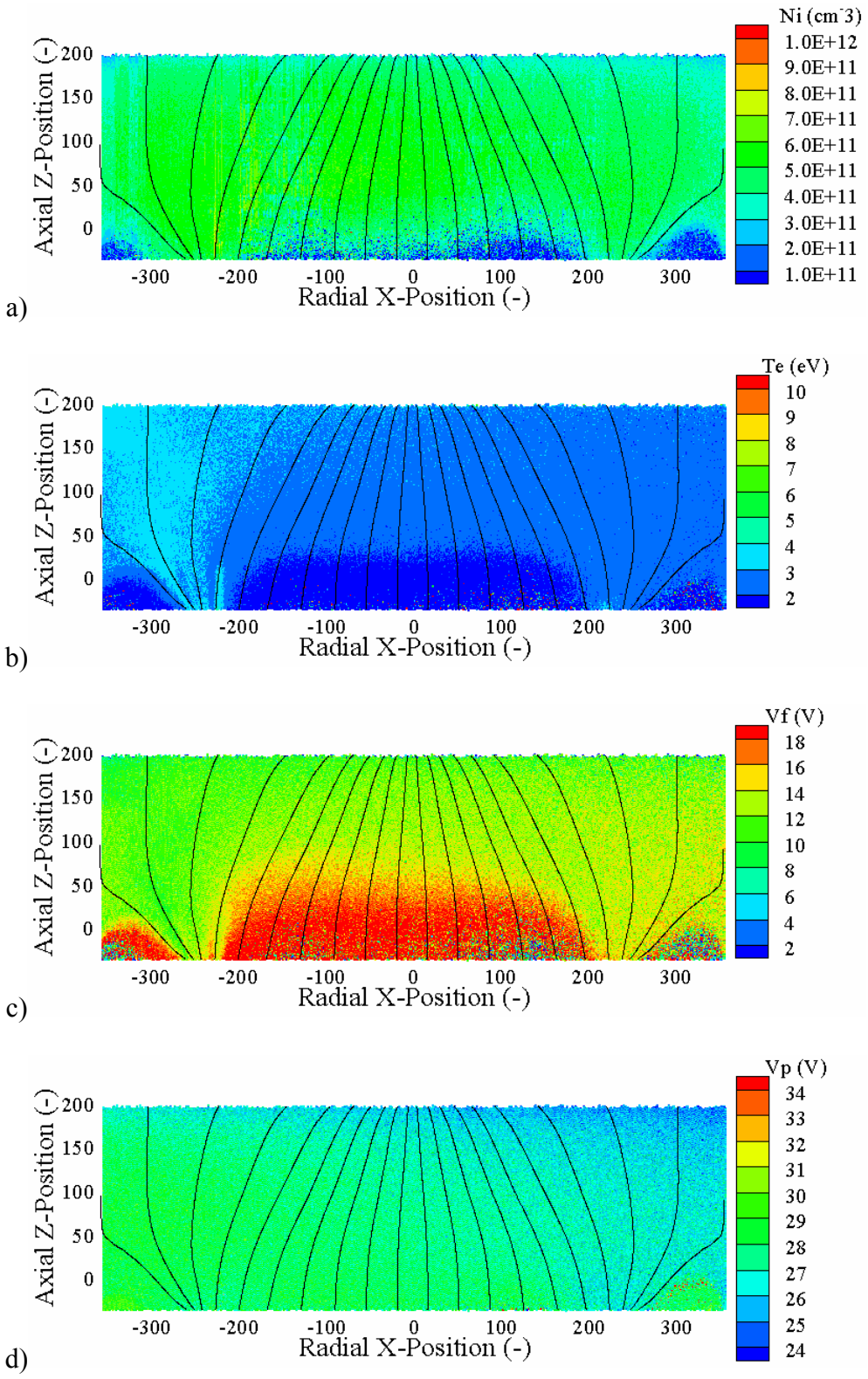

Figure D-30: a) Number density, b) electron temperature, c) floating potential, and d) plasma potential for configuration 5LI at plane 2.

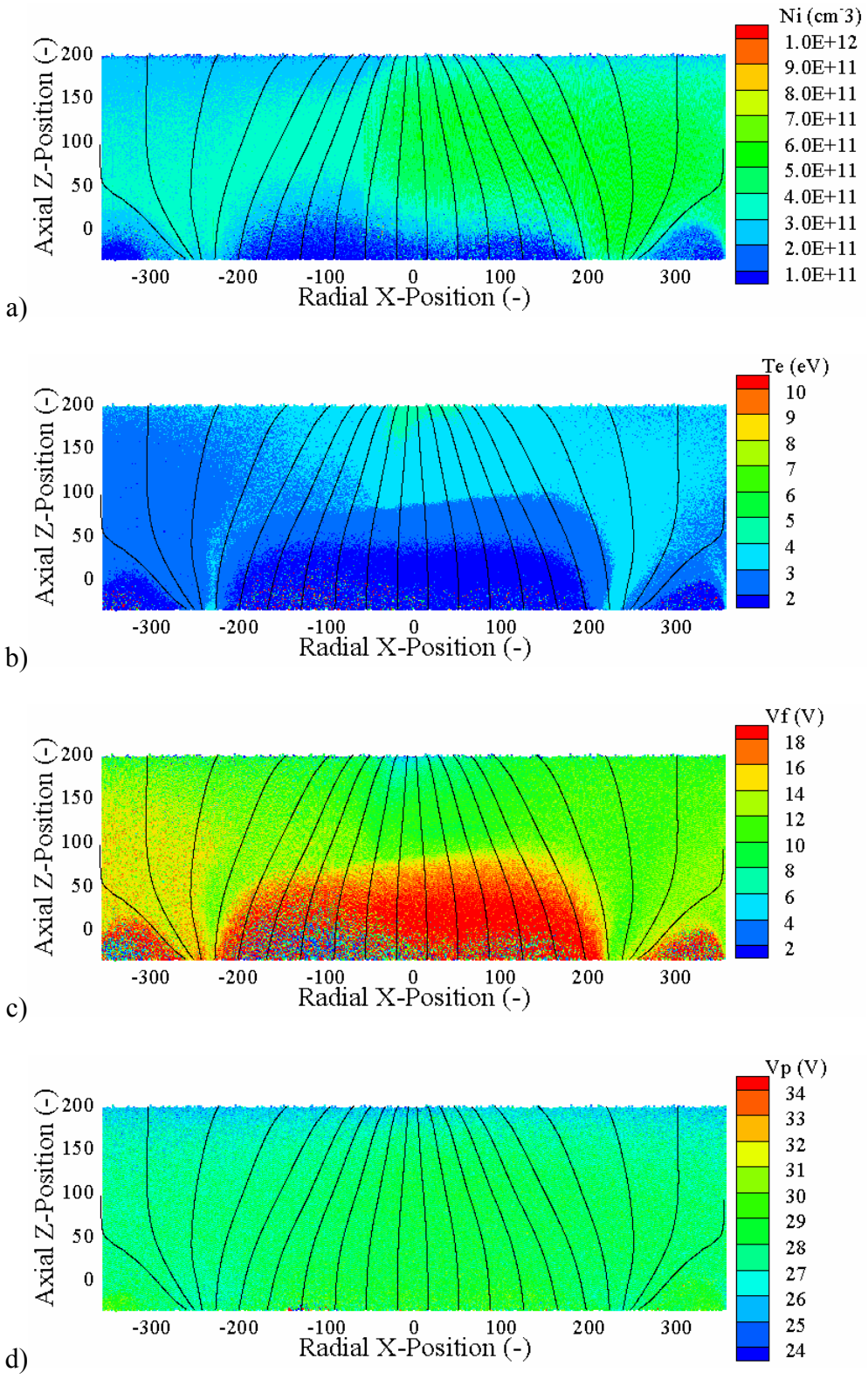

Figure D-31: a) Number density, b) electron temperature, c) floating potential, and d) plasma potential for configuration 5MI at plane 2.

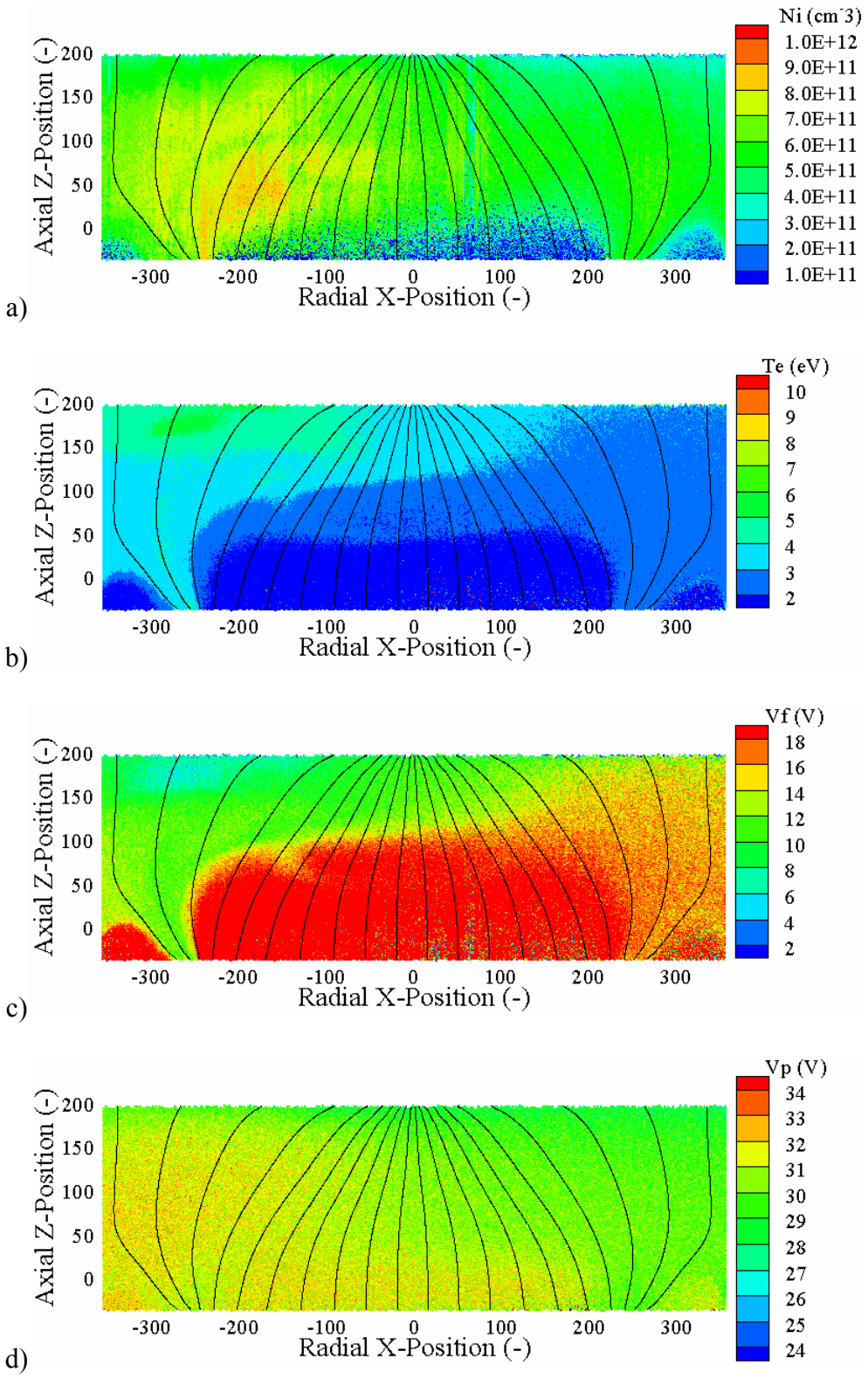

Figure D-32: a) Number density, b) electron temperature, c) floating potential, and d) plasma potential for configuration 10LI at plane 2.

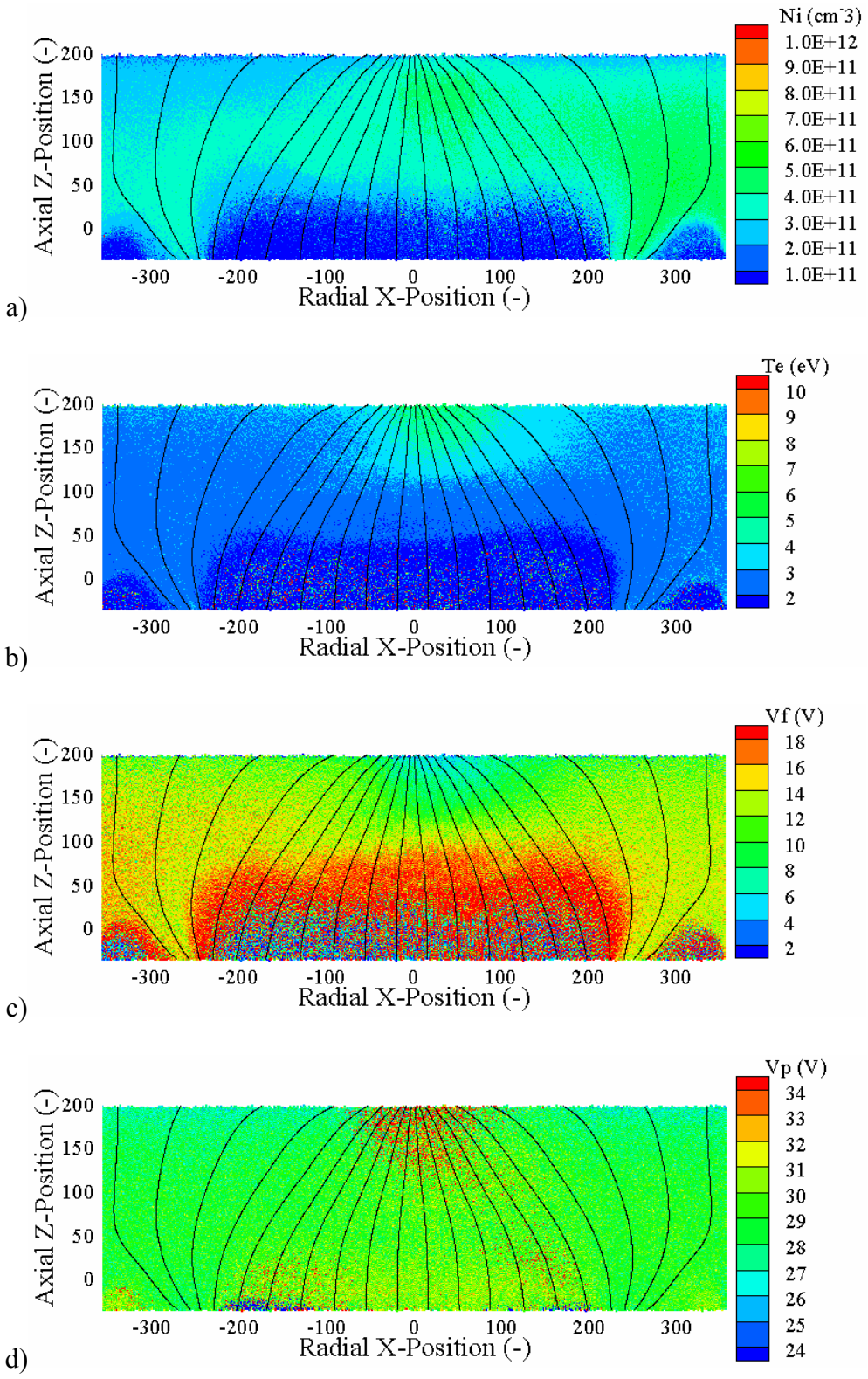

Figure D-33: a) Number density, b) electron temperature, c) floating potential, and d) plasma potential for configuration 10MI at plane 2.

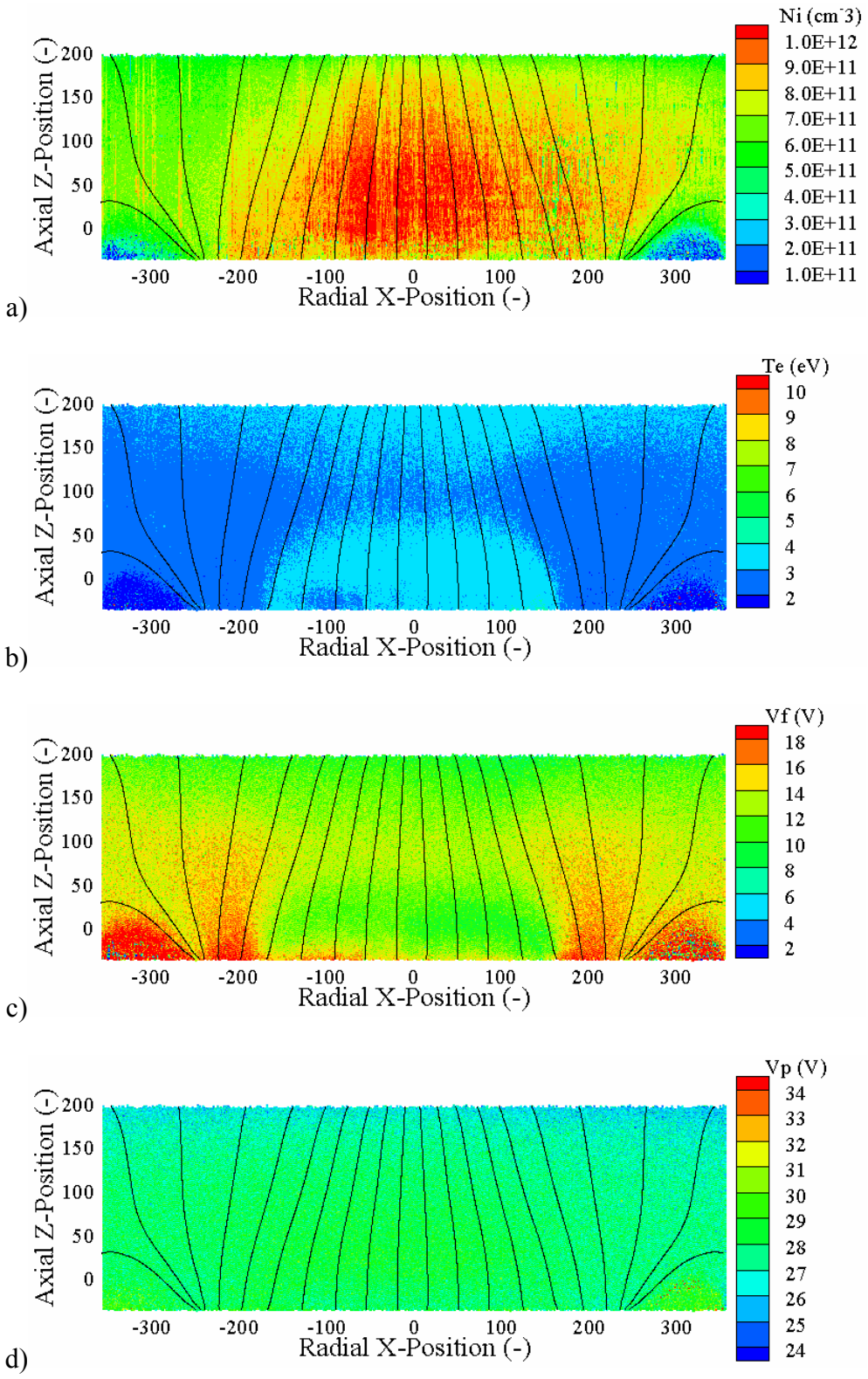

Figure D-34: a) Number density, b) electron temperature, c) floating potential, and d) plasma potential for configuration 0LIH at plane 2.

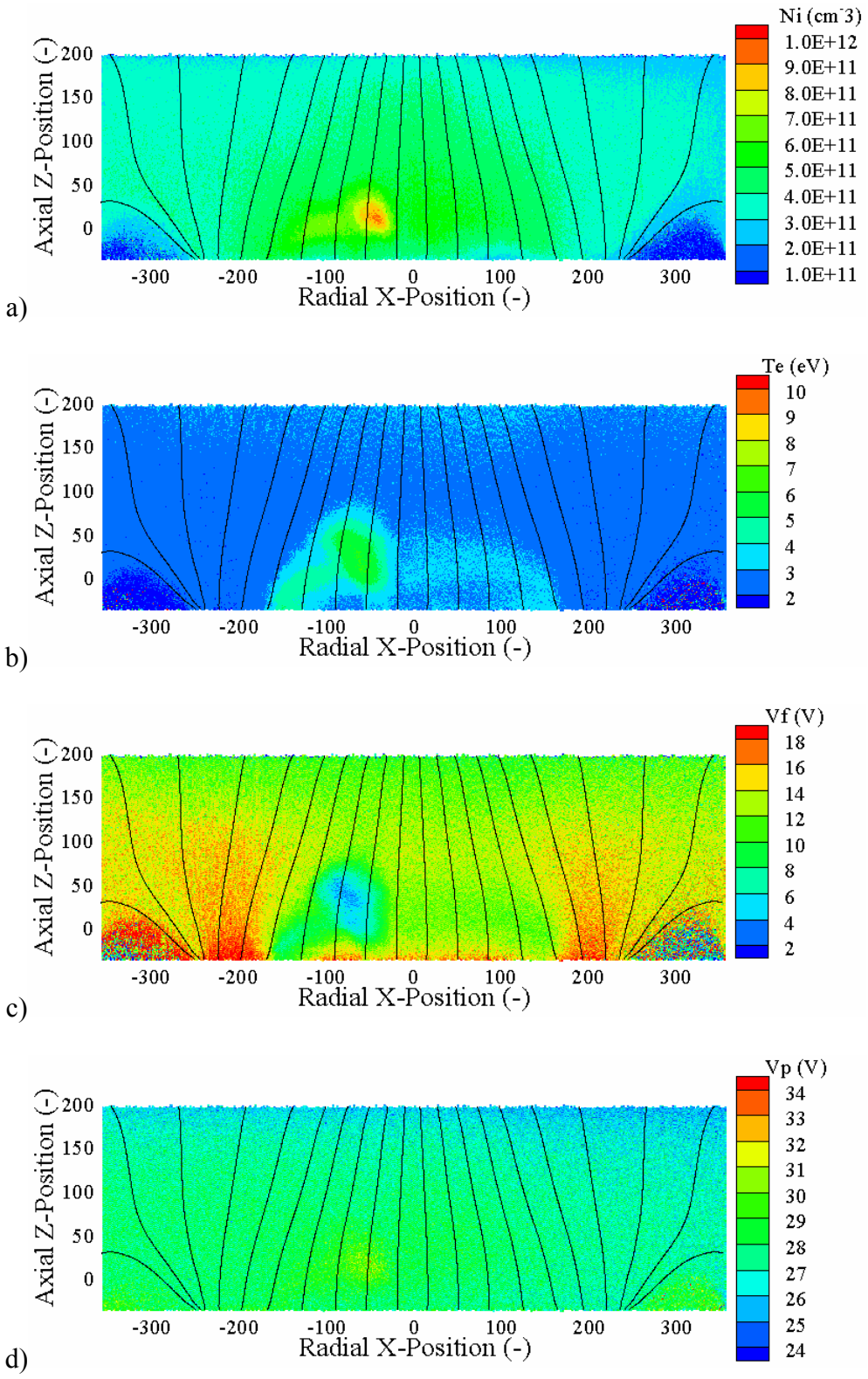

Figure D-35: a) Number density, b) electron temperature, c) floating potential, and d) plasma potential for configuration 0MIH at plane 2.

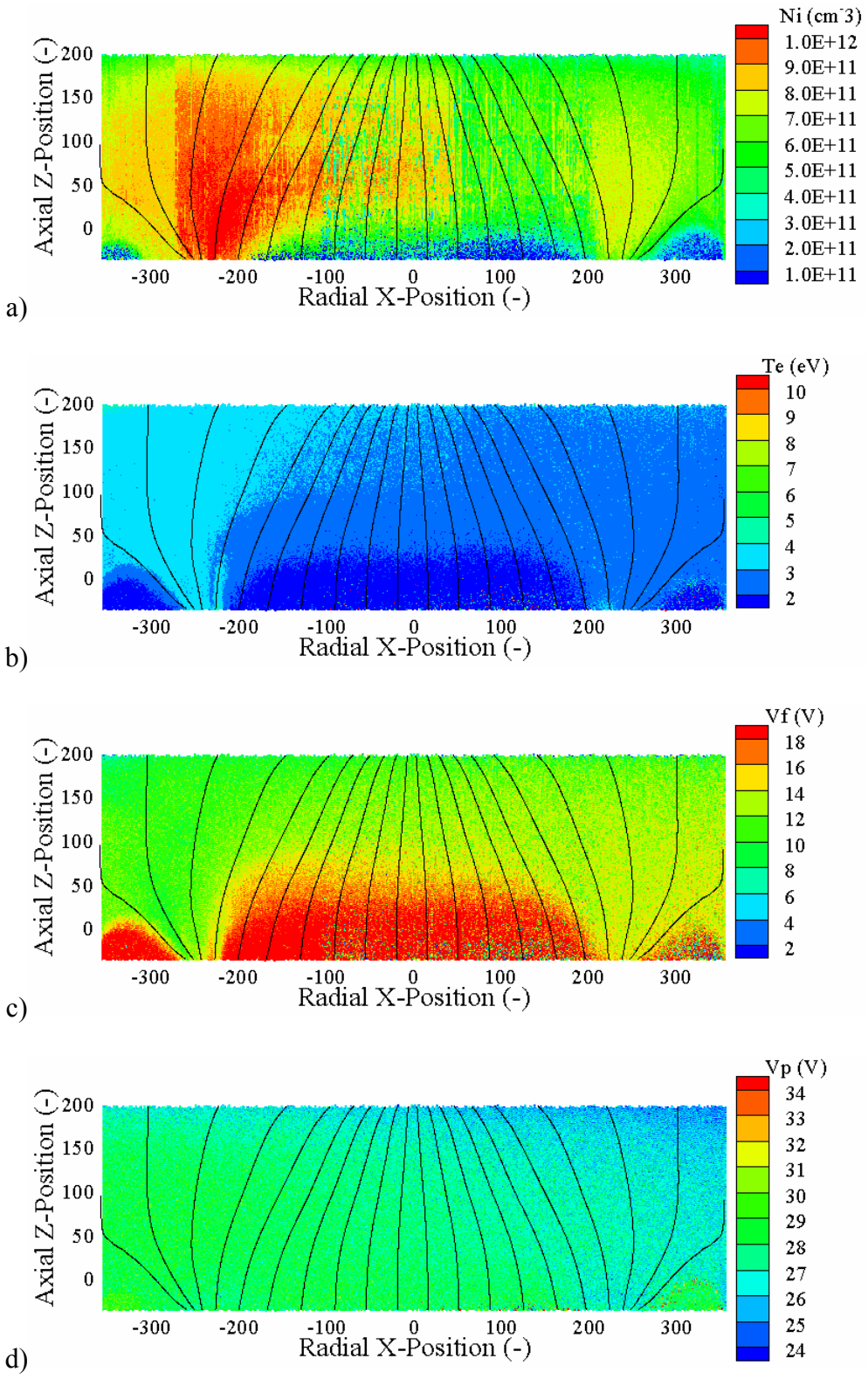

Figure D-36: a) Number density, b) electron temperature, c) floating potential, and d) plasma potential for configuration 5LIH at plane 2.

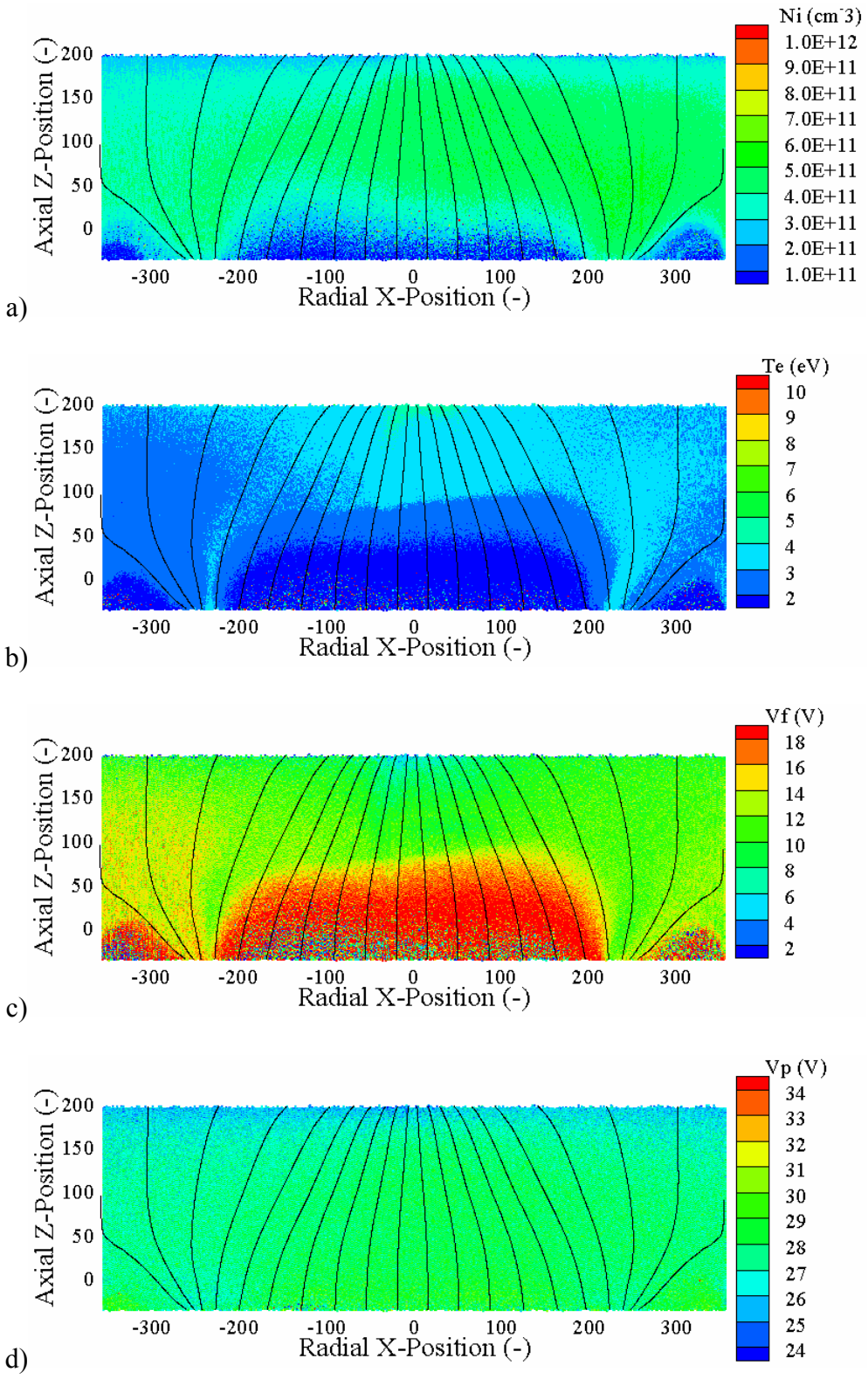

Figure D-37: a) Number density, b) electron temperature, c) floating potential, and d) plasma potential for configuration 5MIH at plane 2.

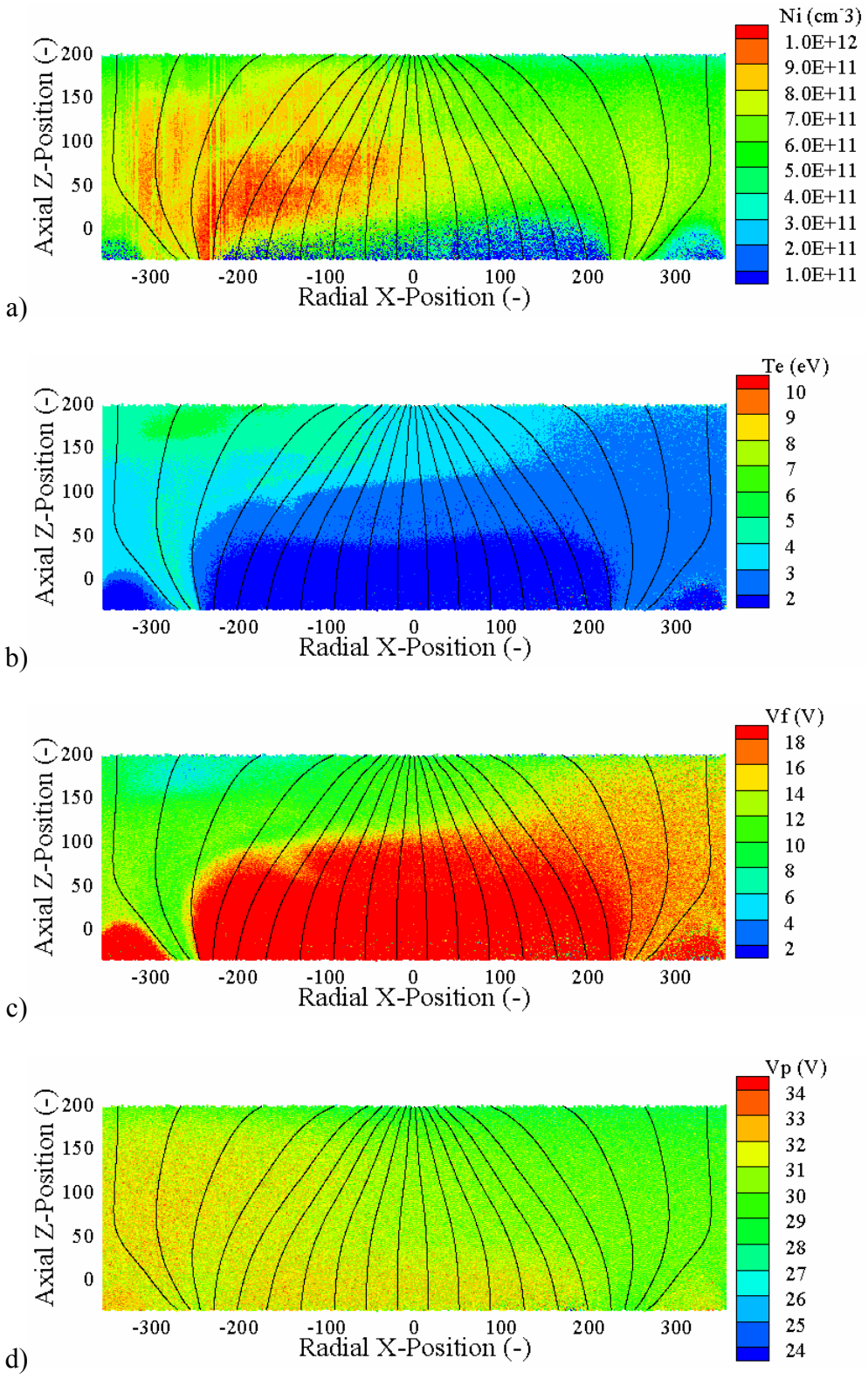

Figure D-38: a) Number density, b) electron temperature, c) floating potential, and d) plasma potential for configuration 10LIH at plane 2.

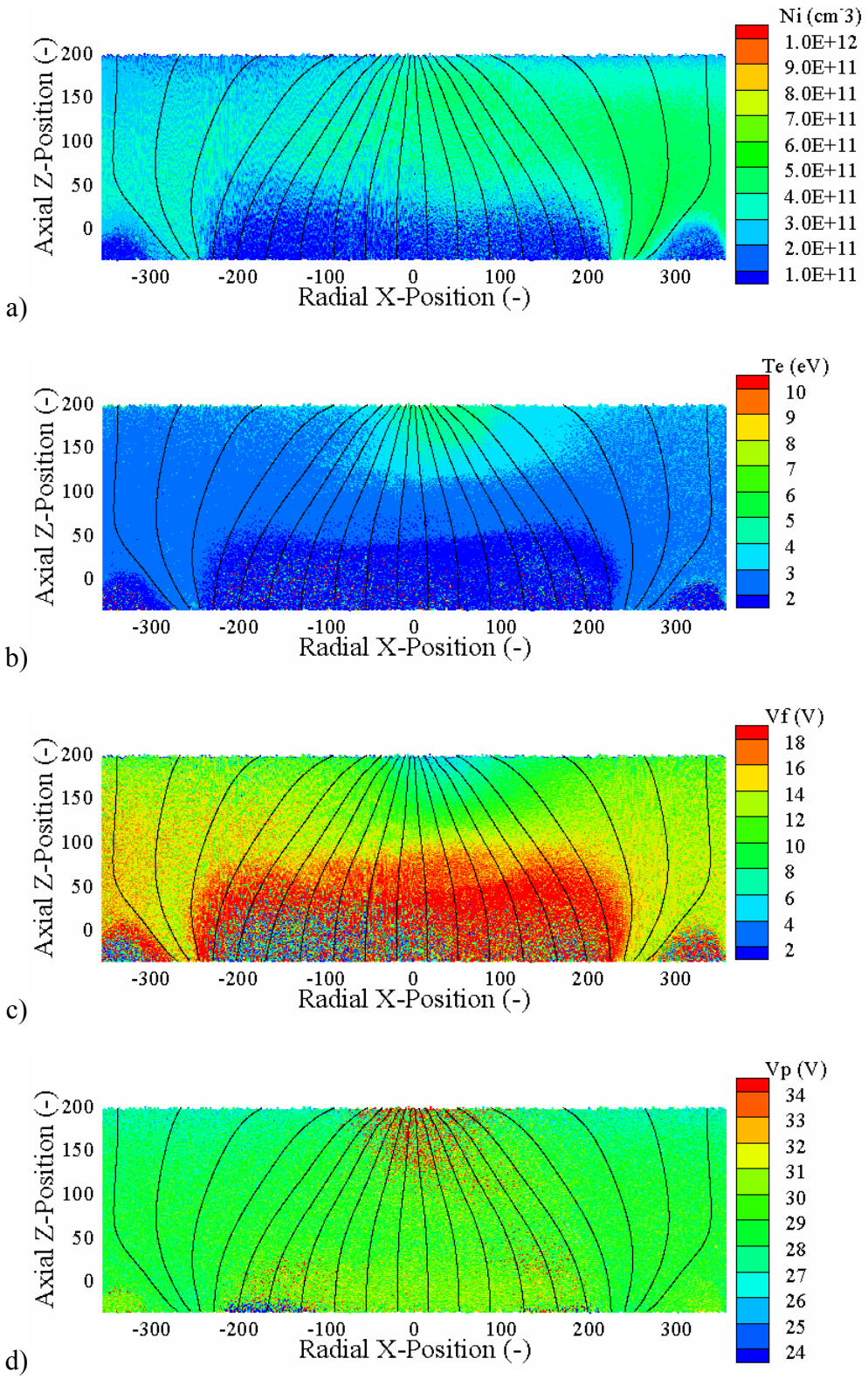

Figure D-39: a) Number density, b) electron temperature, c) floating potential, and d) plasma potential for configuration 10MIH at plane 2.

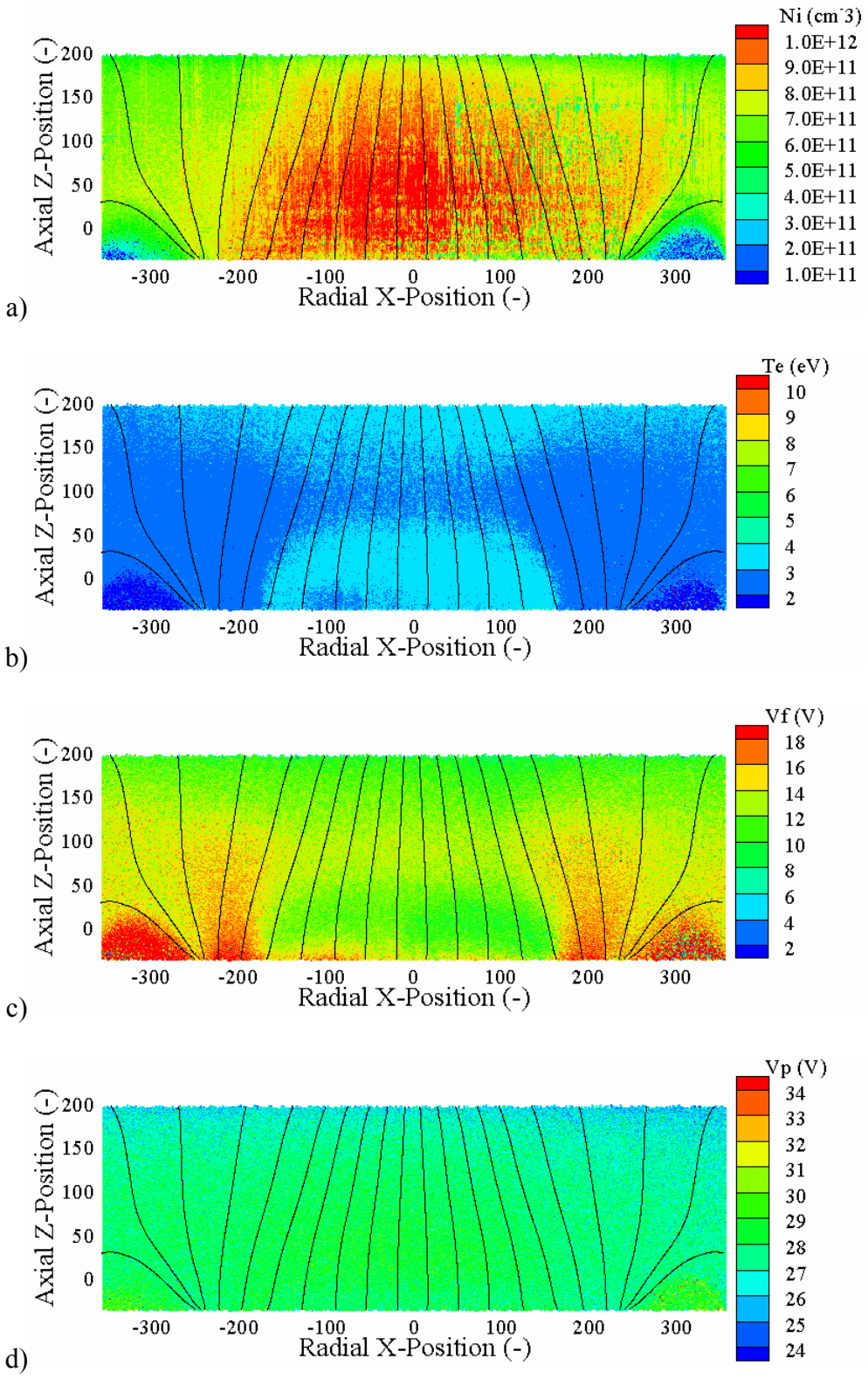

Figure D-40: a) Number density, b) electron temperature, c) floating potential, and d) plasma potential for configuration 0LIF at plane 2.

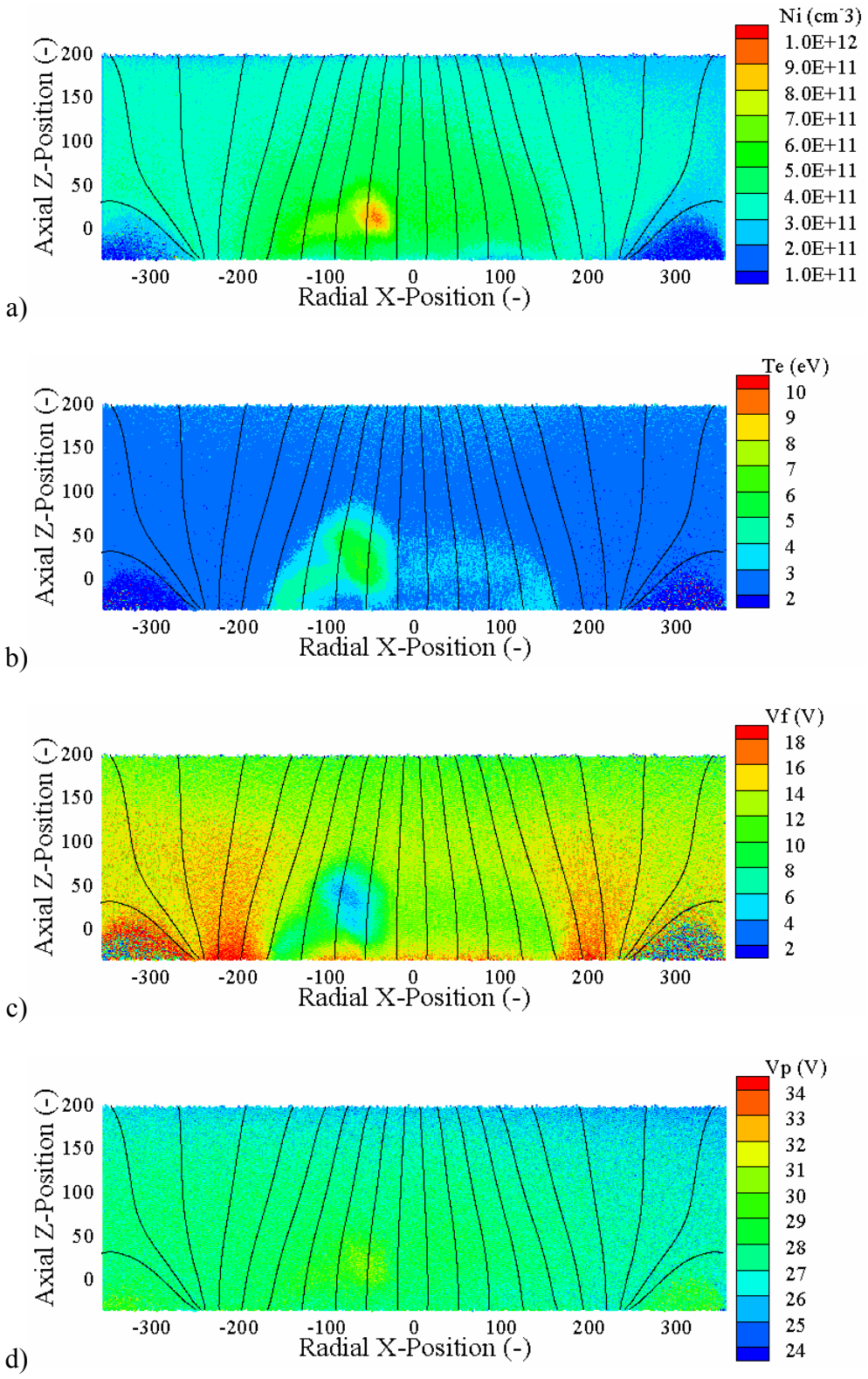

Figure D-41: a) Number density, b) electron temperature, c) floating potential, and d) plasma potential for configuration 0MIF at plane 2.

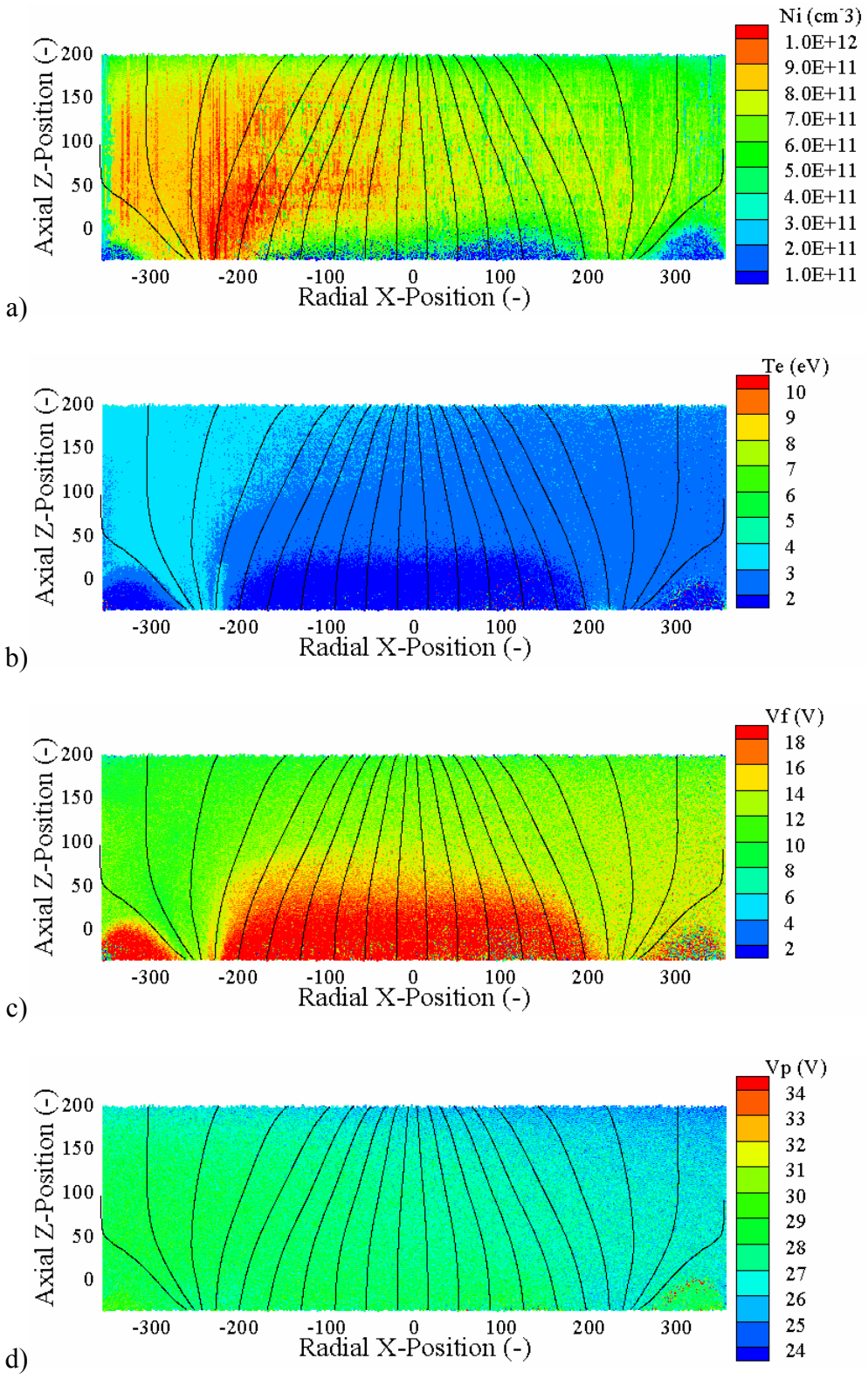

Figure D-42: a) Number density, b) electron temperature, c) floating potential, and d) plasma potential for configuration 5LIF at plane 2.

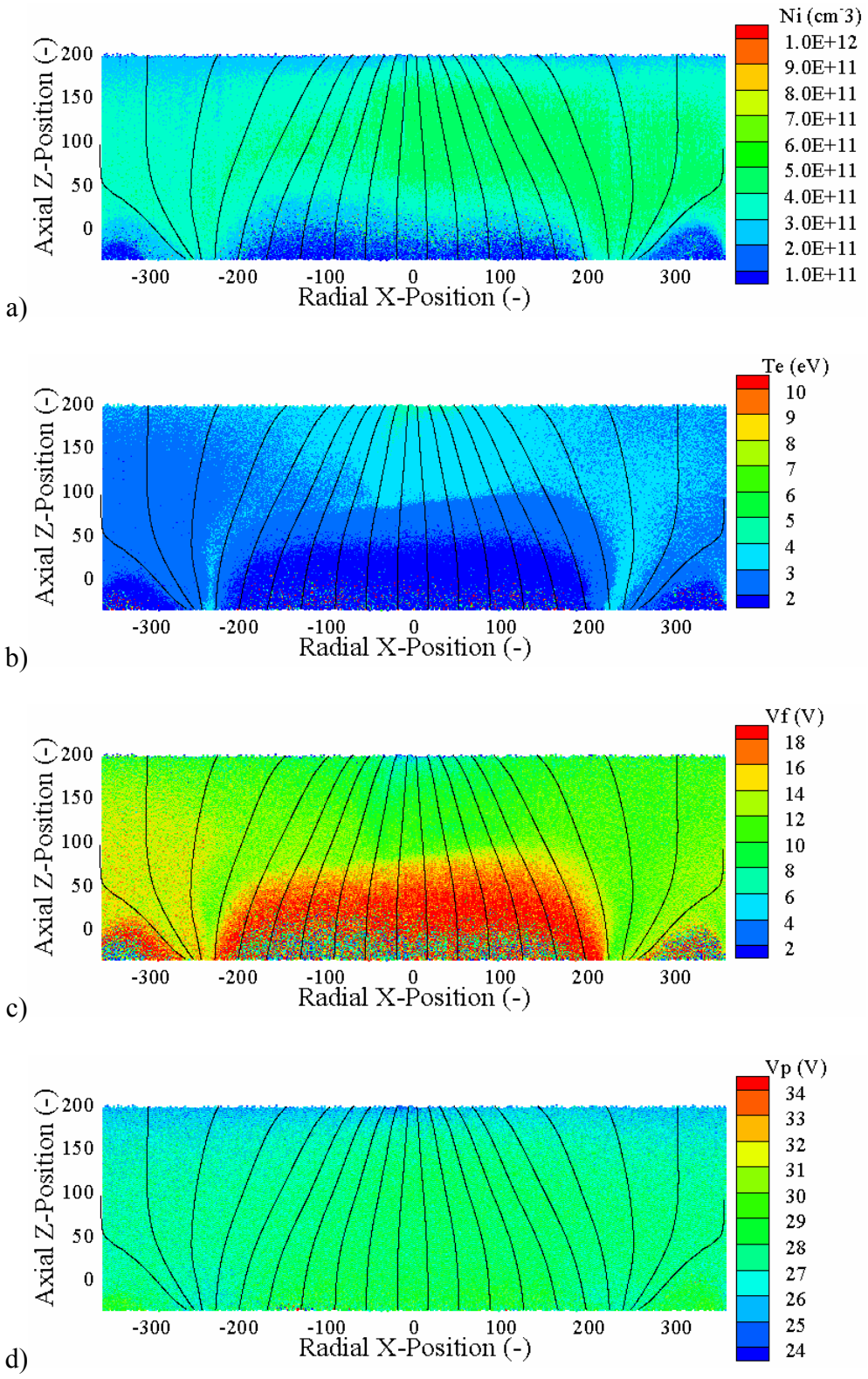

Figure D-43: a) Number density, b) electron temperature, c) floating potential, and d) plasma potential for configuration 5MIF at plane 2.

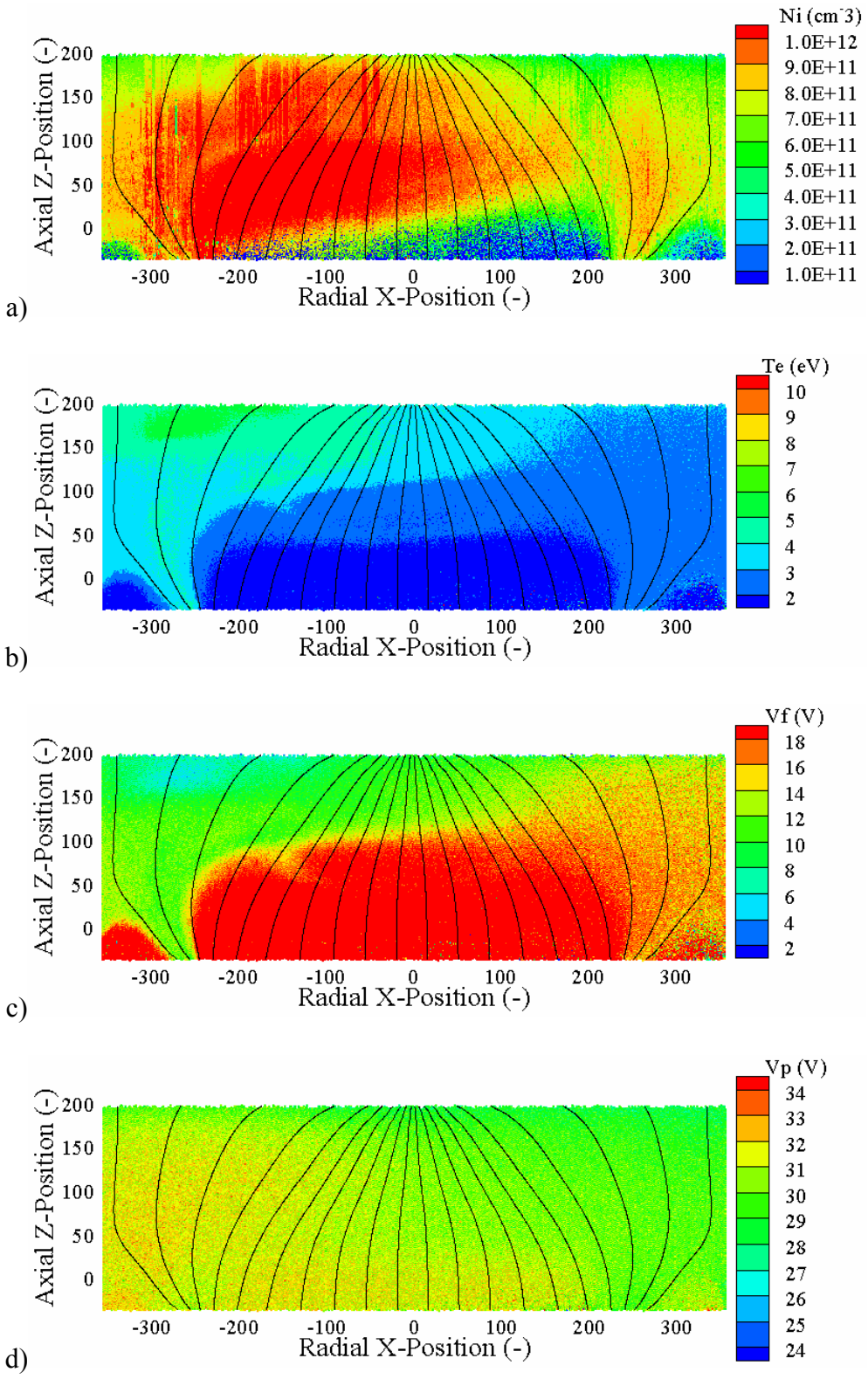

Figure D-44: a) Number density, b) electron temperature, c) floating potential, and d) plasma potential for configuration 10LIF at plane 2.

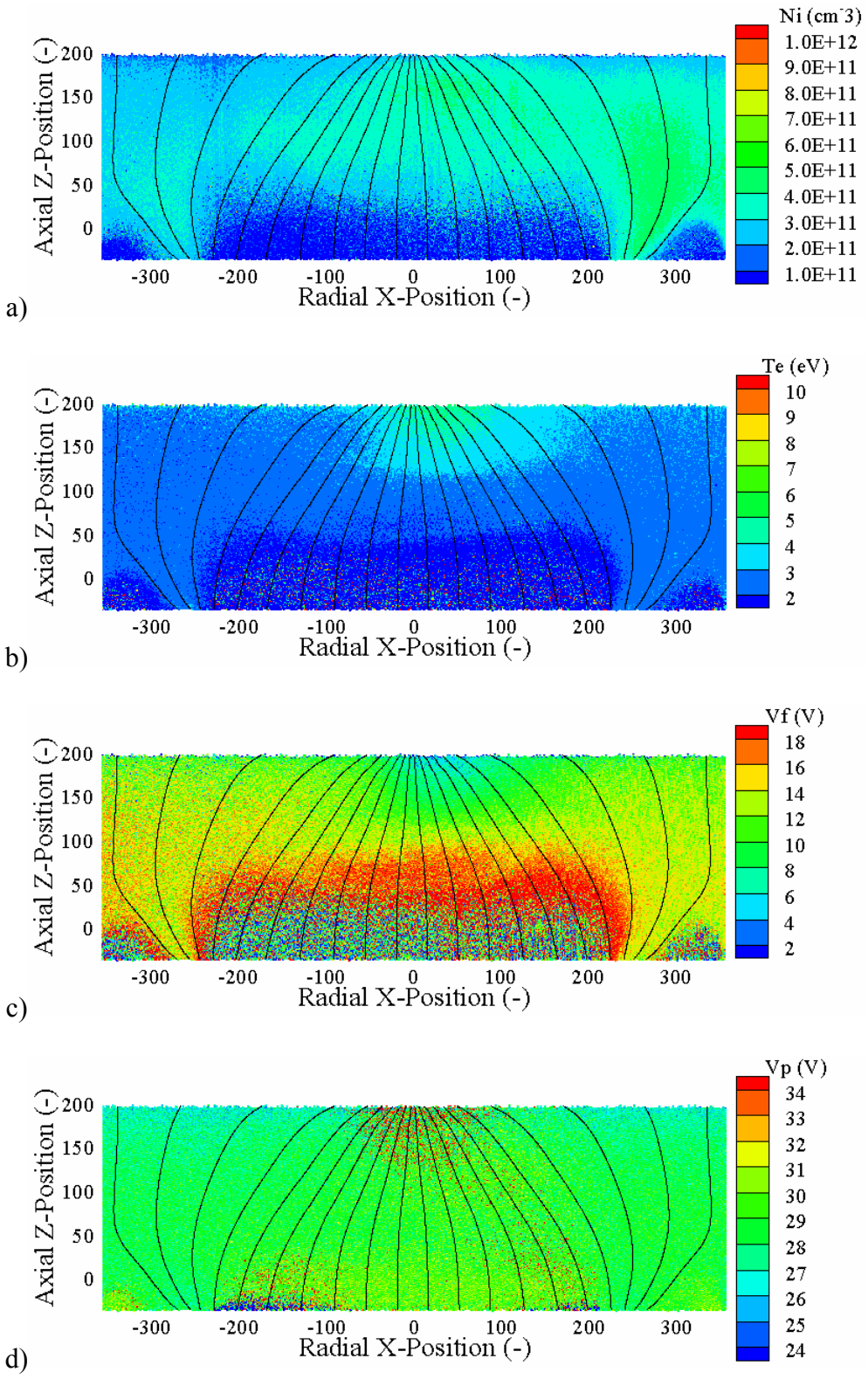

Figure D-45: a) Number density, b) electron temperature, c) floating potential, and d) plasma potential for configuration 10MIF at plane 2.

REFERENCES

1. Patterson, M. J., Roman, R. F., Foster, J. E., "Ion Engine Development for Interstellar Precursor Missions," AIAA-2000-3811, 36th Joint Propulsion Conference, Huntsville, AL, July 16-19, 2000.

2. Oleson, S., "Electric Propulsion Technology Development for the Jupiter Icy Moon Orbiter Project," AIAA-2004-3449, 40th Joint Propulsion Conference, Fort Lauderdale, FL., July 11-14, 2004.

3. Rawlin, V. K., Williams, G. J., Pinero, L., Roman, R. F., "Status of Ion Engine Development for High Power, High Specific Impulse Missions," IEPC-01-096, 27th International Electric Propulsion Conference, Pasadena, CA, October 15-19, 2001.

4. Katz, I., "Electric Propulsion for JPL Missions," AIAA-2005-3674, 41st Joint Propulsion Conference, Tucson, AZ, July 10-13, 2005.

5. Oleson, S., Elliott, F., Randolph, T., Dipprey, N., "The Electric Propulsion Segment of Prometheus 1," AIAA-2005-3888, 41st Joint Propulsion Conference, Tucson, AZ, July 10-13, 2005.

6. Randolph, T., Dougherty, R. C., Oleson, S., Fiehler, D., Dipprey, N., "The Prometheus 1 Spacecraft Preliminary Electric Propulsion System Design," AIAA-2005-3889, 41st Joint Propulsion Conference, Tucson, AZ, July 10-13, 2005.

7. Sengupta, A., Brophy, J. R., Anderson, J. R., Garner, C. E., de Groh, K., Karniotis, T., Banks, B., "An Overview of the Results from the 30,000 Hr Life Test of Deep Space 1 Flight Spare Ion Engine," AIAA-2004-3608, 40th Joint Propulsion Conference, Fort Lauderdale, FL, July 11-14, 2004.

8. Sengupta, A., Brophy, J. R., Goodfellow, K., "Status of the Extended Life Test of the Deep Space 1 flight spare engine after 30,352 hours of operation," AIAA-2003-4558, 39th Joint Propulsion Conference, Huntsville, AL, July 20-23, 2003.

9. Domonkos, M. T., Foster, C., Soulas, G. C., "Wear Testing and Analysis of Ion Engine Discharge Cathode Keeper," Journal of Propulsion and Power, Vol. 21, No. 1, pp. 102-110, Jan.-Feb. 2005.

10. Kamhawi, H., Soulas, G. C., Patterson, M. J., Frandina, M. M., "NEXT Ion Engine 2000 Hr Wear Test Plume and Erosion Results," AIAA-2004-3792, 40th Joint Propulsion Conference, Fort Lauderdale, FL, July 11-14, 2004.

11. Williams, B., Epstein, S., *The Rocket Pioneers: On the Road to Space*, Julian Messner, Inc., New York, 1955.

12. Turner, M. J. L., *Rocket and Spacecraft Propulsion: Principles, Practice and New Developments*, 2nd Ed., Springer, Chichester, UK., 2005.

13. Choueiri, E. Y., Jahn, R. G., "A Critical History of Electric Propulsion: The First Fifty Years (1906-1956)," AIAA-2004-3334, 40th Joint Propulsion Conference, Fort Lauderdale, FL, July 11-14, 2004.

14. Stuhlinger, E., *Ion Propulsion for Space Flight*, McGraw-Hill Book Company, New York, 1964.

15. Sutton, G. P., Biblarz, O., *Rocket Propulsion Elements*, 7th Ed., John Wiley & Sons, Inc., New York, 2001.

16. Hill, P. G., Peterson, C. R., *Mechanics and Thermodynamics of Propulsion*, 2nd Ed., Addison-Wesley Publishing Company, Reading, MA., 1992.

17. Jahn, R. G., *Physics of Electric Propulsion*, McGraw-Hill Book Company, New York, 1968.

18. Manzella, D. H., Penko, P. F., De Witt, K. J., Keith Jr., T. G., "Test-Cell Pressure Effects on the Performance of Resistojets," Journal of Propulsion and Power, Vol. 7, No. 2, pp. 269-274, 1991.

19. Pivirotto, T., King, D., Deininger, W., Brophy, J. R., "The Design and Operating Characteristics of a 30 kW Thermal Arcjet Engine for Space Propulsion," AIAA-86-1508, 22nd Joint Propulsion Conference, Huntsville, AL., June 16-18, 1986.

20. Haag, T. W., "Recent Testing of 30 kW Hydrogen Arcject Thrusters," AIAA-93-1902, 29th Joint Propulsion Conference, Monterey, CA, June 28-July 1, 1993.

21. Smith, Y., Armbruster, Roberts, Lichtin, Beck, "Flight Qualification of a 1.8 kW Hydrazine Arcjet System," IEPC-93-007, 23rd International Electric Propulsion Conference, Seattle, WA, Sept. 13-16, 1993.

22. Goodfellow, K., Polk, J. E., "Design and Development of a 3 to 10 kW Ammonia Arcjet," IEPC-93-078, 23rd International Electric Propulsion Conference, Seattle, WA, Sept. 13-16, 1993.

23. Kaufman, H. R., "Technology of Electron-Bombardment Ion Thrusters," Advances in Electronics and Electron Physics, Vol. 36, pp. 265-373, 1974.

24. Van Noord, J. L., "Thermal Modeling of an Ion Thruster," Doctoral Thesis, Dept. of Aerospace Engineering, University of Michigan, Ann Arbor, MI, 1999.

25. Goebel, D. M., Watkins, R. M., "LaB_6 Hollow Cathodes for Ion and Hall Thrusters," AIAA-2005-4239, 41st Joint Propulsion Conference, Tucson, AZ, July 10-13, 2005.

26. Kamhawi, H., Foster, J. E., "Investigation of Various Microwave Electron Cyclotron Resonance Cathode Configurations," IEPC-2005-283, 29th International Electric Propulsion Conference, Princeton, NJ., Oct. 31-Nov. 4, 2005.

27. Miyamoto, T., Mii, K., Nishijima, T., Hidenobu, I., Takao, Y., Nakashima, H., "Development of a New Microwave Discharge Type Ion Engine," Vacuum, Vol. 73, pp. 391-396, 2004.

28. Kuninaka, H., Satori, S., "Development and Demonstration of a Cathodeless Electron Cyclotron Resonance Ion thruster," Journal of Propulsion and Power, Vol. 14, No. 6, pp. 1022-1026, Nov.-Dec.1998.

29. Foster, J. E., Patterson, M. J., "Discharge Characterization of 40 cm-Microwave ECR Ion Source and Neutralizer," AIAA-2003-5012, 39th Joint Propulsion Conference, Huntsville, AL, July 20-23, 2003.

30. Foster, J. E., Patterson, M. J., "Microwave ECR ion thruster development activities at NASA GRC," AIAA-2002-3837, 38th Joint Propulsion Conference, Indianapolis, IN, July 7-10, 2002.

31. Foster, J. E., Kamhawi, H., Haag, T. W., Carpenter, C., Williams, G. J., "High Power ECR Ion Thruster Discharge Characterization," IEPC-2005-272, 29th International Electric Propulsion Conference, Princeton, NJ., Oct. 31-Nov. 4, 2005.

32. Foster, J. E., Haag, T. W., Kamhawi, H., Patterson, M. J., Malone, S., Elliott, F., Williams, G. J., Sovey, J. S., Carpenter, C., "The High Power Electric Propulsion Thruster," AIAA-2004-3812, 40th Joint Propulsion Conference, Fort Lauderdale, FL, July 11-14, 2004.

33. Medicus, G., "Diffusion and Elastic Collision losses of the 'Fast Electrons' in Plasmas," Journal of Applied Physics, Vol. 29, No. 6, pp. 903-908, June 1958.

34. Brophy, J. R., "Ion thruster performance model," Doctoral Thesis, Dept. of Mechanical Engineering, Colorado State University, Fort Collins, CO, 1984.

35. Brophy, J. R., Wilbur, P. J., "The Flexible Magnetic Field Thruster," Journal of Spacecraft and Rockets, Vol. 20, No. 6, pp. 611-618, Nov.-Dec. 1983.

36. Peterson, P. Y., "The Development and Characterization of a Two-Stage Hybrid Hall/Ion Thruster," Doctoral Thesis, Dept. of Aerospace Engineering, University of Michigan, Ann Arbor, 2004.

37. Peterson, P. Y., Gallimore, A. D., "The Performance and Plume Characterization of a Laboratory Gridless Ion Thruster with Closed Electron Drift Acceleration," AIAA-2004-3936, 40th Joint Propulsion Conference, Fort Lauderdale, FL, July 11-14, 2004.

38. Beattie, J. R., Matossian, J. N., "Mercury Ion Thruster Technology," NASA CR-174974, Hughes Research Laboratories, March 1989.

39. Sovey, J. S., "Improved Ion Containment using a Ring-Cusp Ion thruster," Journal of Spacecraft and Rockets, Vol. 21, No. 5, pp. 488-495, Sept. - Oct. 1984.

40. Patterson, M. J., "Performance Characteristics of Ring-Cusp Thrusters with Xenon Propellant," AIAA-86-1392, 22nd Joint Propulsion Conference, Huntsville, AL, June 16-18, 1986.

41. Beattie, J. R., "Cusped Magnetic Field Mercury Ion thruster," Doctoral Thesis, Dept. of Mechanical Engineering, Colorado State University, Fort Collins, CO, 1976.

42. Beattie, J. R., Kami, S., "Advanced Technology 30-cm-Diameter Ion Thruster," AIAA-82-1910, 16th International Electric Propulsion Conference, New Orleans, LA, Nov. 17-19, 1982.

43. Chen, F. F., *Introduction to Plasma Physics and Controlled Fusion*, Vol. 1: Plasma Physics, Plenum Press, New York, 1984.

44. Foster, J. E., "Intercusp Electron Transport in an NSTAR-derivative Ion thruster," Journal of Propulsion and Power, Vol. 18, No. 1, pp. 213-217, January 2002.

45. Leung, K. N., Hershkowitz, N., MacKenzie, K. R., "Plasma Confinement by Localized Cusps," Physics of Fluids, Vol. 19, No. 7, pp. 1045-1053, July 1976.

46. Knorr, G., Merlino, R. L., "The Role of Fast Electrons for the Confinement of Plasma by Magnetic Cusps," Plasma Physics and Controlled Fusion, Vol. 26, No. 2, pp. 433-442, 1984.

47. Kitsunezaki, A., Mitsumori, T., Sekiguchi, T., "Cusp confinement of high-beta plasmas produced by a laser pulse from a freely-falling deuterium ice pellet," Physics of Fluids, Vol. 17, No. 10, pp. 1895-1902, Oct. 1974.

48. Horiike, H., Akiba, M., Ohara, Y., Okumura, Y., Tanaka, S., "Cusp Width and Power Flow study at a High Power Magnetic Multipole Ion Source," Physics of Fluids, Vol. 30, No. 10, pp. 3268-3275, Oct. 1987.

49. Hershkowitz, N., Leung, K. N., Romesser, T., "Plasma Leakage through a Low-Beta Line Cusp," Physical Review Letters, Vol. 35, pp. 277-280, August 1975.

50. Koch, C., Matthieussent, G., "Collisional Diffusion of a Plasma in Multipolar and Picket Fence Devices," Physics of Fluids, Vol. 26, No. 2, Feb. 1983.

51. Masek, T. D., "Plasma Properties and Performance of Mercury Ion Thrusters," AIAA Journal, Vol. 9, No. 2, pp. 205-212, February 1971.

52. Masek, T. D., "Plasma Properties and Performance of Mercury Ion Thrusters," AIAA-69-256, 7th Electric Propulsion Conference, Williamsburg, VA, March 3-5, 1969.

53. Bohm, D., "Minimum Ionic Kinetic Energy for a Stable Sheath," The Characteristics of Electrical Discharges in Magnetic Fields, A. Guthrie and R. K. Wakerling, eds., McGraw-Hill Book Company, Inc., New York,1949.

54. Dunning, J. W., Hamley, J., Jankovsky, R., Oleson, S., "An Overview of Electric Propulsion Activities at NASA," AIAA-2004-3328, 40th Joint Propulsion Conference, Fort Lauderdale, FL, July 11-14, 2004.

55. Elliott, F., Foster, J. E., Patterson, M. J., "An Overview of the High Power Electric Propulsion (HiPEP) Project," AIAA-2004-3453, 40th Joint Propulsion Conference, Fort Lauderdale, FL, July 11-14, 2004.

56. Williams, G. J., Hickman, T. A., Haag, T. W., Foster, J. E., Patterson, M. J., "Preliminary Wear Analysis Following a 2000-h Wear Test of the HiPEP Ion Thruster," IEPC-2005-260, 29th International Electric Propulsion Conference, Princeton, NJ., Oct. 31-Nov. 4, 2005.

57. Goebel, D. M., Polk, J. E., Sengupta, A., "Discharge Chamber Performance of the NEXIS Ion Thruster," AIAA-2004-3813, 40th Joint Propulsion Conference, Fort Lauderdale, FL, July 11-14, 2004.

58. Martinez, R. A., Buttweiler, M. S., Williams, J. D., Drummond, G., "Evaluation of Sub-scale NEXIS Ion Optics and Strategies for performing Accelerated Wear Testing," AIAA-2004-3628, 40th Joint Propulsion Conference, Fort Lauderdale, FL, July 11-14, 2004.

59. Monheiser, J., Polk, J. E., Randolph, T., "Conceptual Design of the Nuclear Electric Xenon Ion System (NEXIS)," AIAA-2004-3624, 40th Joint Propulsion Conference, Fort Lauderdale, FL, July 11-14. 2004.

60. Randolph, T., Polk, J. E., "An Overview of the Nuclear Electric Xenon Ion System (NEXIS) Activity," AIAA-2004-3450, 40th Joint Propulsion Conference, Fort Lauderdale, FL, July 11-14, 2004.

61. Snyder, J. S., Goebel, D. M., Polk, J. E., Schneider, A. C., Sengupta, A., "Results of a 2000-Hour Wear Test of the NEXIS Ion Engine," IEPC-2005-281, 29th International Electric Propulsion Conference, Princeton, NJ., Oct. 31-Nov. 4, 2005.

62. Soulas, G. C., Foster, J. E., Patterson, M. J., "Performance of Titanium Optics on a NASA 30 cm Ion thruster," AIAA-2000-3814, 36th Joint Propulsion Conference, Huntsville, AL, July 16-19, 2000.

63. Haag, T. W., Patterson, M. J., Rawlin, V. K., Soulas, G. C., "Carbon-based Ion Optics Development at NASA GRC," IEPC-01-94, 27th International Electric Propulsion Conference, Pasadena, CA, October 15-19, 2001.

64. Soulas, G. C., "Improving the Total Impulse capability of the NSTAR Ion thruster with Thick-Accelerator-Grid Ion Optics," IEPC-01-081, 27th International Electric Propulsion Conference, Pasadena, CA, October 15-19, 2001.

65. Foster, J. E., Roman, R. F., Soulas, G. C., Patterson, M. J., "Electron Backstreaming Mitigation via a Magnetic Grid," IEPC-01-91, 27th International Electric Propulsion Conference, Pasadena, CA, October 15-19, 2001.

66. Patterson, M. J., Rawlin, V. K., Sovey, J. S., Kussmaul, M. J., Parkes, J., "2.3 kW Ion Thruster Wear Test," AIAA-95-2516, 31st Joint Propulsion Conference, San Diego, CA, July 10-12, 1995.

67. Polk, J. E., Patterson, M. J., Brophy, J. R., Rawlin, V. K., Sovey, J. S., Myers, R. M., Blandino, J. J., Goodfellow, K., Garner, C. E., "A 1000-Hour Wear Test of the NSTAR Ion Thruster," AIAA-96-2717, 32nd Joint Propulsion Conference, Lake Buena Vista, FL, July 1-3, 1996.

68. Anderson, J. R., Goodfellow, K., Polk, J. E., Shotwell, R. F., Rawlin, V. K., Sovey, J. S., Patterson, M. J., "Results of an On-going Long Duration Ground Test of the DS1 Flight Spare Ion Engine," AIAA-99-2857, 35th Joint Propulsion Conference, Los Angeles, CA, June 20-24, 1999.

69. Polk, J. E., Anderson, J. R., Brophy, J. R., Rawlin, V. K., Patterson, M. J., Sovey, J. S., Hamley, J., "An Overview of the Results from an 8200 Hour Wear Test of the NSTAR Ion thruster," AIAA-99-2446, 35th Joint Propulsion Conference, Los Angeles, California, June 20-24, 1999.

70. Polk, J. E., Anderson, J. R., Brophy, J. R., Rawlin, V. K., Patterson, M. J., Sovey, J. S., "The Effect of Engine Wear on Performance in the NSTAR 8000 Hour Ion Engine Endurance Test," AIAA-97-3387, 33rd Joint Propulsion Conference, Seattle, WA, July 6-9, 1997.

71. Sengupta, A., Anderson, J. R., Brophy, J. R., Rawlin, V. K., Sovey, J. S., "Performance Characteristics of the Deep Space 1 Flight Spare Ion Thruster Long Duration Test after 21,300 hours of operation," AIAA-2002-3959, 38th Joint Propulsion Conference, Indianapolis, IN, July 7-10, 2002.

72. Anderson, J. R., Goodfellow, K., Polk, J. E., Rawlin, V. K., Sovey, J. S., "Performance Characteristics of the NSTAR Ion Thruster During an On-Going

Long Duration Ground Test," IEEE Aerospace Conference, Big Sky, MT, March 18-25, 2000.

73. Sengupta, A., "Destructive Physical Analysis of Hollow Cathodes from the Deep Space 1 Flight Spare Ion Engine 30,000 Hr Life Test," IEPC-2005-026, 29th International Electric Propulsion Conference, Princeton, NJ., Oct. 31-Nov. 4, 2005.

74. Poeschel, R. L., "Development of Advanced inert-gas ion thrusters," NAS3-22474, Hughes Research Laboratories, Malibu, June 1983.

75. King, L. B., "Transport-Property and Mass Spectral Measurements in the Plasma Exhaust Plume of a Hall effect Space Propulsion System," Doctoral Thesis, Dept. of Aerospace Engineering, University of Michigan, Ann Arbor, 1998.

76. Garner, C. E., Brophy, J. R., Polk, J. E., Pless, L. C., "Cyclic Endurance Test of a SPT-100 Stationary Plasma thruster," AIAA-94-2856, 30th Joint Propulsion Conference, Indianapolis, IN, June 27-29, 1994.

77. Garner, C. E., Brophy, J. R., Polk, J. E., Pless, L. C., "A 5,730 Hr Cyclic Endurance Test of the SPT-100," AIAA-95-2667, 31st Joint Propulsion Conference, San Diego, CA, July 10-12, 1995.

78. Day, M., Kim, V., Kozlov, V. I., Popov, G. A., Skrylnikov, A. I., "Investigation of the nonoperating cathode erosion reasons," AIAA-96-2710, 32nd Joint Propulsion Conference, Lake Buena Vista, FL, July 1-3, 1996.

79. Herman, D. A., "The Use of Electrostatic Probes to Characterize the Discharge Plasma Structure and Identify Discharge Cathode Erosion Mechanisms in Ring-Cusp Ion Thrusters," Doctoral Thesis, Dept. of Aerospace Engineering, University of Michigan, Ann Arbor, MI., 2005.

80. Nicholson, D. R., *Introduction to Plasma Theory*, John Wiley & Sons, Inc., New York, 1983.

81. Williams, G. J., Sovey, J. S., Haag, T. W., "Characterization of High-Specific Impulse, High-Power Ion Optics," AIAA-2004-3630, 40th Joint Propulsion Conference, Fort Lauderdale, FL, July 11-14, 2004.

82. Williams, G. J., "Life-limiting Trends of High-Specific Impulse Ion Optics," AIAA-2004-3631, 40th Joint Propulsion Conference, Fort Lauderdale, FL, July 11-14, 2004.

83. Williams, J. D., Laufer, D. M., Wilbur, P. J., "Experimental performance limits on high specific impulse ion optics," IEPC-03-128, 28th International Electric Propulsion Conference, Toulouse, France, March 17-21, 2003.

84. Soulas, G. C., Haag, T. W., Patterson, M. J., Rawlin, V. K., "Titanium Optics for ion thrusters," IEPC-99-149, 26th International Electric Propulsion Conference, Kitakyushu, Japan, October 17-21, 1999.

85. Emhoff, J. W., Boyd, I. D., "Progress in NEXT Ion Optics Modeling," AIAA-2004-3786, 40th Joint Propulsion Conference, Fort Lauderdale, FL, July 11-14, 2004.

86. Emhoff, J. W., "Simulation of Ion Optics Using Particle-In-Cell and Treecode Methods," Doctoral Thesis, Dept. of Aerospace Engineering, University of Michigan, Ann Arbor, 2005.

87. Soulas, G. C., "Performance Evaluation of Titanium Ion Optics for the NASA 30 cm Ion thruster," IEPC-01-092, 27th International Electric Propulsion Conference, Pasadena, CA, October 15-19, 2001.

88. Dushman, S., *Scientific Foundations of Vacuum Technique*, Vol. 4, Wiley, New York, 1958.

89. Walker, M. L. R., Gallimore, A. D., Chunpei, C., Boyd, I. D., "Pressure Map of a Facility as a function of Flow Rate to study Facility Effects," AIAA-2002-3815, 38th Joint Propulsion Conference, Indianapolis, IN, July 7-10, 2002.

90. Walker, M. L. R., "Vacuum Chamber Pressure Maps of a Hall thruster Cold-Flow Expansion," Journal of Propulsion and Power, Vol. 20, No. 6, pp. 1127-1131, Nov. 2004.

91. Walker, M. L. R., Gallimore, A. D., "Neutral density map of Hall thruster plume expansion in a vacuum chamber," Review of Scientific Instruments, Vol. 76, May 2005.

92. Brophy, J. R., "Simulated Ion Thruster Operation Without Beam Extraction," AIAA-90-2655, 21st International Electric Propulsion Conference, Orlando, FL, July 18-20, 1990.

93. Foster, J. E., Personal Communication, NASA Glenn Research Center, Cleveland, OH., October, 2004.

94. Herman, D. A., Gallimore, A. D., "Comparison of Discharge Plasma Parameters in a 30-cm NSTAR Type Ion Engine with and without Beam Extraction," AIAA 2003-5162, 39th Joint Propulsion Conference, Huntsville, Alabama, July 20-23, 2003.

95. Herman, D. A., McFarlane, D. S., Gallimore, A. D., "Discharge Plasma Parameters of a 30 cm Ion thruster measured Without Beam Extraction using a High-speed Axial Reciprocating Probe positioning system," IEPC-03-0069, 28th International Electric Propulsion Conference, Toulouse, France, March 17-21, 2003.

96. Herman, D. A., Gallimore, A. D., "Discharge Chamber Plasma Structure of a 40-cm NEXT-type Ion Engine," AIAA-2005-4250, 41st Joint Propulsion Conference, Tucson, AZ, July 10-13, 2005.

97. Herman, D. A., Gallimore, A. D., "Discharge Chamber Plasma Potential Mapping of a 40-cm NEXT-type Ion Engine," AIAA-2005-4251, 41st Joint Propulsion Conference, Tucson, AZ, July 10-13, 2005.

98. Herman, D. A., Gallimore, A. D., "Discharge Cathode Electron Energy Distribution Functions in a 40-cm NEXT-type Ion Engine," AIAA-2005-4252, 41st Joint Propulsion Conference, Tucson, AZ, July 10-13, 2005.

99. Reader, P. D., "Experimental Effects of Propellant Introduction Mode on Electron-Bombardment Ion Rocket Performance," NASA TN D-2587, 1965.

100. Rizzoni, G., *Principles and Applications of Electrical Engineering*, Third Ed., McGraw-Hill Companies, Inc., New York, 2000.

101. Haas, J. M., Gulczinski, F. S., Gallimore, A. D., Spanjers, G. G., Spores, R. A., "Performance Characteristics of a 5 kW Laboratory Hall thruster," AIAA-98-3503, 34th Joint Propulsion Conference, Cleveland, OH, July 12-15, 1998.

102. Stuart, R. V., Wehner, G. K., "Sputtering Yields at Very Low Bombarding Ion Energies," Journal of Applied Physics, Vol. 33, No. 7, pp. 2345-2352, July 1962.

103. Rosenberg, D., Wehner, G. K., "Sputtering Yields for Low Energy He^+-, Kr^+-, and Xe^+-Ion Bombardment," Journal of Applied Physics, Vol. 33, No. 5, pp. 1842-1845, May 1962.

104. Langmuir, I., "The Interaction of Electron and Positive Ion Space Charges in Cathode Sheaths," Physical Review, Vol. 33, pp. 954-989, June 1929.

105. Mott-Smith, H. M., Langmuir, I., "The Theory of Collectors in Gaseous Discharges," Physical Review, Vol. 28, pp. 727-763, October 1926.

106. Haas, J. M., Gallimore, A. D., "Characterization of the Internal Plasma Structure of a 5kW Hall thruster," IEPC 99-078, 26th International Electric Propulsion Conference, Kitakyushu, Japan, October 1999.

107. Haas, J. M., Gallimore, A. D., "Internal Plasma Potential profiles in a Laboratory-model Hall thruster," Physics of Plasmas, Vol. 8, No. 2, pp. 652-660, February 2001.

108. Hutchinson, I. H., *Principles of Plasma Diagnostics*, Second Ed., Cambridge University Press, Cambridge, 2002.

109. Hofer, R. R., "Development and Characterization of High-Efficiency, High-Specific Impulse Xenon Hall thrusters," Doctoral Thesis, Dept. of Aerospace Engineering, University of Michigan, Ann Arbor, MI, 2004.

110. Azziz, Y., Martinez-Sanchez, M., Szabo, J., "Effect of Discharge Voltage on Plume Divergence of a High Specific-Impulse Hall thruster," AIAA-2005-4403, 41st Joint Propulsion Conference, Tucson, AZ, July 10-13, 2005.

111. Beal, B. E., "Clustering of Hall Effect thrusters for High-Power Electric Propulsion Applications," Doctoral Thesis, Dept. of Aerospace Engineering, University of Michigan, Ann Arbor, MI, 2004.

112. Haas, J. M., Gallimore, A. D., McFall, K., Spanjers, G. G., "Development of a High-speed, Reciprocating Electrostatic probe system for Hall thruster Interrogation," Review of Scientific Instruments, Vol. 71, No. 11, pp. 4131-4138, November 2000.

113. Haas, J. M., "Low-Perturbation Interrogation of the Internal and Near-field Plasma Structure of a Hall thruster using a High-Speed Probe Positioning System," Doctoral Thesis, Dept. of Aerospace Engineering, University of Michigan, Ann Arbor, MI, 2001.

114. Hofer, R. R., Gallimore, A. D., "Recent Results from Internal and Very-Near-Field Plasma Diagnostics of a High Specific Impulse Hall thruster," IEPC-03-037, 28th International Electric Propulsion Conference, Toulouse, France, March 17-21, 2003.

115. Linnell, J. A., Gallimore, A. D., "Internal Plasma Structure Measurements of a Hall Thruster Using Plasma Lens Focusing," AIAA-2005-4402, 41st Joint Propulsion Conference, Tucson, AZ., July 10-13, 2005.

116. Herman, D. A., Gallimore, A. D., "A High-speed Axial Reciprocating probe positioning system for Interrogating the Discharge Plasma of a 30 cm Ion thruster," AIAA-2002-4256, 38th Joint Propulsion Conference, Indianapolis, IN, July 7-10, 2002.

117. Herman, D. A., Gallimore, A. D., "Near Discharge Cathode Assembly Plasma Potential Measurements in a 30-cm NSTAR-type Ion Engine amidst Beam Extraction," AIAA-2004-3958, 40th Joint Propulsion Conference, Fort Lauderdale, FL, July 11-14, 2004.

118. Herman, D. A., Gallimore, A. D., "Discharge Chamber Plasma Structure of a 30-cm NSTAR-type Ion Engine," AIAA-2004-3794, 40th Joint Propulsion Conference, Fort Lauderdale, FL, July 11-14, 2004.

119. Chen, F. F., "Electric Probes," Plasma Diagnostic Techniques, R. H. Huddlestone and S. L. Leonard, eds., Academic Press, New York,1965.

120. Zikeyev, M. V., Shagayda, A. A., "Probe Measurements in Discharge Chamber of Low-Power Ion thruster," IEPC-03-120, 28th International Electric Propulsion Conference, Toulouse, France, March 17-21, 2003.

121. Wilbur, P. J., Isaacson, J., "Plasma Property Contours in a 15 cm Hollow Cathode Kaufman thruster," Dept. of Mechanical Engineering, Colorado State University, Fort Collins, CO, February 1973.

122. Sengupta, A., Goebel, D. M., Fitzgerald, D., Owens, A., Tynan, G., Doerner, R., "Experimentally Determined Neutral Density and Plasma Parameters in a 30cm Ion Engine," AIAA-2004-3613, 40th Joint Propulsion Conference, Fort Lauderdale, FL, July 11-14, 2004.

123. Beattie, J. R., Wilbur, P. J., "Cusped magnetic field mercury ion thruster," Journal of Spacecraft and Rockets, Vol. 14, No. 12, pp. 747-755, Dec. 1977.

124. Hershkowitz, N., "How Langmuir Probes Work," Plasma Diagnostics, O. Auciello and D. L. Flamm, eds., Academic Press, Inc., Boston, pp. 113-184,1989.

125. Bohm, D., Burhop, E. H. S., Massey, H. S. W., "The Use of Probes for Plasma Exploration in Strong Magnetic Fields," The Characteristics of Electrical Discharges in Magnetic Fields, A. Guthrie and R. K. Wakerling, eds., McGraw-Hill Book Company, Inc., New York,1949.

126. Laframboise, J. G., Parker, L. W., "Probe Design for Orbit-Limited Current Collection," Physics of Fluids, Vol. 16, No. 5, pp. 629-636, May 1973.

127. Laframboise, J. G., "Theory of Spherical and Cylindrical Langmuir probes in a Collisionless, Maxwellian Plasma at Rest," UTIAS Report No. 100, Institute for Aerospace Studies, University of Toronto, Toronto, Canada, June 1966.

128. Steinbrüchel, C., Journal of the Electrochemical Society, Vol. 130, pp. 648,

129. Beattie, J. R., "Numerical Procedure for Analyzing Langmuir Probe Data," AIAA Journal, Vol. 13, No. 7, pp. 950-952, July 1975.

130. McCalla, T. R., *Introduction to Numerical Methods and FORTRAN Programming*, John Wiley & Sons, Inc., New York, 1967.

131. Brown, I. G., Compher, A. B., Kunkel, W. B., "Response of a Langmuir Probe in a Strong Magnetic Field," Physics of Fluids, Vol. 14, No. 7, pp. 1377-1383, July 1971.

132. Pytlinski, J. T., Donnert, H. J., Alexeff, I., "Behavior of a single Langmuir probe in a magnetic field," American Journal of Physics, Vol. 46, No. 12, pp. 1276-1278, Dec. 1978.

133. Sugawara, M., "Electron Probe Current in a Magnetized Plasma," Physics of Fluids, Vol. 9, No. 4, pp. 797-800, April 1966.

134. Foster, J. E., Gallimore, A. D., "The effect of an auxiliary discharge on anode sheath potentials in a transverse discharge," Journal of Applied Physics, Vol. 81, No. 8, pp. 3422-3432, April 1997.

135. Reinsche, C. H., "Smoothing by spline functions," Numerische Mathematik, Vol. 10, pp. 177-183, 1967.

136. Domonkos, M. T., "Evaluation of Low-Current Orificed Hollow Cathodes," Doctoral Thesis, Dept. of Aerospace Engineering, University of Michigan, Ann Arbor, MI, 1999.

137. Soulas, G. C., Haag, T. W., Patterson, M. J., "Performance Evaluation of 40cm Ion Optics for the NEXT Ion Engine," AIAA-2002-3834, 38th Joint Propulsion Conference, Indianapolis, IN, July 7-10, 2002.

138. Soulas, G. C., Kamhawi, H., Patterson, M. J., Britton, M. A., Frandina, M. M., "NEXT Ion Engine 2000 Hr Wear Test Results," AIAA-2004-3791, 40th Joint Propulsion Conference, Fort Lauderdale, FL, July 11-14, 2004.

139. Kolasinski, R. D., Polk, J. E., "Characterization of Cathode Keeper Wear by Surface Layer Activation," Journal of Propulsion and Power, Vol. 20, No. 6, pp. 992-999, Nov.-Dec. 2004.

140. Kameyama, I., Wilbur, P. J., "Effects of External Flow near High-Current Hollow Cathodes on Ion-Energy Distributions," IEPC-97-173, 25th International Electric Propulsion Conference, Cleveland, OH, Aug. 24-28, 1997.

141. Kameyama, I., "Characteristics of Ions Emitted from High-Current Hollow Cathodes," Doctoral Thesis, Dept. of Mechanical Engineering, Colorado State University, Fort Collins, CO, 1994.

142. Miller, J. S., Pullins, S., Levandier, D. J., Chiu, Y. H., Dressler, R. A., "Xenon Charge Exchange Cross Sections for Electrostatic Thruster Models," Journal of Applied Physics, Vol. 91, No. 3, pp. 984-991, Feb. 2002.

143. Boyd, I. D., Dressler, R. A., "Far field modeling of the plasma plume of a Hall thruster," Journal of Applied Physics, Vol. 92, No. 4, pp. 1764-1774, Aug. 2002.

144. Sovey, J. S., Patterson, M. J., "Ion Beam Sputtering in Electric Propulsion Facilities," AIAA-91-2117, 27th Joint Propulsion Conference, Sacramento, CA, June 24-27, 1991.

145. Oh, D. Y., "Computational Modeling of Expanding Plasma Plumes in Space Using a PIC-DSMC Algorithm," Doctoral Thesis, Dept. of Aeronautics and Astronautics, Massachusetts Institute of Technology, Cambridge, MA, 1996.

146. Ramsey, W. D., "Inert Gas Ion Thruster Program," NASA CR-165521, Xerox Electro-Optical Systems, Pasadena, CA, Dec. 1980.

147. Brewer, G. R., *Ion Propulsion Technology and Applications*, Gordon and Breach Science Publishers, New York, 1970.

148. Williams, G. J., Smith, T. B., Domonkos, M. T., Gallimore, A. D., Drake, R. P., "Laser-Induced Fluorescence Characterization of Ions Emitted from Hollow Cathodes," IEEE Transactions on Plasma Science, Vol. 28, No. 5, pp. 1664-1675, Oct. 2000.

149. Williams, G. J., Smith, T. B., Hidaka, Y., Gallimore, A. D., "FMT-2 discharge cathode erosion rate measurements via laser-induced fluorescence," AIAA-2000-3663, 36th Joint Propulsion Conference, Huntsville, AL, July 17-19, 2000.

150. Williams, G. J., Smith, T. B., Patrick, T. A., Gallimore, A. D., "Characterization of the FMT-2 discharge cathode plume," IEPC-99-104, 26th International Electric Propulsion Conference, Kitakyushu, Japan, October 1999.

151. Kameyama, I., Wilbur, P. J., "Potential-Hill Model of High-Energy Ion Production near High-Current Hollow Cathodes," ISTS 98-a-2-17, 21st International Symposium on Space Technology and Science, Sonic City, Omiya, Japan, May 24-31, 1998.

152. Sengupta, A., "Experimental Investigation of Discharge Plasma Magnetic Confinement in an NSTAR Ion Thruster," AIAA-2005-4069, 41st Joint Propulsion Conference, Tucson, AZ, July 10-13, 2005.

153. Jameson, K. K., Goebel, D. M., Watkins, R. M., "Hollow Cathode and Keeper-Region Plasma Measurements," AIAA-2005-3667, 41st Joint Propulsion Conference, Tucson, AZ, July 10-13, 2005.

154. Jameson, K. K., Goebel, D. M., Watkins, R. M., "Hollow Cathode and Thruster Discharge Chamber Plasma Measurements Using High-Speed Scanning Probes," IEPC-2005-269, 29th International Electric Propulsion Conference, Princeton, NJ., Oct. 31-Nov. 4, 2005.

155. Goebel, D. M., Jameson, K. K., Watkins, R. M., Katz, I., "Hollow Cathode and Keeper-Region Plasma Measurements using Ultra-fast Miniature Scanning Probes," AIAA-2004-3430, 40th Joint Propulsion Conference, Fort Lauderdale, FL, July 11-14, 2004.

156. Martin, R. H., Farnell, C. C., Williams, J. D., "Direct and Remote Measurements of Plasma Properties nearby Hollow Cathodes," IEPC-2005-294, 29th International Electric Propulsion Conference, Princeton, NJ, Oct. 31-Nov. 4, 2005.

157. Goebel, D. M., "Energetic Ion Production and Electrode Erosion in Hollow Cathode Discharges," IEPC-2005-266, 29th International Electric Propulsion Conference, Princeton, NJ., Oct. 31-Nov. 4, 2005.

158. Raitses, Y., Ashkenazy, J., Appelbaum, G., "Probe Measurements of Plasma Properties inside an Experimental Hall Thruster," AIAA-98-3640, 34th Joint Propulsion Conference, Cleveland, OH., July 13-15, 1998.

159. Kim, V., Grdlichko, D., Kozlov, V. I., Lazourenko, A., Popov, G. A., Skrylnikov, A. I., "Local Plasma Parameter Measurements by Nearwall Probes inside the SPT Accelerating Channel under Thruster Operation with Kr," AIAA-2002-4108, 38th Joint Propulsion Conference, Indianapolis, IN., July 7-10, 2002.

160. Haas, J. M., Gallimore, A. D., "Considerations on the Role of the Hall Current in a Laboratory-Model Thruster," IEEE Transactions on Plasma Science, Vol. 30, No. 2, pp. 687-697, April 2002.

161. Williams, G. J., Smith, T. B., Gallimore, A. D., "30 cm Ion Thruster Discharge Cathode Erosion," IEPC-01-306, 27th International Electric Propulsion Conference, Pasadena, CA, Oct. 14-19, 2001.

162. Williams, G. J., "The Use of Laser-Induced Fluorescence to Characterize Discharge Cathode Erosion in a 30 cm Ring-Cusp Ion thruster," Doctoral Thesis, Dept. of Aerospace Engineering, University of Michigan, Ann Arbor, MI., 2000.

163. Juliano, D. R., Ruzic, D. N., Allain, M. M. C., Hayden, D. B., "Influences on Ionization Fraction in an Inductively Coupled Ionized Physical Vapor Deposition Device Plasma," Journal of Applied Physics, Vol. 91, No. 2, pp. 605-612, Jan. 2002.

164. Stotler, D. P., Skinner, C. H., Budny, R. V., Ramsey, A. T., Ruzic, D. N., Turkot, R. B. J., "Modeling of Neutral Hydrogen Velocities in Tokamak Fusion Test Reactor," Physics of Plasmas, Vol. 3, No. 11, pp. 4084-4094, Nov. 1996.

165. Ruzic, D. N., "Fundamentals of Sputtering and Reflection," Handbook of Plasma Processing Technology : Fundamentals, Etching, Deposition, and Surface Interactions, S. M. Rossnagel, J. J. Cuomo, and W. D. Westwood, eds., Noyes Publications, Park Ridge, N.J., U.S.A.,1990.

166. Shaheen, M. A., Ruzic, D. N., "Evolution of Atomic-Scale Surface Structures During Ion Bombardment: A Fractal Simulation," Journal of Vacuum Science and Technology A, Vol. 11, No. 6, pp. 3085-3091, Nov.- Dec. 1993.

167. Halliday, D., Resnick, R., Walker, J., *Fundamentals of Physics*, Fifth Ed., John Wiley & Sons, Inc., New York, 1997.

168. Williams, G. J., Domonkos, M. T., Chavez, J. M., "Measurement of Doubly Charged Ions in Ion Thruster Plumes," IEPC-01-310, 27th International Electric Propulsion Conference, Pasadena, CA, October 15-19, 2001.

169. Foster, J. E., Patterson, M. J., "Plasma Emission Characteristics from a High Current Hollow Cathode in an Ion Thruster Discharge Chamber," AIAA-2002-4102, 38th Joint Propulsion Conference, Indianapolis, IN, July 7-10, 2002.

170. Kameyama, I., Wilbur, P. J., "Measurements of Ions from High-Current Hollow Cathodes using Electrostatic Energy Analyzer," Journal of Propulsion and Power, Vol. 16, No. 3, pp. 529-535, May-June 2000.

171. Ruyten, W. M., "Density-Conserving Shape Factors for Particle Simulations in Cylindrical and Spherical Coordinates," Journal of Computational Physics, Vol. 105, pp. 224-232, April 1993.

172. Doerner, R. P., Goebel, D. M., "Sputtering Yields of Ion thruster Grid and Cathode Materials during very low energy xenon plasma bombardment," AIAA-2003-4561, 39th Joint Propulsion Conference, Huntsville, AL, July 20-23, 2003.

173. Doerner, R. P., Whyte, D. G., Goebel, D. M., "Sputtering yield measurements during low energy xenon plasma bombardment," Journal of Applied Physics, Vol. 93, No. 9, pp. 5816-5823, May 2003.

174. Wehner, G. K., "Influence of the Angle of Incidence on Sputtering Yields," Journal of Applied Physics, Vol. 30, No. 11, pp. 1762-1765, Nov. 1959.

175. Tartz, M., Manova, D., Neumann, H., Leiter, H., Esch, J., "Sputter Investigation of Ion Thrusters Grid Materials," AIAA-2005-4414, 41st Joint Propulsion Conference, Tucson, AZ, July 10-13, 2005.

176. Cheney, K. B., Pitkin, E. T., "Sputtering at Acute Incidence," Journal of Applied Physics, Vol. 36, No. 11, pp. 3542-3544, Nov. 1965.

177. Yamamura, Y., "An Empirical Formula for Angular Dependence of Sputtering Yields," Radiation Effects, Vol. 80, pp. 57-72, 1984.

178. Yamamura, Y., "Threshold Energies of Light-Ion Sputtering and Heavy-Ion Sputtering as a function of Angle of Incidence," Nuclear Instruments and Methods in Physics Research B2, pp. 627-630, 1984.

179. Kolasinski, R. D., "Oblique Angle Sputtering Yield Measurements for Ion Thruster Grid Materials," AIAA-2005-3526, 41st Joint Propulsion Conference, Tucson, AZ, July 10-13, 2005.

180. Kolasinski, R. D., "Sputtering Yields of Ion Thruster Materials at Oblique Incidence," AIAA-2004-4110, 40th Joint Propulsion Conference, Fort Lauderdale, FL, July 11-14, 2004.

181. Zoerb, K. A., Williams, J. D., Williams, D. D., Yalin, A. P., "Differential Sputtering Yields of Refractory Metals under Xenon, Krypton, and Argon Ion Bombardment at Normal and Oblique Incidences," IEPC-2005-293, 29th International Electric Propulsion Conference, Princeton, NJ., Oct. 31-Nov. 4, 2005.

182. Crofton, M. W., Murray, J. C., Pollard, J. E., "Xe^+-Sputtered Molybdenum Properties at Low Impingement Energy," IEPC-2005-194, 29th International Electric Propulsion Conference, Princeton, NJ., Oct. 31-Nov. 4, 2005.

183. Duchemin, O. B., Brophy, J. R., Garner, C. E., Ray, P. K., Shutthanandan, V., Mantenieks, M. A., "A Review of Low Energy Sputtering Theory and Experiments," IEPC-97-068, 25th International Electric Propulsion Conference, Cleveland, OH, August 24-28, 1997.

184. Kolasinski, R. D., Polk, J. E., "Characterization of Cathode Keeper Wear by Surface Layer Activation," AIAA-2003-5144, 39th Joint Propulsion Conference, Huntsville, AL, July 20-23, 2003.

185. Vincenti, W. G., Kruger, C. H., *Introduction to Physical Gas Dynamics*, Krieger Publishing Company, Malabar, FL., 1965.

186. Nakles, M. R., "Experimental and Modeling Studies of Low-Energy Ion Sputtering for Ion Thrusters," Masters Thesis, Dept. of Aerospace Engineering, Virginia Polytechnic Institute and State University, Blacksburg, VA, 2004.

187. Wilhelm, H. E., "Quantum-statistical Analysis of Low-Energy Sputtering," Australian Journal of Physics, Vol. 38, No. 2, pp. 125-133, 1985.

188. Stuart, R. V., Wehner, G. K., "Sputtering Yields for Low Energy He^+-, Kr^+-, and Xe^+-Ion Bombardment," Journal of Applied Physics, Vol. 33, No. 5, pp. 1842-1845, May 1962.

189. Duchemin, O. B., "An Investigation of Ion Engine Erosion by Low Energy Sputtering," Doctoral Thesis, California Institute of Technology, Pasadena, CA, 2001.

190. Goebel, D. M., Jameson, K. K., Katz, I., Mikellides, I., "Energetic Ion Production and Keeper Erosion in Hollow Cathode Discharges," IEPC-2005-266, 29th International Electric Propulsion Conference, Princeton, NJ., Oct. 31-Nov.4, 2005.

191. Smith, T. B., "Deconvolution of Ion Velocity Distributions from Laser-Induced Fluorescence Spectra of Xenon Electrostatic thruster Plumes," Doctoral Thesis, Dept. of Aerospace Engineering, University of Michigan, Ann Arbor, MI, 2003.

192. Kolasinski, R. D., Polk, J. E., "Cathode Keeper Orifice Wear Measurements Using Surface Layer Activation," AIAA-2005-3664, 41st Joint Propulsion Conference, Tucson, AZ, July 10-13, 2005.